Glass-Ceramics for Ceramic/Ceramic and Ceramic/Metal Joining Applications

Richard Simon Dobedoe

Thesis submitted for the award of
Doctor of Philosophy

Department of Physics
Centre for Advanced Materials

September 1997

Contents

List of Figures

List of Tables

Acknowledgements

First and foremost, my thanks go to Diane Holland for her unflagging support and guidance. Thanks to TWI UK and to EPRSC for financial assistance, and to Dr Wendy Hanson of TWI for technical and moral support.

None of this work would have been possible without the technical expertise provided by Keith Briggs, Dave Hammond, Dan Lee, Gerry Smith and Steve York, and the encouragement of my other friends and colleagues within the Department of Physics.

Finally, my thanks go to Anne, her parents and mine, for their tremendous support throughout the past four years. This thesis is dedicated to my son, Christopher, who has done his best to keep me entertained for the past 19 months.

Richard Dobedoe

Declaration

This thesis is entirely my own work unless otherwise referenced and has not been submitted for the award of a degree at any other university. The thesis is set out as per the guidelines issued by Warwick Graduate School (September 1996). Parts of this work have appeared in the following publications:

Dobedoe R.S., Holland D. and Hanson W.B., "Strength and microstructure of silicon nitride ceramics joined using magnesium aluminosilicate glass-ceramics", Joining Ceramics, Glass and Metal (1997), DVS Berichte pp.23-26.

Dobedoe R.S., Holland D., and Hanson W.B., "Bonding silicon nitride using glass-ceramic", Key Engineering Materials Vols. 99-100 (1995), pp.233-240.

Summary

The use of sintered cordierite/enstatite glass-ceramics as interlayers for joining silicon nitride to itself and to metals has been investigated. The role of the additives B_2O_3 and P_2O_5, which control the dynamics of sintering and crystallisation, has been studied using SEM, XRD and non-isothermal DTA-based measurements of activation energy. The measured activation energies for the crystallisation of μ-cordierite, for compositions with no additives, with B_2O_3 only, and with P_2O_5 only, did not differ significantly and were in the range 415-460 kJ mol^{-1}. When both B_2O_3 and P_2O_5 were present this was increased to 503-524 kJ mol^{-1}. The activation energy for α-cordierite formation when no additives were present was 952 ± 57 kJ mol^{-1}. This was substantially reduced by the presence of B_2O_3 (540 ± 27 kJ mol-1), P_2O_5 (668 ± 41 kJ mol^{-1}) and when both were present (352 ± 26 kJ mol^{-1}).

Cordierite/enstatite glass-ceramics have been successfully used to join silicon nitride to itself. Joining at 1050-1100°C in N_2 with an applied load of ~ 2.5 MPa, resulted in joint strengths, measured in 4-pt bending, of 110-170 MPa. This is comparable to the intrinsic strength of the glass-ceramic and sufficient for practical applications. These strengths were obtained using an interlayer with a TCE (5.7 MK^{-1}) greater than that of the silicon nitride (3.0 MK^{-1}). Suggestions for further improvements to the joint strength are discussed.

The use of a glass-ceramic joint with graded thermal expansion to bridge a TCE mismatch is discussed, and the geometrical restrictions on the joint, which limit possible practical applications, are outlined.

The concept of a ceramic/metal compression joint with a glass-ceramic interlayer has been demonstrated for joining silicon nitride to both Nimonic alloy 80A and Ti. The requirements for continuity of electronic structure at the Nimonic 80A/glass-ceramic and the Ti/glass-ceramic interfaces are satisfied by reaction between the glass/glass-ceramic and, the pre-oxidised surface of the Nimonic alloy to form a $MgTi_2O_5$-Al_2TiO_5 solid solution phase, and the Ti to form Ti_5Si_3. For the lower TCE mismatch (Ti-silicon nitride) the residual joining stresses generated on cooling were marginally too high and need to be further reduced, either by a slight alteration to the joint geometry and/or a smaller TCE mismatch.

Chapter 1: Introduction

1.1 Overview

The range of satisfactory joining solutions available for joining ceramics, both to themselves and to metals, for high temperature applications is limited. Joining materials where a significant thermal coefficient of expansion (TCE) mismatch exists is still a major problem.

The class of materials known as glass-ceramics offer an attractive combination of properties for some joining applications. They offer many of the advantages of glass together with improved mechanical and high temperature properties, and greater flexibility and control of thermal expansion.

1.2 Aim of the thesis

The objective of the following work, was to investigate the use of glass-ceramics as joining media. The possibility of using them to join like materials, and differing materials where a thermal expansion mismatch exists, has been studied.

One of the initial aims of this project was to investigate the possibility of producing a glass ceramic joint, with graded thermal expansion, to bridge the thermal expansion mismatch between Nimonic 80A and silicon nitride. A further objective was the use of a glass-ceramic interlayer for joining silicon nitride to itself for high temperature applications.

The glass ceramic system chosen was a sintered cordierite/enstatite glass-ceramic, due to the good mechanical and high temperature properties, and the flexibility of TCE offered by this system. Some effort has been directed towards improving the understanding and control of the microstructural development, and the role played by minor additives (B_2O_3 and P_2O_5).

1.3 Thesis structure

This thesis consists of 8 chapters of which this is the first. The contents of the other chapters are given below.

Chapter 2 gives a brief review of glass-ceramics including an overview of their properties, an outline of basic nucleation theory and a consideration of surface nucleation. This is followed by a detailed review of sintered cordierite-enstatite glass-ceramics. The structure of the cordierite and enstatite polymorphs and the properties of the resulting glass-ceramics are considered. In particular, the microstructural development, and the role of P_2O_5 and B_2O_3 in sintered cordierite based glass ceramics are discussed.

Chapter 3 considers the problems that must be solved, and the compromises involved, when joining ceramics to themselves and to other materials for high temperature use. The requirements for successful joints are discussed, together with the limitations of current solutions. This includes a brief review of the problems due to residual thermal stress, with typical, and more novel, approaches to solving this problem discussed. The possibilities, and limitations, of using a joint with a graded thermal expansion to bridge a TCE mismatch are considered. The choice of the optimum TCE for an interlayer between like materials is also discussed and the use of glass-ceramics for joining applications, and their advantages and limitations for graded joint applications are considered.

In order that the results presented in Chapters 6 and 7 may be seen in context, the interactions between glass-ceramics and both Nimonic alloy 80A and titanium are considered briefly, together with solutions for joining silicon nitride to itself and to metals. Finally, the outlook for joining of ceramics and the likely role of glass-ceramics in joining applications are discussed.

Chapter 4 briefly describes the experimental techniques used in this work.

Chapter 5 presents results from a study of the microstructural development of MAS glass-ceramics. The effect of B_2O_3 and P_2O_5 on the microstructural development is discussed, together with their effect on the apparent activation energy for crystallisation as measured using non-isothermal DTA methods. Results illustrating the problems encountered when using a glass-ceramic to bridge a TCE mismatch are presented. Finally, the results of an attempt to produce enstatite based glass-ceramics with high fracture toughness are reported.

Chapter 6 presents the results of joining silicon nitride to itself using a glass-ceramic interlayer. The microstructure of, and reactions at the interface are described, together with the results of mechanical testing and suggestions for improved joint

strength. The strength of the silicon nitride used in the joining trials is also measured and consideration given of how this is affected by the joining heat treatment.

Chapter 7 presents the results of joining trials, between silicon nitride and both Nimonic alloy 80A and titanium, using a glass-ceramic interlayer and examines the resulting interfacial microstructure and chemistry. The concept of ceramic-metal joining using a compression joint with a glass-ceramic interlayer is successfully demonstrated using titanium and silicon nitride.

Chapter 8 presents overall conclusions from the results of this work, together with some suggestions for future work.

Note: The references are presented at the end of each chapter

Chapter 2: Glass-ceramics

2.1 Introduction

In this project, the focus has been on the use of sintered cordierite-enstatite glass-ceramics as media for joining similar and dissimilar materials. A considerable amount of work has previously been performed at Warwick on this system [1][2][3][4] and so some of the experimental effort has been aimed at answering some of the questions raised, but not answered, by the previous work.

Sections 2.1 to 2.4 present a brief overview of glass-ceramics, an outline of basic nucleation theory and a consideration of surface nucleation in sintered glass-ceramics. An overview of the properties of glass-ceramics in general, particularly those relevant to joining applications, is given in Sections 2.5 and 2.6.

Section 2.7 onwards considers MAS glass-ceramics in more detail. A brief account of some of the more important earlier work on the system is followed by a clarification of the structure of, and relationship between, the different cordierite and enstatite polymorphs. The properties of the constituent phases and the resulting glass-ceramics are then discussed, leading to a more detailed look at the microstructural development and role of P_2O_5 and B_2O_3, in sintered cordierite based glass-ceramics.

2.2 Definition

Glass-ceramics are defined as polycrystalline solids prepared by the controlled crystallisation of glasses [5]. The resulting materials are usually isotropic and are distinguished by their very fine and uniform microstructure. Crystallite sizes typically vary from 20nm [6] to a few μm. One or more crystalline phases may be present, and there may also be some residual glass. The actual quantity of glass can vary considerably, from being the major phase present to existing only at isolated pockets or grain boundaries.

Glass-ceramics can be produced either by the controlled heat treatment of a bulk glass, enabling bulk glass manufacturing procedures to be used, or via a sintered powder route which allows the use of various powder processing techniques. Glass-ceramics with zero porosity are achievable when crystallised from the bulk route, and

densities > 99% [7] of the theoretical density are possible for the sintered route. A typical microstructure of a sintered cordierite-enstatite glass-ceramic is shown in Figure 2.1.

Among the factors that contribute to the exceptional combination of properties that are sometimes achieved are: the fine microstructure; the accessibility of phases and combinations of phases, often metastable, that could not be easily produced via a conventional ceramic route, and the fact that many phases can be obtained at a lower temperature than would be possible using a conventional ceramic route. These factors, along with the flexibility arising from the versatility of the available production routes, have lead to the increased use of glass-ceramics. Two of the best known applications are ceramic cooker hobs and astronomical telescope mirror substrates. An excellent account of the development of both of these is given by Bach [6].

A detailed discussion of the properties and uses of glass-ceramics is beyond the scope of this work: more details can be found in McMillan [5], Strnad [8], Bereznoi [9], and, more recently Smith [10], James [11], Partridge [12] and Bach [6]. The properties of glass-ceramics relevant for joining applications are discussed in section 2.4.

2.3 Theory of nucleation and crystallisation

Critical to the production of glass-ceramics is the concept of controlled crystallisation. This implies the careful choice of composition and heat treatment resulting in the nucleation and growth of crystalline phases. In order to produce a glass-ceramic with a fine, even microstructure, a high density of nucleation sites is required, typically 10^{10}-10^{15}mm^{-3} [13]. These sites can arise due to either homogeneous or heterogeneous nucleation. In homogeneous nucleation, the structure and composition of the initial seeds are the same as the crystals that grow on them, whereas in heterogeneous nucleation, the resulting crystals are of a different composition to the initial seeds.

2.3.1 Homogeneous nucleation

In the classical theory of homogeneous nucleation, regions of long range order, termed embryos, are considered to arise due to statistical variations of the structure of the parent phase.

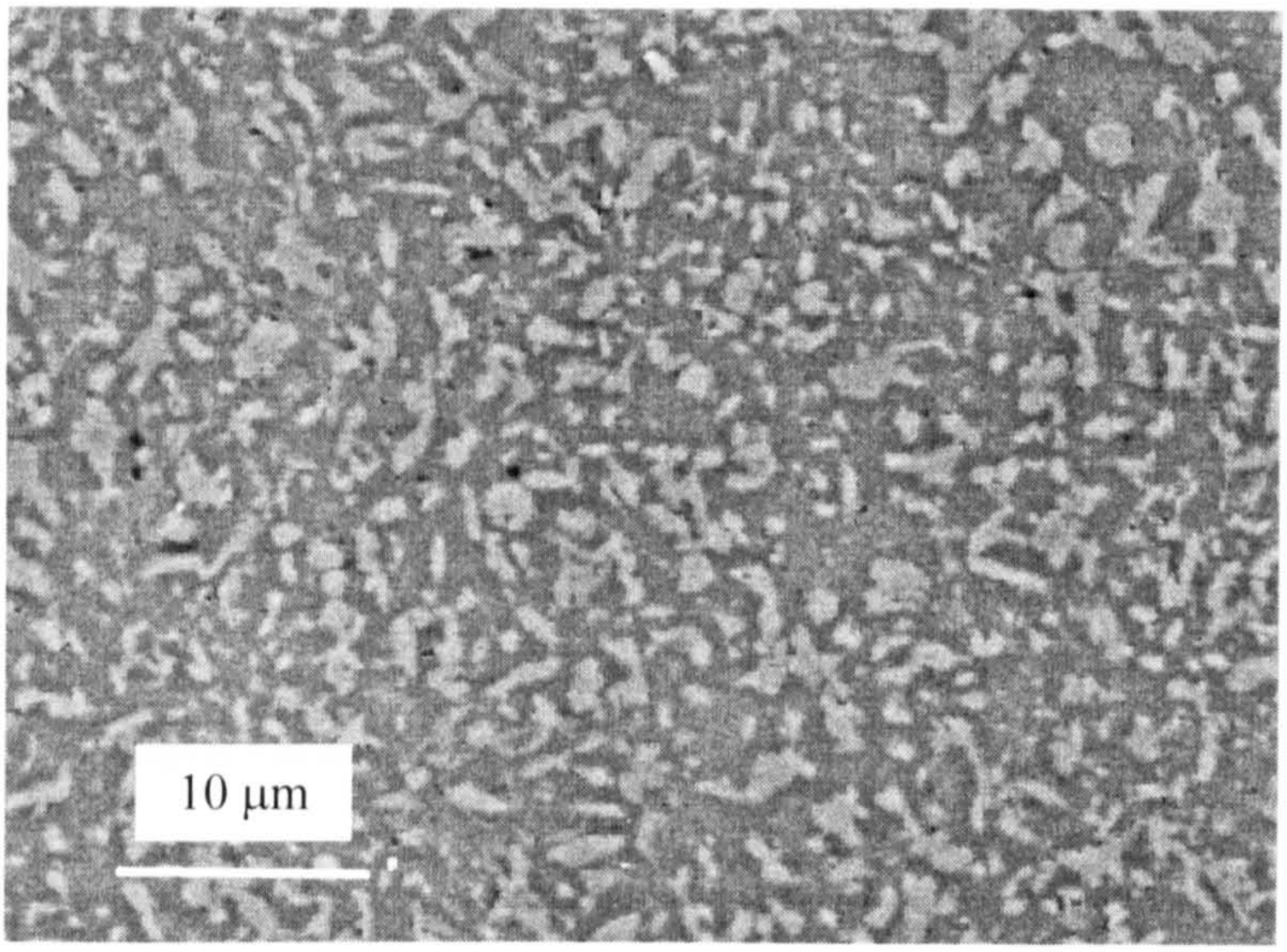

Figure 2.1: Typical microstructure of a cordierite/enstatite glass-ceramic. The dark phase is cordierite and the light phase is enstatite.

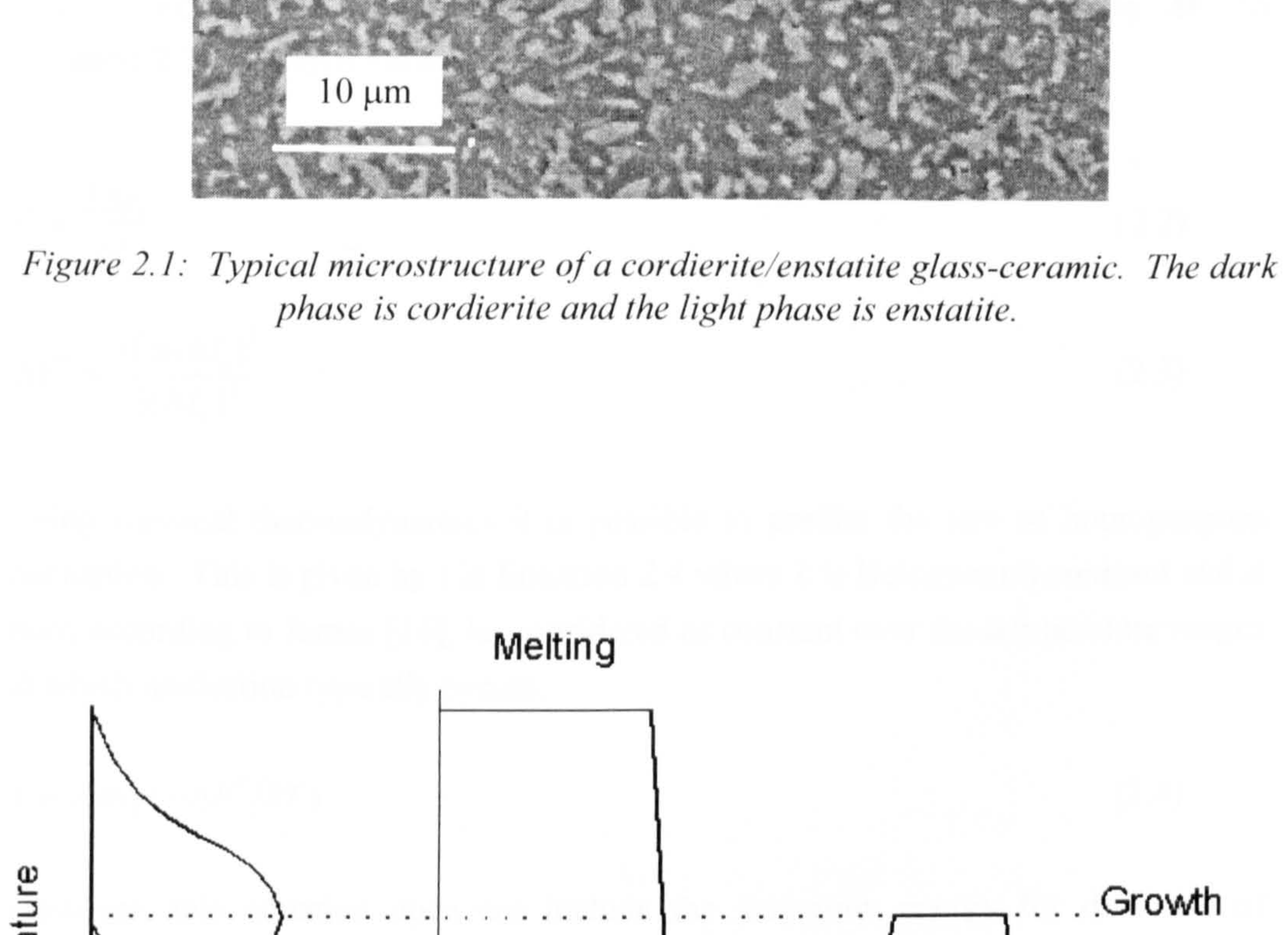

Figure 2.2: Relationship between the classical time-temperature profile for the production of a glass-ceramic and rates of nucleation and growth.

The change in free energy ΔF for a spherical embryo of radius r is given by equation 2.1, where Δf_v is the change in free energy per unit volume arising from the transition and Δf_S is the energy change per unit area of surface between the two phases.

$$\Delta F = -\tfrac{4}{3}\pi r^3 \Delta f_v + 4\pi r^2 \Delta f_s \qquad (2.1)$$

It can be shown that for an embryo to be stable it must exceed a critical radius given by r^* in Equation 2.2, with a corresponding critical free energy given by ΔF^* in Equation 2.3. Embryos exceeding this critical size are termed nuclei.

$$r^* = \frac{2\Delta f_s}{\Delta f_v} \qquad (2.2)$$

$$\Delta F^* = \frac{16\pi(\Delta f_s)^3}{3(\Delta f_v)^2} \qquad (2.3)$$

Using classical thermodynamics it is possible to predict the rate of homogeneous nucleation. This is given by I in Equation 2.4 where k is Boltzmann's constant and A may, according to James [14], be considered as constant over the temperature ranges at which nucleation typically occurs.

$$I = A\exp(-\Delta F^*/kT) \qquad (2.4)$$

However, this equation does not include the activation energy for diffusion of molecules across the phase boundary, which is significant in a highly viscous medium. This can be adjusted for by introducing a term to include the kinetic free energy barrier to nucleation ΔG_D:

$$I = A\exp[-(\Delta F^* + \Delta G_D)/kT] \qquad (2.5)$$

At small supercoolings, the term ΔF^* is small and ΔG_D dominates resulting in a negligible nucleation rate. With increased supercooling, the term ΔF^* increases and in turn starts to dominate. As a result the nucleation rate rises. As the temperature is reduced still further, the increased viscosity of the glass results in the kinetic term, ΔG_D, once again dominating and reducing the nucleation rate. This results in the nucleation rate passing through a maximum with respect to supercooling. The

critical radius, r^*, also increases with temperature due to the volume free energy term in Equation 2.2 diminishing.

The combined effect is a metastable zone of supercooling, in which nuclei do not form at a detectable rate. In this zone, however, crystals can grow if nuclei are provided. In a similar manner, the crystal growth rate also passes through a maximum. As supercooling increases, so does the difference in free energy between the glass and crystal structure. This represents the driving force for crystal growth, the rate of which therefore increases. With further cooling, the rate of crystal growth decreases due to the rise in viscosity increasing the kinetic barrier to growth.

The shape of the nucleation and growth rate curves can be used to understand the classical time-temperature profile for the production of a glass-ceramic, as shown in Figure 2.2. Both crystallisation and nucleation rates pass through a maximum. The separation of the maxima enables the nucleation and growth to be separately controlled, so that growth occurs at the required high density of sites for the production of a fine-grained glass-ceramic.

Homogeneous nucleation is rare in practice but has been observed in some silicate glasses [14].

2.3.2 Heterogeneous nucleation

Heterogeneous nucleation reduces the energy barrier for nucleation. For nucleation on pre-existing surfaces, the activation energy for heterogeneous nucleation is given by:

$$\Delta F^*_{het} = \Delta F^* f(\theta) \qquad (2.6)$$

θ is the contact angle at the heterogeneity-melt-nucleus junction. For a nucleus on a flat substrate, f(θ) is given by:

$$\mathrm{f}(\theta) = \frac{(2+\cos\theta)(1-\cos\theta)^2}{4} \qquad (2.7.)$$

The nucleation rate for heterogeneous nucleation is then given by:

$$I = A\exp[-(\Delta F^*_{het} + \Delta G_D)/kT] \qquad (2.8)$$

For any contact angle, θ, less than 180° (total non-wetting) the free energy barrier for nucleus formation on the surface of the heterogeneity is lower than that for homogeneous nucleation. As a result, heterogeneous nucleation normally occurs in preference to homogeneous nucleation.

The requirements for efficient heterogeneous nucleation, normally considered as due to epitaxial growth on precipitated crystalline phases, are given as: a disregistry of less than 15% on low index planes, and low interfacial tension between the nucleation catalyst and the primary crystal phase [5].

One of the clearest examples of heterogeneous nucleation is the growth of lithium disilicate crystals on metallic colloids previously precipitated by the catalytic use of UV light, as discovered by Stookey and co-workers at Corning.

However, the most common nucleation agents are oxides and particularly TiO_2, ZrO_2 and P_2O_5. Although there is evidence that in some instances these act as simple nucleation agents in the manner previously described [15], it is now realised that the primary process of controlled crystallisation in glass is controlled microphase separation [16]. If we consider a conventional glass-ceramic profile, the first hold in many commercial glass-ceramic systems induces glass-in-glass phase separation to a pre-crystalline state. Nucleation occurs just prior to crystallisation. This may either be homogeneously within the compositionally altered phase or heterogeneously at the boundary between the phases.

2.4 Sintered glass-ceramics

Although most commercial glass-ceramics are produced by volume nucleation, glass-ceramics can also be produced by relying on the tendency of glasses to surface nucleate. In this case, the glass is ground to a fine powder, typically 1-20 μm, to provide the required high density of nucleation sites for the production of a fine grained glass-ceramic. Densification, which occurs initially by viscous flow, may either occur prior to or simultaneous with crystallisation, in which case, the viscosity of the glass in the sintering range increases dramatically. Although this promotes shape retention it must be balanced with problems associated with increased viscosity. Sintering to full density may be prevented and wetting problems may be encountered if the glass-ceramic is being used for joining or coating applications.

However, sintered glass-ceramics have further advantages: lower temperature production; simpler, shorter firing schedules are possible as separate nucleation and sintering holds are not always required, and they may enable the use of less stable glass formers in that such compositions often require cooling rates that are prohibitively high for the production of glass-ceramics from a bulk route.

Because of the additional possibilities offered by sintered glass-ceramics, it is worthwhile to consider in a little detail the mechanisms associated with the surface nucleation of glasses.

2.4.1 Surface nucleation

Surface nucleation in glasses often occurs more readily than bulk nucleation. For example, Strnad and Douglas [17] have shown that a smaller undercooling is required for surface nucleation. An important question is whether the surface is inherently favoured as a nucleation site, or if nucleation occurs more readily at the surface due to the presence of heterogeneities.

The evidence on internal surfaces, which perhaps suffer least from contamination, is mixed. Bergeron et al [18] and Klingsberg [19] report crystallisation on internal surfaces, while Morey [20], Mattox [21], and Scott and Pask [22] report its absence. Neely and Emsberger [23] report nucleation only on internal bubbles containing graphite contaminants.

Uhlmann [24] has demonstrated, based solely on surface energy considerations that the surface is not inherently favoured for nucleation. This is based on the experimental observation that surface melting of quartz and albite crystals, occurs at negligible superheats, resulting in the almost complete wetting of the crystal. This implies that $\gamma_{sv} \geq \gamma_{sl} + \gamma_{lv}$, whereas the preferred formation of a nucleus on the surface would imply that $\gamma_{sv} \leq \gamma_{sl} + \gamma_{lv}$ (γ is the specific surface free energy and s, l and v refer to the solid, liquid and vapour phases). He suggests that crystal nucleation at internal or external surfaces is associated with condensed second phase impurities.

However, glass forming liquids are viscoelastic, that is viscous liquids with an elastic response. Schmelzer et al [25] have shown that if this is taken into account, the elastic strains resulting from crystallisation significantly reduce the thermodynamic driving force for devitrification in the bulk of the glass. This effect is diminished at or near the surface.

Other suggestions for surface nucleation being inherently favoured include: compositional variation due to selective volatilisation, and the increased mobility of species at or near the surface [26].

Whether or not the surface is inherently favoured for nucleation, as appears to be the case, the extent of surface nucleation is strongly dependent on the nature of the surface. Tabatha [27] showed that nucleation is favoured by the presence of surface defects such as cracks or craters. Swift [28] reported that crystallisation occurs more readily on dirty compared to clean surfaces, and Zanotto [26] demonstrated that, for microscope glass slides, surface crystallisation can be reduced by mechanical polishing and eliminated by fire polishing. Treating a glass powder with HF [29], or strong alkali [30], to remove the highly damaged surface layer, has been found to greatly reduce the density of nucleation sites.

The catalytic effect of water on surface nucleation has been widely reported [22][26][29]. For example Scott and Pask [22] found that $Na_2O.2SiO_2$ glass did not crystallise when specimens were heat treated in dry air or a vacuum. This they attributed to surface crystallisation of Na(OH), which developed by reaction with water vapour either in the form of hydroxyl ions or molecular water. This is presumed to reduce Δf_s (Equation 2.1) and ΔG_D (Equation 2.5) due to hydroxyl groups replacing the bridging oxygens.

Current thinking is that surface nucleation occurs from active sites. The nature of these sites is generally not resolved and varies depending on the glass phase and the resulting crystalline phase. The number and nature of these sites is strongly dependent on the surface preparation.

The number of sites may be dominated by the time and temperature of any heat treatment [17], or the surface condition may dominate and the number not be substantially influenced by the time and temperature of any heat treatment [31][32]. Any heat treatment may result in either activation or deactivation of sites.

Nucleation at glass surfaces can be modelled by considering the possible mechanisms of nucleation and the nature of the active sites. Muller, Reinsch and Pannhorst [33] consider three possibilities: firstly, every site on the surface is capable of nucleation if subjected to the correct time and temperature treatment; secondly, potential active sites are present on the surface and can be converted to

nucleation sites by the correct heat treatment; and thirdly, sites may already be present and active. These possibilities give quite different profiles for areal density of nucleation sites as a function of time as shown in Figure 2.3. The saturation of the sites often occurs so quickly that it is difficult to determine whether the sites were already present and active prior to the heat treatment.

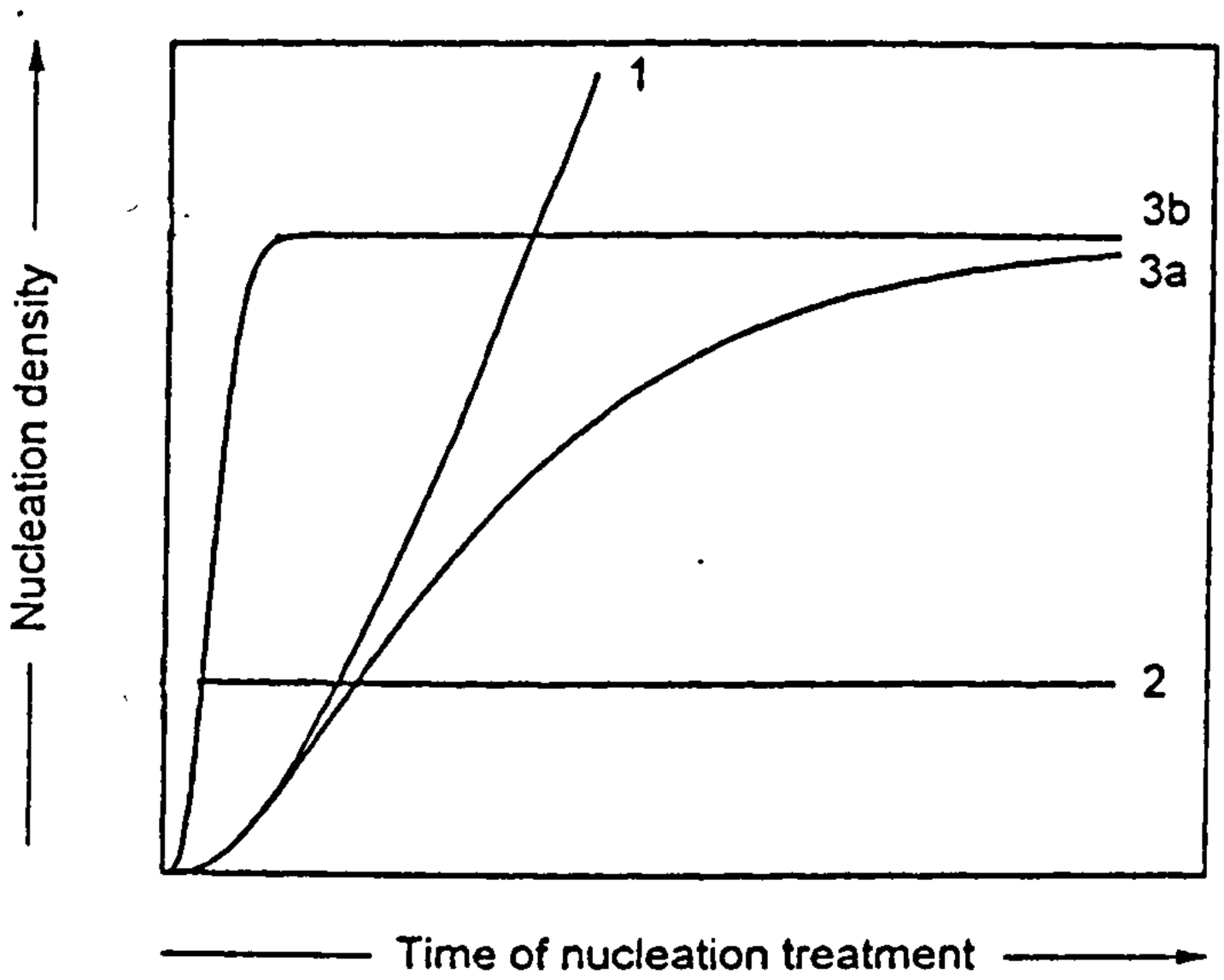

Figure 2.3: Areal density of nucleation sites as a function of time [33].

1. *Every site on the surface is capable of nucleation if subjected to the correct time and temperature treatment.*
2. *Sites are already present and active.*
3. *Potential active sites are present on the surface and can be converted to nucleation sites by the correct heat treatment (3a and 3b represent low and high nucleation rates at active sites).*

2.5 Properties of glass-ceramics

The use of glass-ceramics for joining applications offers significant benefits over competing technologies, due to their excellent high temperature performance, the wide range and flexibility of thermal expansion behaviour, and their mechanical strength and fracture toughness. For some applications other properties, such as thermal conductivity or dielectric constant may also be important.

The properties of glass-ceramics relevant for joining applications are discussed below. Similar considerations would apply where glass ceramics are used for coating applications.

2.5.1 Strength and fracture toughness

The fine, typically sub-micron, microstructure and near absence of porosity in glass-ceramics results in a small inherent defect size. As a result, glass-ceramics normally possess mechanical strengths superior to those of comparable conventional ceramics, in addition to having improved strength and fracture toughness compared to the parent glass.

The fine microstructure allows the use of phases, and combinations of phases, which would result in unacceptable microstresses in more coarsely grained materials, due either to TCE mismatch or thermal expansion anisotropy. In some instances, the resulting microstresses may be used in a positive manner to strengthen and increase the fracture toughness of the glass-ceramic.

Mechanical properties are highly sensitive to testing method, surface condition, specimen size, geometry and preparation. Typical reported results for strength and fracture toughness of glass-ceramics are shown in Table 2.1. It can be seen that the strength and fracture toughness of glass-ceramics still fall short of those obtained by engineering ceramics, although recent reported figures, such as those reported by Beall [34], appear to bridge the performance gap slightly. In this case, the improved fracture toughness is due to the incorporation of microstructural toughening features and is discussed in detail in section 2.7. Similar figures may be obtained by particulate reinforcement [35][36].

Table 2.1: Typical mechanical properties for glasses, glass-ceramics, technical and conventional ceramics

Material	**Fracture Toughness (K_{IC}) MPam$^{1/2}$**	**Strength MPa**
Glasses		
Aluminosilicate glass	0.91 [37]	-
Soda-lime-silicate glass	0.75 [37]	65 [38]
Glass-ceramics		
Lithium aluminosilicate (high quartz)	-	100 [6]
Lithium aluminosilicate (keatite)	-	150 [6]
Corning 9606	1.6-2.1 [39]	123-370 [39]
Enstatite based	4.6 [34]	200 [34]
Conventional ceramics		
Aluminous porcelain	-	120 [38]
Engineering ceramics		
Sintered silicon nitride	5.0-8.5 [37]	600-1200 [37]
99.5% Alumina	4.2-5.9 [37]	379 [37]

It is likely that further improvements to the strength and fracture toughness of glass-ceramics are possible by incorporation of microstructural toughening mechanisms, and understanding and controlling thermal expansion mismatch between the crystalline phases and any residual glass.

2.5.2 Thermal expansion

The thermal coefficient of expansion (TCE) of a polycrystalline material can be estimated by the weighted sum of the properties of the individual phases present. Turner's formula as shown in Equation 2.9 is normally considered a reasonable model of the thermal expansion of a glass-ceramic, where α_i, V_i and K_i represent the thermal expansion, volume fraction and bulk modulus of the individual phases present.

$$\alpha = \frac{\sum_{i=1}^{n} \alpha_i V_i K_i}{\sum_{i=1}^{n} V_i K_i} \qquad (2.9)$$

It is possible to produce silicate and aluminosilicate glass ceramics with a wide range of TCEs, from slightly negative, to values which enable expansion matching with high temperature alloys (15-20 MK^{-1}). Materials with particularly high TCE often rely on the volume increase arising from displacive phase changes from the high to the low form of SiO_2 polymorphs (quartz, tridymite and cristobalite) to contribute to the thermal expansion. If the microstructure of the glass-ceramic is too coarse, or the thermal expansion mismatch between the phases too large, microcracking can result. Thermal expansion hysteresis is then displayed, resulting in a reduced TCE. Because of the fine microstructure, this is not normally a problem in a typical glass-ceramic.

The degree of control possible over thermal expansion is illustrated by Zerodur, a commercial lithium aluminosilicate based glass-ceramic, originally developed for astronomical telescope mirror substrates. The negative thermal expansion of the lithium and zinc stuffed β-quartz phases is balanced by the positive thermal expansion of the magnesium stuffed β-quartz and the residual glass. The resulting thermal expansion is close to zero and can be accurately controlled so that figures such as TCE 0 ± 0.02 MK^{-1} can be quoted [6].

Silicate glasses can also be produced with a wide range of TCEs. However links between the TCE and the glass transition temperature are such that high thermal expansion glasses are unsuitable for high-temperature applications. Glass-ceramics do not suffer from this problem, as the high TCE is caused by the presence of high TCE crystalline phases which may, if required, be specifically chosen because of their high temperature properties.

2.5.3 Upper use temperature

Glass-ceramics are normally more refractory than the parent glass, and may sometimes withstand long term use at temperatures in excess of those used in their production. The high temperature performance is often governed by the composition, quantity and distribution of residual glass. The upper use temperatures for specific systems are discussed in section 2.6 & 2.7.

2.5.4 Other properties

Crystallisation of a glass usually results in improved resistance to chemical attack. An interesting exception to this is lithium silicate 'fotoform' glass-ceramic, where the initial crystallisation product, the development of which is catalysed by exposure to ultra-violet light, can be preferentially etched away. The remaining glass can then be crystallised to a more stable phase to produce the final glass-ceramic product.

The transport properties of a glass-ceramic, such as thermal or electrical conductivity, are generally determined by the quantity and the distribution of the individual phases. For example, where the glass-ceramic microstructure consists of a dispersed phase in a matrix phase, the transport properties may be dominated by the matrix phase, as modified by the dispersed phase.

2.6 Some important glass-ceramic systems

Before magnesium aluminosilicate glass-ceramics are considered in detail, it is relevant to consider key points relating to some of the more important glass-ceramic systems. Recent summaries of values reported in the literature include McHale [40] for general physical properties, and Donald [41] who gives a good summary of reported thermal expansion values for a wide variety of glass-ceramic compositions.

2.6.1 Lithium aluminosilicate (LAS)

Lithium aluminosilicate (LAS) is probably the most important commercial glass-ceramic due to its exceptional dimensional stability and excellent thermal shock resistance. This occurs because LAS glass-ceramics exist with TCEs ranging from slightly negative, through zero, to slightly positive. These are possible due to the availability of crystalline phases with a slightly negative (Li stuffed β-quartz phases) and slightly positive (β-spodumene) TCE.

The high temperature performance of these glass-ceramics is limited. Creep occurs at temperatures in excess of 600°C , with a maximum use temperature with no load of 800-900°C [40].

2.6.2 Lithium silicate (LS)

High TCE lithium silicate (LS) glass-ceramics (8-19 MK^{-1}) can be produced by incorporating lithium disilicate, lithium metasilicate and quartz polymorphs, enabling thermal expansion matching with high temperature alloys. Once again the high temperature performance is limited.

2.6.3 Lithium zinc silicate (LZS)

Lithium zinc silicate phases and quartz polymorphs enable the production of medium to high TCE glass ceramics capable of expansion matching to a variety of metals including steel and Nimonic alloys. It has been shown that further control of the thermal expansion is possible by the addition of small quantities of transition metal oxides which strongly affect the crystallisation behaviour [42]. The T_g of the residual glass is around 530°C [43], so long term use under load would be restricted to low temperatures.

2.6.4 Other silicate/aluminosilicate glass-ceramics

Several other glass-ceramic systems are of interest, for example calcium aluminosilicate (CAS) and barium aluminosilicate (BAS). In some instances these may offer specific properties superior to those of MAS glass-ceramics. For example, BAS-based glass-ceramics have been developed, for composite matrix applications. Their superior high temperature properties rely on the presence of either celsian [44] or osumilite [45]. However, these systems have not yet been shown to offer the combination of attractive properties available from compositions within the MAS ternary system.

2.7 Magnesium aluminosilicate (MAS)

2.7.1 MAS - Introduction

The magnesium aluminosilicate (MAS) ternary, shown in Figure 2.4, is of historical and commercial significance for the development of glass-ceramics. The most important phase specific to the MAS system is cordierite, due to its low TCE, and good mechanical and high temperature properties. This has lead to its use in a wide range of conventional ceramic applications, from electrical porcelains [46] to substrates for automobile catalytic converters [47] and diesel particulate traps [48].

Figure 2.4: The magnesium aluminosilicate (MAS) ternary equilibrium phase diagram [49]

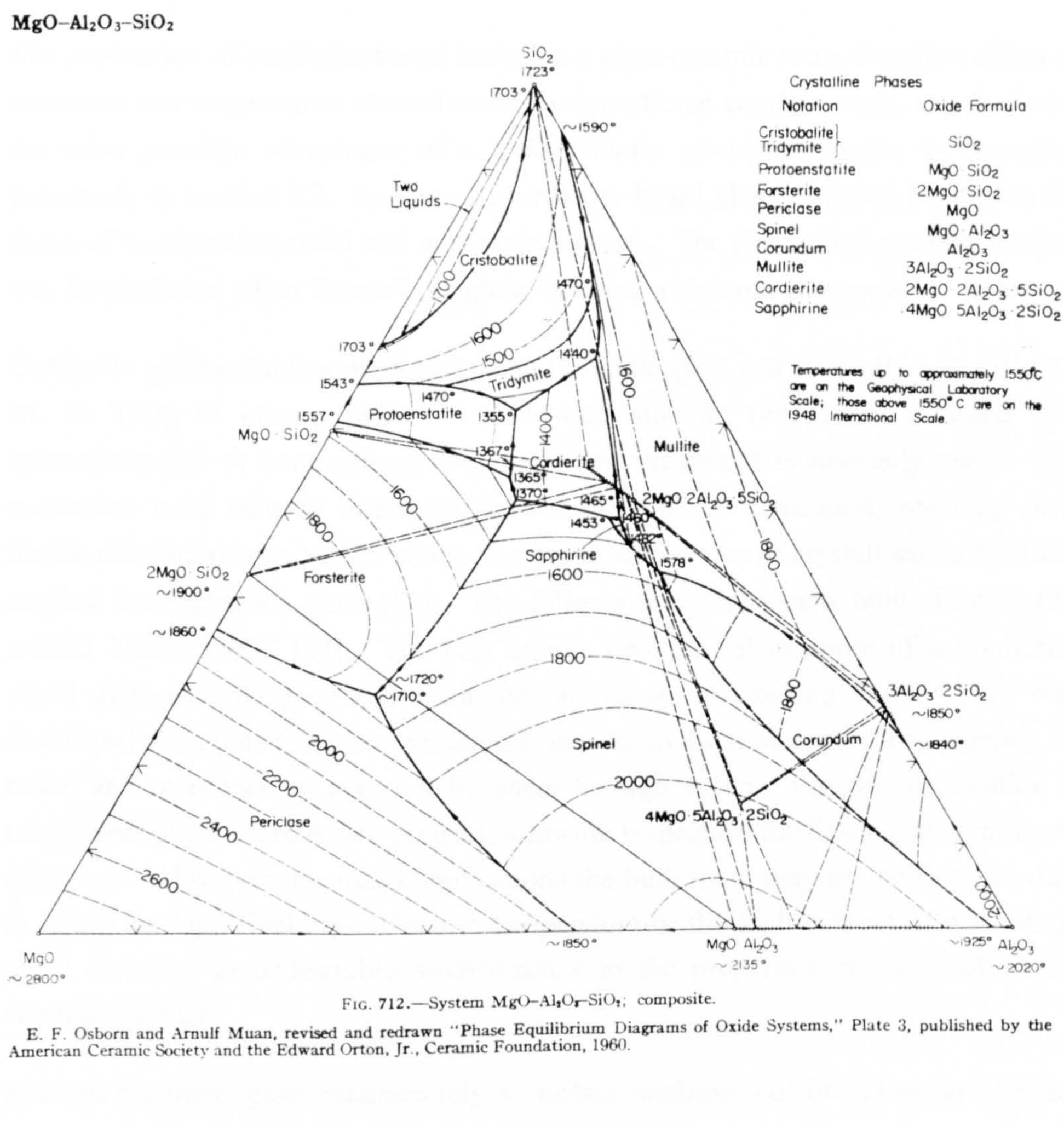

FIG. 712.—System $MgO–Al_2O_3–SiO_2$; composite.

E. F. Osborn and Arnulf Muan, revised and redrawn "Phase Equilibrium Diagrams of Oxide Systems," Plate 3, published by the American Ceramic Society and the Edward Orton, Jr., Ceramic Foundation, 1960.

However, the production of fully dense and strong cordierite ceramics by a conventional ceramic route is not without difficulties. Cordierite melts incongruently at 1465°C, and sintering will only occur in a narrow window within 15 °C of this melting point [50]. An additional problem is caused by water molecules trapped within the channels of the cordierite structure, which are released as a vapour near the melting point of cordierite, resulting in cracks and porosity in the sintered body [51][52].

The production of cordierite-based items via a glass-ceramic route therefore offers an attractive low temperature alternative to a conventional ceramic route, together with the other possible advantages of a glass-ceramic production route, as discussed previously in Section 2.2. As a result, cordierite-based glass-ceramics have been the focus of much commercial and academic interest. The final glass-ceramic product may be produced either from a bulk glass, or using a sintered glass powder route.

Cordierite glass-ceramics produced using the bulk glass route usually rely on ~ 10 wt. % TiO_2 to ensure sufficient nucleation sites to obtain the required fine microstructure. A conventional two stage heat treatment is normally used. The nucleation hold induces fine-scale glass-in-glass phase separation, resulting in a titania-rich amorphous region which is more unstable toward crystallisation than the original homogeneous glass [53]. The following crystallisation hold is typically around 1250-1300°C [54]. The best known commercial example of a cordierite based glass-ceramic produced from the bulk route is Corning 9606. This was developed for guided missile nosecones, due to its high strength, transparency to radar, and resistance to abrasion by water at high speed. For this application a transparent glass intermediate product, allowing inspection for flaws, is a significant advantage. However, for many applications the bulk route may not be suitable, due to either the high final crystallisation temperature or the high content of nucleating agent resulting in undesirable modifications to the properties of the final glass-ceramic product.

Sintered cordierite glass-ceramics rely on surface nucleation of fine glass powders to provide the required fine microstructure and this makes possible the use of production methods associated with powder processing such as isostatic pressing, uniaxial pressing, tape casting and slip casting. Although additives are not necessary to enhance nucleation, they are normally required to control the dynamics of sintering and crystallisation. The addition of a few wt % B_2O_3 and P_2O_5 has been particularly successful in the production of strong, dense cordierite-based glass-ceramics.

The favourable dielectric properties of cordierite compared to alumina, and the ability to produce cordierite glass-ceramics at temperatures below 1000°C, enabling co-sintering with copper [9], has lead to considerable interest in the use of cordierite for electronic substrate applications [2][7]. Control of the thermal expansion, allowing the TCE to be matched to silicon, is possible by controlling the amount of a second phase present. This is usually enstatite [9][10], although mullite [55] can also be used. Cordierite/enstatite glass-ceramic substrates have been used on thermal conduction modules on IBM-390 mainframe computers [10]. By varying the enstatite content, cordierite-enstatite glass-ceramics can be produced with a wide range of TCE, from 1 MK^{-1} [56] to 12.8 MK^{-1} [4].

Cordierite based glass ceramics display superior high temperature properties to LS, LAS or LZS glass ceramics. Creep under load occurs at temperatures in excess of 900°C, with a maximum use temperature , with no load, of 1200°C [40]. There is scope to improve both of these figures by controlling the composition, distribution and quantity of residual glass phase. The favourable high temperature and mechanical properties of cordierite/enstatite glass-ceramics have also led to their consideration as potential matrix materials for high temperature ceramic matrix composite applications [57].

Enstatite glass-ceramics are of interest in their own right due to their exceptional mechanical properties and high temperature performance [34]. Other important glass-ceramics within the MAS ternary include: α-quartz based glass-ceramics with high strengths (400 ± 50 MPa) [16], and magnesium osumilite based glass-ceramics for high temperature composite applications [45].

The glass ceramics in the present work have been cordierite based with enstatite to control the thermal expansion. Traces of forsterite were also present. Sintered MAS glass-ceramics based on cordierite and enstatite are sufficiently refractory to offer benefits over competing joining technologies, with a sufficiently wide range of thermal expansion to investigate the prospects for joints with graded thermal expansion. Although TCE matching with high temperature Ni superalloys is not possible (TCE ~ 15 MK^{-1}) matching to Ti and Ti alloys (TCE ~ 10 MK^{-1}) can be achieved.

In the following sections the nomenclature and structure of the cordierite and enstatite phases are clarified. The properties of the constituent phases and the resulting glass-ceramics are then discussed in a little detail. Finally, the current

understanding of the microstructural development of sintered cordierite/enstatite glass ceramics and the effect of B_2O_3 and P_2O_5 on the crystallisation, sintering and microstructural development is presented.

2.7.2. Structure and properties of cordierite phases

There is considerable confusion in the literature over the naming of the cordierite polymorphs; the phases and their alternative names are set out in Table 2.2. The phase names used in the current work, shown in bold in Table 2.2, are consistent with current practice [58] [59] and in accordance with ASTM crystallographic data files. The drawback of this scheme is that β-cordierite was previously used for a metastable phase that could only be obtained hydrothermally at temperatures below 830°C [60] [61]. However, this phase is rarely encountered in glass-ceramics.

Table 2.2: Cordierite polymorphs

Phase name and alternatives	Chemical formula	JCDPS Ref	Density
μ-cordierite	$2MgO.2Al_2O_3.5SiO_2$	14-249	2.62
stuffed β-quartz	$MgO.Al_2O_3.3SiO_2$	25-511	2.59
β-quartz solid solution	$MgO.Al_2O_3.4SiO_2$	27-716	2.55
high-quartz solid solution			
α-cordierite	$2MgO.2Al_2O_3.5SiO_2$	13-293	2.51
Indialite			
high cordierite			
hexagonal α-cordierite			
β-cordierite	$2MgO.2Al_2O_3.5SiO_2$	13-294	2.50
low cordierite			
α-cordierite			
orthorhombic α-cordierite			
cordierite			

The reported thermo-mechanical properties of cordierite based glass-ceramics, for example the TCE, strength and fracture toughness, show a wide variation. This occurs because the properties are strongly affected by the microstucture, production

route, composition and thermal history. The structural relationship between polymorphs can also have a significant effect, for example transformations between polymorphs such as the μ-α cordierite transformation must occur without microcracking or weakening of the material. For the production of improved glass-ceramics, especially for joining applications, close microstructural control is required, with controlled thermal expansion and robust mechanical properties. This is more likely to be achieved if the structure of the individual phases and the transformations between phases, which are outlined below, are understood.

A detailed summary of the early work on cordierite (up to ~ 1972) was given by Gregory and Veasey [62]. A full description of the current understanding of the structure and relationships between the cordierite polymorphs is given by Putnis [63].

Structure of μ-cordierite

Schreyer and Schairer [64] showed that the structure of the μ-phase, which had previously been described as "silica O" by Roy [65], was a derivative of the structure of high quartz. Quartz itself is a framework silicate; a tetrahedral framework structure with every SiO_4 tetrahedron sharing each of its corners with one other SiO_4 tetrahedron. In quartz these are arranged in such a way that double helical chains of SiO_4 tetrahedra run parallel to the 'c' axis. Quartz exists in a hexagonal β-form (high quartz) at temperatures in excess of 573°C and transforms to the α-form (low quartz) on cooling. The transformation between the high and low polymorphs does not alter the topology of the SiO_4 tetrahedra, and is displacive, rapid and unquenchable. Further details on this phase transformation can be found in Griffen [66].

Quartz derivatives arise when Al^{3+} substitutes for, and takes the tetrahedral role of, Si^{4+}; electrostatic neutrality is maintained by "stuffing" cations into available interstices. These were termed stuffed derivatives by Buerger [67]. By substitution of aluminium for silicon and incorporation of metallic cations in the interstices, the high temperature form of quartz, β-quartz, can be stabilised. The resulting phases are also known as β-quartz solid solutions. The extent of solid solution that is possible in the magnesium aluminosilicate system was investigated by Shreyer and Schairer [64] who demonstrated that up to 58.7 wt % SiO_2 can be replaced by MgO and Al_2O_3, but were unable to investigate lower silica contents due to too high a liquidus temperature. Above 92 wt % silica the stabilising effect is reduced, and the β-α transition is seen but at much reduced temperatures.

Si^{4+} and Mg^{2+} can substitute for 2 Al^{3+} in the μ-cordierite structure and this results in shifts of x-ray diffraction lines to higher angles. This is followed by exsolution of Mg^{2+} and Si^{4+} from the μ-cordierite structure and leads to increased enstatite formation.

The occurrence of stuffed β-quartz solid solution phases in lithium aluminosilicates had previously been demonstrated by Winkler [68] and, given the similar size of the Mg^{2+} (0.66Å) and Li^{1+} (0.68Å) ions, the similarity of the behaviour is not surprising. Complete solid solution exists between the lithium and magnesium based stuffed high quartz aluminosilicates [69]. As a result of this, in Mg^{2+} based stuffed quartz materials Li^{1+} ion exchange can be used as a strengthening mechanism. This is partly due to the lower TCE of the surface lithium phase and partly due to the stuffing effect of the lithium ions [70].

Structure of α-cordierite

Cordierite, also a framework aluminosilicate, exists in two forms: orthorhombic low or β-cordierite stable up to 1450°C and hexagonal high or α-cordierite, the stable high temperature form, which is stable from 1450°C to the melting point of 1465°C. Naturally occurring orthorhombic forms are known as cordierites; naturally occurring hexagonal cordierites were first found in fused clay shales from Vakaro in India and hence hexagonal cordierites are known as Indialites.

The cordierite structure, shared by both the α and β forms, is shown in Figure 2.5, and consists of 6-fold rings of Si (or Al) tetrahedra (termed T2) stacked along the 'c'-axis and joined laterally and vertically by tetrahedra (termed T1) which may also contain Si or Al. Charge compensation occurs by the incorporation of cations into the structure. In the case of magnesium, the cations occupy octahedral sites between the rings. The channels within the cordierite structure, which can be viewed on a TEM with dramatic results [63], have a radius of 2.2Å and can accommodate a wide range of ions (e.g. Na^{+}, Cu^{2+}, Fe^{2+}) and molecules (H_2O, CO_2).

The transition between the hexagonal and orthorhombic forms of cordierite can be understood in terms of ordering of the aluminium and silicon tetrahedra. In orthorhombic cordierite there is a full ordering of the aluminium and silicon tetrahedra so that there are no Al-O-Al linkages. Hexagonal symmetry results from a degree of disorder in the distribution of the Al and Si tetrahedra.

(a)

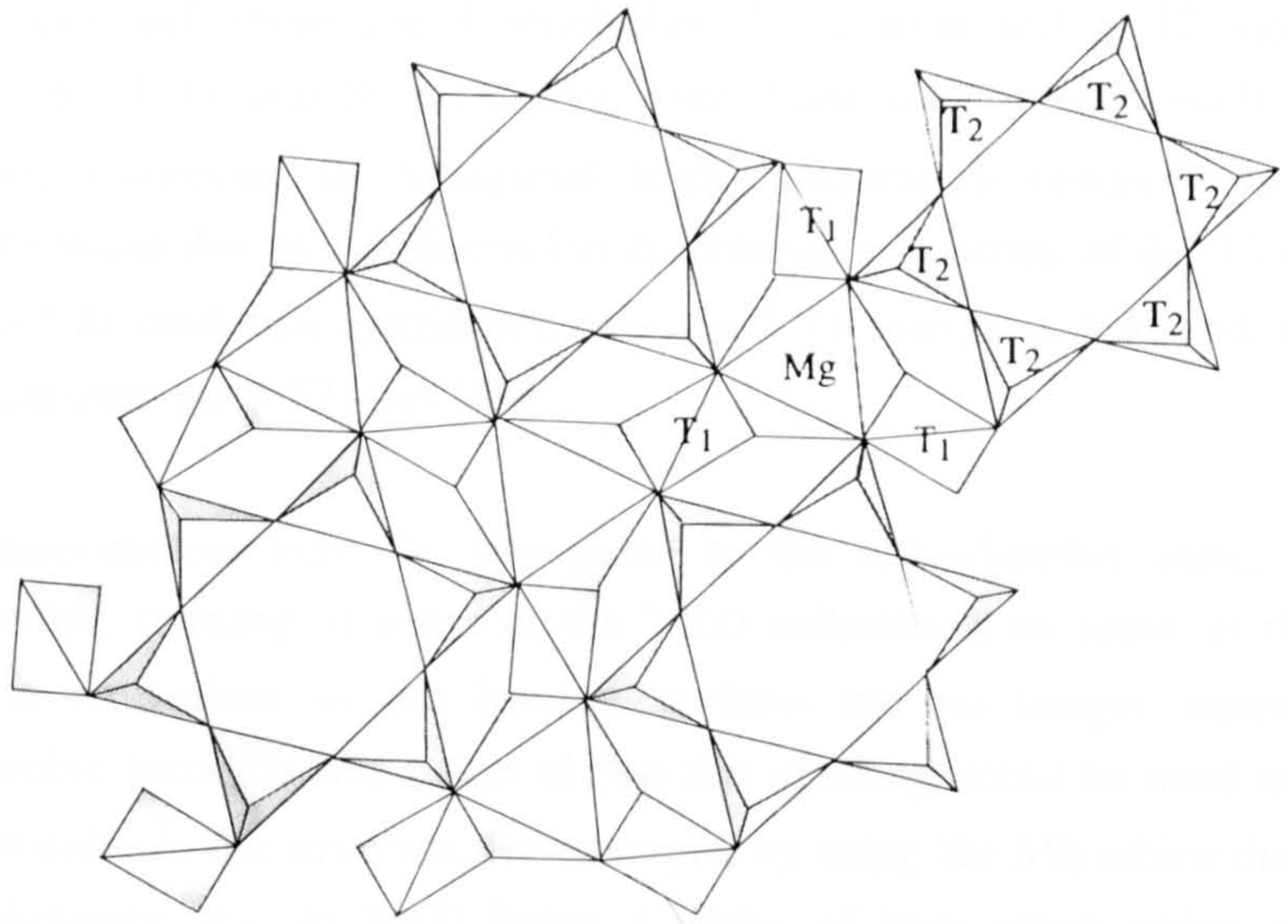

(b)

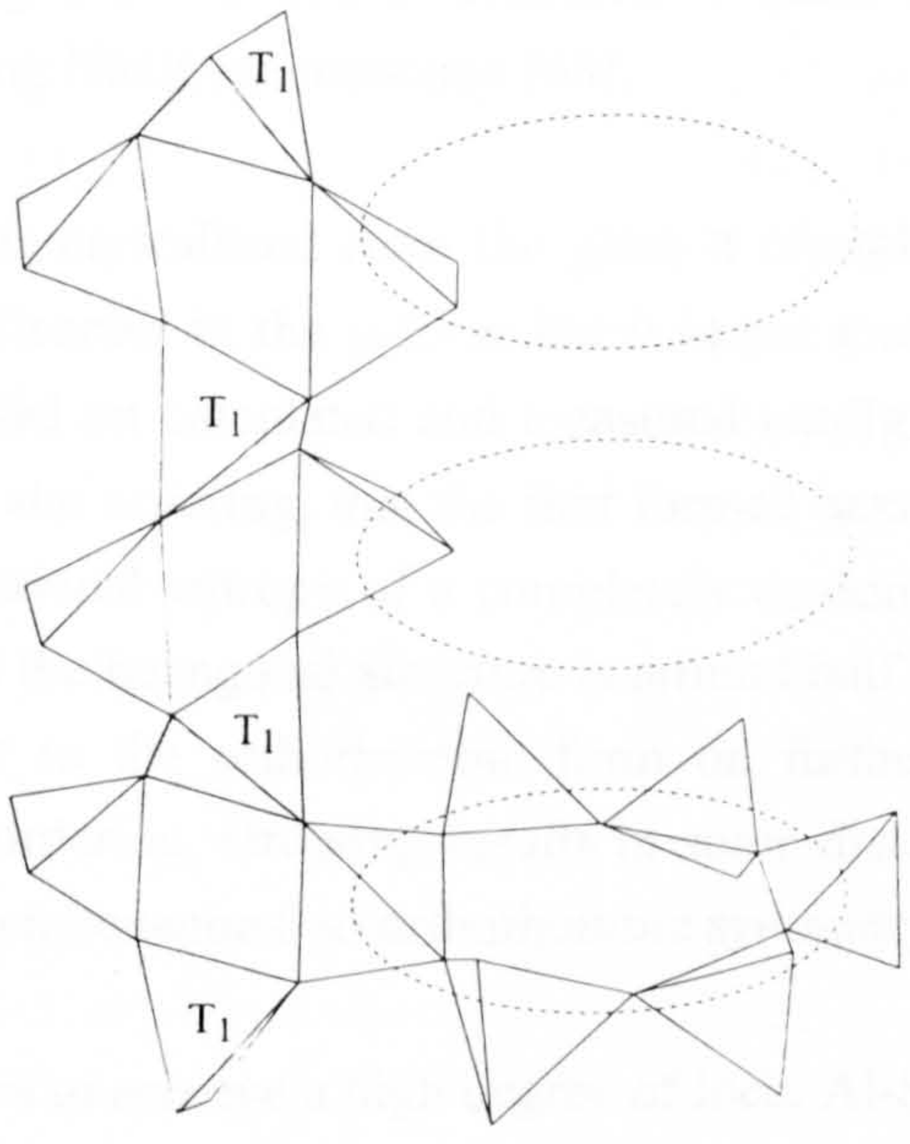

Figure 2.5: Structure of cordierite [63].

(a) The six fold rings of tetrahedra, labelled T_2 are connected via the tetrahedra labelled T_1. The Mg^{2+} cations lie in octahedral sites.

(b) T_1 tetrahedra connect the T_2 rings to form channels.

In each unit cell there are 9 tetrahedra, 3 T1 sites and 6 T2 sites, a random distribution of Al and Si tetrahedra over these sites would result in hexagonal symmetry. However, in hexagonal high temperature cordierite the hexagonal symmetry arises due to a different but disordered occupancy of the T1 and T2 sites - 2 Al and 1 Si randomly distributed over the 3 T1 sites, and 2 Al and 4 Si randomly distributed over the 6 T2 sites [63].

The transformation from the hexagonal to the orthorhombic state, results in an orthorhombic splitting of some of the XRD reflections, as some of the reflections that were equivalent in the hexagonal form are no longer equivalent in the orthorhombic form. It was believed that this splitting could be used to measure the degree of order in the structure, for example, by using the Miyashiro distortion index [71]. However, due to XRD being a probe of long range order, the transition between the hexagonal and orthorhombic forms appears to be discontinuous when measured by XRD, whereas the continuous nature of the ordering process can be revealed by using a probe that is sensitive to short range order. This has been demonstrated using NMR spectroscopy [63].

When cordierite is crystallised from the glass it crystallises in an hexagonal form, this reflects the disorder in the μ-form but it is not totally disordered. Putnis [63] demonstrates, based on calculated and measured configurational entropy and NMR measurements of site ordering, that the first formed hexagonal cordierite has around half the configurational entropy of a completely random structure. The number of Al-O-Al bonds in the hexagonal structure is around half that in the random structure and it transforms to the orthorhombic form on further heating by a continuous process of Al-Si ordering, Ordering results in some distortion of the unit cell and a transformation from hexagonal to orthorhombic symmetry.

Cordierite manages to achieve a high degree of local Al-Si order without any change in the average symmetry or lattice parameters due to the formation of a modulated microstructure which allows local Al-Si order, resulting in local regions of orthorhombic ordering. This occurs within a periodically distorted structure, which on average retains the symmetry of the high temperature hexagonal form. The size of the ordered regions grows with heating and these are only detected by x-ray diffraction when the ordered regions reach a size with detectable long range order. The relationship between Al-Si ordering and the orthorhombic and hexagonal forms of cordierite is more fully described by Putnis [63]

It is interesting that Barry et al [54] noted that, as suggested by previous workers [72], the hexagonal cordierite found in glass-ceramics may comprise micro-domains of low cordierite assembled to give apparently hexagonal symmetry. Workers using TEM [73] have also reported that orthorhombic cordierite crystallises from powdered glass samples, but this may be explained due to TEM measuring local order.

The channels that exist parallel to the cordierite 'c' axis do however result in a further complication. Shreyer and Yoder [74] were able to show that the transition from high to low cordierite may also, in some circumstances, be due to compositional effects rather than polymorphism. In this case the cause was molecular water present in the channels within the structure.

2.7.3. Structure and transformations of enstatite polymorphs

As well as being the second phase used to control the thermal expansion in the glass-ceramics used in this study, enstatite based glass-ceramics are of interest in their own right, since glass-ceramics with exceptional properties have been produced [75][34]. To understand the properties of these materials it is necessary to have a little background about the structure of, and transformations between, the different enstatite polymorphs.

Enstatite (melting point 1557°C), a member of the pyroxene family, is a chain silicate. The general form of a pyroxene is:-

XYZ_2O_6

X - 6 to 8 co-ordinated polyhedron conventionally labelled *M(2)*
Y - distorted octahedral site *M(1)*
Z - tetrahedrally co-ordinated *T* site

The backbone of the structure is a single chain of tetrahedra sharing polyhedral corners with and parallel to bands of edge sharing octahedra that run along the 'c' direction. In the case of magnesium enstatite both the X and the Y site are occupied by Mg^{2+} ions although many other cations can occupy these sites. (eg: X site: Fe^{2+}, Ca^{2+}, Na^{+}, $Li^{+}$and Mn^{2+}. Y site: Fe^{2+}, Fe^{3+}, Mn^{2+}, Al^{3+}, Cr^{3+}, Zn^{2+}) The Z site is occupied by Si^{4+} but substitution of Al^{3+} and Fe^{3+} can occur. Al^{3+} substitution can occur up to 0.8 Al^{3+} per 2.0 tetrahedral cations.

Enstatite occurs in three structural polymorphs: proto, clino and ortho-enstatite. The structure of the three polymorphs is well documented [66] but the stability appears still not to be resolved.

It is interesting to consider what structural changes are occurring in the transformations between polymorphs. Although the arrangement of the silicate chains is different, the three polymorphs are most easily distinguished structurally by examining the sequence of planes of Mg^{2+} ions along the 'a' axis direction as shown in Figure 2.6. Inversions between the polymorphs involve breaking Mg-O bonds and translations of the silicate chains, but do not necessarily involve breaking the strong Si-O bonds.

Figure 2.6: Structure of enstatite

ABABABAB - clino
AABBAABB - ortho
AAAAAAAA - proto

On heating, clino transforms to ortho between 650-900°C, and proto-enstatite is stable at temperatures above around 1000°C (980°C [34], 1042°C [76], from 1000°C to at least 1300°C [77]). The ortho-proto phase transition is preceded at 1000°C by an intermediate structure with stretched silicate chains. At 1100°C the transition to proto is instantaneous.

Protoenstatite normally converts to either the stable ortho or the metastable clino form on cooling. The proto to clino transformation is accompanied by a reduction in volume of around 5% (4% [34], 5.5% [76], 5-6.1% [77]). Both proto-clino and the clino-proto transformations have martensitic characteristics: they are diffusionless, athermal, stress-inducible and an orientation relationship exists between the parent and product phases. The proto to ortho transition is, in contrast, a relatively slow order-disorder transition.

The extent and nature of the transformation of protoenstatite on cooling appears to be a function of crystal size [76], cooling rate [77], the presence of shear stress [77] and doping [77][78]. If proto-enstatite is in the form of small crystals such as in a glass-ceramic then it may retain much of its proto-enstatite character on cooling. The proto that does transform on cooling has a tendency to form twinned clino.

The nature of the ortho/clino transformations is very different to that of the tetragonal-monoclinic transformation in ZrO_2. It occurs in bands on (100) leaving an intimate mix of the product and parent phase in a single grain. For example, clino with intimate ingrowths of ortho has been observed by TEM [77]. This kind of microstructure is never normally observed in ZrO_2, once the tetragonal-monoclinic transformation is nucleated, it proceeds to completion transforming the entire particle or grain.

Table 2.3: Structure and properties of enstatite polymorphs

Phase name	Chemical Formula	JCPDS Ref	Density
Enstatite (Ortho-enstatite)	$Mg_2Si_2O_6$	19-768	3.20
Clino-enstatite	$Mg_2Si_2O_6$	35-610	3.20
Proto-enstatite	$Mg_2Si_2O_6$	11-273	3.10
Forsterite	Mg_2SiO_4	34-189	3.22

Identification of the polymorphs using x-ray diffraction is notoriously difficult [77] and the phases may coexist. When present in MAS glass-ceramics identification may be further complicated by solid solution effects due to substitution of Al^{3+} for Si^{4+} and size broadening due to the sub-micron crystallites present.

2.7.4. Forsterite and other phases encountered in crystallisation of MAS

Forsterite ($2MgO.SiO_2$), a refractory phase with a melting point of 1890°C, is also encountered in small quantities in the current work. Forsterite is an orthosilicate, the structure of which consists of isolated $(SiO_4)^{4-}$ tetraheda linked via additional non-silicate cations, which in the case of forsterite are Mg^{2+}. Forsterite is formed in MgO rich compositions [79], and higher quantities of B_2O_3 result in a tendency for forsterite to form in preference to enstatite [4].

Several other phases have been reported in MAS glass-ceramic. Although these do not normally have a significant impact on the development of crystallisation in cordierite/enstatite glass-ceramics they are briefly summarised below.

Schreyer and Schairer [80] identified two further phases crystallising in MAS glasses; a Mg-petalite type phase, having a structure similar to petalite ($Li_2O.Al_2O_3.8SiO_2$) and a Mg-osumilite type phase with a double ring structure similar to osumilite ($Na_2O.5MgO.12SiO_2$). Barry [54] noted that osumilite and petalite type phases tend to exist in the early stages of crystallisation.

Recent results suggest that Mg-osumilite only crystallises from glasses within a narrow compositional range and requires the addition of BaO or SrO [81]. The crystallisation mechanism is complex involving nucleation of precursor Ba or Sr containing osumilite phases and a high quartz solid solution, which subsequently transforms into Mg-osumilite.

Mg petalite, a metastable phase that transforms irreversibly to high quartz solid solution on heating at 1000°C [82], has subsequently been observed in silica rich cordierite glasses with the addition of either ZrO_2 [82][83], or ZrO_2 and TiO_2 [54]. There are some differences in the characteristic XRD peaks that have been reported for Mg-petalite (Table 2.4) indicating some compositional variation.

Table 2.4: Major XRD reflections reported for Mg-petalite

	d (Å)	I/Io	d (Å)	I/Io
Shreyer and Shairer [64]	3.75	20	3.69	100
Holmquist [82]	3.74	100	3.66	90
Dusil [83]	3.75	8	3.66	100
			3.55	17
Barry [54]	3.72	very strong	3.62	strong

Yuritsin [29] has reported a phase, which he describes as x-phase/petalite forming on a polished surface of stoichiometric cordierite glass. Ziemath [84] also observed lozenge shaped crystals on stoichiometric cordierite and described them as x-phase/magnesium petalite solid solution. However, a similar phase may previously have been observed by Bridge [1] who reported small (~2μm) isolated leaf like crystals on polished cordierite/enstatite glass (typical substrate composition with 1wt % B_2O_3 and 2 wt % P_2O_5) following a heat treatment at 850°C. XRD revealed a single peak corresponding to 3.3-3.35 Å, which developed with further heat treatment into a major and a minor peak corresponding to 3.34 Å and 2.37 Å respectively. This phase was also formed on loosely stacked powders. Although visibly this phase was similar in appearance to the petalite reported by Barry [54],

classification of this phase as petalite would not be consistent with the XRD data. This therefore represents an additional metastable phase that may be present in the early stages of crystallisation. Bridge termed this a quartz like phase due to the location of the main XRD peak at 26.65 2θ compared to pure β-quartz 26.2 2θ or α-quartz 26.6 2θ. Heide et al [85] [86] also reported a "quartz type crystal" with a similar "pseudo orthorhombic" appearance on the surface of stoichiometric cordierite heat treated at 875°C.

Cristobalite, spinel, sapphirine and α-quartz solid solution phases are also sometimes encountered for MAS based glass-ceramics for certain compositions and thermal treatments [87][54][64].

2.7.5. Properties of MAS glasses and glass-ceramics

The thermomechanical properties of MAS glasses, the constituent phases and the resulting glass-ceramics are particularly important when used for joining, coating or composite applications. Where analytical or finite element modelling is involved, the accuracy may be limited by the quality of the data used in the calculation. A summary of the TCE of the constituent phases, parent glasses and resulting glass-ceramics is given below. This is followed by a discussion of the mechanical properties of cordierite and enstatite-based glass-ceramics. Enstatite glass-ceramics are considered separately due to the exceptional properties that have been reported. An understanding of the mechanism resulting in these exceptional properties may enable glass-ceramics with similar/improved properties to be developed and extend the range of possible applications

a) TCE of cordierite/enstatite based glass-ceramics and constituent phases

A summary of some of the reported values for the TCE of the magnesium-aluminosilicate parent glasses and the constituent phases is shown in Table 2.5. Comparison between results is sometimes hindered by a lack of consistency in the temperature range reported. Figures for conventional ceramics are included although in this case some scatter in the values reported is to be expected due to the presence of impurities, and variety of microstructure.

Table 2.5: Reported TCE for MAS parent glasses and constituent phases

Glass	**TCE MK^{-1}**	**Range °C**	**Ref**
Stoichiometric	3.9	25-800	[51]
Mg-rich	3.5-4.25	20-700	[79]
Al-rich	3.0-3.3	20-700	[79]
Si-rich	2.4-2.7	20-700	[79]
Phase			
Cordierite	*2.6*	*25-700*	[5]
Cordierite	2.8	0-1200	[88]
β-quartz (stoichiometric)	4.72	24-800	[56]
Hexagonal (high cordierite)	1.0±0.1	24-800	[56]
Orthorhombic (low cordierite)	1.6±0.1	24-800	[56]
Clino-enstatite	*7.8*	*100-200*	[5]
Steatite ceramic	8-9	25-500	[38]
(enstatite based)	9-10	25-1000	[38]
ortho-enstatite	12	300-700	[88]
proto-enstatite	10	300-700	[88]
clino-enstatite	13.5	300-700	[88]
Forsterite	*9.4*	*100-200*	[5]
Forsterite based ceramics	9-10	25-500	[38]
	10-12	25-1000	[38]
Forsterite	12.2	0-1200	[88]
Sintered forsterite (99.5%)	10.6	20-1000	[89]

The figures most often quoted in the glass-ceramics literature are those given by McMillan [5], who quotes results for polycrystalline materials from Stutzman in 1959 [90]. These are shown in italics in Table 2.5. In the light of more recent measurements the figure reported by McMillan for cordierite looks a little high and does not differentiate between the different cordierite polymorphs (α and β). The figures for clinoenstatite and forsterite are also only over a very limited temperature range. By taking account of more recent reported TCE measurements a fairly

accurate indication of the TCE of the constituent phases and parent glasses may be obtained.

The TCE of the stoichiometric glass (and MgO, Al_2O_3 or SiO_2 rich versions) is intermediate between the TCE of μ and α-cordierite.

The TCE of μ cordierite, which is a solid solution phase, is a function of composition. The value reported by Hirose [56] is for stoichiometric cordierite composition. Similar phases in the LAS system are well characterised and display a negative thermal expansion, as does quartz above the α-β phase transition. The TCE would be expected to increase with increasing Mg substitution.

Hirose et al [56] attributed the scatter in the values for the TCE of single crystal hexagonal cordierites reported by previous workers (0.9-1.5 MK^{-1}) as being due to either microcracking as a result of TCE anisotropy of cordierite or due to the thermal expansion of orthorhombic cordierite being higher than that of hexagonal cordierite. By full conversion to the orthorhombic phase Hirose was able to reduce the scatter in the TCE values to 1.53-1.69 MK^{-1}. However, it is likely that the remaining scatter in the values reported is due not to microcracking but due to XRD not being a sensitive probe of the hexagonal-orthorhombic transition, and is therefore due to differing degrees of Al-Si ordering.

Reported TCEs for mineral cordierites are typically a little higher due to the incorporation of impurities within either the structure or the channels within the structure.

A summary of some reported values for the TCE of MAS glass ceramics is shown in Table 2.6. This encompasses figures for glass-ceramics produced via a bulk glass route, a sintered route and hot pressed material and includes the commercial cordierite based glass-ceramic Corning 9606. However, most of the values in Table 2.6 are collated from previous work at Warwick on sintered cordierite/enstatite glass-ceramics and illustrate the range of thermal expansions that have been achieved from this system, from 2 to 12 MK^{-1}. Low TCE glass-ceramics utilise α-cordierite with minimal residual glass phase and little if any second phase. The thermal expansion may be modified by controlling the extent of the μ-α transformation and the quantity of a second (higher TCE) phase present. Due to their high thermal expansion it is possible to produce enstatite or forsterite based glass-ceramics with fairly high TCE, matching or even exceeding the TCE of Ti and Ti alloys.

Table 2.6: Reported TCE for MAS glass-ceramics: compositions in wt.%.
(Where values can be obtained openly from the literature, example values only are given)

MgO	Al_2O_3	SiO_2	Other	Phases present	TCE (MK^{-1})	Temp Range (°C)	Ref
30.0	14.0	53.0	2 B_2O_3, 1P_2O_5	α-cordierite + enstatite	9.3	0-800	[41]
34.0	10.0	53.0	2 B_2O_3, 1 P_2O_5	enstatite + α-cordierite	10.2	0-800	[41]
39.0	5.0	53.0	2 B_2O_3, 1 P_2O_5	enstatite + clino-enstatite	12.8	0-800	[41]
29.7	13.7	52.5	3 B_2O_3, 1 P_2O_5	α-cordierite + forsterite	8.6	0-800	[41]
29.4	13.7	51.9	4 B_2O_3, 1 P_2O_5	α-cordierite + forsterite	9.9	0-800	[41]
29.7	13.9	52.5	3 B_2O_3, 2 P_2O_5	α-cordierite + forsterite	10.1	0-800	[41]
29.4	13.3	51.9	4 B_2O_3, 3 P_2O_5	α-cordierite + forsterite	7.93	0-800	[41]
30.3	14.1	53.4	1 B_2O_3, 1 P_2O_5	enstatite + μ-cordierite	9.7	0-800	[41]
30.6	14.2	54.0	1 P_2O_5	enstatite + μ-cordierite	10.2	0-800	[41]
14.7	19.8	56.1	8.9 TiO_2, 0.3 As_2O_3, 0.1 CaO, 0.1 Fe_2O_3	Corning 9606	4.8 4.5	25-500 25-1000	[40]
17.4	29.7	47.4	0.5 B_2O_3, 5 P_2O_5	α-cordierite	2.1	50-850	[91]
25.4	19.9	52.6	0.5 B_2O_3, 1.6 P_2O_5	μ + α cordierite + enstatite	7.1	50-850	[91]
33		54	13 ZrO_2	proto and clino-enstatite, zircon, zirconia, cristobalite	8.0	0-1000	[34]
12.4	31.4	46.2	10 TiO_2		2.43	25-800	[54]
12.1	30.5	44.9	7.5 TiO_2, 5 ZrO_2		2.15	25-800	[54]

Table 2.6: Reported TCE for MAS glass-ceramics: compositions in wt. % (continued)

MgO	Al_2O_3	SiO_2	Other	Phases present	TCE (MK^{-1})	Temp Range (°C)	Ref
28.6	28.9	42.6		α-cordierite + forsterite	3.66	25-700	[79]
11.7	44.5	43.7		α-cordierite + μ-cordierite + sillimanite	2.41	25-700	[79]
9.8	24.7	62.5		α-cordierite + μ-cordierite	1.56	25-700	[79]
13.5	34.1	50.0	0.3 Na0	α-cordierite	1.13		[56]
13.5	34.1	50.0	0.3 Na0	β-cordierite	1.7		[56]
24	22	54			7.33	100-900	[57]
24	22	54	2 P_2O_5		6.00	100-900	[57]
18	27	53	3 ZrO_2, 1 CaO		5.59	350-850	[57]
22.0	22.0	53.0	1 B_2O_3, 2 P_2O_5		1.55	30-200	[1]
22.45	22.45	54.1	1 B_2O_3		2.53	30-200	[1]
22.25	22.25	53.5	2 P_2O_5		3.40	30-200	[1]
22.0	22.0	53.0	1 B_2O_3, 2 TiO_2		2.82	30-200	[1]
22.7	22.7	54.6			6.98	30-200	[1]
23.5	20.5	53.0	1 B_2O_3, 2 P_2O_5		1.91	30-200	[1]
25.0	19.5	53.0	1 B_2O_3, 2 P_2O_5		2.89	30-200	[1]

Mechanical properties of cordierite based glass-ceramics

There is a large variation in the reported values for the mechanical properties of cordierite-based glass-ceramics. Although this may be partially attributed to different test procedures, composition and microstructure are more significant effects. For example, the properties are strongly affected by the pattern of residual stress caused by the interplay between grain size and TCE mismatch between constituent phases and the residual glass. This can have a positive or a negative effect on the mechanical properties.

Any volume change accompanying a phase transformation can also have a significant effect and must be accommodated without microcracking or weakening of the material if a strong glass-ceramic is required. For an α-cordierite ceramic produced via a sol-gel route Okuyama [92] obtained bend strengths as low as 30 MPa and attributed this to microcracking due to the volume change arising from the μ-α cordierite phase transformation. Bridge [1] reported that a degradation of the material properties accompanied protoenstatite formation in cordierite/enstatite glass-ceramics, and attributed this to a coarsening of the microstructure and increased porosity.

The bend strengths reported by Bridge [1] of 91-147 MPa are typical for sintered cordierite/enstatite glass-ceramics. The strength was affected by the powder milling route (wet milled compositions were approximately 20 MPa stronger than dry milled).

The bend strength of cordierite glass is often slightly greater than that of the resulting glass-ceramic. For example, Hayashi [93] reported bend strengths of 149 MPa for the glass compared to 113 MPa for polycrystalline cordierite; similar results have been reported by Bridge [1] and Chamberlain [57]. However, the fracture toughness (K_{IC}), elastic modulus (E) and Vickers hardness (H(v)) are all greater for the polycrystalline cordierite compared to the glass (polycrystalline cordierite - K_{IC} 2 MPa $m^{1/2}$, E 127.5 GPa, H(v) 7.5 GPa, cordierite glass - K_{IC} 1 MPa $m^{1/2}$, E 98.7 GPa, H(v) 5.9 GPa [93])

Typical values for cordierite/enstatite glass-ceramics for the fracture toughness range from 1.4-2.1 MPa $m^{1/2}$ [37] and for the elastic modulus from 90 to 120 GPa [57][1].

Knickerbocker [7] has demonstrated that the strength of sintered cordierite-enstatite glass-ceramics is also strongly dependent on glass particle size, ranging from approximately 100 MPa for a particle size of 10 μm up to almost 300 MPa for a particle size of 1 μm.

Strengths obtained for cordierite glass-ceramics produced via the bulk route are largely comparable. For example, Barry [54] reported a strength of 208 MPa for stoichiometric cordierite glass ceramic containing 10 wt % TiO_2 as a nucleating agent.

The strengths reported for the commercial glass-ceramic Corning 9606 (123-370 MPa [39]) are strongly dependent on surface finish. The higher values rely on treatments which hold the surface in compression. Reported values for the fracture toughness (K_{IC} 1.6-2.1 MPa $m^{1/2}$) and the elastic modulus (E 120 GPa) for this material are similar to those for sintered materials.

The incorporation of a second higher expansion phase into a glass-ceramic generally has a beneficial effect on the strength and fracture toughness, although this is subtly dependent on the extent of the TCE mismatch, the grain size, and the distribution, quantity and morphology of the constituent phases and residual glass. Significant improvements to the reported strengths and fracture toughness have been reported for both mullite [55][94] and zirconia [95][96] incorporated into a cordierite matrix.

Particulate reinforced composites with a cordierite matrix can have considerably improved mechanical properties. For example, whisker reinforcement using either β -SiC or β-Si_3N_4 can result in fracture strengths exceeding 400 MPa, combined with a fracture toughness of 4.5-5.8 MPa $m^{1/2}$ [35][36]. The improved properties are not significantly degraded at temperatures of up to 1000°C.

Further attractive properties of cordierite/enstatite glass ceramics include: good chemical durability, low dielectric constant, high electrical resistivity and excellent high temperature performance due to the refractory nature of the phases present. Measurable creep often only occurs above the T_g of the residual glass. The commercial cordierite based glass-ceramic Corning-9606 has a quoted maximum use temperature with no load of 1100°C with measurable creep occurring at temperatures above 900°C.

Mechanical properties of enstatite based glass-ceramics

Exceptional mechanical properties, comparable to those obtained for particulate reinforced glass-ceramics, have been reported for some enstatite based glass-ceramics, for example:

- Beall and co-workers at Corning [34] reported an abraded modulus of rupture of 200 ± 15 MPa, combined with a fracture toughness 4.6 ± 0.6 MPa $m^{1/2}$ for a refractory enstatite based glass-ceramic in which the major phases present were proto-enstatite, clino-enstatite and zircon with small amounts of tetragonal zirconia and cristobalite. The other properties reported for this glass-ceramic were a TCE of 8.0 MK^{-1}, "refractoriness" of 1500°C, elastic modulus (E) of 140 GPa and a fracture energy of 55 Jm^{-2}.

- Partridge, Elyard and Budd [75] obtained fracture strengths of up to 350 MPa, (TCE 8.2 MK^{-1} (20-500°C)) for sintered clino-enstatite based glass-ceramics, which had ZrO_2 added as a nucleating agent.

- Echeverria [97] used a sol-gel route to produce enstatite ceramics, which consisted of a crack free interlocking aggregate of 0.5 μm ortho, proto and clino-enstatite grains, with a fracture toughness of 4.2 MPa $m^{1/2}$.

These materials are of interest not just due to the exceptional mechanical properties, but also because of the possible microstructural mechanism resulting in these properties and the implications this has both for the production of glass-ceramics with improved properties and for extending the possible range of uses.

Beall [34] suggests that the toughening mechanism resulting in the high fracture toughness he reports is not directly related to the presence of the metastable proto in the glass-ceramic, in direct analogy to that from partially stabilised tetragonal zirconia, because the proto-clino volume change is negative. The presence of tetragonal zirconia is also considered unlikely to contribute significantly, as the zirconium is mostly present as zircon. Beall suggests four mechanisms which may contribute to the toughening:

1. Crack deflection and perhaps slippage along fine polysynthetic planes developed during the partial transformation.

2. Energy absorption from the opening of penny shaped cracks along twin boundaries.
3. Splintering due to the intersection of cleavage and twin planes.
4. Further transformation to clino under the shear stress preceding fracture.

Evidence of strain hysteresis of up to 0.01% is presented to demonstrate that point four above at least partially contributes to the toughening.

Partridge [75] gives two possible explanations for the high mechanical strength; either transformation toughening as a result of tetragonal zirconia particles, or a surface compressive layer. It is possible however that the same mechanism that results in the exceptional mechanical properties reported by Beall [34] is at least partially responsible.

The fracture toughness values reported by Echeverria [97] were measured using direct measurement of Vickers indentations which was shown by Beall et al [98] to underestimate toughness in chain silicates compared to short bar or chevron notch techniques. To obtain the reported figure of 4.2 MPa $m^{1/2}$ the value obtained directly from the indentation method of Anstis [99] (2.5 MPa $m^{1/2}$) was multiplied by a factor to compensate for the extent to which this method resulted in understatement of the fracture toughness compared to other techniques. Although this 'correction' may be valid, other values reported in the literature are often produced using similar indentation methods which have not suffered this correction. Some caution is therefore required when comparing this value with other values reported in the literature.

The method used by Beall [34] for measuring fracture toughness is not reported and it is not clear whether the fracture toughness figure represents a "corrected" indentation value as reported by Echeverria [97] based on previous results by Beall and co-workers at Corning [98]. Hence it is possible that 2.75 MPa $m^{1/2}$ rather than 4.6 MPa $m^{1/2}$ may be more appropriate when comparing to other values obtained by direct measurement of indentations. However, this is still outstanding for an oxide glass-ceramic.

Enstatite glass-ceramics do not always have exceptional mechanical properties. For example, Lee and Heuer [77] prepared proto-enstatite by hot pressing $MgSiO_3$ glass at 1150 ± 50 °C and reported a fracture toughness (K_{IC}) of 1.2-2 MPa $m^{1/2}$. It is not clear why the mechanical properties are much poorer in this case but this may be

related to the crystal size and mixture of phases present. Problems may also be encountered in the production of enstatite based glass-ceramics. For example, Budd [100] found that, for enstatite glass-ceramics produced using a sintered powder route, porosity may result due to either the volume change on crystallisation or the release of absorbed gases.

If the mechanism and the microstructure resulting in the exceptional mechanical properties can be understood and controlled it is possible that further improvement to the mechanical properties may be possible.

The possibility of using the martensitic phase transformation between the enstatite polymorphs to produce materials with improved mechanical properties was previously considered by Kriven [76] who included enstatite in his review of possible alternative transformation toughened ceramics to zirconia. However, Kriven observed that the negative volume change on cooling can result in "transformation weakening", which was first observed in some $CaCO_3$ containing steatite ceramics which degraded and fractured after a period of storage at room temperature. The CaO led to enhanced grain growth which took the proto-enstatite above a critical particle size. Kriven concluded that a positive volume change was required for a beneficial toughening effect. However, for joining applications, when joining to a metal of higher TCE, a negative volume change may be beneficial. The volume change accompanying the change between polymorphs may be used to partially accommodate a thermal expansion mismatch or to reduce local stress concentrations and thereby induce a degree of defect tolerance. The 4% volume change accompanying the proto-clino phase transformation represents a length change of ≈ 1.33%. Each MK^{-1} mismatch in TCE represents 0.1% strain in cooling over 1000K. It would therefore seem feasible to bond materials with differing TCEs and to relieve some of the joining stress on cooling by using an enstatite glass-ceramic, or using the same mechanism to introduce a degree of defect tolerance. It is possible to envisage an enstatite glass-ceramic where in response to an applied stress, the Mg-O bonds break but the strong Si-O bonds remain intact as the rearrangement of the silicate chains accommodates the stress.

Both indentation and grinding [77], have been demonstrated to induce the proto-clino transformation. The sensitivity of the transformation to crystal size [76], cooling rate [77], the presence of shear stress [77] and doping [77][78] indicate that a degree of control may be possible.

The concept of designing "structural defects" to relieve thermal stress was suggested by Ishida et al [101], and the possibility of using a phase transition to accomplish this was one of the options he discussed, suggesting that for this a "higher level of understanding" was required. The use of a martensitic phase transformation to accommodate residual stress has been reported by Itoh et al [102] for a zirconia ceramic joined to stainless steel.

Enstatite based glass-ceramics are attractive for joining applications due to their exceptional mechanical properties (high strength and fracture toughness). In addition, by using the martensitic transformation between the refractory enstatite polymorphs to partially accommodate the strain due to TCE mismatch, it may be possible to extend the possibilities of ceramic-metal joining without compromising the high temperature performance of the joint.

2.7.6. Sintered cordierite based glass-ceramics

Sintered cordierite-based glass-ceramics rely on the strong tendency for surface nucleation in the MAS system. In contrast to bulk nucleated glass-ceramics, the addition of specific nucleating agents is not required, although additives are often used to control the dynamics of sintering and crystallisation. In sintered glass-ceramics, the high surface area of a fine glass powder provides the required high density of sites for the production of a fine-grained glass-ceramic.

The nature of the nucleation sites, the transition from glass to μ-cordierite, and the formation of α-cordierite (either directly from the glass or as a result of the transformation from the μ-phase) are of particular importance. The formation of a strong, dense glass-ceramic requires crystallisation to be delayed until sintering is near completion, and for the volume change accompanying the μ-α phase transformation to occur without weakening the glass-ceramic.

A fair amount of work has been reported recently on this system, the majority of which is either for cordierite/enstatite compositions typical of those used in substrate applications [1][103][104][3][105][106][107][108][7], or for stoichiometric cordierite [109][110][85][84][29][32][111][112][33][113][79]. There has also been some interest on the effect of the addition of P_2O_5, either on its own, or in conjunction with B_2O_3, to both stoichiometric cordierite glass [114][92][58] and typical substrate compositions [1][3][7][105][106][107][115]. Stoichiometric

cordierite glass was chosen for a fundamental study on the surface crystallisation of glass by the Technical Commission of the International Commission on Glass/Glass World Forum (TC7 of ICG), and some preliminary results of this work have been reported [84] [112].

Although the morphology and relative stability of the μ and α-cordierite phases are strongly affected by minor additives, compositional changes and the form of the initial glass (whether from the bulk glass or from a fine powder), the general scheme of crystallisation retains many similarities. To obtain an understanding of the surface nucleation mechanism, and in particular the effect of B_2O_3 and P_2O_5, it is necessary to take a fairly broad view, and to encompass results reported for: the surface crystallisation of bulk and powder samples; a wide range of cordierite based compositions, and samples with additives other than B_2O_3 and P_2O_5 where the results are relevant. An attempt to summarise the current understanding is set out below. Results for bulk nucleated cordierites, obtained for example by relying on the addition of TiO_2 and/or ZrO_2, have not been included, as the nucleation mechanism and microstructural development are distinctly different.

The following workers have recently reported detailed transmission electron microscopy relating to the crystallisation of cordierite based glass-ceramics: Chaim and Heuer [59] for stoichiometric glass with BaO addition; Rudolph et al [105] for a typical cordierite/enstatite substrate composition containing 4.5 wt % P_2O_5; Glendenning et al [58] for stoichiometric cordierite containing B_2O_3 and P_2O_5, and Winter et al [116] for a SiO_2 rich composition (molar ratio $MgO:Al_2O_3:SiO_2$ - 2:2:11). Some of these observations are included below, although it is not yet clear whether the results can be extended to a wider range of compositions.

a) Glass to μ-cordierite - nature of nucleation sites

In the general scheme of crystallisation for surface nucleated cordierite glasses the first phase to form is metastable μ-cordierite, which transforms to α-cordierite (hexagonal) on further heating/higher temperatures. This in turn transforms to β-cordierite (orthorhombic) on further heating by a process of Al and Si ordering (Section 2.7.2).

Surface nucleation of μ-cordierite occurs rapidly from a limited number of preferred nucleation sites [33]. The exact nature of these sites is not yet known. One possibility is that they are related to the presence of surface defects. Muller [32] and

Rudolph [105][106] have reported an increased density of sites corresponding to an increase in damage to the surface. The nucleation density of μ-cordierite on both polished and fractured surfaces has been measured by Muller et al [32], ranging from up to 10^{-2} μm^{-2} on polished surfaces, to as low as10^{-7} μm^{-2} on fractured surfaces. This indicates that surface flaws and cracks contribute to the formation of active nucleation sites, and that there is no inherent tendency of the surface to devitrify.

Inclusions have also been suggested as a likely cause of nucleation [58]. The strong nucleating activity of solid foreign particles has been reported by Muller [32]. In this instance, cordierite glass powder was used, demonstrating that a composition difference is not required for nucleation.

Another possibility is that compositional change at the boundaries caused by vaporisation of the least tightly bound species in the glass, may contribute to the formation of active sites [58] [1].

Whatever the exact nature of the nucleation sites, sintered cordierite glass-ceramics exhibit a phenomenon known as the "memory effect". A pellet of powdered glass may be sintered or hot pressed to a fully dense glass, with nucleation occurring on unidentified heterogeneous nuclei at the sites of the former particle surfaces. On further heat treatment a crystalline skeleton forms along the original powder surface [58][105]. Rudolph [105] suggests that the formation of nuclei may start at the glass particle surfaces during the very early stages of densification.

Muller et al [33] have reported that μ-cordierite does not nucleate on internal cracks other than near the surface. This indicates that additional interactions between the crack surfaces and either the atmosphere, or liquid or foreign particles, must play a decisive role in the nucleation. This is confirmed by work reported by Glendenning and Lee [58] who found that, for stoichiometric cordierite with added B_2O_3 and P_2O_5, crystallisation was not observed on closed pores.

The number density of μ-cordierite sites is not substantially influenced by either the time or the temperature of heat treatment, and sites are not deactivated with thermal heat treatment up to the crystallisation temperature [29][33][85].

Rudolph [105] and Watanabe [115] have reported the absence of bulk or homogeneous nucleation. Diaz Mora [112] observed μ-cordierite forming in the bulk of the glass. However, these were heterogeneously nucleated on impurity

particles within the volume of the glass and the growth rates were identical to surface nucleated crystals.

b) Kinetics of activation

The kinetics of nucleation of μ-cordierite on stoichiometric glass surfaces have been studied in detail by Müller et al [33] who measured the mean induction time from the delay in linear crystal growth. The mean induction time varied from 80 minutes at 870°C to 1 minute at 980°C, and the saturation time (the time for all sites to be used up) varied from 100 minutes at 870°C to 0.7 minutes at 1050°C. Diaz-Mora [112] also observed long induction periods for μ-cordierite at low temperatures.

Muller [33] suggests that a similar temperature dependence exists for both the surface nucleation and the crystal growth velocity of μ-cordierite. This indicates that a large nucleation rate can occur simultaneously with a considerable growth velocity, and that nucleation occurs over a very broad temperature interval. As a result, full depletion of nucleation sites is likely to arise from almost any thermal treatment allowing a sufficient growth of μ-cordierite crystals. This represents an obstacle to the use of a conventional two-stage nucleation and growth heat treatment to control nucleation density.

A strong catalytic effect of water on the crystallisation of μ-cordierite on both polished and split surfaces has been reported by Yuritsin [29], who also notes that the water effect on crystallisation can be eliminated or decreased by placing the wetted glass sample in alcohol. Further evidence that water may play a key role in nucleation has been reported by Heide et al [85], working with stoichiometric cordierite glass, who detected the evolution of water (corresponding to a weight loss of 0.025%) during the formation of the metastable quartz type structure. They suggest that the loss of volatile components could be a release process in the formation of nuclei.

Work on the effect of chemical treatment of the surface sites is mixed. Yuritsin [29] was able to reduce the number of μ-cordierite crystals by HF treatment, and Helgesson [117] found that treatment with a strong alkali improved the sintering behaviour by removing nucleation sites from the surface of the glass. In contrast [111], reported that for cleaning the surface of stoichiometric bulk glass with either HF, alcohol or NaOH, the nucleation density shows no characteristic dependence on the cleaning solution used. Muller [32] reported that the number of μ-cordierite

crystals on a SiC ground surface was not significantly affected by the suspending agent used (butanol, n-hexane, distilled water or glycerine).

As well as the sites which are responsible for μ-cordierite, the petalite type phase/x-phase (discussed in Section 2.7.4) occurs on different sites, which are not found on fractured surfaces and can be thermally deactivated [29].

c) Microstructural development

A similar picture emerges for the initial microstructural development over a wide range of compositions whether crystallisation occurs from a powder, a bulk glass, or at the sites of the previous particle surfaces. The initial μ-cordierite formed is randomly orientated, with no preferred orientation with respect to the surface [105] [112][58][116]. The 'c' axis is the preferred growth direction [106][112][116][118], and crystallites grow until they impinge [105][106][112][116][118], when the growth of crystallites perpendicular to the surface is favoured. This results in lamelar growth with the 'c' axis perpendicular to the glass surface [105][116][118][115].

However, composition and temperature also strongly determine the morphology. For example, Bridge [1] found roughly spherical crystals concentrating at the original boundaries of the glass particles for a cordierite/enstatite glass-ceramic with added B_2O_3 and P_2O_5, whereas Rudolph [105] reported a β-$quartz_{ss}$ skeleton along the original particle surfaces for a cordierite/enstatite glass-ceramic with added P_2O_5.

Depending on the composition of the initial glass the growth of μ-cordierite crystals may result in the rejection of impurities that cannot be accommodated into the β-quartz structure. Dendritic growth of μ-cordierite crystals with rejection of barium [59] and phosphorus [105] into the interdendritic glass have been reported.

Glendenning and Lee [58], for a stoichiometric cordierite composition containing 1 wt % B_2O_3 and 2.5 wt % P_2O_5, report the growth of μ-cordierite with a dendritic morphology or growth of α-cordierite with a cellular morphology. They suggest that the morphology is most likely controlled by the glass composition directly ahead of the growth front, and that the different polymorphs associate with the different growth fronts as a result of the ability of the more open crystal structure of α-cordierite, with the large c-axis channel, to accommodate impurities more readily

than μ. "The rejection of impurities into the glass is less likely for α, so that dendritic growth is restricted".

d) Formation of α-cordierite

With higher temperatures, or longer exposure to high temperatures, the metastable μ-cordierite transforms to α-cordierite. However, the relative stability of the μ and α phases is strongly affected by composition.

Muller et al [33], working on a stoichiometric composition, found that μ-cordierite rapidly transforms into α-cordierite at temperatures above 1000°C. However, where short time thermal treatments were applied, μ-cordierite was still the primary phase even up to 1300°C.

Amista [79] showed that excess MgO inhibits the formation of μ-cordierite and lowers the formation temperature of the α-phase. When the molar ratio reaches ($MgO:Al_2O_3:SiO_2$ - 4:2:5) μ-cordierite is not formed and α-cordierite is formed at 900°C. In contrast, excess SiO_2 was shown to stabilise the μ-phase to the extent that for a 2:2:9 composition μ and α-cordierite were both present at 1200°C.

The combined addition of a few wt % B_2O_3 and P_2O_5 (discussed below) also affects the relative stability of μ and α-cordierite. Formation of μ-cordierite is suppressed, promoting direct crystallisation of α-cordierite [58].

Recent results have been reported on the nature of the sites at which the transformation from metastable μ-cordierite to α-cordierite is nucleated, and whether α is able to form directly from the glass or only via the μ-phase.

Winter [116], working on an SiO_2 rich composition (molar ratio $MgO.Al_2O_3.SiO_2$ - 2:2:11) found that the transformation of β-$quartz_{ss}$ to α-cordierite is nucleated at the surfaces of the β-$quartz_{ss}$ crystals. The grain boundaries between the β-$quartz_{ss}$ crystals provide a short circuit growth path, possibly due to their defective structure acting as effective diffusion paths, resulting in cordierite crystals growing over long distances along the grain boundaries of several β-$quartz_{ss}$ crystals. On prolonged annealing, the cordierite rims grow dendritically into the cores of β-$quartz_{ss}$ crystals maintaining the same crystallographic orientation. The transformation from μ-cordierite to α-cordierite maintains neither the composition nor the crystallographic orientation of the original μ-cordierite grain. The orientation of the cordierite within

a β-quartz$_{SS}$ crystal depends only on the orientation of the cordierite seed crystal. In this composition, the growth rate is high compared to the nucleation rate, although this may not necessarily be the case for other compositions, as the crystal growth and nucleation rate are likely to be strongly composition dependent.

Chaim and Heuer [59] found that for a stoichiometric glass containing 2 wt % BaO, β-cordierite crystals were nucleated either at the μ-cordierite-glass boundary or within a μ-cordierite dendrite. The growing β-cordierite grain consumes the μ-cordierite into which it forms at a faster rate than the μ-cordierite is able to grow into the glassy matrix. This results in some direct crystallisation of glass to β-cordierite. For this composition the β-grains were also dendritic. A single β-grain is able to grow into more than one μ-cordierite grain, with no topotactic relationship observed. In this instance BaO was found to suppress the crystallisation kinetics, which may be due to BaO either increasing the melt viscosity or preventing congruent crystallisation of the glass. As previously mentioned (Section 2.7.2), the observation of β rather than α-cordierite may arise due to TEM measuring local order.

The work reported by Rudolph [107] based on optical observations is also of interest. At low temperatures, 1050°C, the growth front is formed by high quartz$_{SS}$ crystals which transform with some delay into high cordierite. At higher temperatures, 1200°C, no intermediate formation of high quartz$_{SS}$ is observed, the high quartz solid solution phase is so unstable that cordierite crystallises instantaneously. A possibility here is that the μ-cordierite growth front has been overtaken by the growing α/β cordierite crystal.

Temperature also strongly affects the crystallisation behaviour. Bridge found that the crystal size of both enstatite and α-cordierite coarsens with increasing temperature above 1000°C: from 0.2 μm for α-cordierite and < 0.1 μm for enstatite at 1000°C, to 0.6 μm for both phases at 1075°C.

Watanabe et al [115] state that the factor controlling the rate of crystal growth for most glass bodies at a small degree of supercooling is the interface kinetics, that is the movement of material across the interface and its attachment to the crystal surface. This can occur in one of two regimes. Firstly, continuous growth, which allows the interface to advance everywhere concurrently. This results in an atomically rough interface and curved growth banding. Secondly, layer growth, either due to surface nucleation or spiral growth. This normally occurs at a small undercooling and results in an atomically smooth interface with straight growth

banding. For a typical substrate composition with added B_2O_3 and P_2O_5 they found that α-cordierite crystals grow by faceted layer growth from 1363°C to 1196°C, and by non faceted growth below 935°C. From 935°C to 1196°C a transition region exists between the two growth regimes

Other factors which may control the rate of crystal growth are: the diffusion of material in the melt, heat transfer - the removal of latent heat of crystallisation from the growing crystal surface, and reconstructive transformation - the arrangement of atoms or ionic species at the solid/liquid interface.

Glendenning and Lee [58] state that, in the case of aluminosilicate glasses, the crystallisation rate is relatively slow (compared to metals) and mass transport through the glass to the growing interface is usually rate controlling. However, Müller et al [33] have reported that the crystal growth velocity of μ-cordierite on stoichiometric glass surfaces is independent of time, suggesting an interface controlled growth mechanism. It is however possible that a difference in composition between the crystal phase and the melt may change the rate controlling mechanism.

The crystal growth velocity is obviously a function of many factors. For the production of a sintered glass-ceramic, one of the benefits of moving away from the stoichiometric composition is a lowered growth velocity [7]. The maximum growth velocity for α-cordierite has been measured as 600 μm min^{-1} at 1250°C for stoichiometric glass [33], compared to 176 μm min^{-1} for the 'c' axis direction, and 35 μm min^{-1} for the 'a' axis direction at 1248°C for a typical substrate composition containing B_2O_3 and P_2O_5 [115].

e) Activation energy

There are many recently reported measurements of the apparent activation energy for the crystallisation of both α-cordierite and μ-cordierite using both isothermal [79][109][33][110][118][115][107][112][29] and non-isothermal methods [1][110][119][115][107][79][109]. The values reported (in kJ $mol^{-1)}$ range from 252 [110] to 628 [29] for μ-cordierite, and from 302 [115] to 901 [110] for α-cordierite. As non-isothermal (DTA based) methods have been used to measure the activation energy in the current work, the range of values reported in the literature is discussed in conjunction with the results from this work in Section 5.5.

f) Formation of enstatite/forsterite

Enstatite and forsterite mostly occur as a secondary phase to control the thermal expansion. As a result, the mechanisms for their formation are less well reported.

Bridge [1], for a typical substrate composition containing both B_2O_3 and P_2O_5, found that the formation of enstatite follows shortly after the μ-α transition, which in this composition occurs rapidly from 875-925°C. Following the initial crystallisation of the μ-phase, a rapid decrease in a_0 and an increase in c_0 of μ-cordierite were reported. This is consistent with a rapid compositional change. The initial μ-cordierite formed is Mg^{2+} and Si^{4+} rich, the exsolution of which aids enstatite formation. Above 960°C increased enstatite formation was observed at the expense of α-cordierite. Reduced enstatite formation was observed in compositions containing both B_2O_3 and P_2O_5. The enstatite converted to proto-enstatite above 1050°C. Watanabe et al [115] reported proto-enstatite formation directly from the glass at temperatures above 1300°C.

The formation of forsterite is favoured by a higher content of MgO [79][1] or B_2O_3 [4].

g) Sintering vs. crystallisation

Sintering occurs by viscous coalescence, starting at temperatures above Tg. For high strength glass-ceramics, sintering to near theoretical density is required. Crystallisation results in a rapid increase in the effective viscosity, and although this may be beneficial and promote shape retention, sintering can be inhibited. Sintering is often viewed as a competing process with crystallisation. The effect is particularly significant when glass-ceramics are used for joining or coating applications as the increased viscosity as a result of crystallisation may inhibit wetting.

Rabinovich [120] found that cordierite glasses containing TiO_2 did not sinter well and had poor strength, and concluded that surface crystallisation is required for sintered glass-ceramics.

The effect of uncontrolled surface nucleation, and the route to a fully dense glass-ceramic is well described by Knickerbocker [7].

"The refractory crystalline phases formed on the surface of the glass particles prevent viscous coalescence of the particles at lower temperatures. At higher temperature the lowered viscosity of the glass below the devitrified crust of the glass particles promotes rapid crystal growth from the surface into the interior of the glass which precludes any possibility of densification at the desired temperature...If one can hinder the crystallisation of the glass particles for a sufficient interval to permit coalescence of the glass, the densified body can eventually crystallise throughout resulting in a fully dense sintered glass ceramic."

Budd [100] found that 25% crystallisation prevented further densification in a sintered enstatite glass-ceramic. However, the degree of crystallisation that is required to prevent further densification may vary according to the morphology of the crystallisation.

Stoichiometric cordierite glass sinters poorly due to premature crystallisation [120]. The sintering behaviour can be improved by:-

- Removing active sites from the surface by a chemical treatment [117].
- Moving away from the stoichiometric composition. Off stoichiometric glasses can be sintered to near theoretical density because: firstly they exhibit lower viscosity compared to stoichiometric glass throughout the sintering regime, and secondly the rate of crystal growth is lower [7].
- Adding components to the glass that improve sintering behaviour. In the cordierite/enstatite system the addition of B_2O_3 and P_2O_5 has been particularly successful (discussed in Section 2.7.7 below). A summary of the effect of other additives on the sintering behaviour is given by Bridge [1].

The **heating rate** can also have a significant effect on the sintering behaviour. For a powdered cordierite glass with added B_2O_3 and P_2O_5 both the sintering and the densification temperatures increase as the heating rate is increased [104]. Panda et al [121] looked at the effect of the heating rate on the relative rates of sintering and crystallisation of an anorthite-cordierite glass, which could be sintered to full density at 2.0°C min^{-1} but not at 0.2°C min^{-1}. At the higher heating rate the crystallisation is delayed to a higher temperature allowing the glass to sinter to full density before sufficient crystallisation occurs to prevent further densification. Rabinovich has also suggested that a more rapid heating rate leads to improved sintering of cordierite glasses.

Rudolph et al [106] found that the optimum heating rate for sintering a modified cordierite glass (nominal composition in wt % 52.5 SiO_2, 24.9 Al_2O_3, 18.1 MgO, 4.5 P_2O_5, 2.5 μm particle size) was 15°C per minute, when 99.7% density was achieved. Heating rates above 15°C min^{-1} were found not to be beneficial as the onset of crystallisation remains almost constant resulting in the densification curve shifting to higher temperature with no corresponding shift of the crystallisation curve. For the optimum heating rate the onset of crystallisation at 940°C resulted in an initial decrease in the sintering rate, this was followed by a sharp increase in the sintering rate from 970°C onwards. They suggested that this may have been due to the weight of the dilatometer (≈70 mN) and specimen leading to additional non isotropic shrinkage of the specimen in the vertical direction (viscosity at 970°C 1.1 X 10^7 dPa.s). It is however possible that the heat evolved as a result of crystallisation may have had an impact, resulting in increased temperature and reduced viscosity of the surrounding glass, leading to improved sintering.

In addition to having a significant effect on the microstructure and strength of the final glass-ceramic, the **particle size** also affects the crystallisation temperature. The crystallisation mechanisms of pellets pressed from coarse and fine powders are identical [58], and the onset of crystallisation is independent of particle size. However, the crystallisation peak maximum (as indicated by DTA) varies. For a fine particle size the number of active sites per unit volume is much greater and each has only a small distance to grow for full crystallisation to occur. For a cordierite/enstatite glass ceramic this can cause the peak maximum to vary from 982°C for a particle size of ≈1 μm compared to 1112°C for a particle size of ≈ 19 μm [7]. It is possible that the heat evolved as a result of crystallisation may be partly responsible for this effect.

The particle size also strongly affects the sintering behaviour. Although normally glass powders that are too fine are believed to inhibit sintering [100], due to a higher density of sites resulting in premature crystallisation, Shyu [114] found that for a typical substrate composition containing 2.4 wt % B_2O_3 and 2.4 wt % P_2O_5, densification of the compacts was improved by decreasing the particle size. He also found that as the particle size is decreased the crystallisation of the metastable phase is accelerated, and for fine particle sizes the metastable-stable phase transformation is restricted by the constraint arising from the surrounding matrix because of the reduced crystal size.

For DTA of stoichiometric cordierite Donald reports one peak attributable to α-cordierite for coarse powder, whereas fine powder produces two peaks corresponding to both μ and α cordierite.

The dynamics of crystallisation and sintering lead to two possible approaches for the production of a fully dense glass-ceramic:-

1. Sinter first, below the onset of crystallisation, and then crystallise. Even with this approach a faster heating rate may be beneficial, for example Bridge [1] showed that 3.5°C per minute resulted in better densification than 1°C per minute.
2. Sinter and crystallise simultaneously. This route was used by Rudolph et al [106] who demonstrated an optimum heating rate of 15°C min^{-1}

For a full understanding of sintering, the heat evolved during crystallisation may be significant, although there is little consideration of this in the literature. Donald [109] reports 361.5 ± 7 J g^{-1} for the enthalpy of crystallisation of cordierite glass, which is nearly 300 times the specific heat capacity of cordierite at 1000°C (1.25 J g^{-1} $°C^{-1}$ [46]). Local heating of residual glass to a higher temperature will affect both the crystallisation and the sintering behaviour. For fine powders, where the number of sites per unit volume is greater, and for faster heating rates the effect will be most significant. Sample geometry may also be critical.

Two other factors which may be significant for the sintering of cordierite glass are firstly the positive volume change on crystallisation from the glass to α-cordierite, and secondly the ability of the channels within the cordierite structure to accommodate a wide range of impurities. It is possible that both factors play a role in the elimination of porosity in the final stages of sintering.

h) Activation energy for viscous flow

Several measurements have been made of the activation energy for viscous flow. For stoichiometric cordierite glass the following values (in kJ mol^{-1}) have been reported: 766 [109], 780 [112], 1004 [29]. In contrast, Watanabe et al [122] reported 585 kJ mol^{-1} for a typical cordierite /enstatite substrate composition containing B_2O_3 and P_2O_5.

When crystals having the same composition as the bulk glass are surface nucleated, the activation energy for crystallisation should be almost equal to that for viscous flow.

2.7.7 Microstructural development of and role of B and P in sintered cordierite based glass-ceramics

A large amount of work on the addition of P_2O_5 and/or B_2O_3 to cordierite glass-ceramics has been carried out by workers at IBM [7][115][122], Warwick [1][3][4] and elsewhere [105][106][107][87][118][114][58][103]. Sintered α-cordierite based glass ceramics with strengths >200 MPa and densities >99% have been produced at temperatures below 1000°C [7]. In comparison, for a similar composition in the absence of B_2O_3 and P_2O_5 complete conversion to α-cordierite was not completed until 1170°C [7], and for the production of conventional cordierite ceramics temperatures of ≈1450°C are required .

Although discussed extensively in the literature [1][115][105][106][7][123][58] the exact roles of P_2O_5 and B_2O_3 are not well understood. The effect of P_2O_5 and B_2O_3 separately are discussed below, followed by a consideration of their combined effect.

a) P_2O_5

The role of P_2O_5 in silicate glasses is discussed briefly by Katzschmann [87], who investigated the effect of P_2O_5 content on $MgO.Al_2O_3.SiO_2.TiO_2$ glasses. In pure silica the P^{5+} ion requires the formation of a P=O bond which breaks up the network. The presence of P^{5+} results in a strong tendency for glass-in-glass phase separation.

When Al^{3+} is present this tends to stabilise the P^{5+} ion. The average ionic radius of P^{5+} and Al^{3+} (0.34 nm and 0.5 nm) of 0.42 nm, is comparable to 0.41 nm for Si^{4+}, which enables the combined substitution of Al^{3+} and P^{5+} for two Si^{4+} cations. Charge compensation occurs between the Al^{3+} and the P^{5+}, the three dimensional network is retained, and there is a reduced tendency for phase separation.

Both Bridge [1] and Rudolph [105] have shown that, in MAS glasses, P_2O_5 induces fine scale glass-in glass phase separation. However, in contrast to bulk nucleated glass-ceramics where phase separation may initiate a homogeneous distribution of

crystallites in the bulk, in this instance the phase separation is believed to have no major influence on the nucleation process due to the inhomogeneous distribution of crystallites. However the phase separation may affect the dynamics of sintering and crystallisation. Based on DTA results, Bridge concludes that the role of P_2O_5 is to delay the onset of crystallisation until sintering is near completion.

Katzschmann [87] has shown that for a $MgO.Al_2O_3.SiO_2.TiO_2$ glass the effect of additions of P_2O_5 additions up to 12 wt %, is to lower the viscosity, improve the processability and reduce Tg.

The evidence for how P^{5+} can be accommodated into the final crystal structures is mixed. Topping and Murphy [124] found that the α-cordierite structure could accommodate up to 20 wt % $AlPO_4$, although for μ-cordierite it was slightly less. The incorporation of $AlPO_4$ reduces the α-μ transition by 75°C. In contrast, Perotta and Savage [125] found that high quartz solid solution phases allowed replacement of a large part (up to 70%) of their SiO_2 content by $AlPO_4$, and noted that in spite of the close similarity in the crystal chemistry of $AlPO_4$ and SiO_2, the substitution is generally very limited in framework silicates.

Recent TEM of an MAS glass containing 4.5 wt % P_2O_5 [105] has shown that high cordierite crystallises to near stoichiometric composition resulting in the rejection of P_2O_5 into an intergranular matrix region (composition in wt % 34.8 SiO_2, 37.5 MgO, 24.7 P_2O_5 3.0 ± 1.3 Al_2O_3) which later crystallises to magnesium ortho-phosphate. The formation of magnesium ortho-phosphate has also been reported by Katzschmann [87].

The range of behaviour exhibited may be related to the suggestion of Stoch [126] that the substitution of $AlPO_4$ for $2.SiO_2$ requires the presence of a modifier in the glass. The resulting weakening, and increased flexibility of the silica network, enables $[AlO_4][PO_4]$ groups to be accommodated.

b) B_2O_3

Bridge [1] has suggested that B^{3+} probably resides in tetrahedral co-ordination and has associated with it a charge compensating ion, and has demonstrated that B_2O_3 promotes the μ-α transition or direct formation of α. This effect was also noted by Sutherland [4], who also observed that increased B_2O_3 content lead to the formation of forsterite rather than enstatite. Both Bridge [1] and Knickerbocker [7] report that

although B_2O_3 favours the crystallisation of α rather than μ-cordierite, the effect is not as pronounced as when both B_2O_3 and P_2O_5 are present.

Okuyama [92] has demonstrated that for stoichiometric cordierite ceramics produced via a sol-gel route, doping with B_2O_3 retards the crystallisation from amorphous to μ -cordierite, and accelerates the crystallisation of α-cordierite. Based on XRD observations, doping concentrations above 1.5 mol. % B_2O_3 promote the formation of α-cordierite directly from the amorphous state. Ceramics produced from an undoped initial material showed average fracture strengths of 160 MPa for μ-cordierite based material which reduced to only 30 MPa following conversion to α-cordierite. This weakening arises due to microcracking from the stresses generated by the volume expansion accompanying the μ-α transformation. For doped material the transformation to α-cordierite occurs from the viscous amorphous matrix which is able to accommodate the volume change by plastic deformation resulting in fracture strengths of 190 MPa. The B_2O_3 was excluded to the grain boundary phase and was associated with a reduction in the fracture strength at temperatures above 1100°C. The effect on the crystallisation behaviour was shown to be characteristic of B_2O_3, similar behaviour was not observed for doping with ZrO_2, TiO_2, and P_2O_5.

It is interesting that B_2O_3 favours both the formation of α-cordierite rather than μ-cordierite and of forsterite (orthosilicate) rather than enstatite (chain silicate). This may reflect the structural role of B_2O_3 in the glass.

c) B_2O_3 and P_2O_5

The combination of B_2O_3 and P_2O_5 has been particularly successful for the production of strong, fully-dense, cordierite based glass-ceramics. Suggestions for their combined role are set out below.

Knickerbocker [7] suggested that the role of 0-3 wt % B_2O_3 is to delay crystallisation and promote the formation of α-cordierite, whereas the addition of 0-3 wt % P_2O_5 is to aid sintering, and also to promote the formation of α-cordierite. The presence of B_2O_3 and P_2O_5 in a glass composition increases the peak crystallisation temperature as a result of suppression of the crystallisation of μ-cordierite. Geiss and Knickerbocker [123] suggest that B_2O_3 and P_2O_5 may also play a role in stabilising glass formation.

Bridge [1] stated that P_2O_5 was added to promote surface nucleation and reduce melt viscosity, whilst B_2O_3 was added to aid melting and sintering. Bridge reports the transformation μ-α occurring at temperatures as low as 875°C for typical substrate compositions with B_2O_3 and P_2O_5, with rapid transformation occurring in the range 875-925°C. Comparing a composition with B_2O_3 and P_2O_5 to P_2O_5 only, B_2O_3 only, no additives, and P_2O_5 replace by TiO_2, all were found to have the μ-α transition shifted to higher temperatures, and did not sinter as well. For the composition with no additives the transition was very sluggish and some residual glass remained at 1100°C. In contrast, for the composition with both B_2O_3 and P_2O_5, no residual glass was detected by XRD at temperatures > 900°C. Shyu [114] was also unable to detect glass from XRD in a similar composition.

Glendenning and Lee [58] reported that the addition of B_2O_3 and P_2O_5 to stoichiometric cordierite extends the gap between Tg and Tx and suppresses formation of μ-cordierite whilst promoting the direct formation of α-cordierite. In stoichiometric powder μ is the first polymorph to form, followed by direct crystallisation of and/or transformation into α. The B_2O_3 and P_2O_5 containing cordierite shows the same initial formation of μ and its transformation to α, but the amount of μ produced is much reduced. The sintering is improved hugely by B_2O_3 and P_2O_5, presumably by acting as fluxes and increasing liquid fluidity during viscous flow.

The viscosity of these glasses is well characterised. Geiss, Fletcher and Herron [127] report that the viscosity of bulk cordierite type glass decreases by an order of magnitude for every 40°C rise in temperature. Geiss and Knickerbocker [123] investigated the viscosity of MAS glasses from 13.3 to 22.3 wt % MgO (ranging from stoichiometric to typical substrate compositions). The separate effect of MgO, SiO_2, Al_2O_3, B_2O_3 and P_2O_5 on the viscosity was determined assuming additivity of constituent contributions. P_2O_5 and MgO reduce the viscosity whereas B_2O_3, Al_2O_3 and SiO_2 increase the viscosity. Giess and Knickerbocker suggest that the increase in viscosity with B_2O_3 arises because some B^{3+} ions change from three to four co-ordination with neighbouring O^{2-} ions, whereas P supplies extra non-bridging oxygens and thereby reduces the viscosity. Work by Bridge [1] using penetration viscometry shows excellent agreement for the viscosity of typical substrate compositions containing: no additives, B_2O_3 and P_2O_5, B_2O_3 only and P_2O_5 replaced by TiO_2. Slightly less good agreement was obtained for the addition of P_2O_5 only. Water in the form of hydroxyl ions substituted for bridging oxygens will also effect the viscosity.

2.7.8. Other information on cordierite glass-ceramics relevant to potential use for joining applications

Boberski and Geiss [128] looked at the substitution of nickel for magnesium in stoichiometric cordierite glasses, and found that complete solid solution exists for $Mg_2Al_4Si_5O_{18}$ and $Ni_2Al_4Si_5O_{18}$ and the crystallisation sequence is unaffected. However the presence of nickel shifts the transformations (glass to high quartz, and high quartz to hexagonal cordierite) to lower times and temperatures. This is of interest for two reasons, firstly because of the possibility of producing glass-ceramics at lower temperatures (particularly for electronic substrate applications) and secondly, because NiO may be used as an adherence oxide due to its low affinity for oxygen, there is the possibility of doping cordierite based glass-ceramics with NiO for joining or coating applications.

It is interesting that similar behaviour has been reported for the other common adherence oxide, cobalt oxide [129]. A complete solid solution series exists between $Mg_2Al_4Si_5O_{18}$ and $Co_2Al_4Si_5O_{18}$ at temperatures below 1160°C. The thermal stability of the cordierite solid solution decreases with increasing cobalt content.

References for Chapter 2

[1] Bridge D.R., Aspects of electronic device packaging, Ph.D. Thesis, Univerity of Warwick, 1986.

[2] Bridge D.R., Holland D. and McMillan P.W., Glass. Tech. Vol. 26, No. 6, December 1985, pp 286-292.

[3] Logan E.A. and Holland D., Alvey 050 Report (1989).

[4] Sutherland S., and Holland D., Glass Ceramic Coatings for the Protection of High Temperature Titanium Alloys, 1991, Department of Physics, University of Warwick, Internal report.

[5] McMillan P.W., Glass-ceramics, 2nd Edn, Academic Press, London, 1979.

[6] Bach H. (Editor), Low thermal expansion glass ceramics, Springer, 1995.

[7] Knickerbocker S.H., Kumar A.H. and Herron L.W., Am. Cer. Soc. Bull. 72 [1] 90-95 (1993).

[8] Strnad Z., Glass-ceramic materials, Elsevier Science, Amsterdam, 1986.

[9] Bereznoi A.I., Glass-ceramics and photositalls, Plenum Press, 1970.

[10] Smith G.P., Materials and Design, Vol. X No. 2, March/April 1989.

[11] James P.F., J. Non-Cryst. Solids, 181, 1-15 (1995).

[12] Partridge G., Glass Tech., Vol. 35 No. 3, (1994) 1.

[13] Muller G., Chapter 2 in Low thermal expansion glass ceramics, Ed. Bach H., Springer, 1995.

[14] James P.F., Volume nucleation in silicate glasses, pp 59-105 in Glasses and glass-ceramics, Ed. M.H. Lewis, Chapman and Hall, 1989.

[15] Headley T.J.and Loehman R.E., J. Am. Ceram. Soc., Vol 67 (No. 9), 1984, pp 620-625.

[16] Vogel W., Glass Chemistry - 2nd Edition, Springer-Verlag, 1994.

[17] Strnad Z. and Douglas R.W., Phys. Chem. Glasses, 14 (1973) 2, pp 33-36.

[18] Bergeron C.G. and De Luca J.P., J. Am. Ceram. Soc., 50 (1967) 116.

[19] Klingsberg C., J. Am. Ceram. Soc., 47 (1964) 97.

[20] Morey G.W., J. Am. Ceram. Soc. 13 (1930) 683.

[21] Mattox D., J. Am. Ceram. Soc. 50 (1967) 683.

[22] Scott W.D. and Pask J.A., J. Am. Ceram. Soc., 44 (1961) 181.

[23] Neely J.E. and Ernsberger F.M., J. Am. Ceram. Soc., 49 (1966) 116.

[24] Uhlmann D.R., J Non-Cryst Solids, 41 (1980) 347.

[25] Schmelzer J., Pascova R., Moeller J. and Gutzow I., J. Non-Cryst. Solids, 162 [1-2] (1993) 26-39.

[26] Zanotto E. D., J. Non-Cryst. Solids, 129 (1991) pp 183-190.

[27] Tabatha K., J. Am. Ceram. Soc., 10 (1927) 6.

[28] Swift H.R., J. Am. Ceram. Soc., 6 (1947) 165.

[29] Yuritsin N.S., Fokin V.M., Kalinina A. M. and Filipovich V. N., Proc. of the XVI Intl. Cong. on Glass, Madrid, Spain, October 1992, (Bol, Soc. ESp. Ceram Vid, 31-C, 5, 1992), pp21-26.

[30] Gonzales-Oliver C.J.R., Johnson P.S. and James P.F., J. Mater. Sci. 14 (1978) 1159.

[31] Bansal N.P. and Doremus R.H., J. Am. Ceram. Soc. 66 (1983) 132.

[32] Muller R., Thamm D., and Pannhorst W., Proc. of the XVI Intl. Cong. on Glass, Madrid, Spain, October 1992, (Bol, Soc. ESp. Ceram Vid, 31-C, 5, 1992) 105-110.

[33] Muller R., Reinsch S. and Pannhorst W., Glasstech. Ber. Glass Sci. Technol. 69 (1996) No1 pp 12-20.

[34] Beall G.H., J. Non-Cryst. Solids, 129 (1991) 163-173.

[35] Nawa M., Makio K., Ishikara M., Kamiya A. and Nakano K., J. Cer. Soc. Japan, 1992, Vol 100, No 6, pp 784-790.

[36] Gadkaree K.P., J. Mat. Sci., Vol 26 (18), p4845-4854.

[37] Engineered Materials Handbook, Volume 4 - Ceramics and Glasses, ASM International, 1991.

[38] Creyke W.E.C., Sainsbury I.E.J. and Morrell R., Design with non-ductile materials, Applied Science Publishers, 1982.

[39] Lewis D. III, Am. Ceram. Soc. Bull., Vol 61 (No 11) 1982 p1208-1214.

[40] McHale A.E., Engineering properties of glass-ceramics, pp870-878 in Engineered Materials Handbook, Volume 4 - Ceramics and Glasses, ASM International, 1991.

[41] Donald I.W., J. Mat. Sci. 28 (1993) 2841-2886.

[42] Donald I.W., Metcalfe B.L. and Morris A.E.P., J. Mat. Sci. 27 (1992) 2979-2999.

[43] Donald I.W., Metcalfe B.L., Wood D.J. and Copley J.R., J. Mat. Sci. 24 (1989) 3892-3903.

[44] Bansal N.P. and Drummond C.H. III, J Mater. Sci. Letts. 13 (1994) 53-55.

[45] Prewo K.M., Fibre reinforced glasses and glass-ceramics, p337-368 in Glass: science and technology, Ed:- Uhlmann D.R. and Kreidel N.J., Academic Press, 1984.

[46] Morrell R., Handbook of properties of technical and engineering ceramics. Part 1: an introduction for the engineer and the designer, National Physical Laboratory, H.M.S.O., London, 1985.

[47] Lachman I.M., Bagley R.D. and Lewis R.M., Am. Ceram. Soc. Bull., 60 [2] 202-205 (1981).

[48] The Economist, Feb 1995.

[49] Phase diagrams for ceramists - Figure 712, Editors: Levin E.M., Robbins C.R. and McMurdie H.F., The American Ceramic Society, 1964.

[50] Lamar R.S. and Warner M.F., J. Am. Ceram. Soc., 37 (12) 602 (1954).

[51] Mussler B.H. and Shafer M.W., Ceram. Bull., 63 (5) 705 (1984).

[52] Kazakos A.M., Komoneni S. and Roy R., J. Mater. Res. 5 5 1990 1095-1103.

[53] Maurer R. D., J. App. Phys., Vol. 33, No 6 June 1962 pp 2132-2139.

[54] Barry T.I., Cox J.M. and Morrell R., J. Mater. Sci. 13 (1978) 594.

[55] Son Y-B., Kim C-H., Jang S-D., Lui J., Sarikaya M. and Aksay A., Jpn. J. Appl. Phys., Vol. 33 (1994) pp1101-1108.

[56] Hirose Y., Doi H. and Kamigaito O., J. Mater. Sci. Letts., 3 (1984) 153-155.

[57] Chamberlain A. PhD Thesis, University of Warwick, 1996.

[58] Glendenning M.D. and Lee W.E., J. Am. Ceram. Soc., 79 [3] (1996) pp705-713.

[59] Chaim R. and Heuer A. H., J. Am. Ceram. Soc., 75(6) (1992) 1512-21.

[60] Karkhanavala, M.D and Hummel, F.A. (1953), J.Am.Ceram.Soc. 36, 393.

[61] Yoder, H.S., Amer.J.Sci. 250, 569, (1952).

[62] Gregory A.G. and Veasey T.J., J. Mat. Sci. 6 (10) 1312 (1971), 7 (11) 1327 (1972), 8 (3) 324 (1973) and 8 (3) 333 (1973).

[63] Putnis A., Introduction to mineral sciences, CUP, 1993.

[64] Schreyer W. and Schairer J.F., Z. Krist., 116, 60 (1961).

[65] Roy R., Zeit. fur Krist., Bd. 111 S. 185-189 (1959).

[66] Griffen D.T., Silicate crystal chemistry, O.U.P., 1992.

[67] Buerger M.J., Am. Mineralogist, 39 (7-8) 600-14 (1954).

[68] Winkler H.G., Acta Cryst. 1, 27 (1948).

[69] Ray S. and Muchow G.M., J. Am. Ceram. Soc. 51(12), 678 (1968).

[70] Beall G.H., Karstetter B.R. and Rittler H.L., J. Am. Ceram. Soc., Vol 50 No 4 (1967) p181-190.

[71] Miyashiro A., Amer. J. Sci., 255 (1957) 43.

[72] Langer K. and Schreyer W., Am. Miner. 54 (1969) 1442.

[73] Chaim R. and Heuer A.H., J.Am.Ceram.Soc., 75[6] 1512-21, 1992.

[74] Shreyer W. and Yoder H.S., Neues. Jahrb. Mineral Akstr., 101, 271, 1964.

[75] Partridge G., Elyard C.A. and Budd M.I., pp 226-271 Glass-ceramics in substrate applications, Glasses and glass-ceramics, Ed. M.H. Lewis, Chapman and Hall, 1989

[76] Kriven W.M., J. Am. Ceram. Soc., 70 [5] 349-60 (1987).
[77] Lee W.E. and Heuer A.H., J. Am. Ceram. Soc., 70 [5] 349-60 (1987).
[78] Sarver J.F. and Hummel F.A., J. Am. Ceram. Soc., 45 (4) 152-156 (1962).
[79] Amista P., Cesari M., Montenero A., Gnappi G. and Luo Lan, J. Non-Cryst. Solids 192-193 (1995) 529-533.
[80] Schreyer W. and Schrairer J.F., Amer. Min., 47, 90 (1962).
[81] Winter. W., Berger A., Muller G. and Pannhorst W., J. Am. Ceram. Soc., 76 (7) (1993) 1837-43.
[82] Holmquist S.B., Zeit. fur Krist., Bd 118, S. 477-478 (1963).
[83] Dusil J. and Cervinka L., Glass Tech. Vol. 17 No. 3 June 1976 pp 106-111.
[84] Ziemath E.C., Diaz-Mora N. and Zanotto E.D., Phys. Chem. Glasses, 1997, 38 (1) 1-5.
[85] Heide K., Volksch G. and Hanay Ch., J. Therm. Anal., Vol. 40 (1993) 171-180.
[86] Heide K., Volksch G. and Heide K. Proc. of the XVI Intl. Cong. on Glass, Madrid, Spain, October 1992, (Bol, Soc. ESp. Ceram Vid, 31-C, 5, 1992) 111-116.
[87] Katzschmann A. and Wange P., Glastech. Ber. Glass Sci. Technol. 68 (1995) No. 4 111-116.
[88] Dictionary of Ceramics, 3rd Edition, Dodd A. and Murfin D., The Institute of Materials, 1994.
[89] Kingery W.D., Oxides for High-Temperature applications, High Temperature technlogy, Proc. of International Symposium arranged by Stanford Research Institute, Asilomar, Calif. (Oct 6-9, 1958), Mcgraw-Hill, New York.
[90] Stutzman R.H., Salvaggi J.R. and Kirchner H.P., (1959). An investigation into the theoretical and practical aspects of the thermal expansion of ceramic materials, U.S. Dept. of Commerce, Office of Technical services.
[91] Moxey T., Final year project report, University of Warwick, 1995.
[92] Okuyama M., Fukui T. and Sakurai C., J. Mater. Sci. 28 (1993) 4465-4470.
[93] Hayashi K., Yamada T., Okamoto Y. and Nishikawa T., J. Cer. Soc. Japan, 1993, Vol 101, No 11, pp 1264-1267
[94] Ishmael M.G.M.U., Tsuatori H., and Nakai Z., J. Am. Ceram. Soc., 73 (1990) 537.
[95] Hirano M. and Inada H., J. Mat. Sci., 1993, Vol 28, No 1, pp 74-78.
[96] Oh Y.J., Oh T.S. and Jung H.J., J. Mat Sci., 1993, Vol. 26, N023, pp 6491-6495.
[97] Echeverria L.M., J. Non-Cryst. Solids, 147-148 (1992) 559-564.

[98] Beall G.H, Chyung K., Stewart R.L., Donaldson K.Y., Lee H.L., Baskaran S. and Hasselman D.P.H., J. Mat. Sci. 21 (1986) 2365-72.

[99] Anstis G.R., J.Am. Ceram. Soc. 64 (1981) 533.

[100] Budd M. I., J. Mater. Sci. 28 (1993) 1007-1014.

[101] Ishida Y., Wang J. and Suga T., Acta. Met. Mater., Vol 40 Suppl., pp5289-5293, 1992.

[102] Itoh M., Miyama K., Tanaka T., Taniguchi M., Mori S., and Kato N., J. Jap. Inst. of Metals, 1995, Vol. 59, No. 5. p580-583.

[103] Sung Y-M., J. Mat. Sci. 31 (1996) 5421-5427.

[104] Panda P.C. and Raj R., J.Am.Ceram.Soc., 72 [8] 1564-66 (1989).

[105] Rudolph T., Szabo D.V., Pannhorst W., Weisskopf K.L. and Petzow G., Glastech. Ber. 64 [8] (1991) pp 218-224.

[106] Rudolph T., Weisskopf K.L., Pannhorst W. and Petzow G., Glastech. Ber. 64 [12] (1991) pp 305-309.

[107] Rudolph T., Pannhorst W. and Petzow G., J. Non-Cryst. Solids 155 (1993) 273-281.

[108] Watanabe K. and Giess E.A., J. Non-Cryst Solids 169 (1994) 306-310.

[109] Donald I.W., J. Mat. Sci. 30 (1995) 904-915.

[110] Goller M. and Pye L.D., Glasstech. Ber. Glass Sci. Technol. 68 C1 (1995) 169-174.

[111] Szabo I., Pannhorst W. and Rappensberger M., Proc. of the XVI Intl. Cong. on Glass, Madrid, Spain, October 1992, (Bol, Soc. ESp. Ceram Vid, 31-C, 5, 1992) 119-124.

[112] Diaz Mora N., Ziemath E.C. and Zanotto E.D, Bol. Soc. Esp. Ceram. Vid. 31-C (1992) 5 pp 117-118.

[113] Alekseenko V.I., Volkova G.K., Konstantinova T.E. and Popova I.B., Phys. Stat. Sol. (a) 144 (1994) 271.

[114] Shyu J-J., Wang C-Y. and Chang T-Y., J. Am. Ceram. Soc., 79 [7] 1971-74 (1996).

[115] Watanabe K., Giess E.A. and Shafer M.W., J. Mat. Sci. 20 (1985) 508-515.

[116] Winter W., Berger A., Muller G. and Pannhorst W., J. Eur. Ceram. Soc., 15 (1995) 65-70.

[117] Helgesson C.I., Sci. Ceram. 8 (1976) 347.

[118] Sue Y-J., Chen S-Y., Lu H-Y. and Shen P., J. Mater. Sci. 26 (1991) 1699-1704.

[119] Sung Y-M., J. Mat. Sci., 31 (1996) 5421-5427.

[120] Rabinovich E.M., p327-333 in Advances in ceramics, Vol. 4, Editors - Simmons J.H., Uhlmann J.R. and Beall G.H., Am. Ceram. Soc. 1994.
[121] Panda P.C., J. Am. Ceram. Soc., 72 [12] 2361-64 (1989).
[122] Watanabe K. and Giess E.A., J. Non-Cryst. Solids, 169 (1994) 306-310.
[123] Giess E.A. and Knickerbocker S.H., J. Mater. Sci. Letts., 4 (1985) 835-837.
[124] Topping J.A. and Murphy H.K., J. Can. Ceram. Soc., 46 (1977) 19.
[125] Perotta A.J. and Savage R.O., J. Am. Ceram. Soc. 50, (1967), 112.
[126] Stoch L., Fundamentals of glass science and technology 1993. Proc. 2nd Conference of the European Soc. of Glass Science and Technology, Venice (Italy) 1993, pp 487-490.
[127] Giess E.A., Fletcher J.P. and Herron L.W., J. Am. Ceram. Soc. 67 [8] 549-552 (1984).
[128] Boberski C. and Geiss E.A., J. Mater. Sci., 1994, Vol.29, No. 1, pp 67-72.
[129] Wandschneider P. and Seifert F., J. Am. Ceram. Soc., 1984, Vol. 67, No. 8, C163-164.

Chapter 3: Joining of ceramics

"the successful utilisation of ceramics implies an ability to assemble simple components into structures that will function effectively and here the current state of the art falls short of effective solutions...little progress has been made in the last ten years and a technical gridlock has developed...The development of generic joining technology for ceramic materials is vital and should be pursued in the context of both basic and applied science."

Zdaniewski - 1993 [1]

3.1 Introduction

Due to their high strength to weight ratio, dimensional stability and chemical inertness at high temperature, there are many promising high temperature applications for ceramics. However, ceramic components are brittle, with a corresponding scatter in strength, and ceramic components with large or complicated shapes are difficult and expensive to produce, with increased quality control problems. In order for ceramics to be used to the full, techniques must be developed to enable them to be successfully joined to themselves and other high temperature materials. Zdaniewski [1] described ceramic joining technology as "the missing link", Shwartz [2] also sees joining as a key technology for ceramic composite applications.

Joining solutions are inevitably a compromise, in which the ease of the joining operation must be offset against any degradation in the desirable properties of the final product. For many joining applications, the performance requirements of the joint may differ significantly from those required elsewhere in the joined body and there is therefore scope for a range of different joining solutions.

3.2 Requirements for a successful joint

For low temperature and low stress applications the use of an adhesive is often an appropriate solution. However, adhesives often suffer from temperature limitations and are sensitive to environmental degradation, for example due to exposure to moisture.

Joints usually need to be permanent but sometimes demounting is required when the use of mechanical fasteners are advantageous. Siemens have successfully used mechanical fasteners in heat exchangers for joints that withstand 1350°C [3].

However, for a strong high performance joint, where the reliability and performance limitations of adhesives or mechanical fasteners are not acceptable, a strong chemical bond is normally required. The main requirements for the formation of a strong chemical bond and a successful joint are summarised in 3.2.1 to 3.2.5 below. For more detailed accounts see ASM Engineered Materials Handbook, Volume 4 Ceramics and Glasses - Section 7 - Joining [4], Nicholas [5][6] and Donald [7].

3.2.1 Wetting

One of the most important requirements for the formation of a strong chemical bond and a successful joint is that the two surfaces to be bonded (or each surface and some third adhesive material) must be brought into intimate contact. Most joining operations such as brazing, and glass/metal seals, involve a liquid phase, and an intimate atomic interface may be achieved if wetting occurs.

Consider a sessile drop (Figure 3.1). The driving force for wetting is related to the difference in energy between the solid-vapour and the solid-liquid interfaces. As spreading also tends to increase the surface area of the liquid-vapour interface there is an additional force resisting the spreading.

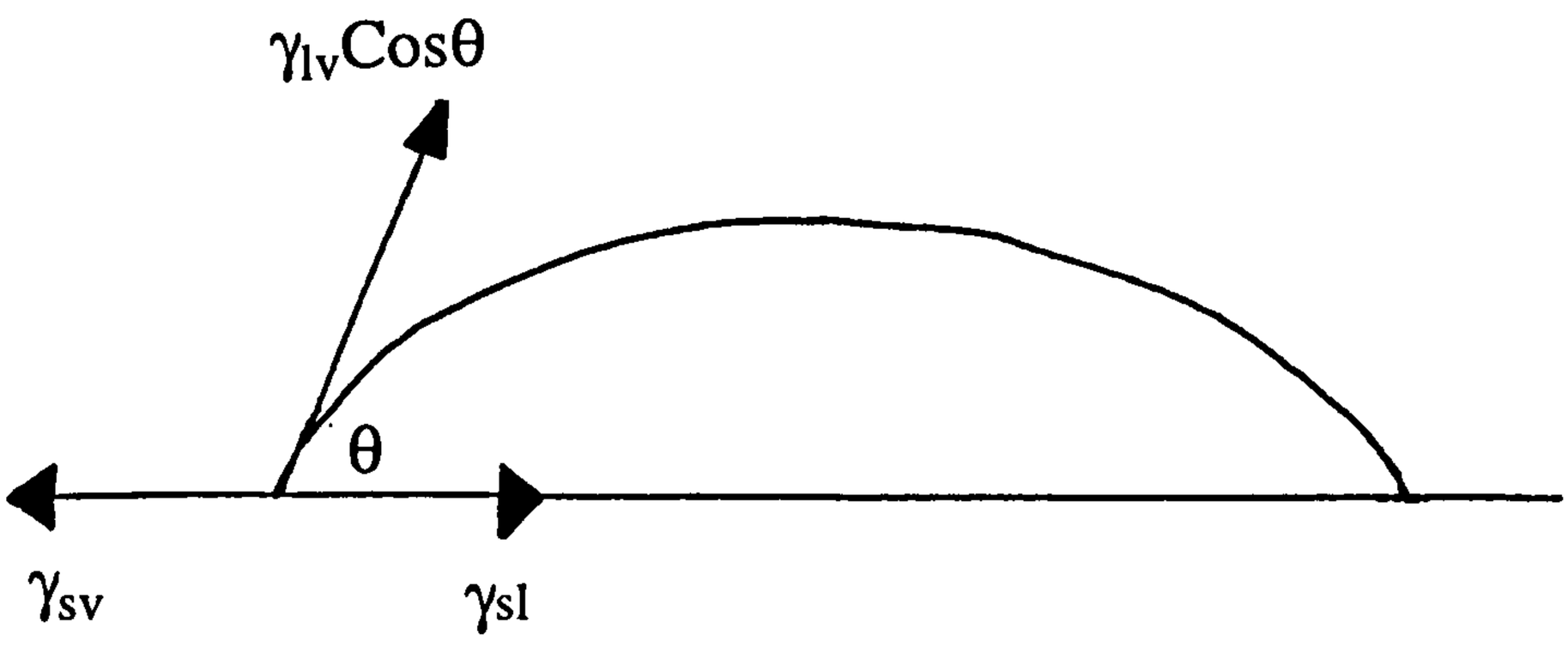

Figure 3.1: Sessile drop demonstrating wetting behaviour.

The shape of a sessile drop may be described in terms of the interfacial energies (γ) and the wetting angle (θ) by Young's equation (Equation 3.1), where s, l and v refer to the solid, liquid and vapour respectively. This equation applies for a solid-liquid interface in stable or metastable thermodynamic equilibrium.

$$\gamma_{sv} = \gamma_{sl} + \gamma_{lv}\cos\theta \qquad \text{Young's equation} \qquad (3.1)$$

In order to separate the solid and the liquid the work of adhesion (W_A) has to be overcome. This is given by:

$$W_A = \gamma_{sv} + \gamma_{lv} - \gamma_{sl} \qquad (3.2)$$

A positive work of adhesion results in a stable interface. If Equations 3.1 and 3.2 are combined the work of adhesion can be re-expressed so that the bonding strength is directly related to the wetting angle (Equation 3.3).

$$W_A = \gamma_{lv}(1+\cos\theta) \qquad (3.3)$$

For joining applications non-wetting behaviour is unfavourable because of poor penetration of surface and grain boundary irregularities due to a lack of capillary behaviour. For glass/glass-ceramic on metal, the molten oxide-glass must wet the surface of the metal. The metal surface is often covered with an oxide layer and this often enhances the wetting behaviour.

A more detailed discussion of wetting behaviour, which may be affected by interfacial reactions, residual stress, surface roughness and atmosphere, is given by Pask and Tomsia [8] and Pask and Fulrath [9].

3.2.2 Chemical bonding

Even if wetting occurs and intimate contact is achieved it may be difficult to determine by observation alone whether a strong chemical bond or weak Van der Waals forces exist. It is often assumed that, in the absence of residual stress and for similar defect populations, failure along the interface corresponds to Van der Waals bonding. Conversely, if failure occurs partially through one or both of the adherent materials, it implies that bonding across the interface is roughly as strong as the bonding within the material, and a strong chemical bond is present. Mechanical

bonding or keying may make a contribution to bond strength but is not the dominant mechanism when a strong chemical bond is present.

Pask [9] and King [10] demonstrated the requirements for the formation of a strong chemical bond for the case of an oxide glass on metal. To maintain a strong chemical bond at the interface, a balance of bond energies and continuity of electronic structure is required. For example, when bonding metals to glasses or glass-ceramics, a transitional zone is required between the metallic bonding in the metal and the ionic-covalent bonding in the glass. This is normally obtained by the formation of an oxide layer on the metal. This may be a thin oxide monolayer or an oxide-rich transitional layer, in which case the resulting bond will only be strong if the oxide is mechanically strong and well bonded to the metal substrate.

The oxide layer may be produced by pre-oxidising the metal parts prior to bonding. The pre-oxidation stage may be critical as too thick or too thin an oxide layer, or the wrong type of oxide, give a bond which is mechanically weak. For the oxide layer to be stable the glass at the interface must be saturated with the appropriate metal oxide, otherwise a state of dynamic equilibrium at the metal/glass interface cannot be maintained.

For many Cr-containing alloys, controlled pre-oxidation to form a thin Cr_2O_3 layer a few microns thick results in a mechanically robust, strongly adherent oxide layer. Cr^{3+} is believed to occupy the role of an intermediate in the glass resulting in a low rate of diffusion away from the interface, saturation of the interface with the appropriate metal oxide and low rate of dissolution of the oxide scale. In contrast, Cr^{2+} takes on the role of a modifier in the glass, resulting in rapid diffusion away from the interface and rapid dissolution of the oxide layer. Saturation of the interface is not maintained, resulting in poor adherence.

An alternative way to ensure that the glass at the interface remains saturated with the substrate metal oxide is by the use of adherence oxides (eg: NiO), which are added to the glass and reduced by the substrate. Adherence oxides are widely used for enamelling and their role has been well described by Borom and Pask [11].

For ceramic to metal bonding an alternative approach to ensure continuity of electronic structure at the interface is to metallize the surface of the ceramic. The best known example is the widely used Mo-Mn process for joining Ni-Co-Fe alloys to alumina for vacuum sealing applications. The Mo-Mn process is described in detail by Kohl [12] and Mizuhara and Oyama [13].

However the continuity of bonding is obtained, thermodynamically stable chemical equilibrium must exist at the interface; this is achieved by chemical reaction at the interface. In practice, the equilibrium compositions are obtained rapidly at the bonding temperature and continued heating will normally result in a maintenance of that equilibrium, with an increase in the reaction product and a corresponding increase in the thickness of the reaction zone. For a stable interface, no further growth of the reaction zone must occur at the temperature at which the joint is to be used.

3.2.3 Microstructural change

It is important to avoid changing the microstructure and hence the physical properties of the two materials being bonded. For example, many alloys require specific heat treatments to control the microstructure and to give the required properties; this must not be compromised by any joining heat treatment.

Glass-ceramic microstructural change can also be a problem. If the microstructure and/or phase composition of the glass-ceramic are changed significantly the physical properties, including the TCE change. When this occurs, in order to determine the interfacial stresses, the TCE of the reaction zone is important. Kunz and Loehman [14] developed a method based on a bimetallic strip analysis of measuring the thermal expansion mismatch at the glass-ceramic to metal interface. This involved bonding a TCE matched glass ceramic to a thin metallic film. The change of curvature as the glass ceramic was ground away enabled the residual stresses at the interface to be calculated. They found that the thermal expansion coefficient of the reaction zone measured using this method was very close to that predicted from a microstructural analysis based on the phases present.

3.2.4 Unwanted reaction products

The formation of unwanted reaction products which disrupt the interfacial microstructure must normally be avoided. For example, if carbides are present they may react to give CO or CO_2 (this can be avoided by decarburising the metal surface prior to bonding [15]), or the presence of water in the starting glass can result in the evolution of hydrogen gas [16][17].

$$xM(alloy) + yH_2O(glass) \rightarrow M_xO_y(glass) + yH_2 \qquad (3.4)$$

This reaction is particularly severe when chromium metal is in contact with the glass as ΔG for the above reaction is -129 kJ mol^{-1}. The effect can be minimised by producing the glass in dry conditions, bonding at increased pressure so that the formation of bubbles is suppressed, or including oxides in the glass that will react preferentially with the chromium ions. The addition of 1% CuO to lithium silicate on nickel based alloys results in a high quality bubble free seal [16] due to the following reaction (ΔG -381 kJ mol^{-1}) occurring in preference to Equation 3.4.

$$Cr + 3CuO \longrightarrow \tfrac{1}{2}Cr_2O_3 + \tfrac{3}{2}Cu_2O \qquad (3.5)$$

If a mechanism exists to remove unwanted reaction products from the interface then a satisfactory joint microstructure may still be obtained. For example, when enamelling steel, Fe may react with any water present to form hydrogen in the manner of Equation 3.4. One of the functions of the Ni flash used when steel is enamelled is to catalyse the breakdown of any hydrogen molecules to hydrogen atoms, enabling the hydrogen gas to dissolve into the steel [18].

However, in some cases the microstructural changes and reaction products that arise from the joining process can be favourable. For example, the metallic dendrites produced during enamelling improve the adhesion of the enamel to the substrate.

3.2.5 Thermal expansion mismatch

Although many of the problems associated with joining dissimilar materials (wetting, interfacial microstructure and chemistry) can normally be solved, mismatch in TCE between the materials to be joined remains the fundamental thermo-mechanical problem if a joint is to be fabricated or used at high temperature. Typical values for the TCE of a range of ceramics, metals and glass-ceramics are shown in Figure 3.2.

Where a significant mismatch exists, the resulting residual stress on cooling from the joining temperature, or due to thermal cycling during use, is often sufficient to cause failure of the joint. To avoid residual stresses and a weak bond, it is normally necessary to match closely the TCE of the materials to be bonded. As this is not always possible, the causes of residual stress and some of the key problems it creates are outlined below, particularly as they relate to the effect of an interlayer and a graded interlayer to reduce residual joining stress.

Considering elastic deformation only, and for simple geometries, simple analytical solutions are often available. Some of these are presented below. However for more

Figure 3.2: Typical values for the TCE of a range of ceramics, metals and glass-ceramics

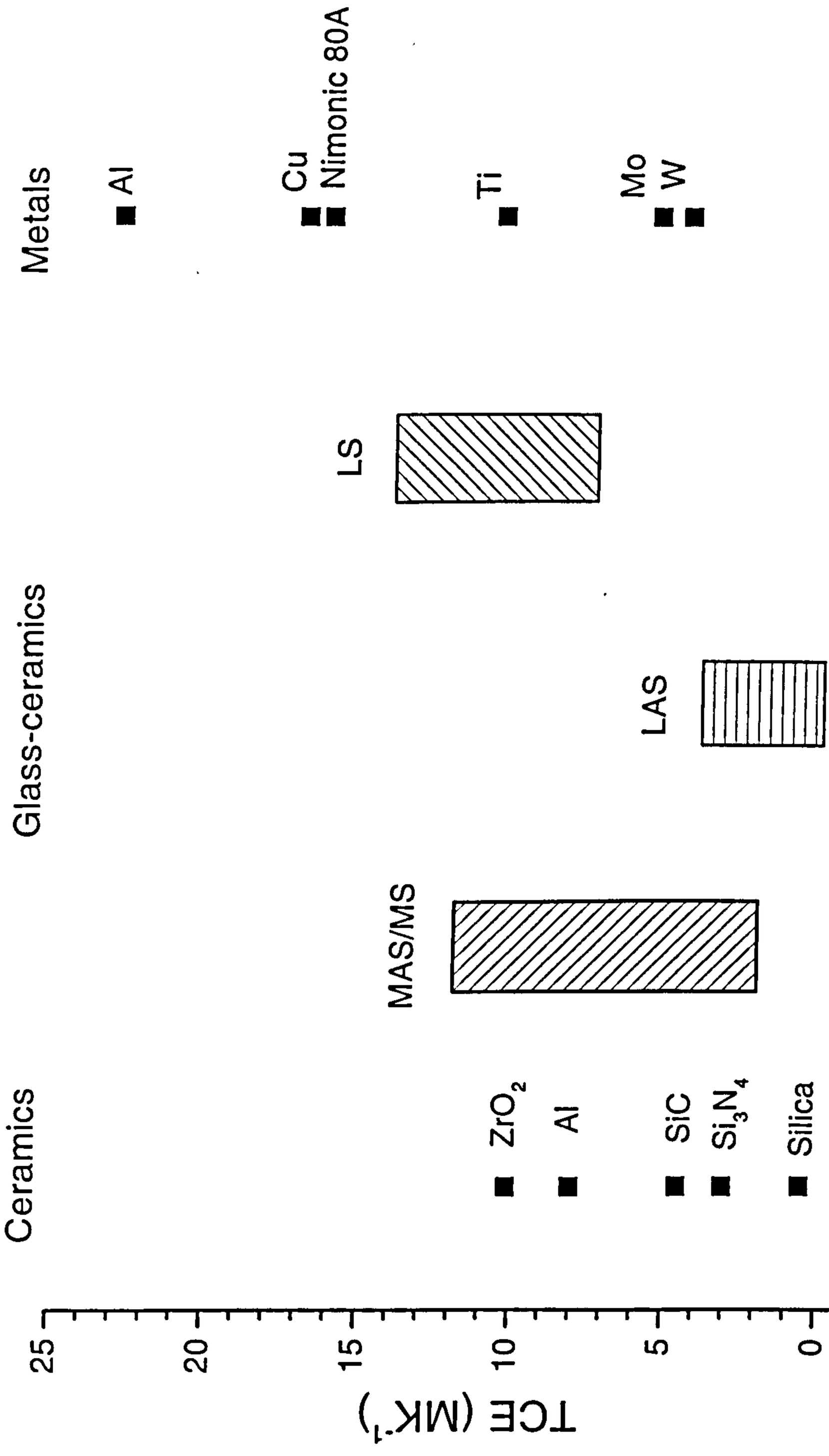

complex geometries and in order to include plastic deformation, edge effects, and elastic modulus mismatch, the analysis is more involved and finite element methods are normally used.

A full review of residual stress due to joining is not possible within the scope of this work.

3.3 Residual thermal stress

Stress arises due to restrained thermal expansion due to one of two causes:

1. A temperature gradient - known as thermal stress, or dynamic thermal stress when it occurs due to heating or cooling
2. When two materials with differing thermal expansions are joined and remain in contact over a range of temperatures - known as residual thermal stress or residual stress.

Residual stress is particularly a problem when joining ceramics to metals because of their differing TCE. It is also encountered in composite materials, where the pattern of residual stress is critical in order to fully understand the microstructure-property relationships. Maier [19] makes the distinction between residual thermal stress that arises due to joining two bodies with differing TCEs (joining stress) and residual stress generated within a body due to TCE mismatch between the constituent phases (residual stress), and suggests that joining stress and residual stress should be differentiated and discussed separately as they are often separate problems that need to be addressed individually. For example, in the case of a glass-ceramic coating on a metallic substrate, residual stress will exist in the glass-ceramic due to thermal expansion mismatch between, and thermal anisotropy of, the phases present within the glass-ceramic. Residual joining stress will occur due to any TCE mismatch between the glass-ceramic as a whole and the metallic substrate. The term joining stress or residual joining stress will be used in this work to refer to joining related stress.

Even if the level of joining stress is insufficient to result directly in failure of the joint, it can induce flaws in the joint and increase the scatter in strength [20]. This review will principally be concerned with the implications which residual joining stress has for ceramic-metal joining. Often, residual joining stress does not prevent two materials being successfully joined but it does impose severe constraints on possible joint geometries and dimensions.

3.3.1. Residual joining stress

In order to gain an insight into the nature and magnitude of stress generated, the elastic modulus and TCE are assumed to be temperature invariant.

The simplest case to consider is a thin coating on a thick substrate, with a TCE mismatch, $\Delta\alpha$. The magnitude of the residual joining stress generated in the coating on cooling, assuming elastic deformation only, can be estimated by:

$$\sigma_g = \frac{E_c \Delta\alpha \Delta T}{1-\nu} \tag{3.6}$$

where E_C and ν are the Young's modulus and Poisson's ratio of the coating and ΔT represents the temperature range over which the thermal expansion mismatch can only be accommodated by elastic deformation. For the case of glass, enamel or glass-ceramic coatings, the behaviour is elastic below the set point of the glass and any differential thermal contraction below this set point will result in residual joining stresses at the interface. As ceramics are stronger in compression, the TCE of the coating will typically be chosen to be slightly lower than that of the substrate so that mild compressive stresses exist in the coating. Thicker coatings require closer expansion matches otherwise spalling of the coating may result.

This equation can also be used to calculate the residual joining stress in oxide scales. Since they are only a few microns thick they can be mechanically stable even if subjected to compressive stresses of several hundred MPa. A recent review of the stresses in NiO, Cr_2O_3 and Al_2O_3 scales was given by Huntz [21].

When two bulk materials (1 and 2) with Young's moduli E, and TCE α are joined, assuming elastic deformation only and ignoring edge effects, the level of residual joining stress (σ) can be estimated using the following equation [22].

$$\sigma_1 = -\sigma_2 = \frac{E_1 E_2}{E_1 + E_2}(\alpha_1 - \alpha_2)\Delta T \tag{3.7}$$

Assuming mode I or opening mode failure, that is failure by the application of tensile stress normal to the plane of the crack (a reasonable assumption for brittle materials),

the relationship between the fracture toughness (K_{IC}), residual stress and defect size resulting in failure is given by:

$$K_1 = \sigma(\pi a)^{1/2} f(c/w) \qquad (3.8)$$

Where $f(c/w)$ is a dimensionless parameter (often close to unity) which depends on the geometry of the defect (characteristic length c) and sample (width w). For an embedded circular defect where c << w this becomes:

$$K_1 = \frac{2}{\pi}\sigma(\pi a)^{1/2} \qquad (3.9)$$

By combining Equations 3.7 and 3.8 it is possible to estimate the critical defect size that will result in failure of two joined materials. Akselsen [23], assuming $\pi/2$ for $f(c/w)$ showed that in the case of a large TCE mismatch (>$4x10^{-6}°C^{-1}$) the critical flaw size is reduced to a few μms which may be less than the pore size. This can lead to spontaneous fracture in ceramic joints without the application of an applied load.

In reality, the pattern of residual joining stress is likely to be far more complex than suggested by Equation 3.7. For example, failure of ceramic-metal joints normally occurs at the edge of the joint, either through the joint or in the ceramic close to the interface. The pattern of stress at the edge of the joint therefore needs to be considered in a little more detail.

3.3.2 Ceramic-metal butt joints - edge effects

In ceramic to metal joints high stresses develop at the free edge of the interface due to a change in temperature or mechanical loading. An analytical expression allowing the stress to be calculated as the sum of two terms is given by Munz and Jang [24][25] (following work by Bogy [26] and Williams [27]). One of the terms is independent of the distance from the free edge (similar in form to Equation 3.7) and the second term, the 'stress singularity term' is strongly localised close to the ceramic-metal interface and is dependent on the material properties and joint geometry. For a butt joint between silicon nitride and a metal or alloy of higher thermal expansion and lower elastic modulus, large tensile stresses are predicted in the silicon nitride near the free edge of the interface due to the singular stress term.

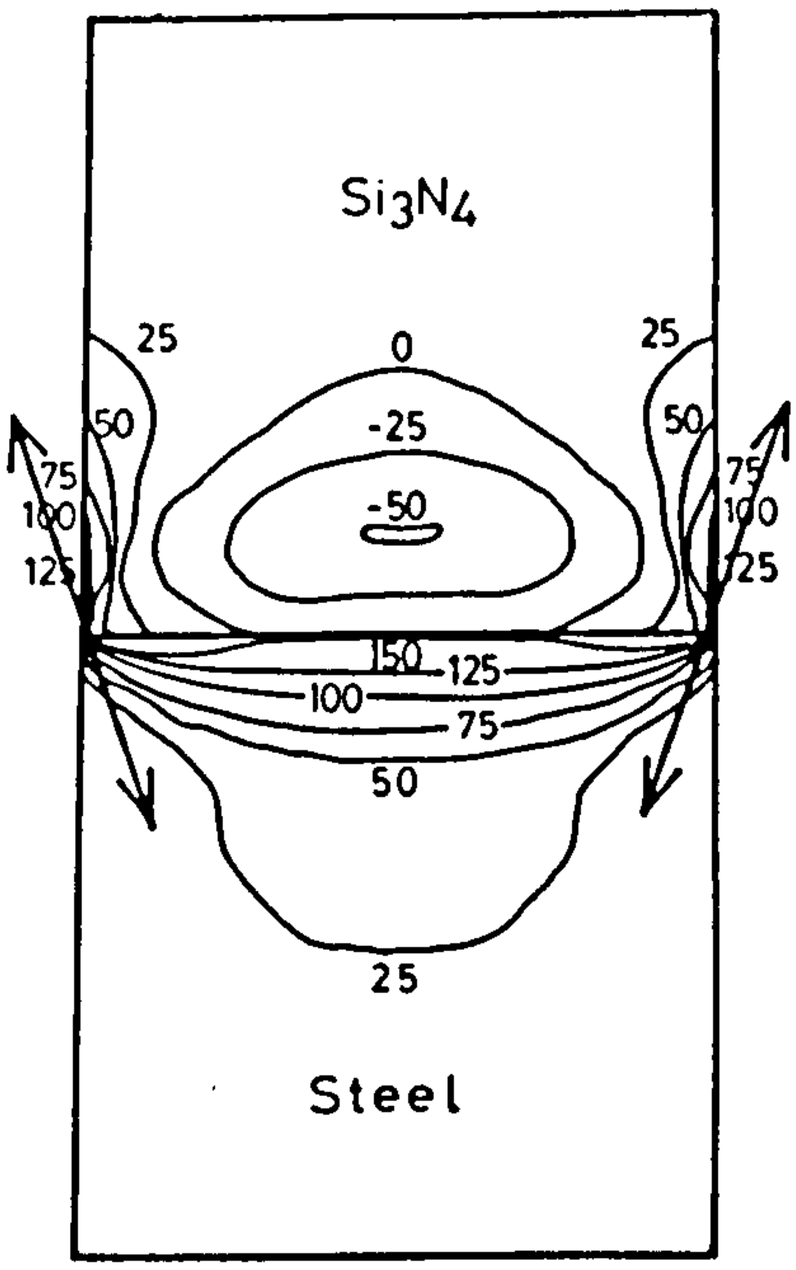

Figure 3.3: Stress contours developed in a cylindrical butt joint between silicon nitride and steel. The arrows represent both the location and the direction of the maximum tensile stress [30].

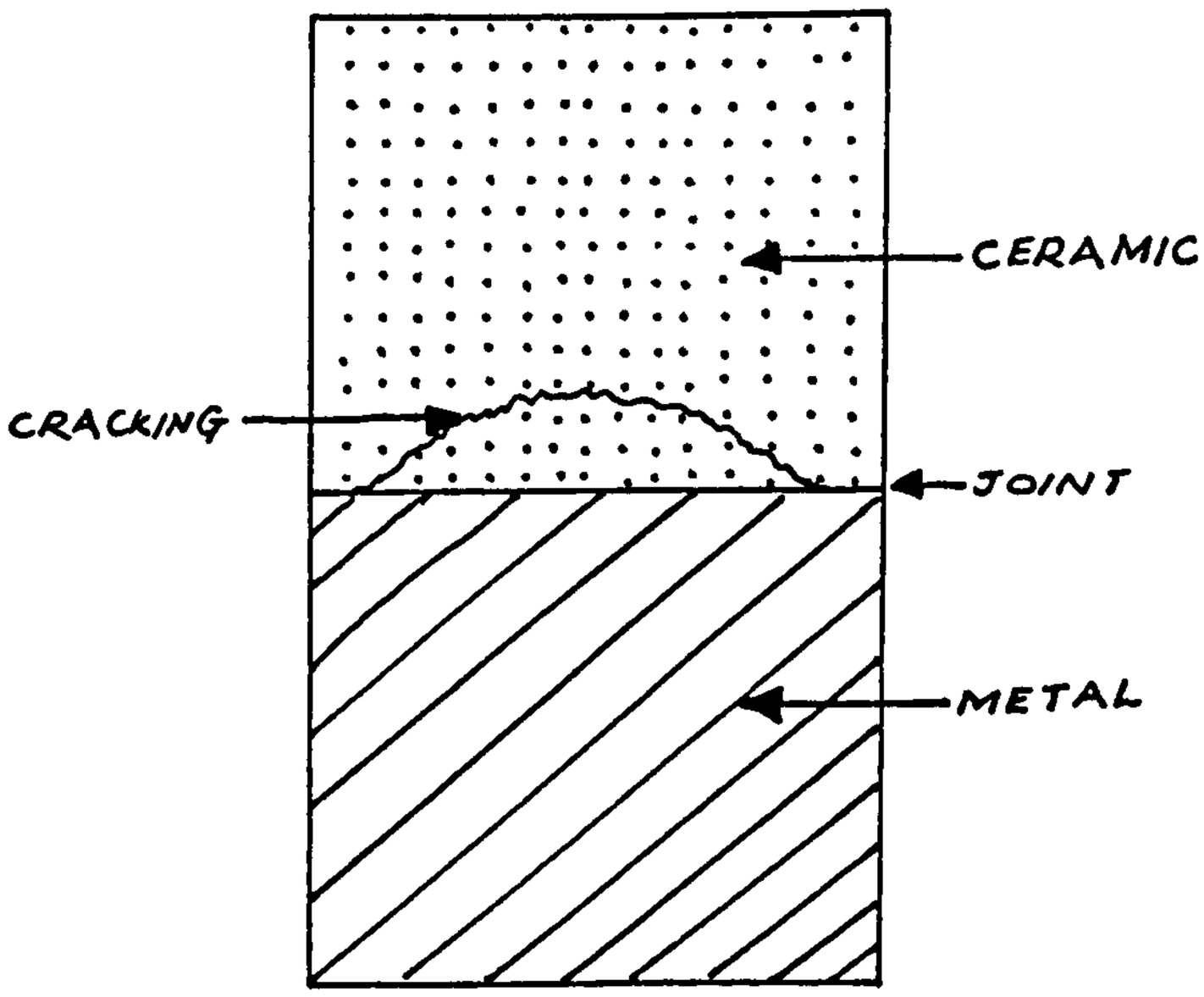

Figure 3.4: Schematic representation of typical 'dome-like' cracking in a ceramic-metal butt joint.

The nature of the stresses generated are backed up by finite element work. For example, Figure 3.3 shows the well known result of Suganama et al [28] for the stress contours developed in a cylindrical butt joint between silicon nitride and steel. The arrows represent both the location and the direction of the maximum tensile stress.

Both the analytical and finite element results are based on purely elastic models, perfect bonding between the ceramic and the metal, and assume no other stress relieving mechanisms. Clearly in practice some mechanisms (eg: microcracking or local plasticity) act to limit or partially relieve the residual stress. However, the general nature of residual joining stress is as indicated.

The high tensile stresses near the free edge of the interface may cause failure at the interface or within the ceramic. Often failure is initiated in the ceramic close to the interface and dome-like cracking (similar to Figure 3.4) is observed.

For ceramic-metal joints plastic deformation of the metal component often limits the extent of these stresses. Many high temperature materials only undergo limited plastic deformation so that this effect is only able to accommodate a small TCE mismatch. Relying on plastic deformation may also lead to problems with susceptibility to fatigue if the joint is to be thermally cycled.

One of the conclusions of Munz and Yang [25] is that a large effect of the component size on the stress at the free edge of the interface exists, especially for thermal loading. Presumably this partially explains why many joining solutions fail as the joined area becomes larger.

3.3.3 Effect of an interlayer on residual joining stress

Considering the effect of elastic deformation only, Yu et al [29] provide a simple analytical solution to estimate the trend of the residual joining stresses in a metal(1)-interlayer(3)-ceramic(2) butt joint, with cylindrical geometry (radius r), as a function of the shear moduli (μ), the TCE of the constituent materials (α), and the thickness of the interlayer (h).

$$\sigma = -\frac{4(1+\nu_1)\mu_1\mu_2\Delta T}{\mu_1+(3-4\nu_1)\mu_2}\left[(\alpha_2-\alpha_1)[1-h/\sqrt{h^2+a^2}]+(\alpha_2-\alpha_3)[h/\sqrt{h^2+a^2}]\right] \tag{3.10}$$

This assumes that the physical constants are temperature invariant and that the elastic constants and Poisson's ratio of the interlayer are assumed to be equal to those of material 1 (the metal).

The nature of the first geometrical term $[1-h/\sqrt{h^2+a^2}]$ can be viewed as the interlayer shielding the ceramic from the expansion of the metal, whereas the second geometrical term $[h/\sqrt{h^2+a^2}]$ represents the interlayer imposing its own thermal expansion on the ceramic as it increases in thickness. Although this gives an estimate of the stress value at the centre of a 'semi-infinite cylindrical inclusion' the authors note that in the case of a direct joint the stress levels predicted agree closely with the maximum tensile stresses predicted by finite element work. For example, for joining alumina to steel Equation 3.10 predicts a stress of 890 MPa whereas Suganama et al [30] predict a maximum tensile stress of 940 MPa using finite element methods.

However, Equation 3.10 ignores edge effects and seems to correspond more closely to the non-singular stress term, which is not responsible for the maximum tensile stress in the ceramic. The close agreement with finite element work is due to the magnitude of the 'non-singular' residual stress being close to that of the tensile stress due to the 'singular term'. It can it seems be used to estimate the magnitude of the tensile stresses generated in the ceramic when an interlayer is present.

Although the assumptions used in arriving at equation 3.10 are not valid when considering a ductile metal interlayer, they are reasonable when a glass-ceramic interlayer is to be used, and it provides a reasonable estimate of the extent to which residual stress may be relieved by a glass-ceramic interlayer.

In practice, a soft metallic interlayer or braze is often effectively used to accommodate residual joining stresses. However, as the area of the joint becomes larger the effectiveness of these ductile interlayer/braze solutions becomes less.

Other possible benefits of using an interlayer include: reducing the joining temperature, modifying the wetting behaviour and controlling the interfacial chemistry.

The use of more than one interlayer is often effective to reduce the level of residual joining stress seen by the ceramic component. Typically an interlayer of similar or lower TCE is used next to the ceramic to remove the residual joining stress away

from the ceramic; additional layers may be used to solve joining problems and to relieve residual stress by plastic flow. For example, for joining alumina to steel Suganama et al [30] have reported the use of a Mo interlayer next to the steel and a Nb interlayer next to the ceramic. The effect of the stiff, low TCE Mo interlayer is to shield the alumina from the TCE mismatch with the steel , and the soft Nb interlayer, which is closely expansion matched to the alumina, is able to plastically deform and accommodate some of the remaining residual joining stress.

3.3.4 Graded interlayers

The use of an interlayer with graded properties is often proposed as a solution to bridge the mismatch in properties between two joined materials. Whilst in this section the effect of graded TCE on the residual joining stress will be considered, the elastic modulus and other properties (such as thermal conductivity) may also be graded from one side of the joint to the other and this may improve the resistance to thermal shock, as well as removing the problem of an edge stress singularity due to elastic modulus mismatch.

The concept of a 'linearly graded joint' has been criticised by Li [31] who notes that any chemically or mechanically weak layer or interface controls the strength of the entire joint.

A graded joint is an example of a functionally gradient material (FGM). Ravichandran [32] reported a linear elastic one dimensional calculation of the residual thermal stresses in a FGM; although the narrow scope of the model may restrict the validity of some of the conclusions others bear repetition. Firstly, the effect of temperature dependence of material constants (for Ni and Al_2O_3) on residual joining stress are insignificant, and secondly, as the size of the fully ceramic and fully metal regions adjoining the FGM structure become larger, the levels of residual joining stress are much higher and begin to approach the pattern of stresses seen in a bimaterial.

Kimura [33] has developed an exact theory for the thermal joining stresses generated in a cylindrical butt-joint due to TCE mismatch. The joint is assumed to be elastically homogeneous and plasticity is ignored. This allows the stress reduction to be calculated for a joint with a number of layers or for a graded joint.

Table 3.1 shows the stress reduction (as a fraction of the stress for the direct joint) that is possible using an interlayer. This is a function of the number of layers in the

joint and the ratio of the radius to the thickness of the joint. An infinite number of layers represents the stress reduction possible using a perfect graded joint.

Table 3.1: Stress in a multi-layered interlayer (thickness h) as a function of layer number [33], as a fraction of the stress for the direct cylindrical joint (radius a).

	Fraction of stress of direct joint				
No. of layers	1	2	5	10	∞
h = 2a	0.500	0.372	0.302	0.280	0.256
h = a	0.558	0.516	0.494	0.486	0.480
h = 0.5a	0.714	0.710	0.710	0.710	0.710

From the above for $h < 0.5a$ there is no significant benefit of a graded interlayer over an interlayer of intermediate thermal expansion. The value of a graded interlayer becomes greater as the width of the graded region approaches the diameter of the joint.

Graded joints have been used for many years for graded glass-seals. The requirement suggested by Kimura [33] for a the length of the graded joint to be significant compared to the diameter is backed up by J.H.Partridge [34], Glass-to-Metal Seals, 1949: "The overall length of a graded joint is about equal to the diameter of the tubing in the case of silica-Pyrex seals and of about three diameters in the case of silica to GEC-L1 glass seals.". The thermal expansions of silica, Pyrex and GEC-L1 are 0.5, 3.2 and 8.7 MK^{-1}.

Using Kimura's result it is possible to estimate the residual stress that is generated in the two graded glass seals mentioned above.

Firstly, the stress due to direct joining must be estimated: either using Equation 3.7 to estimate the stress at the centre of the ceramic, or Equation 3.10 which provides an estimate of the tensile stress in the ceramic close to the free edge.

Secondly, the effect of a graded joint must be allowed for. If the figures calculated by Kimura for a graded joint are fitted to an exponential model and extrapolated this allows the effect of extending the graded joint length to 2 or 3 joint diameters to be estimated. This is shown in Figure 3.5 and predicts that, for graded joints with

lengths corresponding to 2 and 3 joint diameters, the level of residual joining stress is reduced to approximately 9 % and 6 % respectively of the stress for a direct joint.

If we assume that stresses are generated on cooling from the upper annealing temperature of the glass which forms the mid point of the seal (750°C for silica-Pyrex, and 600°C for silica to GEC-L1) and assume a Young's modulus of 70 GPa and Poisson's ratio of 0.20 for all glasses, this gives an estimate of the maximum tensile stresses in the ceramic for the direct joins using Equation 3.10 of 89 MPa, and 215 MPa, which are reduced to 8 MPa and 13 MPa by the graded joints. Using Equation 3.7 to estimate the stresses at the centre of the direct joints, 71 MPa and 172 MPa are predicted which are reduced to 6 MPa and 10 MPa by a graded interlayer.

These calculated levels of stress can be compared to levels of stress which are known to be acceptable in glass to metal seals. Beauchamp and Burchett [35] state that a rule of thumb developed from past experience with seals is that calculated tensile stresses in the glass less than 6.9 MPa are acceptable, 6.9-34.5 MPa marginal and in excess of 34.5 MPa unacceptable. However, lower levels of stress would be required on the surface of the glass due to the possible presence of severe flaws.

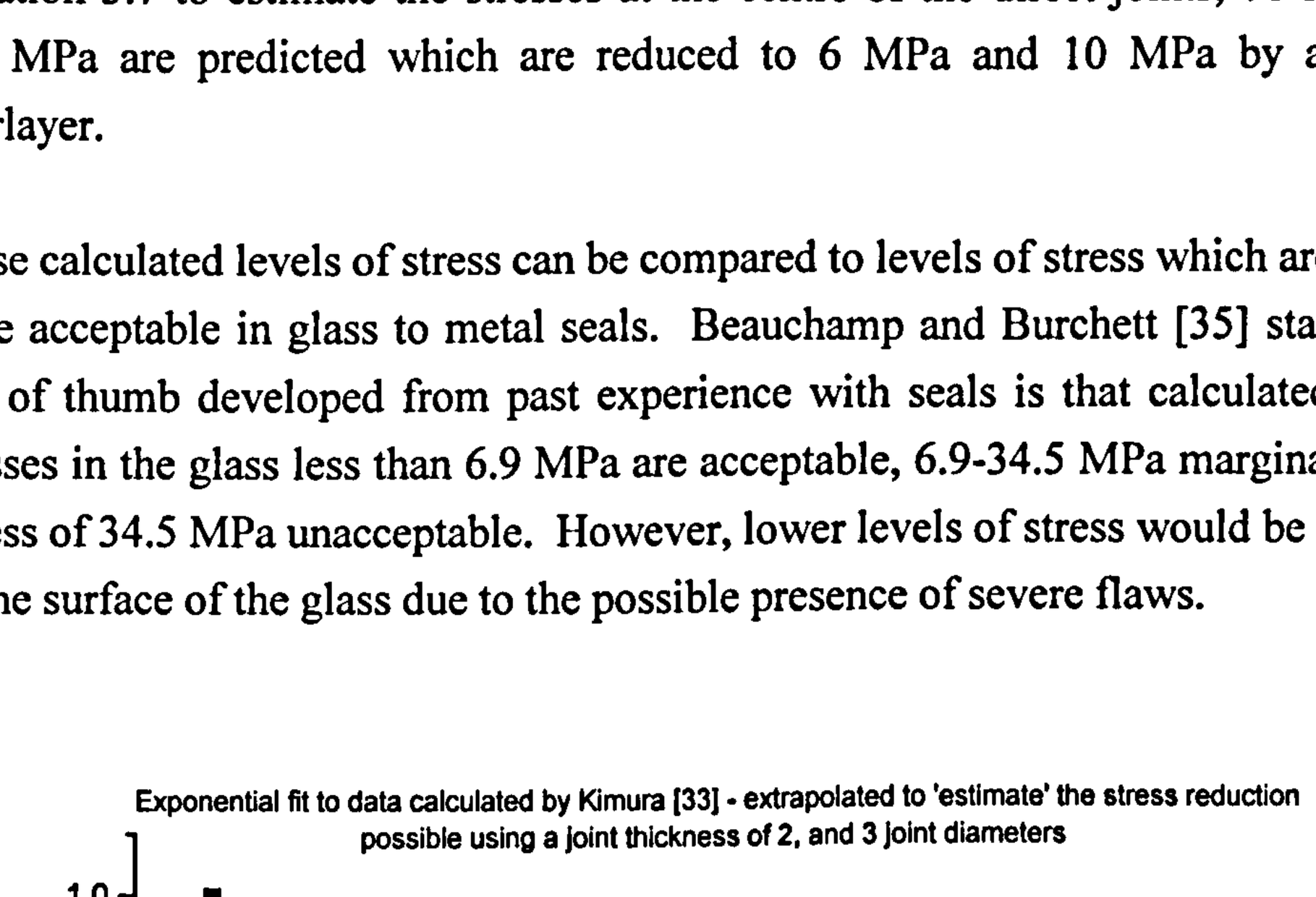

Figure 3.5: Estimate of the stress reduction possible using a graded interlayer as a function of joint thickness.

The calculated stresses for the graded glass joints fall at the lower end of the range of marginal stresses. For a graded glass joints it would appear necessary to restrict the stresses predicted by Equation 3.10 to < 15 MPa or that using Equation 3.7 to < 10 MPa.

Graded joints offer the positive benefits that the stress due to the edge singularity can be removed and the thermal shock performance improved. However, the extent to which the residual stress resulting from thermal expansion mismatch may be reduced by a graded joint is limited by the ratio of the thickness to the diameter of the joint. This appears to place practical limitations on the use of graded joints. The extent to which the use of glass-ceramics extend the possibilities of graded joints compared to the use of glass is discussed in Section 3.4.1.

3.3.5 Circular/cylindrical geometry

As ceramics are weak under tension but strong in compression, an alternative approach is to attempt to keep the ceramic in mild compression. This can be achieved using a circular or cylindrical geometry where the lower TCE ceramic is held in compression by the outer frame of higher TCE metal. The extent of the TCE mismatch, and the range of joint geometries that are possible using this approach are however limited.

Compression seals are widely used for glass-metal vacuum seals. With hard glasses (TCE < 5 MK^{-1}, working temperature 1000-1300°C) the TCE of the outer metal frame is typically 5 MK^{-1} higher than that of the glass with the TCE of the Kovar pin matched to the glass [36].

3.3.6 Residual joining stress - typical solutions

Residual joining stress remains the key problem and fundamental limitation when joining ceramics to metals. By considering Equation 3.7 the key approaches to minimising residual joining stresses can be understood.

The simplest solution is to minimise the TCE mismatch. However, for many desirable material combinations (such as silicon nitride to nickel superalloys) this is not possible. A novel approach to minimise the level of TCE mismatch was taken by Larker [37], who used silicon nitride which incorporated a second higher TCE phase (TiB_2 or TiN). The composite materials were produced by glass encapsulated hot isostatic pressing at 1600°C and the TCE was modified from 3.5 MK^{-1} (20-1000°C)

for the silicon nitride, to 6 MK^{-1} for 50 volume percent TiB_2, and 7.5 MK^{-1} for 60 volume percent TiN.

If the TCE mismatch cannot be avoided, the magnitude of the residual joining stress generated can be reduced by minimising the temperature range encountered by the joint. The use of low elastic modulus materials may also lower residual stress. In some instances, the presence of porosity may be beneficial to lower the elastic modulus, if this does not compromise joint strength.

If residual joining stresses cannot be avoided the high compressive strength of ceramics can be used to advantage by using a joint geometry that ensures the ceramic is kept in compression. Additional advantages of compression geometries are that firstly, the metal heats up quicker than the ceramic resulting in partial relief of the compressive stresses rather than the generation of tensile stress, and secondly uniform heating of the ceramic component is ensured.

For a successful ceramic-metal joint, joint design is critical. Stress concentrating geometries and a large bonded area, must normally be avoided. Finite element analysis (FEA) is normally used, and this is now able to account for the effect of ductile interlayers. Yamada et al [38] demonstrate that for a silicon carbide-aluminium interlayer-Kovar joint the bending strength of the joint (113 MPa) is roughly equal to the strength of the silicon carbide (280 MPa) less the calculated maximum tensile residual joining stress (170 MPa) using an elasto-plastic method. A brief review of finite element methods and comparison between elastic and plastic FEA is given by Foley [39].

Successful ceramic-metal joints often use a combination of ductility and appropriate geometry, an excellent example is a Housekeeper seal where a feather edge of highly ductile copper is able to accommodate the strain mismatch.

For ceramics, failure is controlled by the defect population. The nature of defects which may be generated in a ceramic-metal joint and the importance of their avoidance, if consistent joint performance is to be obtained, is discussed by Suganama [20].

Where ceramics are subjected to residual stress, the long term stability of ceramic-metal joints needs to be considered. Stress must be maintained at such a level that sub-critical crack growth is effectively eliminated. According to Beauchamp and

Burchett [35], in order to ensure high reliability in a seal containing oxide ceramics or glasses, for many materials K_I must be maintained at $< K_{IC}/3$

3.3.7 Residual joining stress - other possible solutions

A selection of more novel approaches to overcoming residual joining stress are outlined below.

Ishida et al [40] discuss the possibility of designing structural defects to relieve thermal stress, and list the following interfacial structures as possibilities, suggesting that 3. and 4. require "a higher level of designing and controlling the system".

1. A reaction layer free (direct) interface to take advantage of the ductility of the metal.
2. A nanocrystalline layer interface to take advantage of superplastic deformation.
3. A columnar precipitate layer interface to blunt the crack tip.
4. The use of plasticity or other transformation related strain.

The common principle behind this structural design approach is the introduction of a structural instability to reduce the stress concentration.

Given the success of transformation toughening in improving the fracture toughness of zirconia ceramics, the possibility of utilising a martensitic transformation to reduce residual stress is of particular interest. Some examples of this concept have been reported. Ito et al [41] report increased joining strength due to martensitic transformation in heat resistant steel and Ni-Cr-Mo steel joined to Si_3N_4, and Wang [42] attribute the difference between the experimentally measured residual stress and that due to FEA as being possibly due to martensitic transformation of ZrO_2.

A review of alternative transformation toughened to zirconia was provided by Kriven [43] who concluded that in order for a beneficial toughening effect the volume change on transformation should be positive. However, this is not necessarily the case where residual tensile stress is to be alleviated. As previously discussed in section 2.7.5, the use of martensitic phase transformations between the enstatite polymorphs to alleviate residual stress or reduce stress concentrations remains an exciting possibility.

Dynamic thermal stress also needs further consideration. Li [31] suggests that dynamic rather than static mismatch usually leads to failure of ceramic-metal joints and considers the possibility of designing ceramic joints to minimise the effect of dynamic thermal stresses. A solution is presented where the properties (TCE, elastic modulus, thermal conductivity) of the joint are graded from the centre to the edge of the bonding interface region.

A further alternative approach rather than attempting to avoid residual stress and defects, is to use the residual stress and to control the defect population. It is possible that the defect population may be controlled by allowing tolerable defects. For example, Johnson and Rowcliffe [44] joining silicon nitride to itself using a glass interlayer, Hadian and Drew [45] joining silicon nitride to itself using a Ni-Cr-Si interlayer and Suganama et al [46] joining silicon nitride to Invar alloy using an Al interlayer, all demonstrate that a strong joint is possible containing TCE mismatch cracks perpendicular to the joint.

The possibility of using residual stress to strengthen weak parts of the joint is discussed in section 3.3.8 below.

3.3.8 Joining like materials

When joining like materials, interlayer thickness has a critical effect on joint strength with thinner interlayers generally resulting in higher strengths, although this must not be at the expense of incomplete coverage of the joint area. Part of the benefit of a thin joint is that it acts as a natural limit on the size of certain defects that are present in the joint.

When using a brittle interlayer for joining, it is normally assumed that the optimum joint strength can be achieved by matching the TCE of the interlayer to the thermal expansion of the materials being joined. Indeed, Zdaniewski et al [47] reported that the measured fracture toughness and strength (varying from 30 to 90 MPa) of ceramic adhesive joints decreases with increasing thermal expansion mismatch both positive and negative. However, the defect populations were not consistent and this may have influenced the results.

A second approach is to choose an interlayer of slightly lower TCE so that the interlayer is strengthened by being in compression. However, the stresses at the free surface of layered materials are different from those within the bulk. Finite element calculations have shown that although a lower TCE interlayer is under residual

compressive stress far from the surface, tensile stress perpendicular to the interlayer exists near the free surface [48]. These stresses are highly localised and decrease rapidly from the surface to become negligible at a distance roughly corresponding to the layer thickness. Ho et al [49] demonstrate that this can cause cracks to occur parallel to the interface. Such cracks are likely to be severely detrimental to joint strength as they will act as notches induced on the interface

Similarly, an interlayer of higher thermal expansion, although under residual tensile stress away from the edge, may be strengthened due to compressive stresses in the interlayer at the free surface. It is possible that, in such a manner, the weaker interlayer may be strengthened at the expense of weakening the material either side.

Johnson et al [44] joined silicon nitride to itself using an MAS glass interlayer of higher TCE, a joint strength of 460 MPa was obtained compared to 175 MPa for the interlayer glass. This demonstrates firstly, that strong joints can be achieved for an interlayer with higher thermal expansion, and secondly, that a thin glass or glass-ceramic bond line (strength 100-200 MPa) does not necessarily limit the strength of the joint to similarly low values under certain loadings.

The reason for this increased strength remains unclear. Johnson and Rowcliffe [44] suggest that the increased strength is due to thermal expansion cracks perpendicular to the joint which divert cracks into the silicon nitride, and it is possible that this may contribute to the increased strength. A further possibility is that an interlayer of higher thermal expansion results in a layer of compressive stress at the surface of the joint as discussed above.

In addition, size-strength scaling effects, for samples with identical geometries, where the strength is well modelled by a Weibull distribution, may explain, in the absence of other factors, a significant increase in joint strength compared to that of the interlayer material.

The ratio of the effective volumes (V) under test in 4 pt bend testing for a monolith (1) and a joint (2) with the same dimensions is given by the ratio of the width of the inner span to the width of the joint.

For an interlayer material with Weibull modulus m, the ratio of the strengths (σ) is then given by Equation 3.11.

$$(\sigma_1/\sigma_2) = (V_1/V_2)^{1/m} \qquad (3.11)$$

In the case of the figures reported by Johnson and Rowcliffe the joint thickness was 30 μm compared to a total sample length of 50 mm for the glass alone (an inner span of 20 mm is assumed).

An estimate of the Weibull modulus (m) is required for the glass interlayer. According to Davidge [50] the typical values for the Weibull modulus of ceramics vary from 5-20. For glasses, where failure usually occurs from surface flaws, typical reported values for the Weibull moduli range from 3.5 to 8 [51][52][53][54][55][56][57][58], although this can increase dramatically if the surface is put into compression, which may be due to polishing [57], a coating of higher TCE [55] or chemical strengthening due to ion exchange [51][56]. Kasuga et al [51] report a Weibull modulus of 50 with all samples fracturing in excess of 450 MPa for an alkali aluminosilicate glass with a compressive layer 120-160 μm thick.

Using a Weibull modulus of 5 in Equation 3.11 above, and the geometry used by Johnson and Rowcliffe, an increase in strength of approximately a factor of 4 would be expected, and even a Weibull modulus as high as 10 should result in a strength increase by a factor of two. The size effect is therefore enough on its own to account for the reported strength measurements if the Weibull size-strength relationship holds. Obviously this assumes that the glass limits the strength of the joint, ignores the effect of residual stress and elastic mismatch, and assumes that no additional strength limiting defects are generated as a result of the joining operation. Nevertheless, the size strength scaling relationship may make a significant contribution to the joint strength.

The issue of the optimum TCE for the interlayer is still not resolved and is likely to be a function of joint geometry. It is however possible that a carefully chosen TCE mismatch can result in the pattern of residual stress generated contributing to the joint strength.

3.4 Glass-ceramics for joining applications

The use of glass-ceramics for joining related applications has been reviewed recently by Partridge [59][60][61], Donald [7] and Tomsia and Pask [62] and can be split into three categories:

1. Joining of bulk glass ceramics to metals to provide high quality, hermetic assemblies.

2. Coatings on metals.
3. As high temperature joining media to join ceramic to ceramic or ceramic to metal.

In each case the interactions that occur at the interface are with an oxide glass and the technologies involved have much in common with those used in glass processing. A great deal can therefore be learnt from the history and science of glass to metal seals [34][12] and enamelling [63]. For example, the technology associated with obtaining appropriate interfacial chemistry, by modifying the joining surface by for example pre-oxidation, or modifying the glass/enamel composition by the use of adherence oxides, is directly relevant for glass-ceramics.

Glass-ceramics offer many of the advantages of glass-metal seals with the possibility of by-passing the temperature, strength and TCE limitations of glass. The range and flexibility of TCE of glass-ceramics is much greater than that of glasses. For example, silicate glasses with high TCE have low softening points and are not suitable for high temperature use; this is not the case for high TCE glass ceramics as their high TCE arises from high TCE phases within the glass-ceramic which can be chosen to be refractory if necessary. A glass-ceramic seal may be capable of withstanding temperatures higher than those used in its production for extended periods of time. For example, Paschke and Daimer [64] produced glass ceramic seals that were able to withstand 1300°C for unlimited time, this is in excess of the joining temperature (1220°C).

Where the glass-ceramic is crystallising during the joining heat treatment, the viscosity may be quite high, and the application of pressure may be required if the use of high temperatures is to be avoided. For example, Paschke and Daimer [64] used an aluminosilicate sinter glass-ceramic for joining alumina. They required the application of additional weight due to the limited flowing ability of the aluminosilicate glass. It is interesting to compare the typical viscosity of solder glasses and enamels, to that of sintered glass-ceramics. According to Hohne and Dusdorf [65] the half sphere point is the range within which soldering is possible and this corresponds to a clearly defined viscosity ($\log \eta = 3.55 \pm 0.1$ Pa.s). For solder glasses joining normally takes place 20 to 30K above the temperature of the half sphere point. For enamelling, the viscosity of the enamel must normally be "in the region 75 Pa.s [63] ($\log \eta = 1.87$ Pa.s). This can be compared with the viscosity of a sintered glass ceramic in the MAS system with added B_2O_3 and P_2O_5. A typical viscosity at 900°C is $\log \eta = 8$ Pa.s, and would be expected to decrease an order of magnitude for every 40°C [66]. This would imply that to obtain a viscosity suitable

for joining a temperature in excess of 1100°C should be used. However, this is further complicated because considerable crystallisation will have occurred resulting in an increase in the viscosity (this increase in viscosity has been measured for LAS glass-ceramics [67]). Further complications also arise due to the possibility of reaction induced wetting and the heat evolved as a result of crystallisation.

Some examples of the successful use of glass-ceramic joints are:-

- Paschke [64] - joining alumina to itself. The joint is able to withstand long term temperatures in excess of those used in its production
- Clark and Reed [68] - as an alternative to glass bonded alumina abrasives
- Hayward [69] - As a corrosion resistant cement for refractory blocks
- Hauth III [70]- to produce vacuum tight seals for large and complex oxide ceramics.
- Batfalsky [71] - as seals in solid oxide fuel cells (SOFCs)

One of the main barriers to the successful operation of SOFCs is solving the associated joining and sealing problems [71]. An insulating, hermetic seal with closely controlled TCE and the capability of operation at 800-1000°C is required. This represents an 'ideal' application for glass-ceramic joining technology enabling the potential advantages to be fully realised. SOFCs are likely to be a major future application of glass-ceramic joining technology.

Although the technology is still only at the developmental stage, Batfalsky et al [71] have reported promising results using magnesium aluminosilicate based glass-ceramics as sealants for SOFCs (continuous operation for > 1000 hours at 800°C).

3.4.1 Graded glass-ceramic joints

Joints with graded composition and TCE may be produced using glasses or glass-ceramics. Barry et al [72] (fused quartz to titanium), Partridge et al [60] (SiC to Nilo K) and Budd [73] give examples of bonds where a glass-ceramic joint with graded TCE has been successfully demonstrated, although results of mechanical testing have not been reported.

Budd [73] used a TCE graded joint of alkali earth aluminosilicate glass-ceramics to bridge a TCE mismatch from 16.0 to 8.2 MK^{-1} (0-1000°C). For a sample ≈ 7 mm in diameter, an 11 layer joint 12 mm thick was required in order to produce a crack free

joint. Budd recommends that the TCE mismatch between layers should be no more than 0.8 MK^{-1} to ensure the low incidence of expansion mismatch cracks.

The residual stress in the graded joint can be calculated in a similar manner to that of the graded glass joint. A Young's modulus of 90 GPa, Poisson's ratio of 0.24 and ΔT of 1000°C, are assumed for the glass-ceramic.

Using Equation 3.10, the maximum tensile stress estimated in the ceramic for a direct joint is 462 MPa. Using equation 3.7 to estimate the stress at the centre of a direct joint gives 369 MPa. For a graded joint about 1.5 joint diameters in length (allowing for the end members) this reduces the stress to 14.3% of that for the direct joint giving 66 MPa and 53 MPa.

If this provides a reasonable estimate of the stresses in the joint, it indicates that the glass-ceramic joint is able to withstand higher levels of residual joining stress than a graded glass joint. This is largely due to the improved fracture toughness of the glass-ceramic, typically (1.5-2.1 MPa $m^{1/2}$ compared to 0.8 MPa $m^{1/2}$ for a glass). Taking Equation 3.8 at face value, the ratio of the stress resulting in failure for two identical joints should be proportional to the ratio of the squares of the fracture toughness of the joints. Although the full benefit of improving the fracture toughness of the interlayer stresses is unlikely to be realised due to other failure mechanisms, such as sub critical crack growth, occurring at higher stress levels, the development of higher fracture toughness glass-ceramics would enable the level of tolerable residual stress to be increased still further and ease the geometrical restrictions of a graded glass-ceramic joint.

It is possible that, as demonstrated by Ravichandran [32] for a one dimensional model of an FGM, the small size of the materials joined by the graded area results in the stress being lower than that predicted above. If this were the case, it is likely that a still thicker joint would be required if the size of the materials being joined were to increase.

3.4.2 Interactions of glass-ceramics with Nimonic alloy 80A

In common with many other Cr_2O_3 forming alloys (and discussed in section 3.2.2), controlled pre-oxidation to give a mechanically robust, strongly adherent oxide scale is normally required prior to coating with a silicate glass ceramic.

Coating on a surface that has not been pre-oxidised may cause problems due to the formation of Cr^{2+} ions, which take on the role of a modifier in the glass and are able to diffuse rapidly away from the interface. This can disrupt the microstructure of the interface and the glass-ceramic. For example Hong [74] found when bonding lithium silicate glass-ceramic to Ni-Cr-Co alloy that Cr^{2+} ions diffused away from the interface into the glass and reacted with the P_2O_5 nucleating agent to produce acicular precipitates of $Cr_{12}P_7$. The presence of this phase alters the physical properties of the interfacial region and removal of the nucleating agent results in a coarse microstructure.

The interactions of glass-ceramics with Nimonic alloys, and other Cr_2O_3 forming alloys is discussed in more detail by Donald [7].

3.4.3 Interactions of glass-ceramics with titanium

Work at Warwick, by Hong [74] and Sutherland [75][76] on glass-ceramic coatings on Ti, and Ti alloys, has resulted in some success both with and without an initial pre-oxidation stage.

Hong [74] studied the interactions between glass-ceramic coatings and titanium metal. He found that either of the following two reactions could occur.

$$8Ti + 5SiO_2 = Ti_5Si_3 + 3TiO_2 \qquad (3.12)$$

$$5Ti + 3SiO_2 = Ti_5Si_3 + 3O_2 \qquad (3.13)$$

If Equation 3.13 occurs rather than 3.12 then the gaseous O_2 produced disrupts the structure of the glass-ceramic coating, which becomes porous and weak. The oxygen produced if equation 3.13 dominates may also form a variety of titanium oxides or be taken into solid solution within the titanium, increasing the α-case formation.

Whether Equation 3.13 or 3.12 occurs may be critically dependent on furnace atmosphere, temperature and glass composition.

A heat treatment in air (970°C for 5 min) on unoxidised titanium resulted in a dense coating with a very few small isolated pores, with Ti_5Si_3 and TiO_2 produced at the interface. However, it was found that under these conditions the uncoated area was severely oxidised. Firing in argon resulted in the P_2O_5, which was present as a

nucleating agent in the glass-ceramic, acting as a further source of oxygen for the stabilisation of α-case.

A mild pre-oxidation (20 minutes at up to 800°C) did not produce a sufficient barrier to prevent the reaction occurring between the glass ceramic and the titanium. The TiO_2 dissolved to give a ternary $SiO_2.Li_2O.TiO_2$ glass system and titanium was detected up to 20 μm from the interface. When the pre-oxidation heat treatment was increased to 900°C for 20 minutes resulting in a 8-10 μm oxide coating this was sufficient to prevent damaging interactions between the glass-ceramic and the titanium resulting in an "excellent coating structure" however it was found that the intermediate layer was non-adherent.

Sutherland et al [75][76] looked at producing a glass-ceramic coating for Ti base alloy (IMI 834) compressor blades, to enable the alloy to operate at temperatures of up to 700°C. The coating was to provide a barrier to oxygen diffusion, to be chemically and phase stable at the operating temperature and to be thermal expansion matched to the substrate (TCE 9.9 MK^{-1}). For this alloy, formation of α-case (which degrades the low temperature fatigue behaviour) can be a problem and the amount of α-case formation increases drastically at temperatures in excess of 1000°C.

This work concentrated on MAS glass-ceramics with additions of B_2O_3 and P_2O_5. An adherent coating with little porosity was achieved with a heat treatment of 1000° C for 10 minutes in argon or a vacuum of 10^{-4} Torr on a polished substrate. Heat treatment in air also lead to an adherent coating but resulted in excessive oxidation of the alloy where not covered by the glass ceramic coating. Interestingly, heat treatment in air lead to a layer of TiN between the glass-ceramic and the Ti alloy.

The adherence of the coating was found to be improved by polishing. Polishing to a 0.3 μm alumina finish resulted in an improvement in the interfacial microstructure with a reduction of cracking at the interface and significantly reduced porosity.

Sintering the coating above the crystallisation temperature consistently gave coatings with least porosity Presumably, this is at least partially due to operating in a lower viscosity regime.

It proved possible to match the thermal expansion of the alloy using a forsterite/cordierite glass-ceramic. However, an enstatite/cordierite glass-ceramic with a slightly lower thermal expansion (8.1 MK^{-1}) proved more successful. The

forsterite/cordierite glass ceramic had a higher B_2O_3 content resulting in increased α -case formation due to the B_2O_3 acting as a source of oxygen for the stabilisation of α-case.

The microstructure of the MAS coating was shown to be stable to long term heat treatment. For example, 100 hours at 750°C and 1000 hours at 700°C resulted in no observable change in the microstructure of the coating. However, the heat treatment at 750°C resulted in the development of an unidentified interlayer at the glass-ceramic to titanium alloy interface. The coating did not suffer from loss of adhesion or spalling due to thermal shock under simulated thermal fatigue cycling Most significantly the coating acted as an effective barrier to oxygen, resulting in a protective, stable, adherent coating.

The interactions of glass-ceramics with Ti and Ti-alloys are discussed in more detail by Donald [7].

3.5 Joining silicon nitride to itself

3.5.1 Silicon nitride - introduction and properties

The silicon nitride/SiAlON family of materials possess high strength and fracture toughness, good high temperature properties, excellent thermal shock resistance, and outstanding properties for some tribological applications. They are a potential substitute for high temperature alloys for many high temperature applications. Although initially it was envisaged they would find a major application in gas turbines, there has been more impact within diesel engines, where they have been used for pre-combustion chambers and glowplugs. The combination of attractive high temperature properties with low density (approximately 3.3 g cm^{-3}) also make them an attractive material where reduced moment of inertia is advantageous, and they are extensively used in automobile ceramic turbocharger rotors and for ceramic bearings. The tribological properties have also lead to their widespread use in cutting tool applications.

Silicon nitride exists in two hexagonal crystallographic forms, β-Si_3N_4 the stable high temperature form and α-Si_3N_4. Both forms consist of corner sharing Si_3N_4 tetrahedra arranged into layers of connected six membered puckered rings, but differing in the stacking sequence of the layers. In β this is ABAB resulting in channels parallel to the c-axis whereas in α it is ABCD, the CD layers being shifted relative to the AB layers. This results in two large interstitial sites in α-Si_3N_4 which

can incorporate cations resulting in stabilisation of the α form. Partial substitution of Al^{3+} and O^{2-} for Si^{4+} and N^{3-} is possible in both the α and β forms resulting in α' and β' phases with a slightly expanded unit cell. Partially substituted forms are generically known as SiAlONs, in which the possibility of including other phases, and tailoring the microstructure and properties, increases the range of properties that are possible. For example, the hardness and fracture toughness may be controlled by varying the ratio of α' to β' [77].

Silicon nitride of up to 85 % density can be produced by a reaction bonded route (RBSN) via the nitridation of compacted silicon powder. A 4 pt bend strength of 250-300 MPa may be achieved which is maintained to 1400°C. RBSN is widely used in metal and ceramic processing industries.

Fully dense silicon nitride is normally produced via either a hot pressed or a pressureless sintered route. Sintering required the additions of sintering additives (typically Y_2O_3 or MgO, in conjunction with Al_2O_3) which combine with the silica film on the surface of the silicon nitride grains to give a transient glassy phase enabling sintering to full density. The sintering additives may be retained in the residual glass and impair the high temperature properties or they may be incorporated into the SiAlON grains. The nature, extent and distribution of residual glass/intergranular crystalline phase strongly effects the mechanical properties, especially at high temperature. The high temperature properties may be retained by incorporating the cations used as sintering aids into the α' grains and reducing the quantity of intergranular phase.

Silicon nitride dissociates in one atmosphere of N_2 at 1882°C, but dissociation rates become appreciable at temperatures in excess of 1500°C. Sintering of silicon nitride is therefore normally performed in a nitrogen atmosphere or in an effective overpressure of nitrogen which may be obtained by the use of a powder bed. Material with optimum mechanical properties and minimal porosity is normally produced by hot-pressing or hot isostatic pressing. For further details of the synthesis and processing of silicon nitride see Weimer [78].

Reported values for the strength of silicon nitride, measured in 4-pt bending, range from 450-1200 MPa, and for fracture toughness from 4.5-8 MPa $m^{1/2}$. The strong covalent bonding results in a high elastic modulus (sintered silicon nitride 260-320 GPa) and a low thermal expansion (sintered silicon nitride 2.8-3.5 MK^{-1}). Further details of the typical mechanical properties of silicon nitride materials are given by Hampshire [79].

Riley [80] for silicon nitride and Ekstrom [77] for SiAlON have provided recent concise reviews.

3.5.2 Joining silicon nitride to silicon nitride

Solutions for joining silicon nitride to itself are reviewed briefly below, more detailed reviews are available in the literature [81][82][28].

In common with many other ceramics it is not possible to join silicon nitride using fusion welding, because sublimation occurs rather than melting. However, Kaba et al [83] have demonstrated that diffusion bonding of hot pressed silicon nitride to itself is possible such that it is nearly impossible to detect the join. A temperature of 1800°C and a pressure of 3 GPa were used. However, distortion of the joined material remained a problem.

Most solutions for joining silicon nitride to itself require an interlayer. A range of solutions reported in the literature is shown in Table 3.2.

3.5.3 Joining silicon nitride using an interlayer

When choosing a suitable interlayer it is important that the joint does not compromise the performance of the silicon nitride for the application in question. Typically it is the high temperature and/or mechanical properties which should not be compromised.

One extreme of this is attempting to join with the material itself, so that the properties of the joint are identical and there are no problems with property mismatch. However, this normally involves subjecting the silicon nitride joint to a similar temperature profile to that involved in the manufacture of the material. This is likely to be a costly, high temperature process and may affect the microstructure of the parent material. If the materials are joined in the green state this problem does not occur as the joining heat treatment can be combined with the silicon nitride firing schedule.

Bates et al [84] joined green Si_3N_4 parts with an interlayer of the same nominal composition using glass encapsulation hot isostatic pressing. The average room temperature strength of joined bars was 941 MPa (original material 967 MPa) and this was still 526 MPa at 1370°C (original material 570 MPa). There was an

Table 3.2: Examples of interlayers and joining conditions used for joining silicon nitride to itself, and the resulting joint strengths.

Interlayer	Temp.	Pressure	Atmosphere	Strength	Test method	Ref
GreenCeramic	1800 °C	3.0 GPa	-	-	-	[83]
ZrO_2	1440-1550°C	1.5 MPa	Vacuum	175 MPa	3 pt	[90]
CaO-SiO_2-TiO_2 glass solder (TCE 1.29)	1500°C	None	N_2	30 MPa	4 pt	[95][96]
MgO-Al_2O_3-SiO_2 glass	1550-1650°C	None	N_2	460 MPa	4 pt	[44]
Si_3N_4, Y_2O_3, Al_2O_3 and SiO_2 powders	1600°C	2 MPa	N_2	650 MPa	4 pt	[91][2]
Active metal braze	1100°C	10 kPa	Vacuum 10^{-4} Torr	400 MPa	4 pt	[87]
Al-plasma sprayed	700°C	0.5 MPa	Vacuum 1.3×10^{-3} Pa	340 MPa m = 6.3	4 pt	[85]
Al plate	700°C	0.5 MPa	Vacuum 1.3×10^{-3} Pa	230 MPa m = 0.9	4 pt	[85]
Al 0.2 mm				332 MPa m = 3.3	4 pt	[86]
Ni.18Cr.19Si (at. %) braze	1220°C		pN_2 = 15 Pa	115 MPa at 20°C 220 MPa at 900°C	4 pt	[45]

increase in scatter in the joined parts which appeared to exhibit a different flaw population from the original material.

Joining using an interlayer of differing composition introduces problems due to mismatch of elastic modulus and TCE. The use of metallic and ceramic interlayers is discussed below.

a) Joining using a metallic interlayer

Joints utilising brazes [87] or ductile metal interlayers [88] often place a severe restriction on the temperature capability of the joint (eg Al 200°C, Ag-Cu-Ti brazes 400°C [89]), and strengths in use would tend to be limited to the yield strength of the interlayer, which is often low.

There has been some recent interest in the use of high temperature Ni-Cr-Si brazing alloys to extend the temperature capabilities of brazed joints. Hadian and Drew [45] were able to join silicon nitride to itself using this system, and although the interlayer was cracked perpendicular to the bond line, strengths of 115 MPa were obtained at room temperature, which was not only maintained at 900°C, but increased to 220 MPa. The increase in strength was attributed to the residual thermal stresses being relieved by reheating the joints.

b) Joining using a ceramic interlayer

For high temperature applications a ceramic interlayer may be a suitable solution.

Becher and Halen [90] showed that hot pressed silicon nitride (HPSN) could be successfully bonded to both itself and reaction bonded silicon nitride (RBSN) if a thin layer of ZrO_2 or $ZrSiO_4$ was placed between the samples to be bonded and a temperature of 1450°C and a pressure of less than 1.5 MPa was applied. Under optimum bonding conditions the strength of the HPSN/RBSN joint (175 MPa) was limited by the RBSN rather than the joint.

Walls and Ueki [91] joined SiAlON ceramics using what they termed a balanced adhesive. A mixture of Si_3N_4, Y_2O_3, Al_2O_3 and SiO_2 powders were used and heated at 1600°C for 10 minutes. The bond line consisted of a 60:40 (β-SiAlON:glass) glass ceramic consisting of acicular β-SiAlON in an YSiAlON glass. Optimising this joining treatment (1600°C, 10 minutes, 2 MPa) resulted in a joint strength (650 MPa) 85% of that of unbonded material. A post-joining HIPing

treatment resulted in the joint strength of the joined material being only 4% lower than that of the unbonded material [92]. The solution presented by Walls and Ueki does not significantly compromise the strength or high temperature performance, as the join line is essentially a fine grained version of the original material. This has been successfully used to make large complex components and "greatly widened the field of applications" [93]. It does however require a joining temperature of 1600°C which may prove a problem for some applications.

A solution that heats the joining area only so that the microstructure of the original material is unaffected was reported by Okuda et al [94] who bonded sintered silicon nitride (preheated to 700-800°C) which had been screen printed with a 70:30 mixture of kaolinite and CaF_2, by passing a current of 0.6A for 10 minutes through the bonding layer. This resulted is dissolution of the Si_3N_4 at the interface which formed a glass containing Al, Si, Y, O and N. Up to 800°C bend testing produced a joint strength of 300 MPa and failure was by brittle fracture. Above this temperature the strength dropped rapidly and ductile failure occurred due to softening of the glass bond line.

There has also been some interest in the use of silicate based glasses as joining media. Iwamoto et al [95][96] used a CaO-SiO_2-TiO_2 glass with no applied load at 1500°C which resulted in a TiN interfacial layer. The reported strengths (~30 MPa in 4 pt bending) were however quite low.

Mecartney and Sinclair [97] joined Si_3N_4 between 1550°C and 1650°C with no applied pressure using a magnesium aluminosilicate glass that had its composition matched to the intergranular phase in the Si_3N_4. The glass penetrated the Si_3N_4 grain boundaries and the Si_3N_4 dissolved in the molten oxide glass. This was followed by precipitation of Si_2N_2O as the nitrogen content in the glass reached saturation. They suggested that the driving force for joining was the lowering of the Si_3N_4 interfacial energy when it was wet by the molten silicate, augmented by the negative Gibbs free energy of the following reaction:

$$SiO_2(l) + Si_3N_4 \rightarrow 2Si_2N_2O$$

The joint consisted of acicular Si_2N_2O and Si_3N_4 growing across the joint into the residual oxynitride glass. Johnson and Rowcliffe [44] found that the maximum joint strength of 460 MPa (4-pt) exceeded the measured strength of the glass (175 MPa). This was for samples joined at 1600°C in a nitrogen atmosphere with an interlayer 30 μm thick. A preliminary glazing and grinding step was used which eliminated the

problems of incomplete coverage of the joint area. The thermal coefficient of expansion (TCE) of the interlayer was higher than that of the silicon nitride resulting in a network of fine cracks perpendicular to the interface. As discussed in section 3.3.9, they suggested that the thermal expansion cracks that run through the glass into the silicon nitride, may contribute to the strength of the joint by deflecting cracks formed in the glass into the much stronger silicon nitride.

Brittain et al [98] did further work on this bonding system and found that joints heated to 1300°C were weak and concluded that at high temperatures the joint degrades, that MgO becomes an unsatisfactory refractory material due to the evolution of atomic Mg (verified by Knudsen mass spectrometry) and that considerable chemical transport must be expected for intergranular phases if significant chemical gradients are present when an oxide glass is used as a joining material.

An attempt was made to crystallise the joint with a post joining heat treatment to improve the thermal and mechanical properties. However, crystallisation resulted in joint strengths considerably lower than those of the untreated samples, as has also been reported for alumina joined with a calcium aluminosilicate glass [99].

These results are not surprising, uncontrolled crystallisation is likely to result in an uneven, coarse microstructure, and low strength. However, controlled crystallisation to produce a fine grained glass-ceramic interlayer should result in a joint with superior mechanical and high temperature properties. In addition, glass-ceramics offer control and flexibility of thermal expansion. Joining using glass-ceramics offers the possibility of a refractory bond obtained via a comparatively low temperature route.

3.6 Joining silicon nitride to metals

Silicon nitride may be joined to metals either directly or using an interlayer. However for a rigid direct joint the residual joining stress will normally be sufficient to fracture the joint or the ceramic, and a dome like fracture in the silicon nitride is often observed, as shown in Figure 3.4.

Suganama et al [100] demonstrated that although silicon nitride can be bonded directly to steel via a strong, thin iron silicide reaction layer the geometrical restrictions to avoid failure due to the high residual joining stress on cooling impose severe restrictions on joint geometry. Either a very slender joint (below 1mm in

diameter) or a thin layer of silicon nitride (< 0.2 mm) are necessary for joints with significant strength.

Silicon nitride is normally joined to metals using an interlayer; the chemical problems are increased as two interfaces have to be optimised. However, residual joining stress is still the main problem. The range of interlayers normally used to combat this problem are listed below

- Low TCE metallic interlayer (eg W or Mo)
- Ductile metal interlayers (eg Cu or pure Ni)
- Active metal brazes
- Al brazes
- High temperature brazes
- An interlayer which is a composite of the materials to be joined [101]

If a low TCE interlayer, such as W or Mo, is used on its own, the TCE mismatch is still sufficient to cause fracture. However, they may be used successfully in conjunction with a soft interlayer to relieve the thermal stress. In this case the high temperature performance of the joint may be restricted by the poor high temperature oxidation performance of Mo and W.

Other solutions which rely wholly on plastic deformation to accommodate the residual stress can be effective. However, they becomes less effective as the joint area becomes larger (the maximum area for brazed ceramic-metal joints is 200 mm^2 [*89*]), are susceptible to fatigue if subjected to thermal cycling and the temperature that the joint can withstand is likely to be a major limiting factor (temperature constraints discussed for silicon nitride-silicon nitride joining still hold).

Recently attempts have been made to overcome some of the limitations by using a flexible joint geometry, such as a mesh or dimple geometry. The flexibility of the interlayer accommodates the strain due to TCE mismatch. These are normally used in conjunction with metallic brazing.

The composite interlayer solution demonstrated by Suganama [101] enabled Mo to be joined to silicon nitride and Fe to be joined to alumina. Further developments by the use of a graded interlayer were suggested. If such a solution is able to combine ductility and high fracture toughness it may restrict joint geometries less than the use of a graded glass or glass-ceramic joint. However, it is likely that significant joint thickness will still be required.

Although the development of reliable ceramic-metal joining is not easy, there have been many notable successes. Two well known examples of the successful use of ceramic-metal joining technology, which have enabled the benefits of ceramic materials to be realised, are outlined below:

1. The successful development of reliable joining technology for joining a silicon nitride turbocharger rotor to a steel shaft was critical for their commercial application. Katona et al [102] report a solution based on the use of an active metal braze in conjunction with a W and Ni buffer layer between the ceramic rotor and the steel shaft. In order that the temperature limitations of the joint are not exceeded, the temperature 'seen' by the joint is restricted to 450°C. The paper by Katona provides a model of the development of a ceramic component for a high technology application.

2. Yamada et al [103] used a combination of metallic interlayers to successfully bond silicon nitride to Nimonic 80A for use in an exhaust valve in marine diesel applications. A Ni layer was used to join to the silicon nitride, and the thermal stress was reduced by a combination of a low TCE layer (tungsten or Kovar) and a ductile copper layer. The use of such a metallic interlayer limits use of the joint to temperatures below approximately 700°C. The burnout resistance of a silicon nitride faced exhaust valve was 10 to 50 times higher than a conventional valve.

Recent reviews of silicon nitride to metal joining have been provided by Suganama[28] and Larker [37]

3.7 Outlook for joining of ceramics

Many recent reviews of ceramic to ceramic and ceramic to metal joining exist [4][5][6]. A wide range of satisfactory joining solutions are available for joining ceramics to themselves. For some applications a glass-ceramic joint offers an attractive combination of properties not offered by other materials.

More progress is still required in the development of solutions for joining ceramics to metals if the full benefits of ceramic materials are to be realised. This is principally related to the fundamental thermomechanical problem of TCE mismatch. The production of practical joints for high temperature applications, especially where

large joined areas are involved remains problematic. The long term stability of joints also needs further consideration.

For some applications the use of a joint with graded composition (and TCE) may offer a satisfactory solution. The use of graded glass joints has been successful in joining glasses with mismatched TCE. A graded glass-ceramic joint is able to offer a more refractory solution than a graded glass joint and withstand a higher level of residual joining stress. A procedure for estimating the stress in the joint has been outlined. In order to bridge a significant TCE mismatch the length of the graded joint must be significant compared to the diameter. In order to bridge a significant TCE mismatch (eg: silicon nitride to nickel superalloy) a graded glass-ceramic joint several diameters in length would be required. This restriction may be eased by the development of higher fracture toughness glass-ceramics.

The use of ceramic interlayers with designed microstructures, which allow transformation related strain to accommodate TCE mismatch may be an idea worth further investigation. The possible use of the martensitic phase transformation between enstatite polymorphs is particularly promising.

Further progress in ceramic metal joining technology is likely to arise from a methodical interdisciplinary approach, to quote Li [31]

"Because of the complexity of the metal-ceramic bonding process and the many worldwide attempts to develop better bonding methods with the best available resources, simple trial and error approaches are unlikely to provide breakthroughs in ceramic-metal joining. The chance of major success from one or two innovative ideas, equipment, methods, or materials is therefore not great. Rather a methodic scientific analysis must be made with a system's approach from the chemical, mechanical, thermal, electronic, thermochemical, and mechanochemical (stress induced phase transition) viewpoints."
Li - 1991 [31]

References for Chapter 3

[1] Zdaniewski W.A., Am. Cer. Bull. Vol 72 [3] 38 (1993).

[2] Schwartz M., Joining of Composite Matrix Materials, ASM International, 1994.

[3] Turwitt M., Joining Ceramics, Glass and Metal 1997, 1-14, DVS-Berichte.

[4] ASM Engineered Materials Handbook, Volume 4 - Ceramics and glasses, Section 7 - Joining, Section editor Loehman R.E., ASM international 1991.

[5] Nicholas M.G., Joining of ceramics, Institute of Ceramics, Chapman and Hall, 1990.

[6] Nicholas M.G., pp 261-291 in Materials Science and Technology - A comprensive treatment: Volume 17B - Processing of Ceramics Part II, VCH, 1996.

[7] Donald I.W., J. Mat. Sci., 28 (1993) 2841-2886.

[8] Pask J.A. and Tomsia A.P., Wetting, Surface Energies, Adhesion, and Interface Reaction Thermodynamics, p482-492, ASM Engineered Materials Handbook, Volume 4 - Ceramics and Glasses, 1991, ASM International.

[9] Pask J.A. and Fulrath R.M., J. Am. Ceram. Soc., 45 [12] 592-596 (1962).

[10] King B.W., Tripp H.P. and Duckworth W.H., J. Am. Ceram. Soc. 42 [11] 504-25 (1959).

[11] Borom M.P. and Pask J.A., J.Am.Ceram.Soc., 49(1) 1-6 (1966).

[12] Kohl W.H., Vacuum, Vol. 14 pp 333-354.

[13] Mizuhara H. and Oyama T., Ceramic-Metal Seals, p502-510 in ASM Engineered Handbook , Volume 4 - Ceramics and Glasses, ASM International 1991.

[14] Kunz S.C. and Loehman R.E., Adv. Cer. Materials, 2(1) 69-73 (1987).

[15] Notis M. R., J Am Ceram Soc 45 (1962) 412.

[16] Craven S.M., Kramer D.P. and Moddeman W.E., Chemistry of glass-ceramic to metal bonding for header applications, Monsanto research corporation report, MLM-3403, (December 1986).

[17] Haws L.D., Kramer D.P., Moddeman W.E. and Wooten G.W., High strength glass-ceramic to metal seals, Monsanto research corporation report, MLM-3288(OP), (December 1985).

[18] Salamah M.A. and White D., Surfaces and interfaces in ceramic and ceramic/metal systems, p411. Eds Pask J.A. and Evans A., American Society for Metals, 1981.

[19] Maier H.R. - verbal communication at Joining, Ceramics, Glass and Metal 1997.

[20] Suganama K., Mat. Res. Soc. Symp. Proc., Vol 314 (1994).

[21] Huntz A.M., Mater. Sci. Eng., A201 (1995) 211-228.
[22] Ning X.S., Okamoto T., Mujamoto Y. and Koreeda A., J. Mater. Sci 24 (1989) 2865-2870.
[23] Akselsen O.M., J. Mat. Sci., 27(1992) 1989-2000.
[24] Munz D. and Yang Y.Y., J. Eur. Ceram. Soc., 13 (1994) 453-460.
[25] Munz D. and Yang Y.Y., J. Appl. Mech.Vol 59, December 1992, p857-861.
[26] Bogy D.B., J. Appl. Mech., 38 (1971) 377-89.
[27] Williams, M.L., J. Appl. Mech., 19, (1952) 526-8.
[28] Suganama K., Okamoto T., Koizumi M. and Shimada M., J. Am. Ceram. Soc., 68 [12] C334-5 (1985).
[29] Yu H-Y, Sanday S.C. and Rath R.B., J. Am. Ceram. Soc., 76 [7] 1661-1664 (1993).
[30] Suganama K., Okamoto T., Koizumi M. and Shimada M., J. Am. Ceram. Soc. C-256-257, 1984.
[31] Li C.H., Metal-Ceramic Joining - Edited by P.Kumar and V.A.Greenhut, The Minerals, Metals and Materials Society, 219-227 (1991).
[32] Ravichandran K.S., Mater. Sci. Eng. A201 (1995) 269-276.
[33] Kimura O. and Kamashima T., J. Am. Ceram. Soc., 76 [3] 757-59 (1993).
[34] Partridge J.H., Glass-to-Metal Seals, 1949, p116.
[35] Beauchamp E.K. and Burchett S.N., pp 532-541 in ASM Engineered Materials Handbook, Volume 4 - ceramics and glasses, ASM International, 1991.
[36] Tomsia A.P. and Pask J.A., Glass-metal seals, Chapter 4 in Joining of Ceramics, Ed. Nicholas M.G., Institute of Ceramics, Chapman and Hall, 1990.
[37] Larker R., Doctoral thesis, Lulea University of Technology, 1992.
[38] Yamada T., Motohiro S., Kohno A. and Yokui K., J. Mater. Sci. 26 (1991) 2887-2892.
[39] Foley A.G. and Winters C.G., Br. Ceram. Proc. No 48 April 1991, p107-122.
[40] Ishida Y., Wang J. and Suga T., Acta metall. mater. Vol 40, Suppl., S289-S293, 1992.
[41] Ito M., Miyama K., Tanaka T., Taniguchi M., Mori S. and Kato N., J. Jap. Inst. Met., 59(5) 578-583, (1995).
[42] Wang, Mat. Sci. Eng., A211 45-53 (1996).
[43] Kriven W.M., J. Am. Ceram. Soc., 70 [5] 349-60 (1987).
[44] Johnson S.M. and Rowcliffe D.J., J. Am. Ceram. Soc., 68(9) 468-472 (1985).
[45] Hadian A.M. and Drew R.A.L., J. Am. Ceram. Soc., 79 [3] 659-65 (1996).
[46] Suganama J. Mat. Sci. 22 (1987) 1359-64.

[47] Zdaniewski W.A., Conway C.J. Jnr., Kirchner H.P., J. Am. Ceram. Soc., 70 [2] 110-118 (1987).

[48] Kirchner H.P., Conway J.C. and Segall A.E., J. Am. Ceram. Soc., 70 [2] 104-109 (1987).

[49] Ho S., Hillman C., Lange F.F. and Suo Z., J. Am. Ceram. Soc. 78 [9] 2353-2359 (1995).

[50] Davidge R.E., Mechanical behaviour of ceramics, Cambridge University Press, (1987).

[51] Kasuga T., Uno T., Eda S. Tachewana K. and Ikushida A.J., Glass Tech., 33(2) 57-59 (1992).

[52] Alarcón O.E., Medrano R.E. and Gillis P.P., Mater. Met. Trans. A Phys. Met. & Mat. Sci., 25(5) 961-968 (1994).

[53] Migliore A.R. and Zanotto E.D., Glass Tech., 36(2) 65-66 (1995).

[54] Ritter J.E., Service T.H. and Giullement C., Glass-tech, 26(6) 273-278 (1985).

[55] James P.F., Chen M. and Jones F.R., J. Non-Cryst. Solids, 155(2) 99-109 (1993).

[56] Donald I.W., Hill M.J.C., Metcalfe B.L., Bradley D.J. and Bye A.D., Glass. Tech 34(3) 114-119 (1993).

[57] Dielhof M.H., Dortmans L.J.M.G. and de With G., J. Eur. Cer. Soc., 12 215-220 (1993).

[58] Entwistle K.M., 28(8) 2007-2012 (1993).

[59] Partridge G., Glass Tech., Vol 35 No. 4 pp171-181, (1994).

[60] Partridge G. and Hales T., Br. Cer. Proc., 48 161-176 (1991).

[61] Partridge G., Chapter 3 in Joining of Ceramics, Ed. Nicholas M.G., Institute of Ceramics, Chapman and Hall, 1990.

[62] Tomsia A.P., Pask J.A. and Loehman R.E., Glass/Metal and Glass-Ceramic/Metal Seals, pp 493-501, ASM Engineered Materials Handbook - Volume 4 Ceramics and Glasses, 1991.

[63] Maskall K.A. and White D., Vitreous Enamelling - a guide to modern enamelling practice, Pergamon Press, 1986.

[64] Paschke H. and Daimer J., Joining ceramics, glass and metal, Proceedings of the fourth international conference 1993, pp 68-75, Verlag der Glastechnischen Gesellschaft.

[65] Hohne D. and Dusdorf W., Proceedings of the fourth international conference 1993, pp 76-84, Verlag der Glastechnischen Gesellschaft.

[66] Geiss E.A. and Knickerbocker S.H., J. Mat. Sci. Lett. 4 (1985) 835-837.

[67] Bach H., Low thermal expansion glass ceramics, Springer, 1995.

[68] Clark T.J. and Reed J.S., Am. Cer. Soc. Bull., 65 [11] 1506-12 (1986).

[69] Hayward P.J., Glass-Tech., 19 (2) 27-31 (1978).

[70] Hauth W.E. III, Am. Cer. Soc. Bull., 58 [6] 584-586 (1979).

[71] Batfalsky P., Diekmann U., Godziemba-Maliszswski J. and Koppitz T. pp72-76, Joining Ceramics, Glass and Metal 1997, DVS-Berichte.

[72] Barry T.I., Lay L.A. and Evans D.T., Glass Tech, 19 (2), 27-31 (1978).

[73] Budd M., pp 187-189. Joining Ceramics, Glass and Metal 1997, DVS-Berichte.

[74] Hong F., Interactions Between Glass-Ceramic Coatings and Metals, PhD Thesis, University of Warwick, 1991.

[75] Sutherland S. and Holland D., Glass-Ceramic Coatings for the Protection of High Temperature Titanium Alloys, 1991.

[76] Sutherland S., Holland D and Mathers H.J., Coating for advanced engine use - 1st Year Report, 989.

[77] Ekstrom T., pp 2444-2451 in The Encyclopedia of Advanced Materials - Volume 4, Editors - Bloor D., Brook R.J., Flemings M.C. and Mahajan S., Pergamon 1994.

[78] Weimer A.W., Carbide, Nitride and Boride Materials - Synthesis and Processing, Chapman and Hall, 1997.

[79] Hampshire S., Engineering Poperties of Nitrides, p812-820 in ASM Engineered Materials Handbook - Volume 4 Ceramics and Glasses, ASM International 1991.

[80] Riley F.L., pp 2512-2516 in The Encyclopedia of Advanced Materials - Volume 4, Editors - Bloor D., Brook R.J., Flemings M.C. and Mahajan S., Pergamon 1994.

[81] Bates C.H., Foley M.R., Rossi G.A., Sundberg G.J.and Wu J.F., Am. Cer. Soc. Bull. Vol 69, No 3, 1990 p350-356.

[82] Suganama K., p523-531 in Engineered Materials Handbook, Volume 4 - Ceramics and Glasses, ASM International, 1991.

[83] Kaba.T, Shimada M. and Koizumi M., J. Am. Ceram. Soc., C135-C136, 1983.

[84] Bates C.H., Foley M.R., Rossi G.A., Sundberg G.J. and Wu F.J., Am. Cer. Soc. Bull. 58(6) 582-586 (1990).

[85] Pan W.X., Okamoto K. and Ning S.S., J. Mater. Sci. 29 [6] 1436-1440 (1994).

[86] Ning X.S, Okamoto K., Miyamota Y., Koreeda A., Suganama K. and Goda S., J. Mater. Sci. 26 [8] 2050-2056 (1991).

[87] Ramsey M.J. and Lewis M.H., Mater. Sci. and Eng., 71 [1-2] (1985) 113-122.

[88] Suganama K., Okamoto T., Koizumi M., Shinada M.: J. Mater. Sci., Vol. 22, (1987) 1359-1364.

[89] Foley A.G. and Andrews D.J., GEC Alsthom Technical Review No 13 (1994) 49-64.

[90] Becher P.F. and Halen S.A., Am. Cer. Soc. Bull. 58(6) 582-586 (1979).

[91] Walls P.A. and Ueki M.., J. Am. Ceram. Soc., 75(9) 2491-97 (1992).

[92] Walls P.A. and Ueki M., J. Am. Ceram. Soc., 78(4) 999-1005 (1995).

[93] Jack K.H., Key Engineering Materials, 1994, Vols 89-91, p345-349.

[94] Okuda K., Takai H., Nishi T. and Yanagida H., J. Am. Ceram. Soc., 76(6) 1459-1465 (1993).

[95] Iwamoto N., Umesaki N. and Haibara Y., Yogyo-Kyokai-Shi 94 [8] 881-886 (1986).

[96] Iwamoto N., Umesaki N., Haibara Y. and Sibuya K., Ceramic Materials and Components for Engines, 2nd symposium 1986, Editors - Bunk W. and Hausner H.

[97] Mecartney M.L., Sinclair R. and Loehman R.E., J. Am. Ceram. Soc., 68(9) 472-478 (1985)

[98] Brittain R.D., Johnson S.M., Lamoreaux R.H. an Rowcliffe D.J., J. Am. Ceram. Soc., 67(8) 522-526 (1984)

[99] Cawley J.T. and Cawley J.D., Metal-Ceramic Joining, Ed. by Kumar P. and Greenhut V.A., The Minerals, Metals and Materials Society, 1991, p 181-201.

[100] Suganama K., Okamoto T., Koizumi M. and Shimada M., J. Am. Ceram. Soc., 68 [12] C334-C335 (1985).

[101] Suganama K., Okamoto T., Shimada M. and Koizumi M., J. Am. Ceram. Soc., 66 (1983) C117-118.

[102] Katano Y., Ando M., Itoh T. and Sasaki M., ASME Trans., J. of Eng. for Gas Turbines and Power. Jan 1993,115, 9-16.

[103] Yamada T., Sekiguchi H., Okamoto H., Azuma S., Kitamura A. and Fukaya K., Nippon Kokan Technical Report, Overseas No 48 (1987) 67-74.

Chapter 4. Experimental techniques

4.1 Preparation Techniques

4.1.1 Glass preparation

Glasses were prepared in batches of 100 or 200 g. Details of the precursor materials composition and source are given in Appendix I. Prior to melting the constituent powders were tumble-milled for 24 hours to ensure even mixing. Batches were melted in an electrically heated furnace, using a Pt/10Rh crucible, for 3 hours at 1475-1600°C. The melt was cast into de-ionized water to form a frit, which was then dried. The cycle of melting, casting into de-ionized water and drying was repeated to ensure homogeneity of the glass.

4.1.2 Powder preparation

a) Ball milling

The glass frit was ball-milled to produce a fine powder suitable for the production of a sintered glass ceramic. The goal of ball-milling is to achieve efficient size reduction with minimal contamination. The speed of revolution of the mill is important. Above a critical number of rpm, given by ω_c in Equation 4.1, centrifuging occurs and the efficiency of milling is highly reduced. If the revolution speed is too low, cascading occurs. The level of contamination is also sensitive to the powder being milled, the size and nature of the milling media and the milling jar. For wet milling, the liquid milling medium also affects contamination.

$$\omega_c = (60/2\pi)(2g/D)^{1/2} \qquad (4.1)$$

D = diameter of ball mill

g = acceleration due to gravity

The conditions used for ball milling were:

- Aluminous porcelain milling jar, 12 cm internal diameter
- Magnesium silicate (primarily proto-enstatite [1]) milling media.
- Milling media of three different sizes (0.9, 1.5 and 2.2 cm diameter).
- Milling liquid - methanol

The milling speed used, typically 79 rpm, corresponds to 65% of ω_c, which is within the normal range of revolution speeds for wet milling (50-65% [2]).

This combination has been previously shown by Bridge [1] to result in acceptable levels of contamination. Bridge [1] was unable to detect contamination from either the aluminous porcelain jar or the magnesium silicate milling media, using magic angle spinning nuclear magnetic resonance (MASNMR), to detect sites specific to contamination.

An additional benefit of magnesium silicate media is that any contaminant is likely to be compatible with, and to have minimal adverse effect upon, the resulting cordierite/enstatite glass-ceramic. It is possible that even very small quantities of contaminants, arising from the magnesium silicate milling media, may act as seeds for the nucleation of enstatite, and affect the dynamics of the crystallization process. However, as this milling route has been used previously with success to produce glass-ceramics, this possibility is not a cause for concern.

Due to the small batch sizes used in this project, the charge of glass milled was smaller than that regarded as optimal practice, which may have resulted in less efficient comminution and higher levels of contamination. Milling times employed were from 24 to 72 hours. The contents of the ball mill jar were wet screened to 38 μm immediately after ball-milling and then allowed to dry in a drying oven. When dry, the powder was passed through a 38 μm sieve to minimize problems due to hard agglomerates. It is possible that sieving to 38 μm also reduces contamination of the glass powder by removing any large chips of magnesium silicate milling media.

b) Uniaxial pressing

Uniaxially pressed pellets of the glass powders were used to investigate crystallization and sintering behaviour. A saturated solution of stearic acid in acetone was used to lubricate the die, but no organic compaction aids or lubricants were added to the glass powder. Cylindrical dies of diameter 13, 16, and 25 mm were used. Problems due to cracking of the green body were found to be substantially reduced by the use of pressures of 20 MPa or below. It was not possible to reproducibly achieve pressures this low using either the 13 mm or the 16 mm die, and the 25 mm die was therefore used exclusively after the initial trials.

Uniaxial pressing was also used to produce graded glass-ceramic structures. Each layer was partially pressed prior to pressing the entire body. Joints with up to five layers of glass-ceramic were produced in this manner.

c) Isostatic pressing

Wet bag isostatic pressing was used to prepare samples for TCE measurements using a pressure of approximately 120-150 MPa. This has the advantages, compared to uniaxial pressing, of: greater compaction, improved densification, a more even distribution of density, and avoidance of any preferred orientation problems. This is particularly important, as anisotropic shrinkage of uniaxially pressed pellets with similar composition has been reported [3]. Isostatic pressing should result in more reliable TCE measurements than would be obtained using uniaxially pressed samples.

d) Tape casting

A cast tape was chosen as one of the means of applying the unfired glass ceramic for joining trials. Tape casting results in a flexible sheet that maintains green strength and can be easily handled. Controllable and consistent thickness can also be obtained. In tape casting the glass powder is suspended in an organic vehicle plus plasticiser. In this case the composition of the organic constituents had previously been developed by Lockyer and co-workers at Warwick [4], whilst working on tape casting of similar MAS compositions, and is shown in Table 4.1. The preparation procedure is as follows (for details of abbreviations used see Table 4.1):

1. The organic vehicle is weighed out and warmed on a hot plate to 120-130°C.
2. This is stirred and allowed to dissolve and form a clear solution.
3. D.P.M is added to adjust back to the starting weight.
4. The glass powder is mixed in using a shear blender.
5. The final consistency is adjusted to resemble single cream by the addition of a small quantity of B.C.A.
6. This is left to stand or preferably evacuated to remove air bubbles.
7. The mixture is doctor bladed onto a Mylar substrate.
8. Tape thickness is controlled by setting the blade height using a feeler gauge.
9. The solvent is allowed to evaporate resulting in a flexible tape.
10. The solvent for cleaning is ethoxy-2-propanol.

Table 4.1: Composition of tape cast material

Vehicle	20 wt %	Bohm and Hoerst - Paraloid A11: acrylic resin (binder)
	75 wt %	Dowanol D.P.M. methoxy propoxy propanol or dipropylene glycol monomethyl ether
	5 wt %	B.C.A.: butyl carbutol acetate or butyl diglycol acetate
Plasticiser		D.B.P: di-n-butyl phthalate
Weight ratio of vehicle to plasticiser		6:1
Weight ratio of glass powder to organics		1:1

Glass powder ~ 8 μm in diameter resulted in a successful tape cast material using the above procedure. However, when a much finer particle size was used (~2μm), problems were encountered due to agglomeration. Although a solution to this problem was not pursued due to time limitations, it is likely that this could be solved by manipulation of the pH of the dispersant.

4.2 Characterization techniques

4.2.1 Differential Thermal Analysis (DTA)

DTA of the glass powders was performed to identify thermal events in the samples. For example: Tg, onset of crystallization, crystallization peak maximum, and onset of melting, A Stanton Redcroft DTA 673-4 with a high temperature head (maximum 1500°C), and a Netzsch high temperature DSC 404 were used.

The conditions employed for DTA were:

- Sample mass ~80 mg for Stanton Redcroft, 30 mg for Netzsch
- Crucible platinum
- Atmosphere still air
- Heating rate 2-40°C min^{-1}
- Reference quartz

The temperature and heating rates were calibrated using quartz and $SrCO_3$ standards (details of the source and composition of the standards used is given in Appendix II). Both of these are recommended as calibration standards by the International Commission for Thermal Analysis (ICTA). The accepted values for the extrapolated onset and the peak maximum temperatures, which are based on the results of round robins involving various contributing labs, are shown in Table 4.2.

Table 4.2: Recognized calibration temperatures for ICTA standards [5]

	Extrapolated Onset (°C)	Peak Maximum (°C)
Quartz	571	574
$SrCO_3$	928	938

DTA was also used to measure the apparent activation energy of crystallisation using the modified Kissinger, Ozawa and Marseglia methods. The modified Kissinger method, suggested by Matsusita [6][7], relates the heating rate $\dot{T}$, to the peak crystallisation temperature(T_p) using Equation 4.2.

$$\ln(\dot{T}^n / T_p^2) = -(mE / RT_p) + \text{constant} \qquad \text{Modified Kissinger} \quad (4.2)$$

E is the apparent activation energy, R is the gas constant and n and m are numerical factors related to the crystallisation mechanism. The activation energy is found from the slope ($-mE/R$) of a plot of $\ln(\dot{T}^n / T_p^2)$ against $1/T_p$. For the special case of surface crystallisation from a fixed number of nuclei $m = n = 1$, and Equation 4.2 reduces to the standard Kissinger equation.

Alternative related approaches are the modified Ozawa [6][7], and Marseglia [8] methods using Equations 4.3 and 4.4 respectively.

$$\ln(\dot{T}^n) = -(mE / RT_p) + \text{constant} \qquad \text{Ozawa} \quad (4.3)$$

$$\ln(\dot{T} / T_p) = -(E / nRT_p) + \text{constant} \qquad \text{Marseglia} \quad (4.4)$$

The conditions that must practically be met in order for these methods to be valid are:

- For each heating rate used, the fraction of glass crystallised must be constant at the characteristic temperature for T_p (peak maximum is normally used but peak onset has also been used [9]).
- The temperature must be even across the sample. This is more readily satisfied for small sample sizes and low heating rates.
- The crystallisation mechanism must be known, and remain constant, over the range of temperatures and heating rates investigated.

However, problems arise with the interpretation of the measured activation energy. Often, this is a composite activation energy as several processes occur simultaneously. This may be nucleation and growth, or the crystallisation of two or more phases. As a result, the measured activation energy is normally described as the apparent activation energy.

In a similar manner the apparent activation energy for structural relaxation occurring around the glass transition (T_g) can be found by monitoring the change in T_g with heating rate using Equation 4.5 [10].

$$\ln(\dot{T}) \approx -E_{relax} / RT_g \qquad (4.5)$$

4.2.2 Particle sizing

The particle size of milled powders was measured using a Malvern Mastersizer/E which uses the intensity distribution of laser light scattered by a suspension of the powder to determine the particle size distribution. By comparison of the measured and theoretical data the computer finds a volume size distribution by a constrained least squares fit of the theoretical scattering characteristics to the observed data. The fundamental instrumental measurement is one of volume, all other output information is derived from these results by numerical transformation based on spherical particles.The model used for the fitting routine was the "Model Independent Analysis" mode which allows more than one mode or peak in the volume size distribution. The goodness of fit achieved by the model can be estimated by the residual percentage. According to Malvern [11], less than 1% residual indicates a good fit.

The dispersion fluid used was water and disaggregation of the glass powder was achieved by continuous stirring and ultrasound. Measurements were repeated until the measured distribution stabilized. All measurements were performed with the 100 mm lens which is suitable for measuring particles sizes from 1.2-118 μm. It is however unable to measure particles smaller than 0.5 μm and this may lead to slight overestimation of the mean particle size. However, the contribution to the cumulative mass percentage is likely to be small and, if significant, would result in an unacceptable residual percentage. The figures that are reported are cumulative volume or size distributions, therefore D(v,P) is the diameter at percentage point P, that is the size under which a certain percentage of the volume (or weight) falls.

4.2.3 XRD

Powder X-ray diffraction was used to verify the amorphous nature of the glasses and to identify phases present in other samples in conjunction with data from the Joint Committee for Powder Diffraction Standards (JCPDS). A copper tube with a nickel filter was operated at 40 keV and 30 mA resulting in Kα1 and Kα2 with a mean wavelength of 1.54178 Å. Scans were typically from 5-75° 2θ. Where necessary the alignment was checked either by painting a thin layer of colloidal silicon standard on the surface of samples, or by using a polycrystalline silicon standard.

4.2.4 SEM

Scanning electron microscopy was performed on both polished microsections and fracture surfaces, coated using either gold or carbon, using either a JEOL 6100 or a Cambridge S250. Both machines are equipped with a backscattered detector for compositional contrast, and facilities for energy dispersive X-ray analysis (EDX). This enables both quantitative and qualitative analysis of composition to be performed, and can be used to produce maps and line scans giving compositional information. The size of the interaction volume, that is the volume of sample contributing to the X-ray signal, does however place a limitation on the spatial resolution that can be achieved using EDX. Reed [12] gave the following relationship to estimate resolution in μm as a function of incident electron energy (E_0, keV), critical excitation energy (E_c, keV), and density (ρ, g cm-3):

$$d = 0.077(E_0^{1.5} - E_c^{1.5})/\rho \qquad (4.6)$$

However the spatial resolution for quantitative analysis is often considered to be the size of the region of the specimen producing 99% of the generated X-rays [13]-[14] (not including those produced due to X-ray fluorescence) and this is approximately three times d as calculated by Equation 2.34 [7]. Table 4.1 gives appropriate values for spatial resolution, and resolution for quantitative analysis purposes, for Si in a cordierite glass ceramic for incident electron energy of 5, 10 and 15 keV calculated using Equation 4.6. For a glass ceramic the particles being analysed are normally micron size or smaller embedded in a matrix, and excitation of this matrix can confuse the results. According to Scott and Love [13], analysis problems are worsened if any elements present in the particle are contained in appreciable concentration within the matrix and this may make it impossible to carry out a meaningful analysis.

Table 4.3: EDX resolution (d) and resolution for quantitative analysis (3d) for Si as a function of incident electron energy.

Incident electron energy (keV)	*d* (μm)	3*d* (μm)
5	0.26	0.79
10	0.87	2.61
15	1.65	4.96

Both machines are equipped with facilities for recording and analysing digital images.

4.2.5 Optical microscopy

Optical microscopy was used to provide complementary information to that obtained using SEM. A Carl Zeiss Jena Ultraphot II was used for macroscopic work at low magnifications. Oblique illumination using an external light source resulted in improved visibility of many microstructural features (especially cracks) due to

enhanced contrast. Work at slightly higher magnifications (up to 500X) was performed using an Olympus BH-2 and an Olympus B061. For glass-ceramic samples, problems due to glare from internal surfaces can be alleviated by gold coating.

4.2.6 TCE

Thermal coefficient of expansion (TCE) was measured using a Netzsch 402E push-rod dilatometer, with the furnace controlled by a Netzsch 410 furnace controller and the data logged and recorded on a PC via a Netzsch 414/1. This dilatometer uses a linear variable differential transducer (LVDT) to measure the difference in the expansion of the body under test and an alumina push-rod, and the alumina sample support as a function of temperature. The temperature is measured by a thermocouple next to the sample. Measurements may be made from 20-1700°C for samples of length 25-50 mm.

There is some confusion over the terminology used when reporting thermal coefficient of expansion. Although α is often used for the instantaneous thermal expansion, that is $(1/L_T)(dL_T/dt)$, in this work it refers to the thermal expansion over a temperature range. This is also known as the engineering TCE.

$$TCE(T_2 \quad to \quad T_1) = \Delta L / L_0 \Delta T \qquad (4.7)$$

L_0 = original length
ΔL = the change in length
ΔT = temperature range (T_2 to T_1)

The values are reported in MK^{-1}, this is equivalent to ppm/°C or x 10^{-6}/°C. To obtain the expansion due to the test body alone a correction is made to the recorded data to allow for the thermal expansion of the sample holder. This has previously been calibrated by Netzsch. To verify this calibration, thermal expansion measurements were made of silica and platinum standards, this covers the whole range of thermal expansion that is likely in the MAS/MS glass-ceramic system. The results are summarized in Table 4.4 below

Table 4.4: Calibration check of Netzsch dilatometer with silica and platinum standards

Sample	Sample length (mm)	Temperature Range (°C)	Measured TCE (MK^{-1})	Quoted TCE (MK^{-1})	Difference (MK^{-1})
Silica	50.0	50-550	1.18	0.57 [15]	0.75
			1.17		0.68
Platinum	48.1	100-1000	11.08	10.33 [16]	0.61
			11.01		0.60

In both cases the measured figures are high, the range of error is 0.60-0.75 MK^{-1} and to increase the accuracy of the reported result 0.67 MK^{-1} has been deducted from the figure *after* the adjustment for sample holder. The repeatability of the measurements is however encouraging, and give confidence that the final reported measurements are likely to be accurate to $\pm$ 0.1 MK^{-1}.

4.2.7 Densitometry

The density of samples was measured by recording the mass in air and suspended in a fluid using Archimedes Principle. The immersion fluid used was distilled water. The density (ρ) is then given by:

$$\rho = M_a \rho_f / (M_a - M_f) \qquad (4.8)$$

ρ_f= density of immersion fluid at temperature of measurement
M_a = weight in air
M_f= weight in immersion fluid

4.3 Joining trials

4.3.1 Introduction

Three separate furnaces were used for the joining trials, brief details of each are given in Sections 4.3.2 to 4.3.4 below.

4.3.2 TWI brazing furnace

The initial work in this project was performed at TWI using an RF induction furnace designed for brazing. The sample was placed inside a graphite susceptor which was induction heated to the required temperature. The furnace was held under vacuum throughout the joining run and the temperature monitored by a thermocouple next to the sample

Heating rates and temperatures were controlled by manually adjusting the power to the furnace. Normal heating rates used were approximately 60-70°C per minute. The samples were allowed to cool by turning off the power to the furnace and allowing to cool. This resulted in an overall cooling rate of approximately 15-20°C per minute. It was possible to apply a controlled load to the sample throughout the bonding run. For most joining runs in this furnace an initial load of ~ 0.55 MPa was applied at room temperature and subsequently increased to ~ 1.1 MPa at the bonding temperature. The glass-ceramic was applied in the form of a loose powder.

As will be seen in Chapter 6, the control of temperature and heating rate using this furnace were not adequate in order to achieve reproducible results.

4.3.3 Sintering furnace

Further joining trials were performed in a cold-wall, graphite element, resistance heated furnace, which enabled choice of atmosphere (vacuum, or backfill with controlled atmosphere), together with improved control of temperature and heating and cooling rates. Temperatures of up to 1650°C were used in this furnace. Unfortunately this furnace was limited by not being able to apply a joining pressure to the sample. However, it was suitable for high temperature joining trials where the viscosity of the glass was sufficiently low to ensure a good bond in the absence of an applied pressure.

Figure 4.1

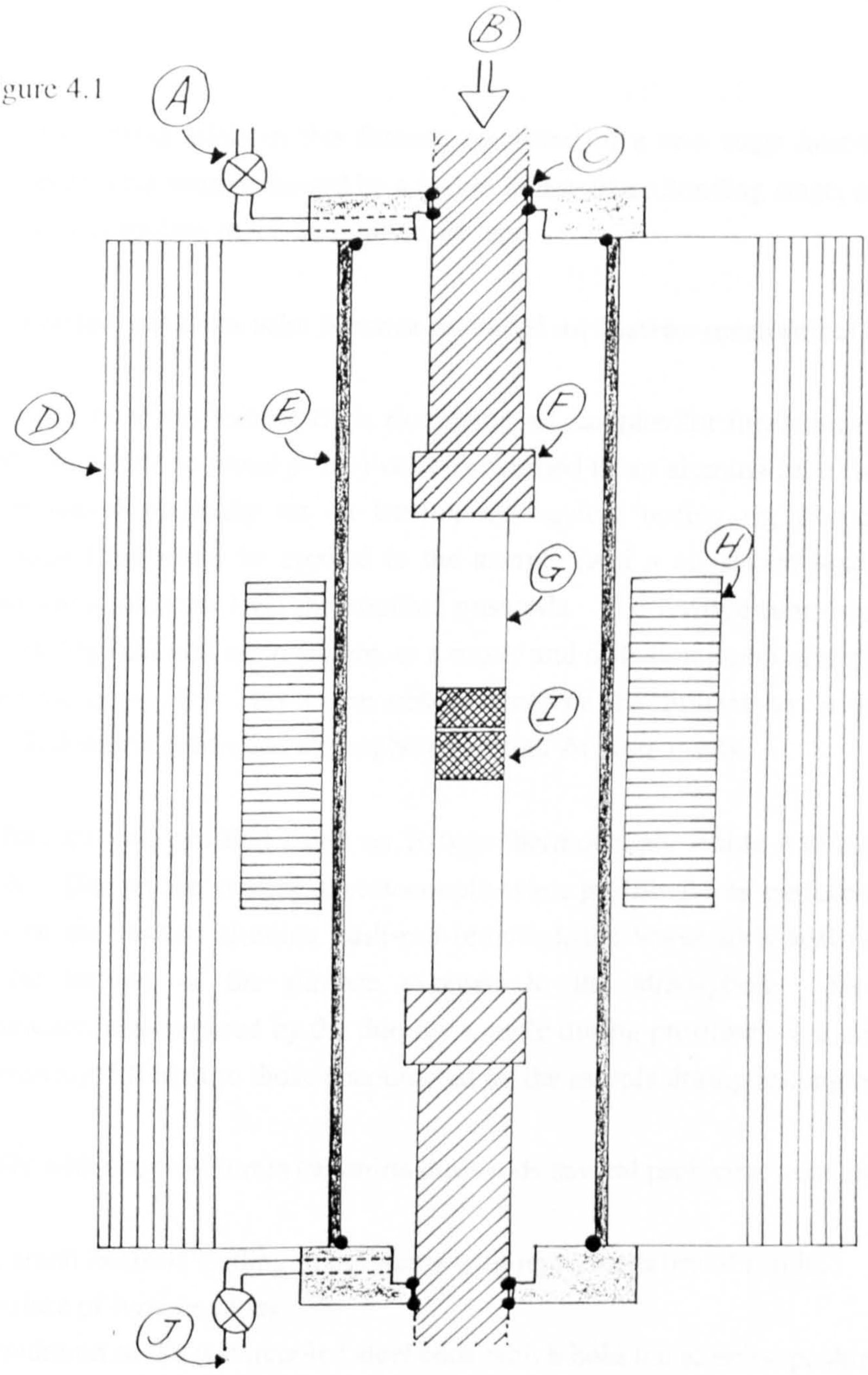

Figure 4.1: Alumina tube furnace mounted vertically on an Instron mechanical testing rig.

A. Rotary/diffusion pump assembly
B. Load controlled by Instron mechanical test rig
C. Sliding seal arrangement
D. Furnace insulation
E. Alumina tube
F. Water-cooled steel push rod mountings
G. Alumina push rods
H. Furnace hot zones
I. Sample
J. Controlled atmosphere - N_2, Ar

Typically joining trials in this furnace consisted of a two stage heat-treatment, an initial degassing stage followed by a higher temperature bonding stage, and the glass-ceramic was applied in the form of a cast tape.

4.3.4 Vertical alumina tube furnace mounted on Instron mechanical test rig

The majority of the joining trials (including all samples for mechanical testing and all silicon nitride to metal joints) were performed in an alumina tube furnace which was mounted vertically on an Instron mechanical testing rig (Figure 4.1). A controlled load could be applied to the sample (and a consistent load maintained during the joining run) via the alumina pushrods. The furnace tube was connected, via a sliding end seal arrangement, to a rotary and diffusion pump assembly enabling a vacuum of ~ 10^{-4} Torr to be obtained and/or the furnace to be subsequently backfilled with a controlled atmosphere (N_2 and Ar were used).

The furnace was profiled using an R-type thermocouple inside a dummy alumina sample. Due to the trailing thermocouple wire, profiling was performed with the collet on the bottom alumina push-rod removed, the lower slide seal not engaged, and the bottom of the furnace exposed to the atmosphere. However, the temperatures encountered by the dummy sample during profiling were unlikely to be significantly different to those encountered by the sample during joining trials.

Initially with short (~35 mm) alumina push-rods several problems were encountered:

- A small hotzone leading to problems with reproducibility of results
- Failure of furnace tubes
- Oxidation of the watercooled steel ends which hold the alumina push-rods

For later work, the length of the alumina push-rods was modified to the maximum length (~80mm) that still allowed the largest proposed samples to be inserted . This resulted in: a larger more stable hot zone, reduced problems due to oxidation as a result of the watercooled steel ends being moved further from the hot zone, and a less severe temperature gradient being seen by the alumina tube. The maximum heating rate that the manufacturer (Degussa) will guarantee the alumina tube to withstand is 3°C per minute. However, in order to perform a realistic number of joining experiments (involving heating to ~ 1200°C) faster heating rates must be used. As a working compromise the heating rate was restricted to ~5°C per minute

on overnight cooling and heating up to 650°C, and to below 15°C per minute on heating above 650°C. This 'rule of thumb' in conjunction with the lengthening of the alumina push-rods resulted in the failure of alumina tubes being virtually eliminated.

One weakness of this furnace set up is that the vacuum is recorded at the head of the diffusion pump. This means that the pressure seen by the sample may be at least an order of magnitude higher.

For butt joints the glass-ceramic was applied in the form of a cast tape; for the ceramic to metal compression seals a loose glass powder was used.

4.3.5 Sample preparation

Silicon nitride samples for joining trials were cut on a Jones and Shipman surface grinder using a diamond embedded steel wheel. Joining was performed on as cut surfaces, with no subsequent polishing. Although defects may be created in the silicon nitride from surface grinding, failure of glass-ceramic joints is more likely to occur from within the glass ceramic interlayer (σ~120 MPa K_{IC} ~ 1.5 MPa $m^{1/2}$) rather than from within the silicon nitride (σ ~ 650 MPa, K_{IC} ~ 4.5 MPa $m^{1/2}$). Cylindrical silicon nitride nitride specimens for joining trials were cut from a 15 mm diameter cylindrical bar.

Prior to joining, the following cleaning regime was performed twice. The samples were cleaned ultrasonically using a commercial cleaning solution and ultrasonically degreased in acetone.

4.3.6 Compression joint geometry

The geometry for the Nimonic 80A and Ti samples for compression joints is shown in figure 4.2. Under the applied joining pressure, the reservoir of glass in the bottom of the compression joint fills the gap between the metal and the ceramic, crystallises to form a glass-ceramic and is held strongly in compression on cooling. The mass of powder used (0.7 g) was calculated to ensure that sufficient glass was present that the glass/glass-ceramic extruded over the top of the silicon nitride.

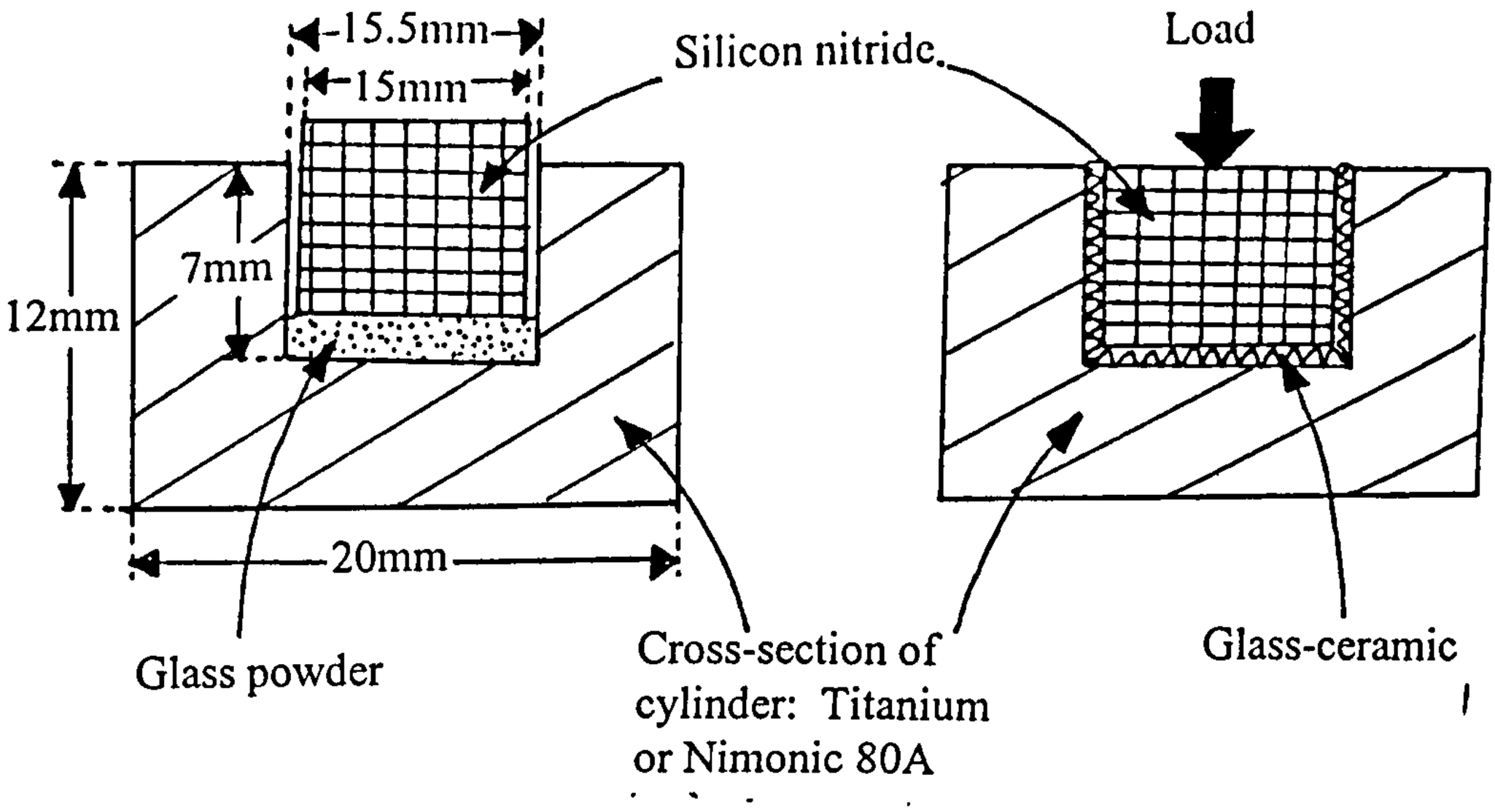

Figure 4.2: Geometry used in compresion joint trials.

4.4 Mechanical Testing

4.4.1 Mechanical testing - introduction

To determine whether a joint has sufficient strength for practical applications, and to quantify the strength of the joint, mechanical testing is required. In order to understand some of the problems associated with mechanical testing of ceramic joints it is worthwhile to first consider the problems associated with mechanical testing of monolithic ceramics.

Failure of a ceramic under load usually occurs by brittle fracture, at a strength limiting defect. The strength is therefore determined by the defect population resulting in a statistical distribution of strength when a number of samples are measured. The Weibull distribution (Equation 4.9) is often used to model the distribution of strength.

$$F(\sigma) = 1 - \exp[-V_e(\sigma_{max} / \sigma_0)^m] \qquad (4.9)$$

Where $F(\sigma)$, σ, σ_0, m and V_e are the failure probability distribution function, tensile stress, material constant, Weibull modulus, and effective volume respectively. The Weibull modulus describes the narrowness of the distribution, a high value of m

implies a narrow distribution. Conversely, a low value of m implies a wide distribution and a correspondingly greater chance of a piece having low strength. Because failure occurs at a critical defect, if fractography is employed to identify the critical defect, mechanical testing can be used to characterise the defect population.

The failure stress is strongly dependent on the effective volume (V_e). For two different sized specimens (1 and 2), the relationship between the stress at equal probability of failure (σ) and the Weibull modulus (m) is given by Equation 4.10.

$$\frac{\sigma_1}{\sigma_2} = \left(\frac{V_{e2}}{V_{e1}}\right)^{1/m} \tag{4.10}$$

If the sample population is a Weibull distribution then the standard deviation (S.D) in the mean strength (σ_{mean}) and the Weibull modulus are given by Equations 4.11 and 4.12 [17] (J is the number of specimens):

$$(S.D)_m = m/\sqrt{J} \tag{4.11}$$

$$(S.D)\sigma_{mean} = 1.2\ \sigma_{mean}/m\sqrt{J} \tag{4.12}$$

Uniaxial tensile testing of ceramics is possible, and has the advantage that a large effective sample volume may be tested. However, it is not often used as alignment during testing is critical. Any misalignment introduces bending and thus stress concentrations at surface flaws, which can result in uncertainty in the tensile strength measurements. More commonly, the strength (modulus of rupture) is measured by bend or flexure testing, which is cheaper and simpler. The stress at failure (σ) is given by:

$$\sigma = Mc/I \tag{4.13}$$

M = the moment
c = the distance from the neutral axis to the tensile surface
I = the cross-sectional moment of inertia

The failure stress obtained is the peak stress on the tensile surface at the time of fracture. Most commonly, samples with rectangular cross-section are tested using 3

or 4-point bend testing. For 3-point bending the maximum tensile stress occurs only on a single line on the surface of the test sample opposite the central loading point, decreasing linearly along the bar to zero at the outer load points. The tensile stress also decreases linearly through the thickness of the bar to the neutral axis (the midplane of the bar).

For 4-pt bending, the maximum tensile stress on the surface of the sample is within the inner span on the opposite surface, and is approximately constant. Once again the tensile stress decreases linearly through the thickness of the bar to the neutral axis. A larger effective sample volume is under test for 4-point bending compared to 3-point bending resulting in lower measured strengths. The true fracture stress is lower if failure is not from (or close to) the tensile surface. For 4-point bend testing with rectangular geometry, (Figure 4.3):

$$\sigma = 3\,Wa/bd^2 \qquad (4.13)$$

Where W is the load at failure.

The results of bend testing are particularly sensitive to specimen size, shape and surface finish. Even for a surface polished to a mirror finish, failure may occur from hidden subsurface damage.

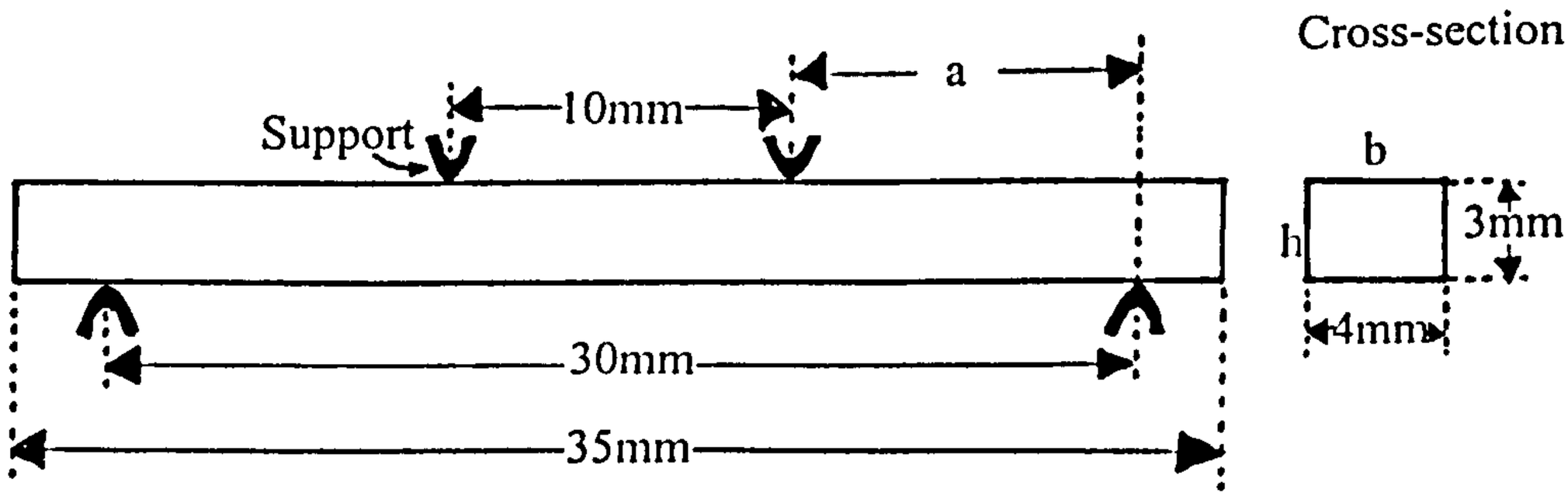

Figure 4.3: Geometry of 4-pt bend tests.

For a detailed discussion of flexure testing see Quinn and Morrell [18], who give details of the assumptions that must be satisfied for Weibull modulus to be appropriate for a design criterion.

4.4.2 Mechanical testing of ceramic joints

The napkin ring test (ASTM F-19 - Method for Tension and Vacuum Testing Metallurgical Ceramic Seals - metal washer joined between test pieces) is recommended by the ASTM. Although this was used for the characterisation and development of the Mo-Mn process for joining alumina (where strengths of ~ 100 MPa [19] were typical) it is not widely used in the current literature. This standard has been criticised due to the complicated shape of the test pieces and the lack of control of joint thickness. It is not considered suitable for developmental work unless appropriately shaped test pieces and a suitable furnace are readily available.

The most commonly reported methods of mechanical testing of ceramic joints are 3 and 4-point bend testing. The advantage of 4-point bending is that the placement of the joint within the test fixture is less critical. However, the use of flexure testing for characterising the strength of joints is open to criticism. For a thin joint, the effective sample volume under test is very small and it is not clear that the following requirements (which must be fulfilled in order for the distribution of strengths to be modelled by a simple Weibull distribution (Equations 4.9 to 4.12), are satisfied:

- The material is a homogeneous medium.
- The defect population that limits strength is the same whatever shape or preparation method is used for the tested specimens or components.
- The defect population is invariant with time.
- The defects are randomly distributed and are small relative to the specimen or component size.
- There is a statistically significant number of defects within each specimen or component.
- Only one failure mechanism is in operation.

In addition, joint strengths greater than the strength of the interlayer material have been reported for both glass [20] and metallic interlayers [21][22]. The possible reasons for the higher strength of the glass joint have been discussed in Section 3.3.8. Where results for brazes or metallic interlayers result in joint strengths greater than the yield strength of the interlayer, it is possible that the behaviour of the joint is not

entirely linear elastic, and joint strengths should be treated with caution. According to Quinn and Morrell [18], fast fracture data are only valid for precise strength evaluation if collected under conditions such that the material is linearly elastic, otherwise the elastic stress formulation is seriously in error.

In the current work 4-point bend testing was carried out in accordance with the Japanese standard JIS R 1601 - Testing Method for Flexure Strength (Modulus of Rupture) of High-Performance Ceramics - December 1981. This standard was adopted as according to Quinn and Morrell [18] it is less stringent in some technical details (than other comparable standards), is simple to use and has been widely used in Japan which has led to much improved consistency of results. The requirements of JIS R 1601 are set out in Table 4.5.

Mechanical testing using this standard was carried out on silicon nitride/MAS/silicon nitride joints, silicon nitride as received and silicon nitride after a typical joining heat treatment. Some samples were tested without the required bevel. Where the specimens were beveled, the bevel was produced by mounting 2 test bars at a time in right angle grooves in a brass block. The polishing procedure adopted was 4 minutes using a 30 μm diamond grinding wheel, followed by 3 minutes using a 1 μm diamond suspension. The polishing was performed by hand with only the "dead" weight of the hand and specimen and no further applied load. This was found consistently to produce a 300μm bevel on the sample in accordance with the requirements of the standard.

The Japanese standard (JIS R 1601) is however open to the following criticisms [18]:

- The chamfer may result in a 4% stress error
- The fixed fixture means that specimens must be parallel
- The fixed loading pins may result in a 5-15% error
- As the specimen preparation is not described in detail this may lead to polished specimens with concealed damage

A further problem may be encountered due to the manner in which the standard was employed in the current work. For flexure testing of ceramic samples, recommended practice is that the loading pins should be 5 to 10 mm in diameter [23] to avoid stress concentrations. However the test fixture employed in the current work had a much smaller radius of curvature.

The small sample sizes used in this work, partially due to significant sample losses during specimen preparation, resulted in large standard errors in the mean strength and Weibull modulus (as reported in Sections 6.7 and 6.8). Where similar measurements are required for practical engineering applications, larger sample sizes are recommended. The United States flexure standards, MIL-STD 1942 (1983) and ASTM C 1161 (1990) [18], recommend a minimum of 30 specimens for Weibull analysis.

Table 4.5: The requirements of flexure testing standard JIS R 1601 (1981).

Fitxture	Three or four point
Spans	10 mm x 30 mm
Fixture	Fixed
Fixture load pins	Fixed
Specimen sizes	3mm x 4 mm x 35 mm
Specimen chamfers	Up to 0.3 mm
Specimen preparation	Polished or as fired
No of specimens (minimum)	10
Loading rate	0.5 mm min^{-1}

References for Chapter 4

[1] Bridge D.R., Aspects of electronic device packaging, Ph.D. Thesis, University of Warwick, 1986

[2] G. de With, Process Control in the Manufacture of Ceramics, Chapter 2 in Materials Science and Technology - A Comprehensive Treatment - Edited by R.W.Cahn, P Haasen and E.J.Kramer, Volume 17A Processing of Ceramics Part I, Volume Editor R.J.Brook, VCH, 1996.

[3] Exner H.E. and Giess E.A, J. Mater. Res. 3 (1988) 122.

[4] Lockyer M.W., private communication.

[5] Dodd J.W. and Tonge K.H., Thermal Methods - (Analytical Chemistry), Wiley, 1987.

[6] Matsusita K., Saaka S. and Matsui Y., J. Mater. Sci. 10 (1975) 961.

[7] Matsusita K. and Saaka S., J. Non-Cryst. Solids 38 & 39 (1980) 741.

[8] Marseglia E.A., J. Non-Cryst. Solids 41 (1980) 31.

[9] Rudoolph T., Pannhorst W. and Petzow G., Glastech. Ber. 64 [12] (1991) 218-224.

[10] Moynihan C.T., Easteal A.J. and Wilder J., J. Phys. Chem. 78 (1974) 2673.

[11] Malvern Mastersizer/E - User Manual, 1990.

[12] Reed S.J.B., X-ray optics and Microanalysis, p339, Eds Castaing R., Deschamps P. and Philibert J., Paris: Hermann, 1966.

[13] Scott V.D. and Love G., Quantitative Electron-Probe Microanalysis, Ellis Horwood Press, 1983.

[14] Reed S.J.B., Electron Microprobe Analysis, Cambridge University Press, 1975.

[15] Instrument Manual - Netzsch 402E, data reported for silica standard supplied with dilatometer.

[16] Data sheet for pure platinum supplied by Engelhard Sales Limited, Metallurgical Division, St. Nicholas House, St. Nichlas Road, Sutton, Surrey.

[17] Rilter J.E.Jnr., Bandyopadyay N. and Jakus K, Bull. Am. Cer. Soc. 60[8] 798 (1981).

[18] Quinn G.D. and Morell R., Design Data for Engineering Ceramics: A review of the Flexure Test, J. Am. Ceram. Soc. 74 [9] 2037-66 (1991).

[19] Kohl W.H., Vacuum, Vol. 14 (1967) 333-354.

[20] Johnson S.M. and Rowcliffe D.J., J. Am. Ceram. Soc., 68 (9) 468-472 (1985).

[21] Pan W.X., Okamoto K. and Ning S.S., J. Mater. Sci. 29 [6] 1436-1440 (1994).

[22] Ning X.S, Okamoto K., Miyamota Y., Koreeda A., Suganama K. and Goda S., J. Mater. Sci. 26 [8] 2050-2056 (1991).

[23] Morrell R., Handbook of properties of technical and engineering ceramics. Part 1: an introduction for the engineer and the designer, National Physical Laboratory, H.M.S.O., London, 1985.

Chapter 5: Sintered magnesium aluminosilicate glass-ceramics

5.1 Introduction

In this chapter, the phase development of the glass-ceramic compositions used in the joining experiments has been investigated. This has concentrated on MAS1 which was used as the interlayer in the silicon nitride joints for mechanical testing, and in the compression joints. Some information is also presented on MAS2 which is closely expansion matched to silicon nitride.

These glass-ceramics rely on the presence of B_2O_3 and P_2O_5 to control the dynamics of sintering and crystallisation and therefore some work has been performed to investigate the role of B_2O_3 and P_2O_5 in these glasses. To enable comparison with the results of a similar study by Bridge [1], identical compositions (MASX, MASB, MASP, MASBP) to those used by Bridge were chosen for this part of the work. The effects of B_2O_3 and P_2O_5 on the phase development have been investigated, as a function of temperature, and the apparent activation energy for crystallisation has been measured using non-isothermal DTA methods. The measured activation energies are discussed, together with measurements reported in the literature for similar compositions and for stoichiometric cordierite.

This chapter also includes the key results from the final year projects of two undergraduate students, in order that these results may be seen in context:

- Tim Moxey [2] looked at producing glass ceramic joints with a graded thermal expansion.
- Dan Hillman [3] investigated the measurement of residual stress using indentation methods and attempted to replicate the high fracture toughness (4.6 MPa $m^{1/2}$) enstatite glass-ceramics reported by Beall [4].

Where appropriate the student's contribution has been acknowledged.

5.2 Compositions studied

The compositions studies are detailed in Table 5.1. Aluminium orthophosphate was used as the source of P_2O_5, and boric acid as the source of B_2O_3. Attempts were made to produce glass-ceramic MS1 using both ZrO_2 and $ZrSiO_4$ as the source of ZrO_2.

Table 5.1: Compositions studied.

	Composition (wt.%)							
	MASBP	MASB	MASP	MASX	MAS1	MAS2	MAS3	MS1
MgO	22.0	22.25	22.45	22.7	24.55	17.4	21	33.0
Al_2O_3	22.0	22.25	22.45	22.7	19.06	29.7	24.4	
SiO_2	53.0	53.5	54	54.6	53.57	47.4	49.1	54.0
P_2O_5	2	2			2.3	5.0	5.0	
B_2O_3	1		1		0.5	0.5	0.5	
ZrO_2								13.0

	Composition (mol.%)							
	MASBP	MASB	MASP	MASX	MAS1	MAS2	MAS3	MS1
MgO	32.7	33.0	33.0	33.2	37.8	27.8	32.2	44.9
Al_2O_3	12.9	13.0	13.0	13.2	11.6	18.7	14.8	
SiO_2	52.8	53.2	53.2	53.6	49.2	50.8	50.5	49.3
P_2O_5	0.8		0.8		1.0	2.3	2.2	
B_2O_3	0.8	0.8			0.4	0.4	0.4	
ZrO_2								5.8

5.3 Particle size

The particle sizes obtained after ball milling are shown in Table 5.2. D(V,P) is the diameter at percentage point P, that is the size under which a certain weight or volume falls. D(V,50) is discussed as the average particle size. The results from this work are superimposed on data reported by Bridge [1] in Figure 5.1, who concluded, based on his data, that there was little reduction in average particle size after 24 hours. Although there is some scatter in the data, Figure 5.1 indicates that milling for 48 hours reduces the average particle size to 3-4 μm, and this is further reduced to 2-3 μm after 72 hours.

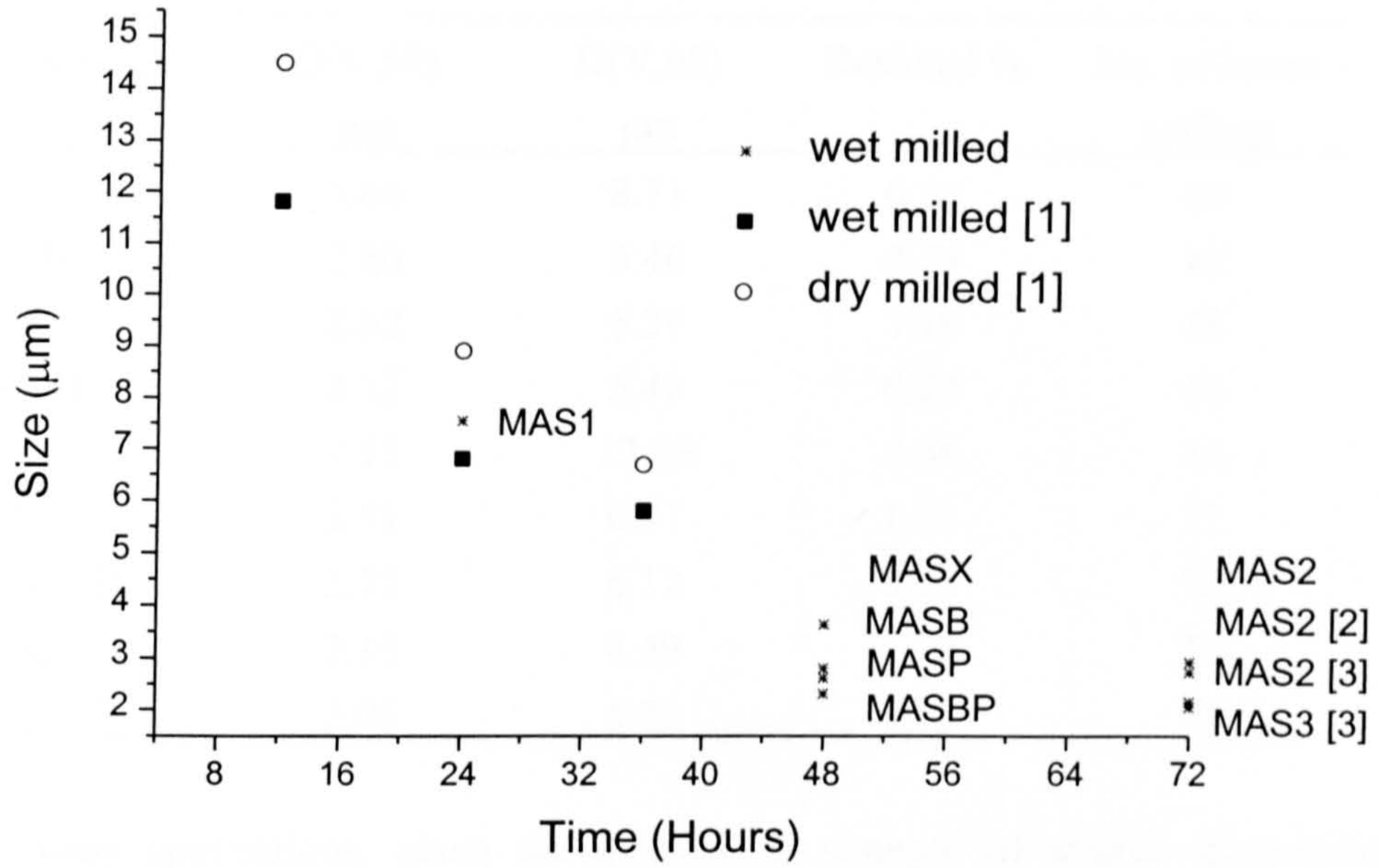

Figure 5.1: Particle size reduction as a function of milling time, superimposed on data from Bridge[1]

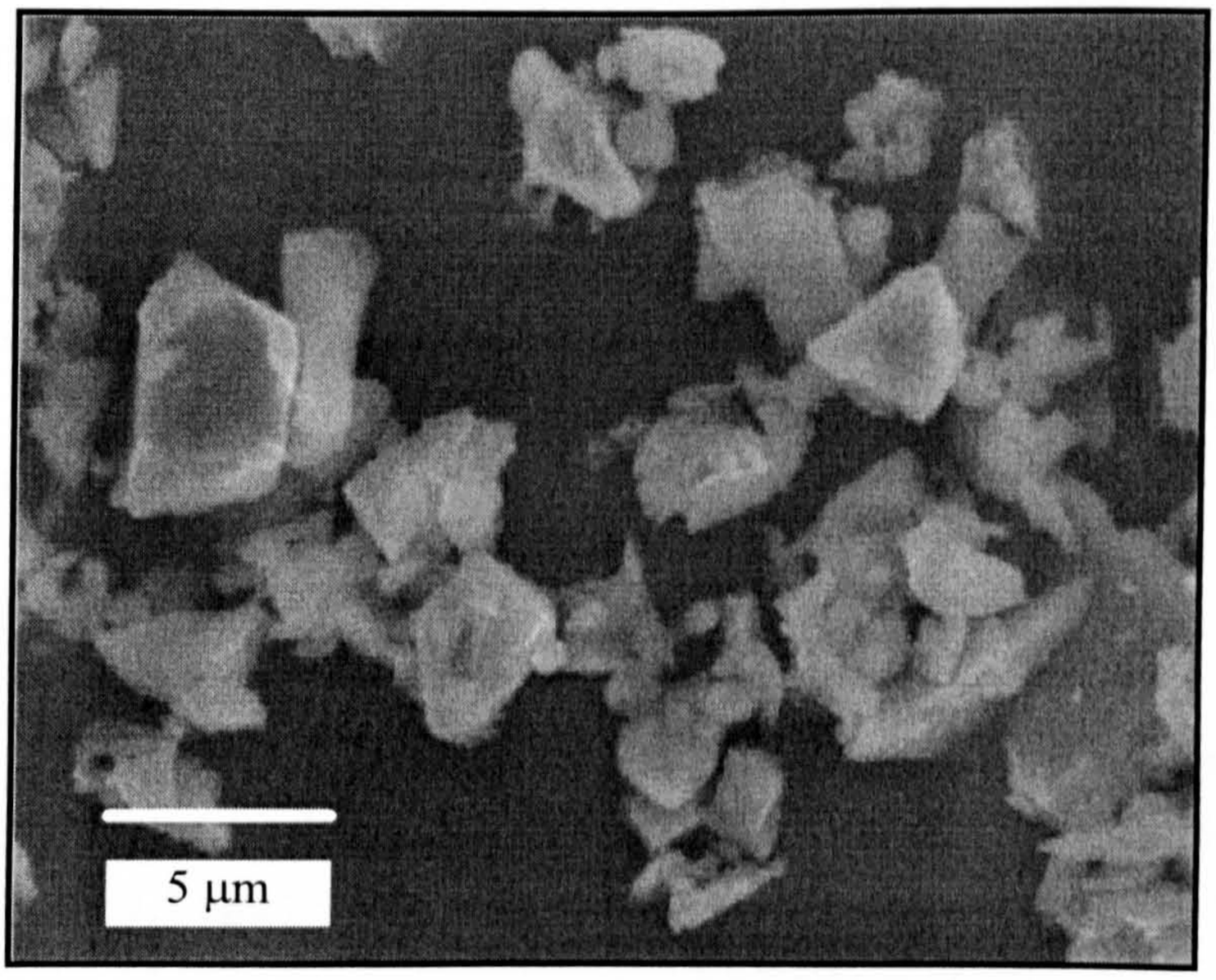

Figure 5.2: Glass powder (MASX)

Table 5.2: Reduction in particle size as a function of milling time

Composition	D(V,50) μm	D(V,90) μm	Residual %	No. of hours milling
MASX	3.64	8.71	0.24	48
MASB	2.80	6.46	0.74	48
MASP	2.62	5.39	1.19	48
MASBP	2.32	5.49	0.27	48
MAS1	7.55	17.26	0.66	24
MAS2	2.91	6.07	1.11	72
MAS2 [2]	2.72	6.12	0.75	72
MAS2 [3]	2.16	4.49	1.29	72
MAS3 [3]	2.06	4.32	0.98	72

For many applications, given the increase in strength of similar glass-ceramic compositions with reduction in particle size reported by Knickerbocker [5], the benefits of a longer milling time will outweigh the problems due to increased levels of milling contamination.

Both Bridge [1] and Logan [6], working on similar materials and preparation routes, reported multimodal particle size distributions, typically consisting of three peaks. In this work, a single peak was found to adequately fit the data. The small residual % indicates that a good fit was obtained.

The shape and size of MASX glass-powder particles are shown in Figure 5.2. The particles still display sharp edges and significant rounding has not occurred

5.4 Phase development - MAS1

5.4.1 Results

A representative DTA trace for MAS1 (D (V,50) at 10°C min^{-1} using the Stanton Redcroft DTA 673-4 is shown in Figure 5.3. The average particle size for this composition was 7.5 μm.

The phase development as a function of temperature for the glass-ceramic used in the majority of the joining experiments (MAS1) has been studied using XRD and SEM. Uni-axially pressed pellets were inserted into a preheated muffle furnace, and

removed from the furnace after 45 minutes. Figures 5.4 and 5.5 show the phases that are present in a pellet of a glass after heat treatments at 950, 1000, 1050, 1100 and 1150°C.

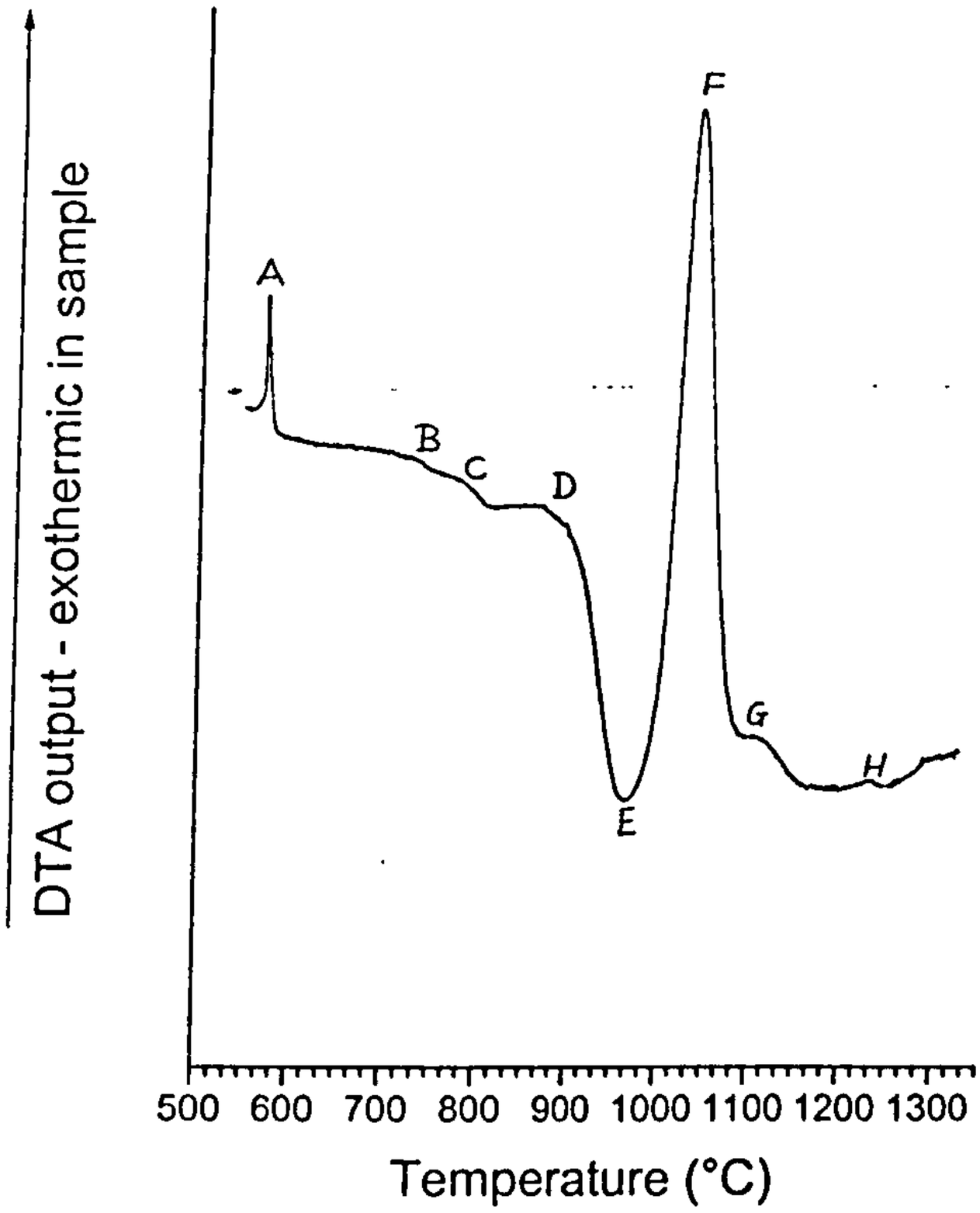

Figure 5.3: Representative DTA trace for MAS1 at 10°C min^{-1}. The marked features are: A - α-β quartz reference peak (574°C), B - possibly due to phase separation (737°C), C - Tg (784°C), D - onset of sintering 867°C, E - onset of crystallisation (959°C), F - crystallisation of μ-cordierite (1019°C), G - crystallisation of α-cordierite (1084°C), H - related to compositional or structural changes in the enstatite polymorphs.

The identification of which lines could be attributed to the specific enstatite polymorphs (ortho, clino and proto), which may co-exist, was particularly problematic. In this instance, this was further complicated by the fact that, at temperatures up to 1199°C, considerable solid solution appears to have occurred, with Al^{3+} substituting for both Mg^{2+} and Si^{4+}. As mentioned in Section 2.7.3, Al^{3+} substitution in enstatite of up to 0.8 Al^{3+} per 2.0 tetrahedral cations can occur. Some XRD peaks have been identified as due to generic enstatite (E), rather than attempting to attribute them to a specific polymorph. At low temperatures this is due to the co-existence of ortho and clino. The presence of proto-enstatite is more easily detected and is observed at higher temperatures (above 1100°C).

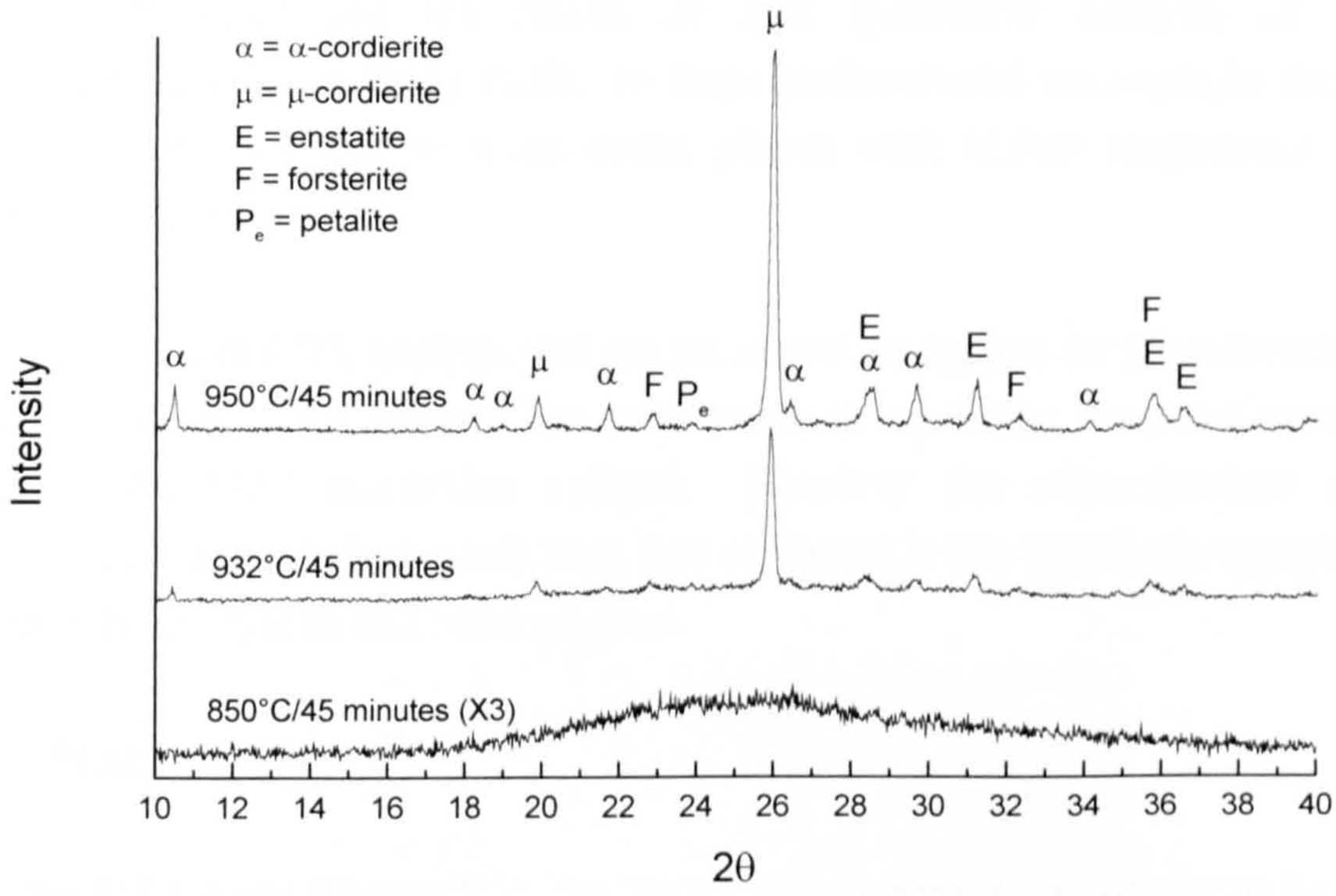

Figure 5.4: XRD of MAS1 showing crystallisation from 850-950°C.

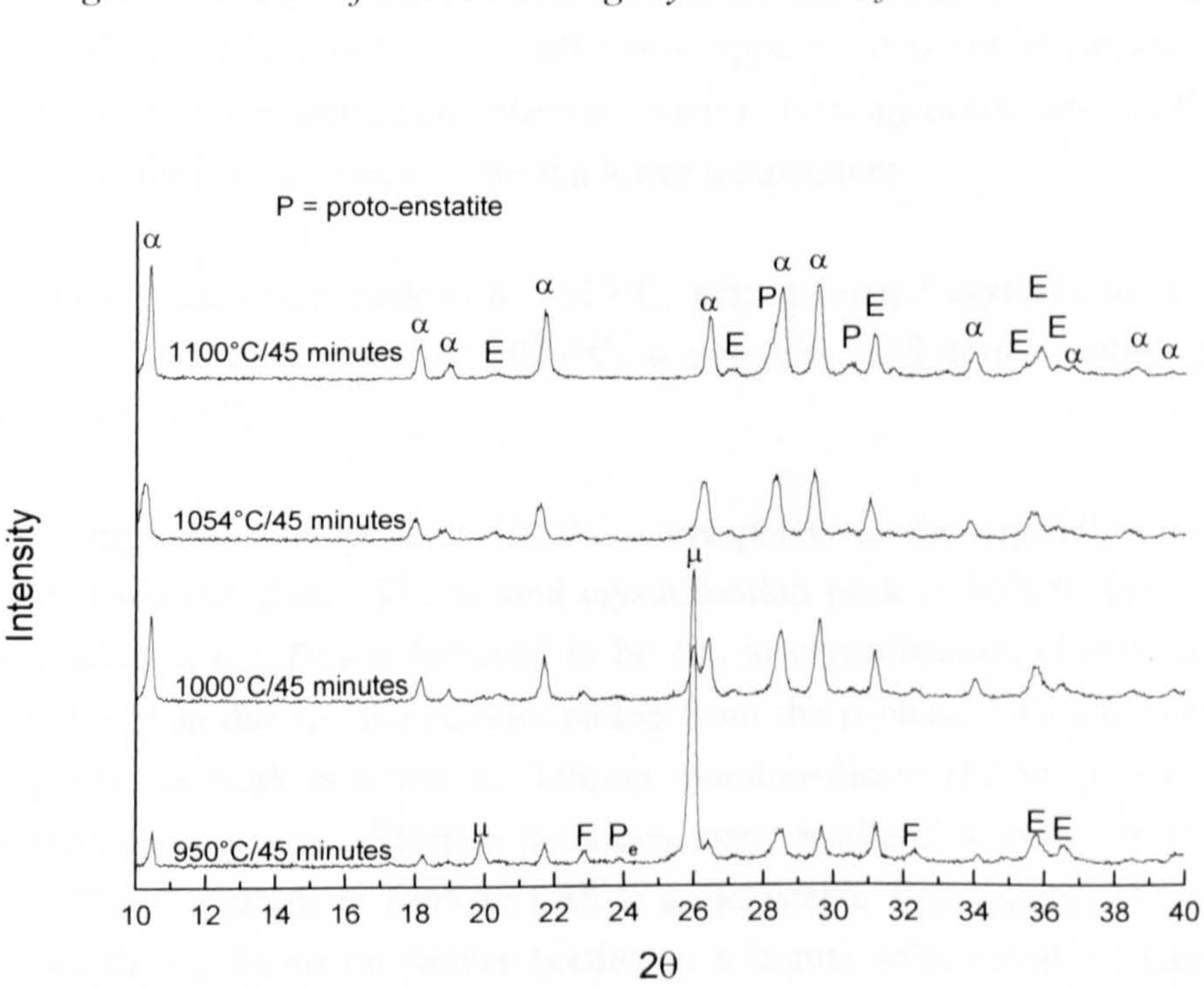

Figure 5.5: XRD of MAS1 showing crystallisation from 950-1100°C.

The XRD results need to be considered together with Figures 5.6 to 5.9 which show the microstructures and the results of spot qualitative analysis of specific microstructural features using EDX. In these backscattered micrographs the lighter phases are normally due to more dense phases with higher magnesium content (enstatite, forsterite).

The results of spot EDX analysis that are presented are typical for the microstructural features observed. An attempt has been made to minimise contribution of other phases to the EDX interaction volume. However, the microstructure may be distributed on a much finer scale than that observed in the SEM micrographs, with intergrowths of crystals and residual glass.

5.4.2 MAS1 - DTA

From the DTA trace (Figure 5.3), the Tg for this composition appears to be around 784°C, although there is another minor feature at around 737°C. This may be related to fine-scale, glass-in-glass phase separation which is known to occur in similar compositions when P_2O_5 is present (Section 2.7.7). The onset of sintering occurs around 867°C. The onset of crystallisation appears to occur at around 959°C. However, since a competing endothermic event (sintering) occurs around the same temperature, the actual onset may be at a lower temperature.

The main crystallisation peak is at 1019°C, with a second crystallisation peak (a shoulder on the main peak) at 1084°C, a possible third crystallisation peak is observed at 1205°C.

The first crystallisation peak at 1035°C corresponds to the crystallisation of μ-cordierite from the glass. The second crystallisation peak at 1090°C is due to the crystallisation of α. This is believed to be due to crystallisation directly from the glass, rather than due to the transformation from the μ-phase. This conclusion is based partly on work reported for lithium aluminosilicate (LAS) glass-ceramics, where the pattern of crystallisation possesses many similarities to that in the MAS system. The first phase to form in LAS is a metastable high quartz solid solution phase, which transforms on further heating to a keatite solid solution phase. The reaction enthalpy for both transitions has been measured by Günter [7]: 27.7 kJ mol^{-1} for the transition from the glass to the high quartz solid solution phase, and 1.9 kJ mol^{-1} for the transformation from high quartz solid solution to keatite solid solution.

Figure 5.6

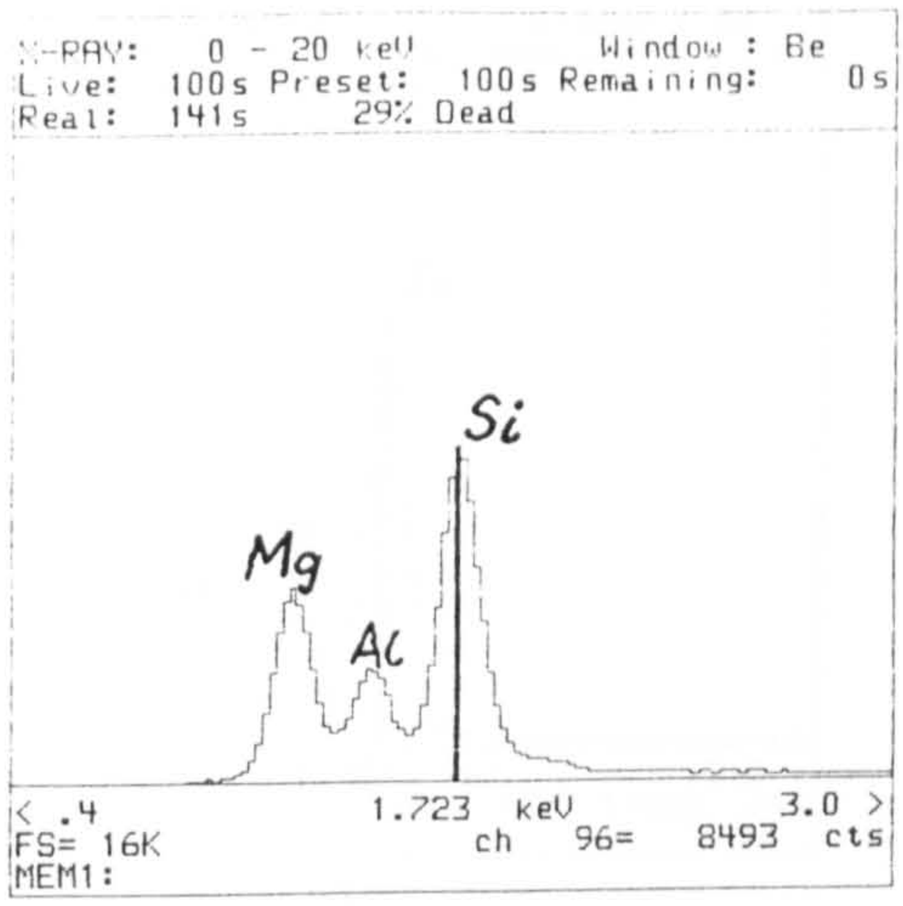

A

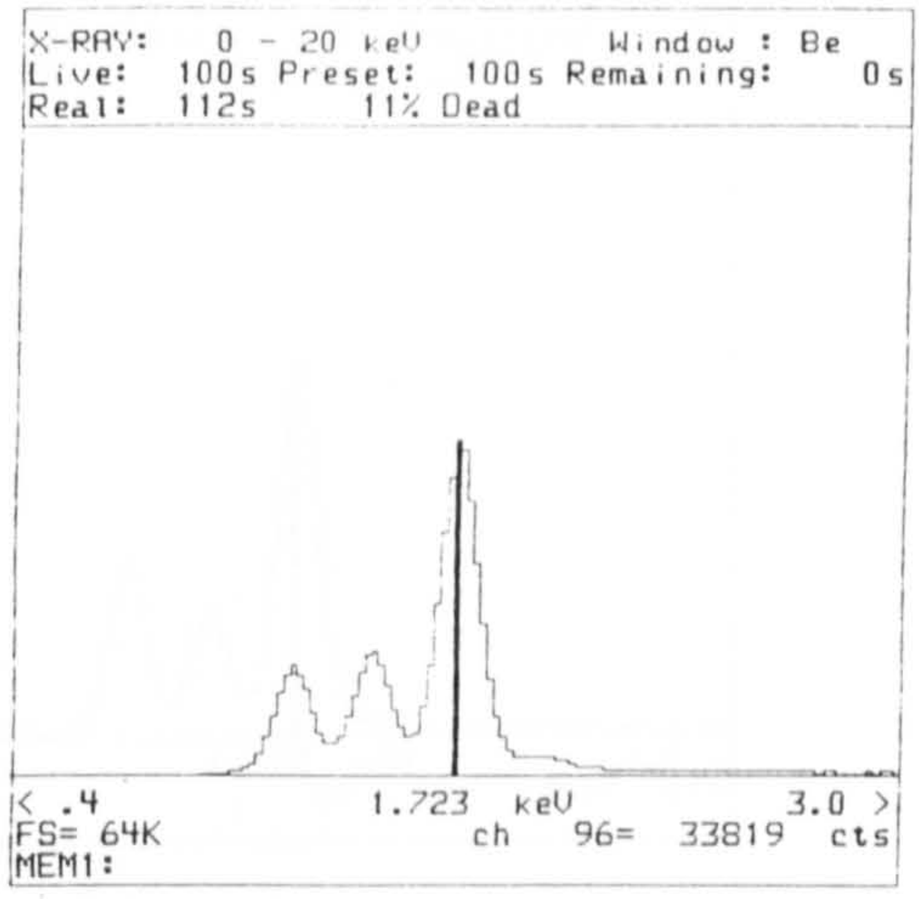

B

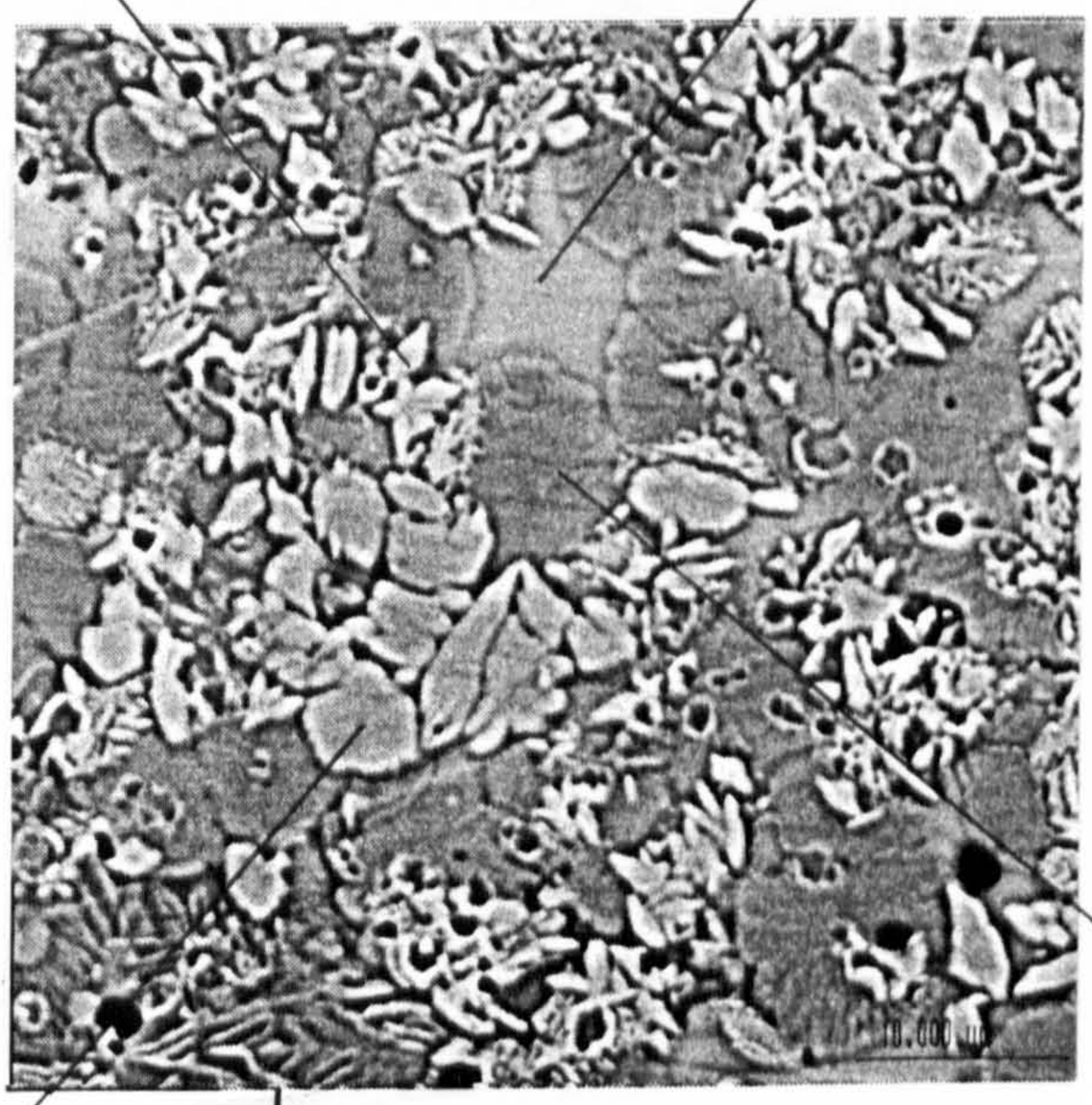

C

D

E

MAS1
45 minutes
at 945°C

10 µm

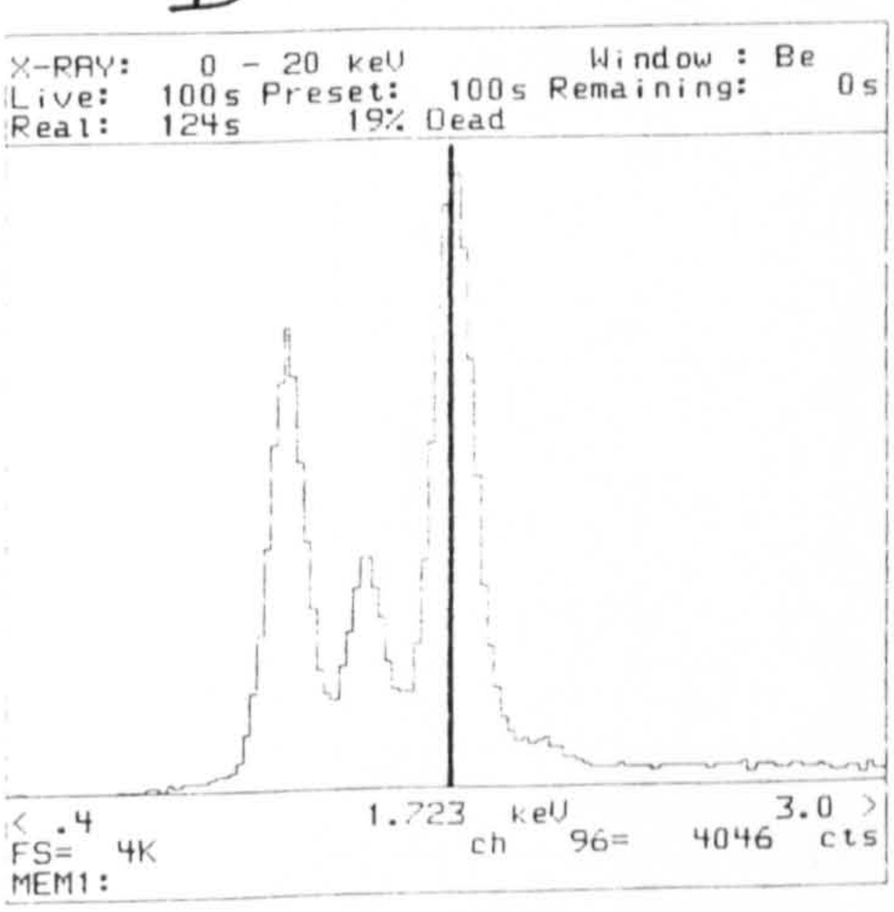

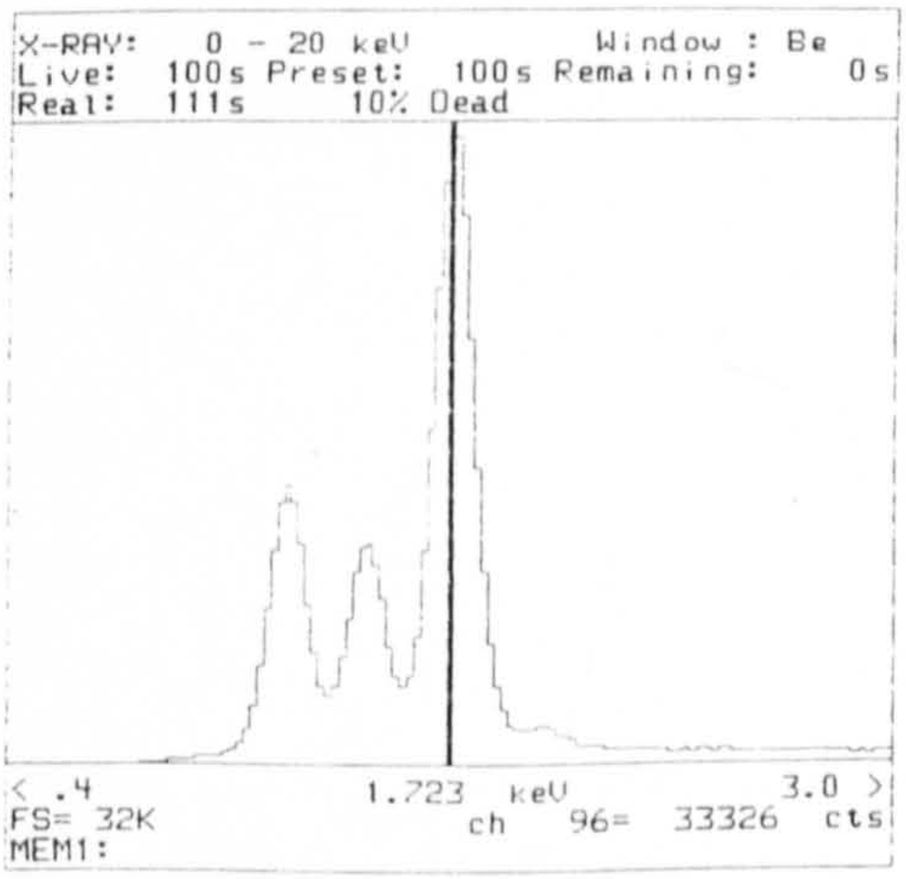

Figure 5.7

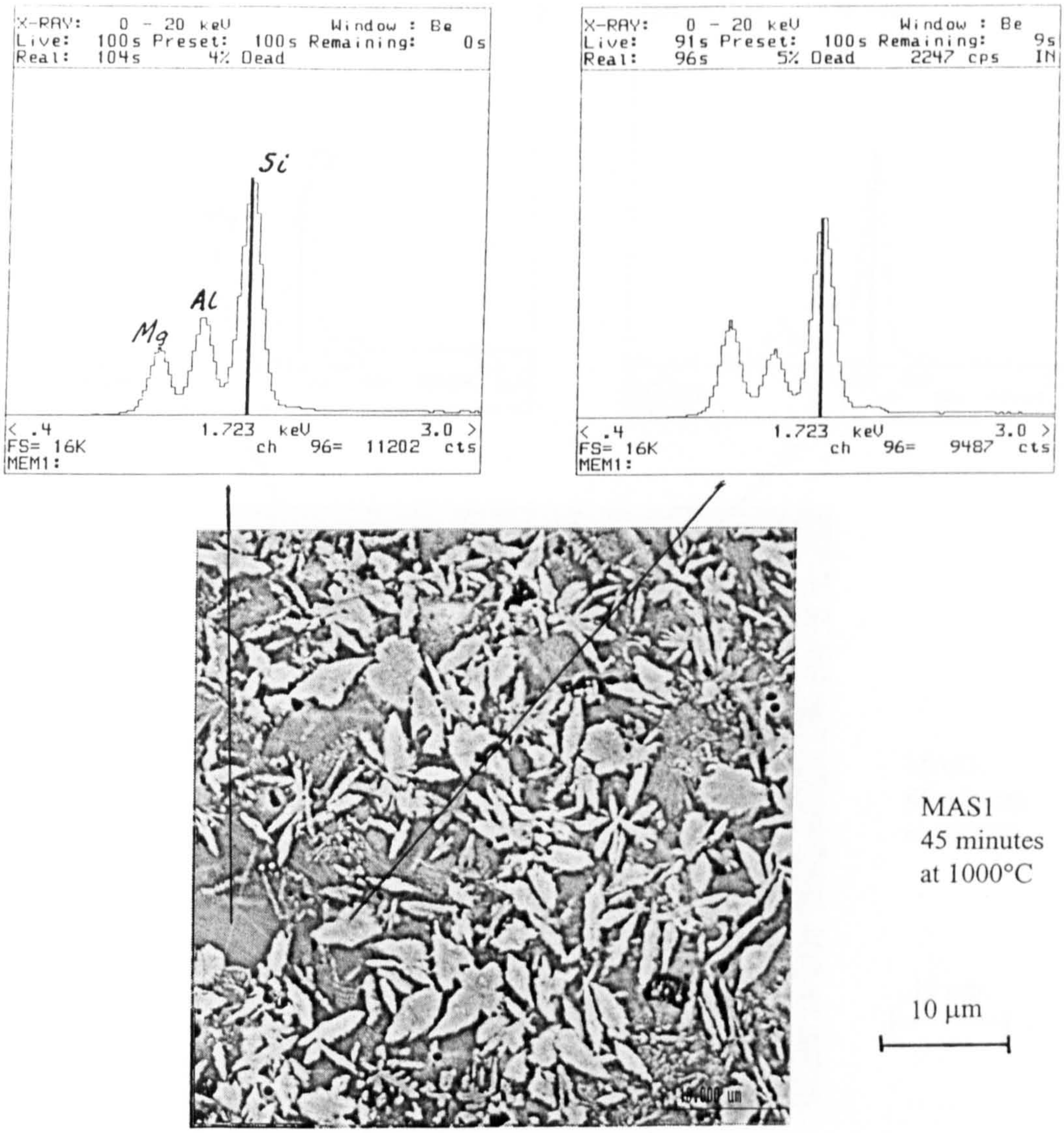
X-RAY: 0 - 20 keV Window : Be
Live: 100s Preset: 100s Remaining: 0s
Real: 104s 4% Dead
Si
Al
Mg
< .4 1.723 keV 3.0 >
FS= 16K ch 96= 11202 cts
MEM1:
X-RAY: 0 - 20 keV Window : Be
Live: 91s Preset: 100s Remaining: 9s
Real: 96s 5% Dead 2247 cps IN
< .4 1.723 keV 3.0 >
FS= 16K ch 96= 9487 cts
MEM1:
MAS1
45 minutes
at 1000°C
10 µm

Figure 5.8

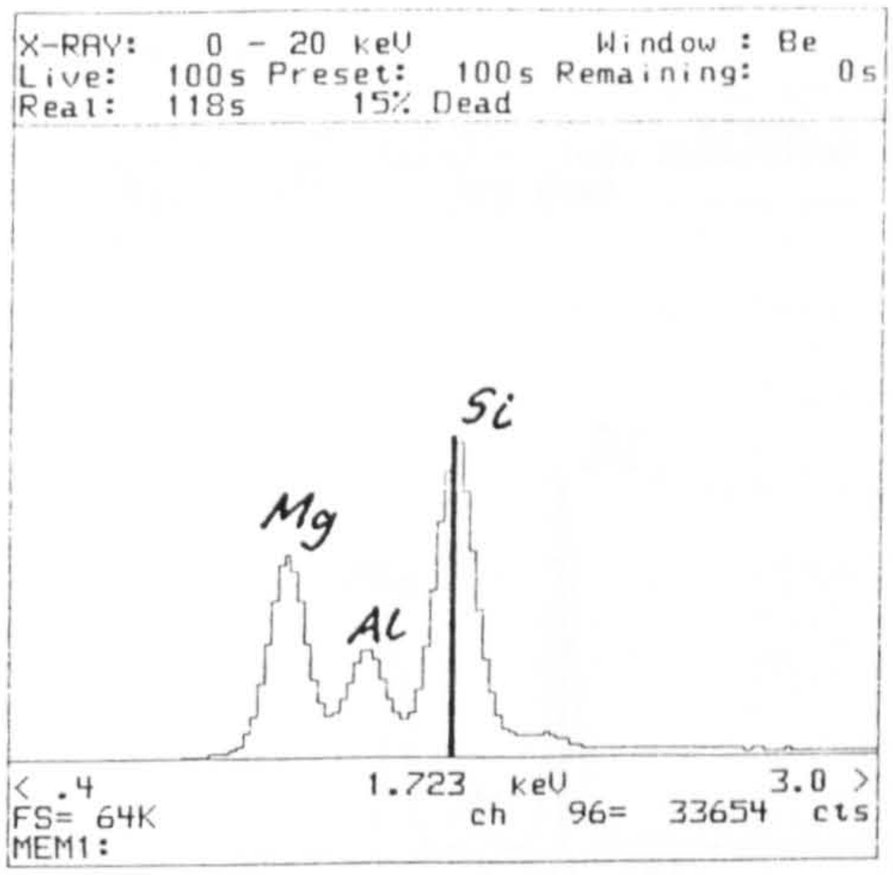

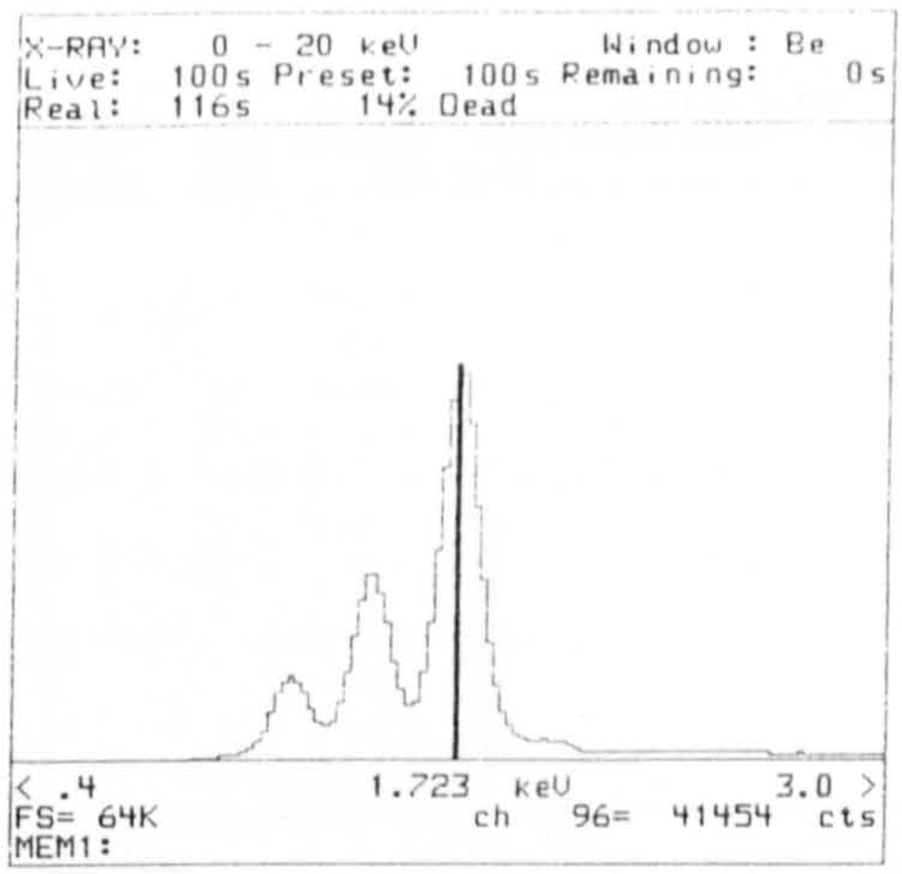

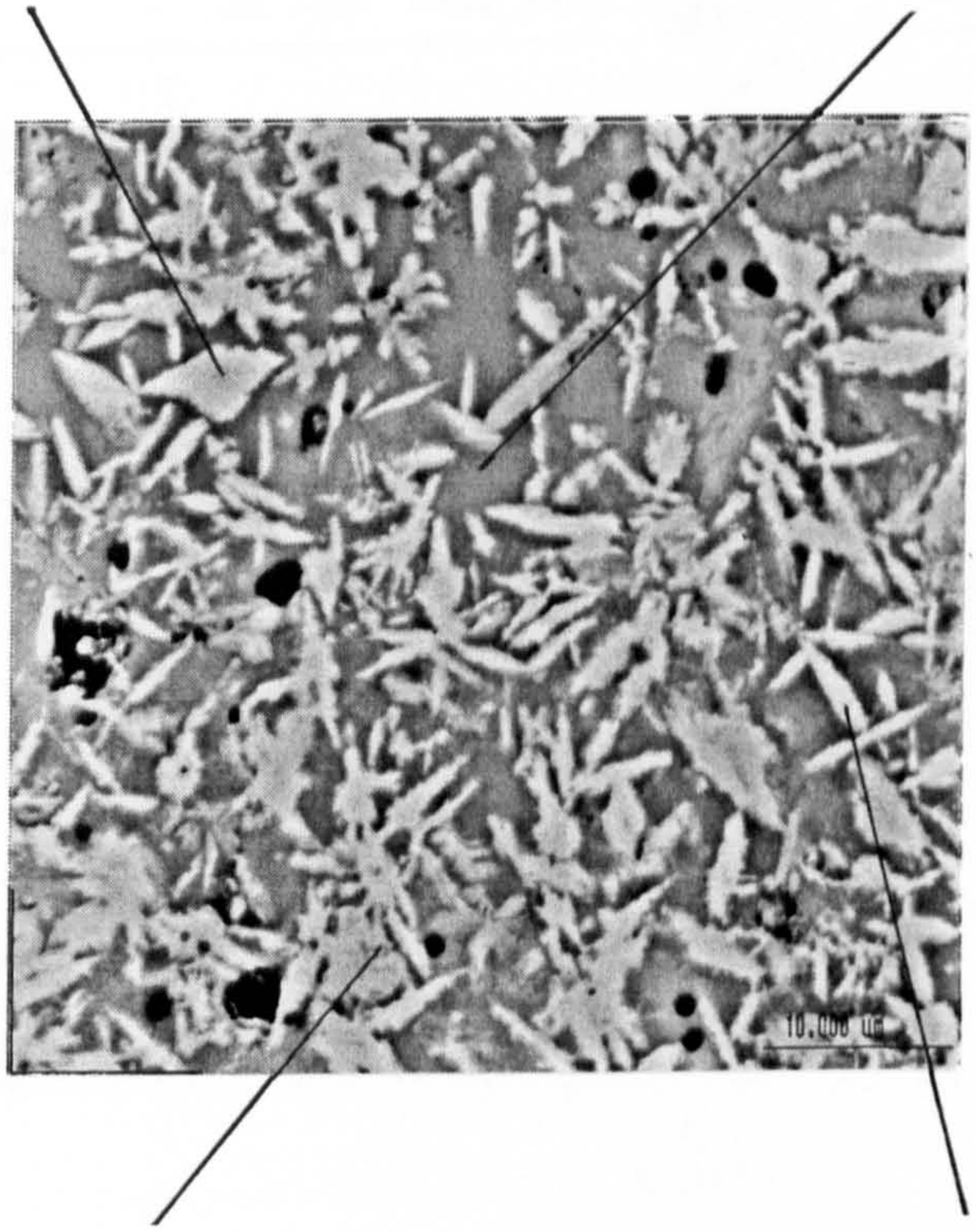

MAS1
45 minutes
at 1054°C

10 μm

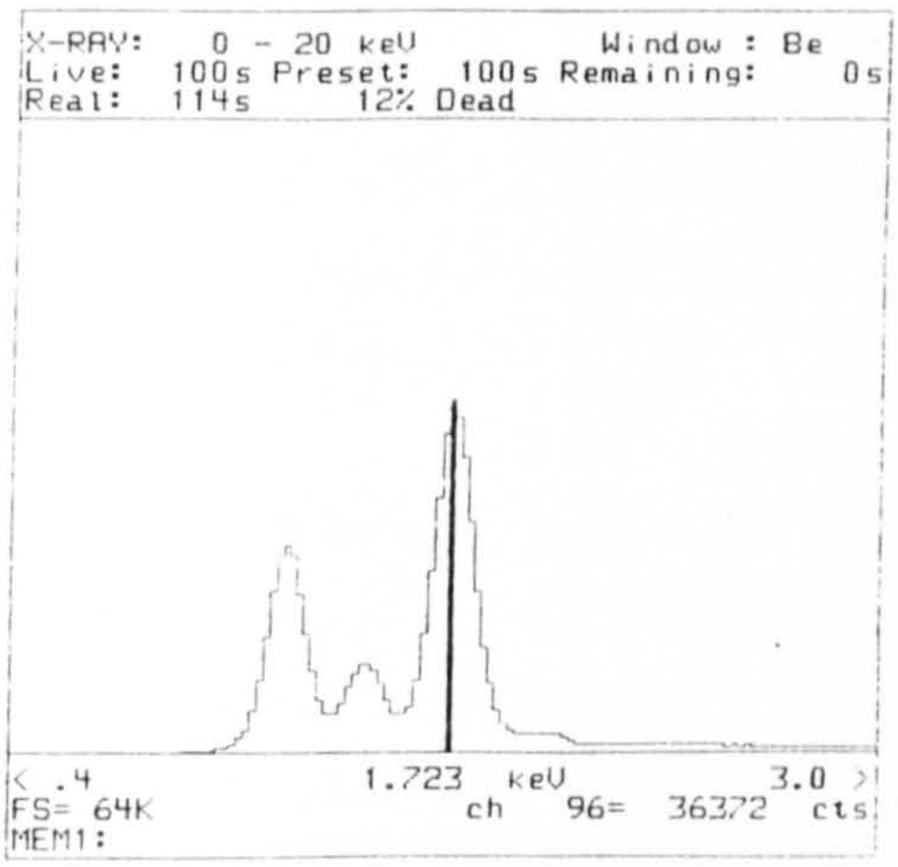

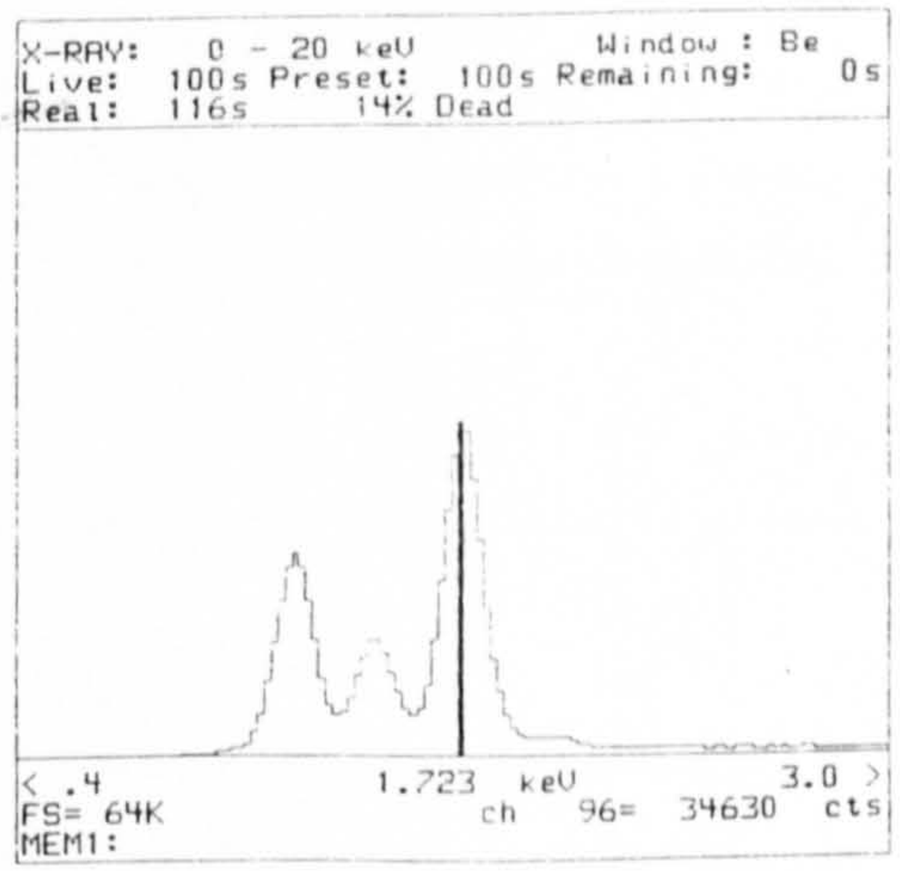

Figure 5.9

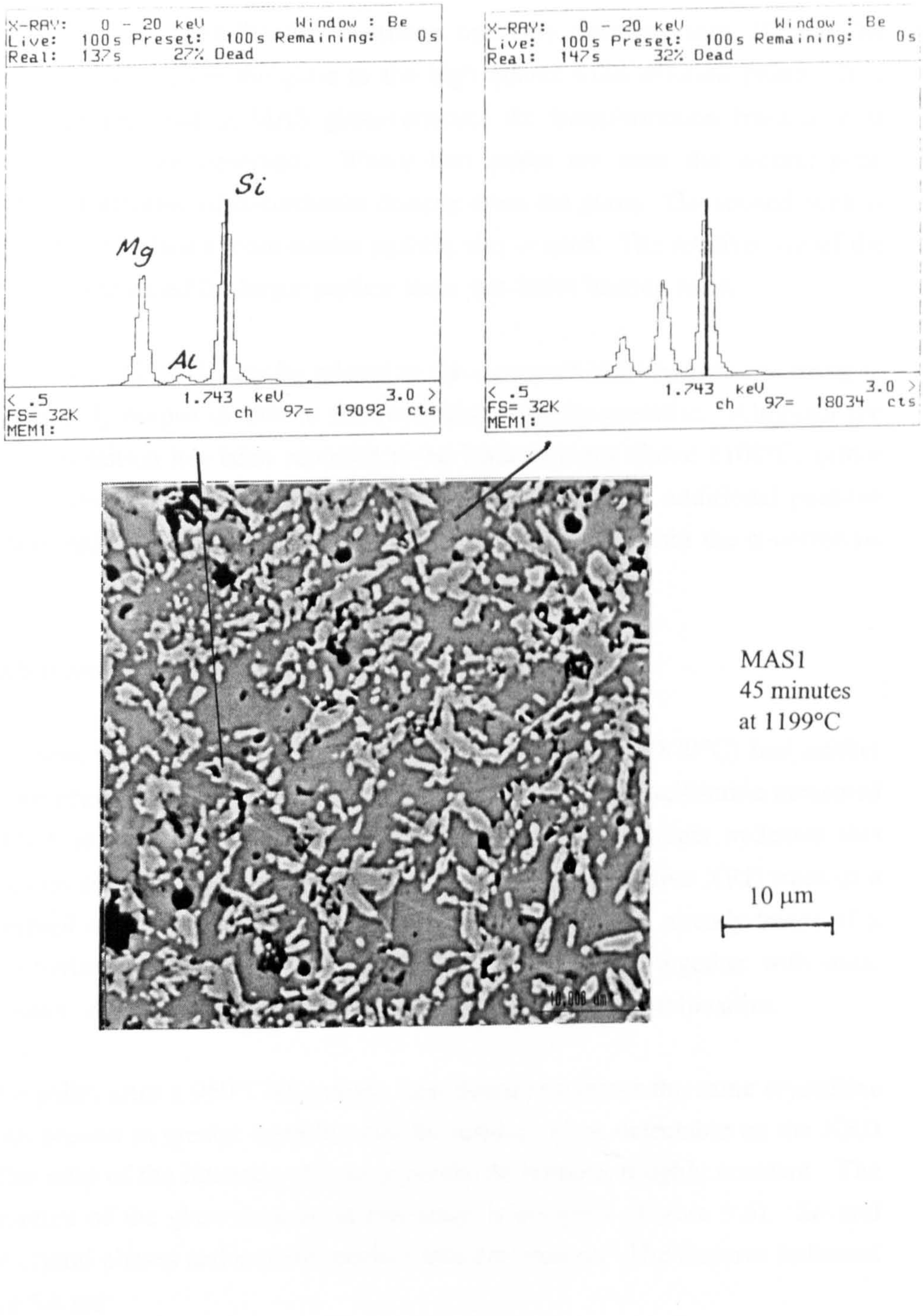
X-RAY: 0 - 20 keV Window : Be
Live: 100s Preset: 100s Remaining: 0s
Real: 137s 27% Dead
Si
Mg
Al
< .5
FS= 32K
MEM1:
1.743 keV
ch 97= 19092 cts
3.0 >
X-RAY: 0 - 20 keV Window : Be
Live: 100s Preset: 100s Remaining: 0s
Real: 147s 32% Dead
< .5
FS= 32K
MEM1:
1.743 keV
ch 97= 18034 cts
3.0 >
MAS1
45 minutes
at 1199°C
10 µm

As a result, the only crystallisation exotherm normally detected using DTA is the initial transformation from the glass to the high quartz solid solution phase. It is similarly suggested, that in MAS glass-ceramics the transformation from μ to α cordierite is not often observed. Where two peaks are seen the second peak represents the formation of α-cordierite directly from the glass. The second peak is normally observed when a more coarse particle size is used. The relative size of the second peak is increased for larger particle sizes and faster heating rates.

The third peak at 1210°C, may be related to the compositional changes occurring in the enstatite polymorphs or due to the formation of proto-enstatite. Although the ortho-proto transition has been reported to be instantaneous above 1100°C, ortho-enstatite is known to be stabilised by doping with Al [8]. An additional possible minor contribution to the third peak may be Al-Si ordering within the α-cordierite phase.

5.4.3 XRD and SEM of MAS1

A sample heat treated at 850°C, below the onset of sintering (870°C) had neither sintered nor crystallised (Figure 5.4). Although the onset of crystallisation measured by the DTA is at 959°C, evidence from XRD of sintered pellets indicates that crystallisation starts at a much lower temperature. A representative XRD trace of a pellet sintered at 932°C for 45 minutes in shown in Figure 5.4, already traces of μ and α-cordierite, enstatite, forsterite, and petalite can be seen, together with some residual glass. All these phases appear in the initial stages of crystallisation.

XRD of a pellet after a 950°C/45 minute heat treatment shows the same crystalline phases, all present in greater quantity with no residual glass detectable on the XRD trace. The ratio of the intensity of μ to α cordierite remains roughly constant. The microstructure of the glass-ceramic at this stage is complex (Figure 5.6). Several different crystal phases and growth mechanisms are present. The features indicated on Figure 5.6 are:

- A - this may be enstatite, forsterite or petalite, the morphology is similar to that of petalite reported in the literature.
- B - pocket of residual glass.
- C - spherulitic crystallisation.
- D - the light phase may be enstatite or forsterite.
- E - dendritic crystallisation.

On heat treatment at 1000°C for 45 minutes, the XRD trace shows partial conversion from μ to α-cordierite (Figure 5.5). Forsterite and petalite are still present but in smaller quantities. No residual glass is observed in Figure 5.7 where the dark phase is due to α and μ-cordierite, and the light phases are enstatite and forsterite with small quantities of petalite still present.

Heat treatment at 1050°C for 45 minutes results in near total conversion from μ to α-cordierite, with the amount of forsterite and petalite also significantly reduced (Figure 5.5). The micrograph at this temperature (Figure 5.8) displays distinct differences from Figure 5.7. The proportion of darker (cordierite) phase has increased and the light phase has reduced in volume with many crystals taking on an acicular morphology. The amount of Al present at 1050°C in the light phase is reduced compared to that at 1000°C. In both cases it is not clear whether this indicates considerable solid solution of Al in the enstatite phase, or whether the microstructure is organised on a much finer scale than that observed in the micrographs.

At 1100°C, no forsterite or petalite is detected by XRD (Figure 5.5), and proto-enstatite starts to appear. The formation of proto-enstatite in glass-ceramics of similar composition was reported by Bridge [1] after heat treatment at temperatures in excess of 1050°C.

At 1199°C, the morphology of the light enstatite phase has changed considerably with the enstatite crystals becoming more rounded and having lower aspect ratios (Figure 5.9). Spot analysis reveals that the enstatite phase now has very low levels of Al^{3+} substitution, if any. The remaining Al detected may be due to some cordierite within the interaction volume contributing to the EDX signal.

The presence of proto-enstatite in the glass-ceramic at higher temperatures is demonstrated by Figure 5.10, which is of some MAS1 glass-ceramic attached to silicon nitride after a 1250°C/45 minutes heat treatment. The only phases present are α-cordierite and proto-enstatite. The XRD trace corresponding to Figure 5.9 was intermediate between the 1100°C trace in Figure 5.5 and Figure 5.10.

MAS1 may be heat treated at 950°C to produce a μ-cordierite/enstatite glass ceramic with a TCE of 7.1 MK^{-1} (50-800°C) [2] or at 1050-1100°C to produce an α-cordierite/enstatite glass ceramic with a TCE of 5.7 MK^{-1} (50-800°C).

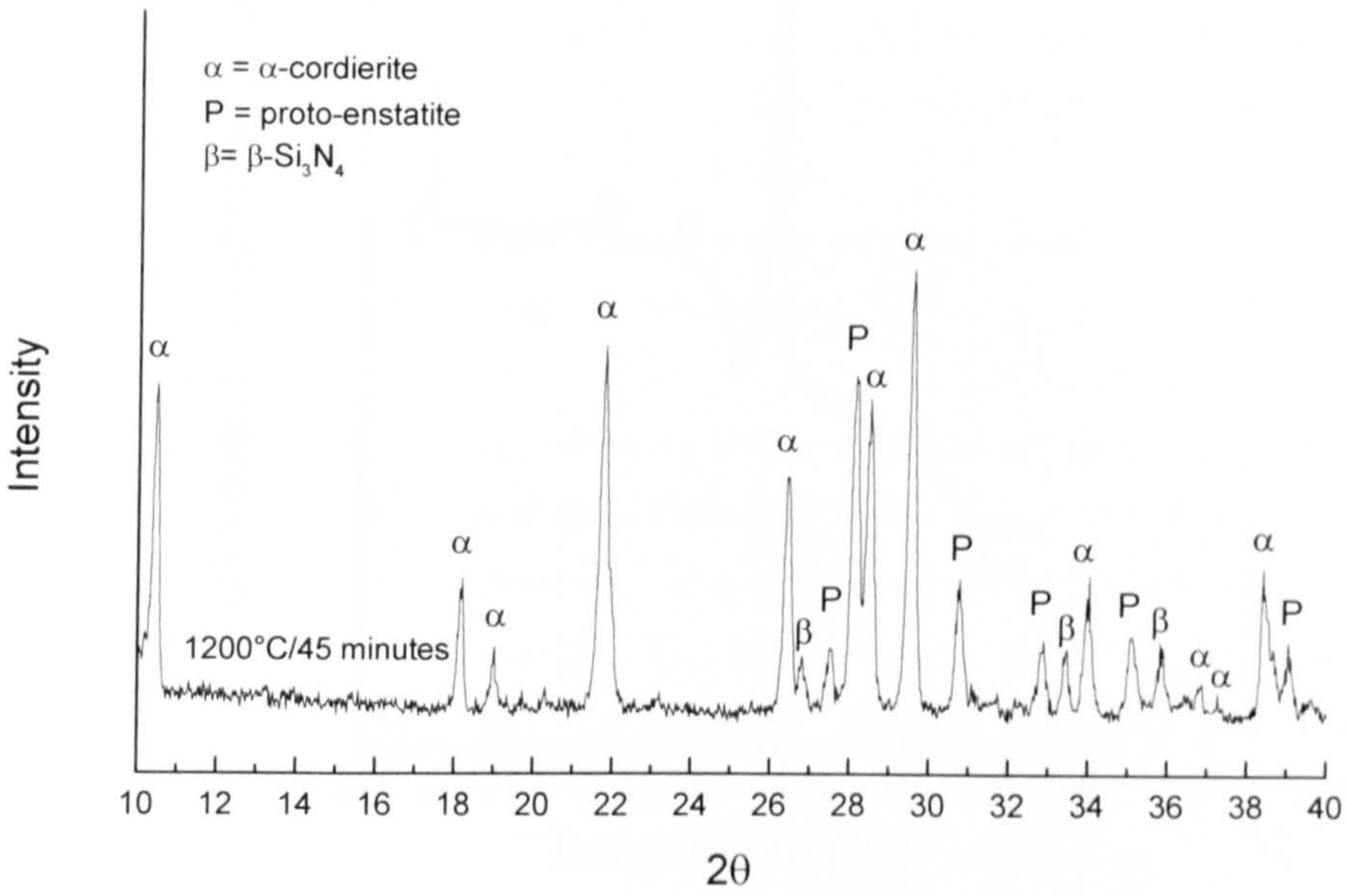

Figure 5.10: XRD of MAS1 attached to silicon nitride after 1250°C, heat treatment.

5.4.4 Phase development - MAS2

MAS2 is a low thermal expansion glass-ceramic, a DTA trace at 5°C min^{-1} is shown in Figure 5.11. Tg for this composition occurs at 778°C with the onset of sintering at 855°C. The onset of crystallisation is at 925°C with the crystallisation peak at 971° C. The main peak is due to α-cordierite formation directly from the glass, the "lower temperature shoulder" is due to crystallisation of μ-directly from the glass.

The phase development in this composition is much more straightforward compared with MAS1, with total conversion to α-cordierite at 950°C with small traces of enstatite present (Figure 5.12). A 950°C heat treatment produced a glass-ceramic with a TCE of 2.1 MK^{-1} (50-850°C) [2].

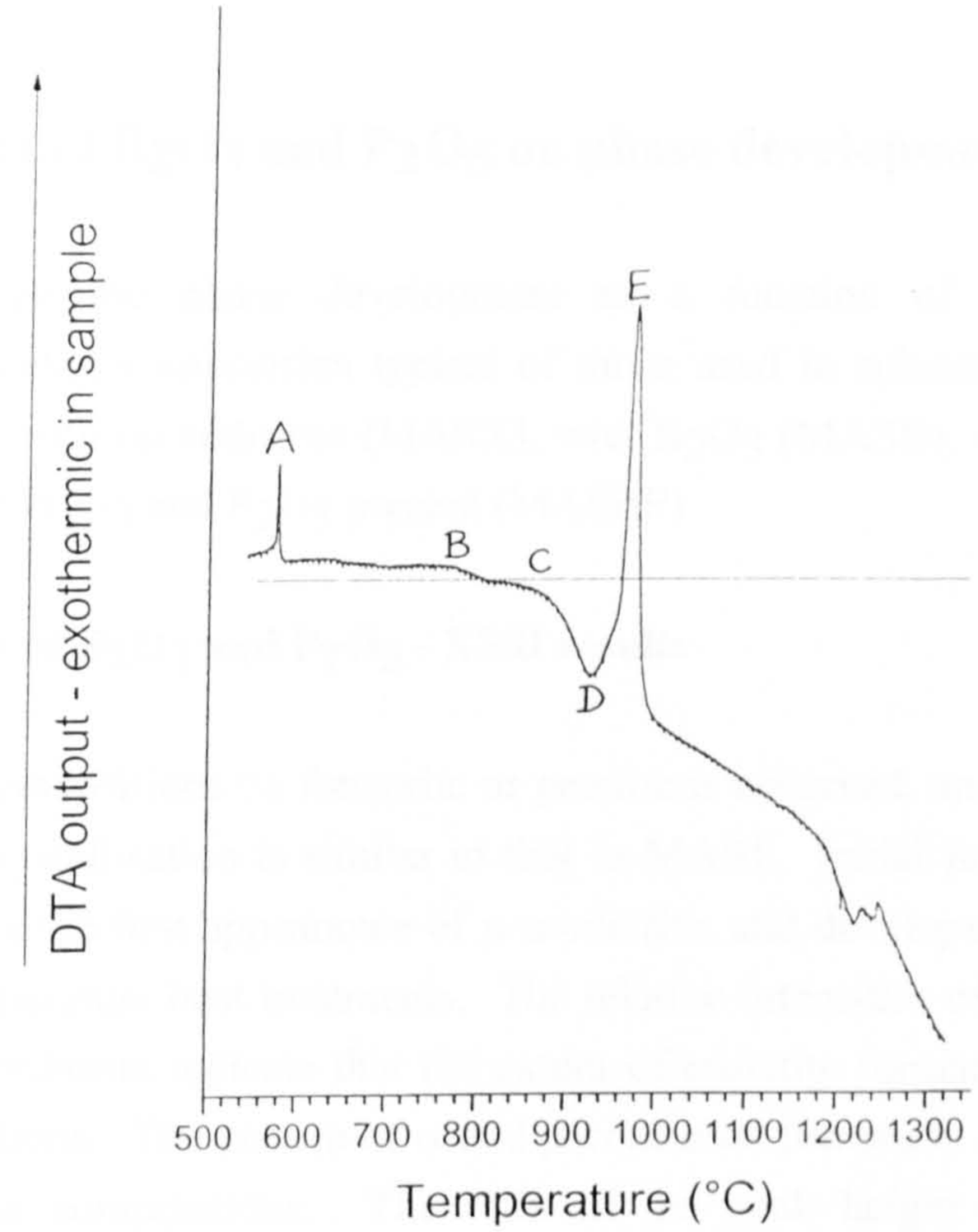

Figure 5.11: DTA trace of MAS2 at 5°C min^{-1}. The marked features are: A - α-β quartz reference peak (576°C), B - Tg (778°C), C - onset of sintering (855°C), D - onset of crystallisation (925°C), E - crystallisation of α-cordierite (971°C) with lower temperature shoulder due to crystallisation of μ-cordierite.

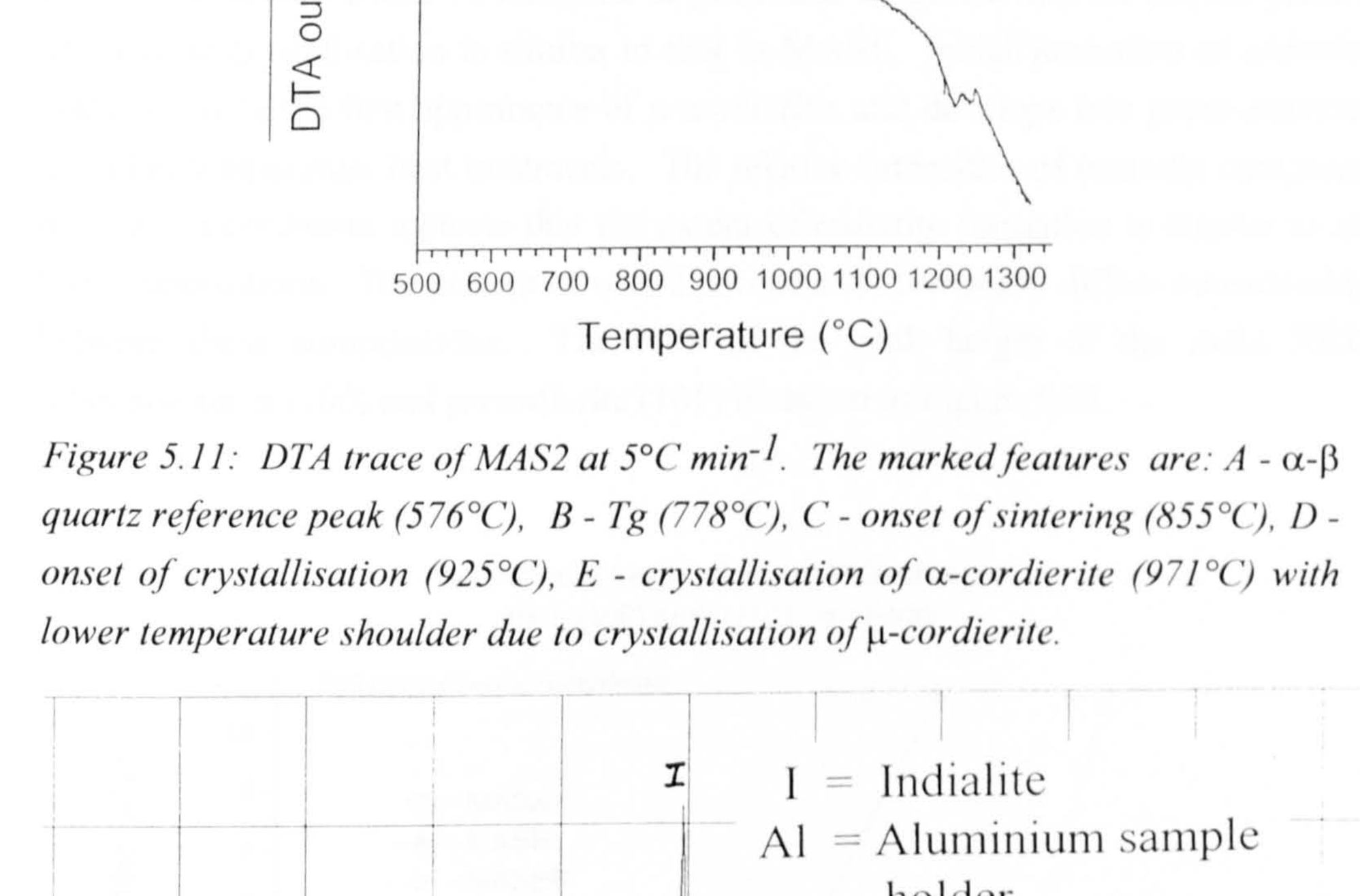

Figure 5.12: XRD of MAS2 after a 950°C heat treatment.

5.5 Effect of B_2O_3 and P_2O_5 on phase development

In this section the phase development as a function of temperature, for a cordierite/enstatite composition typical of those used in substrate applications, has been studied: with no additives (MASX), with B_2O_3 (MASB), with P_2O_5 (MASP), and with both B_2O_3 and P_2O_5 present (MASBP)

5.5.1 Effect of B_2O_3 and P_2O_5 - XRD results

In all these compositions no forsterite or petalite is observed, and the overall pattern of enstatite crystallisation is similar to that in MAS1. Initial formation of enstatite coincides with the first appearance of μ-cordierite, and develops into proto-enstatite at higher temperature heat treatments. The relative intensities of enstatite compared to μ and α-cordierite indicate that the extent of enstatite formation is similar in all four compositions. The pattern of α and μ-cordierite formation differs considerably between these compositions. The ratio of the peak height of the main XRD reflection for α (100) and μ-cordierite (101) is shown in Figure 5.13.

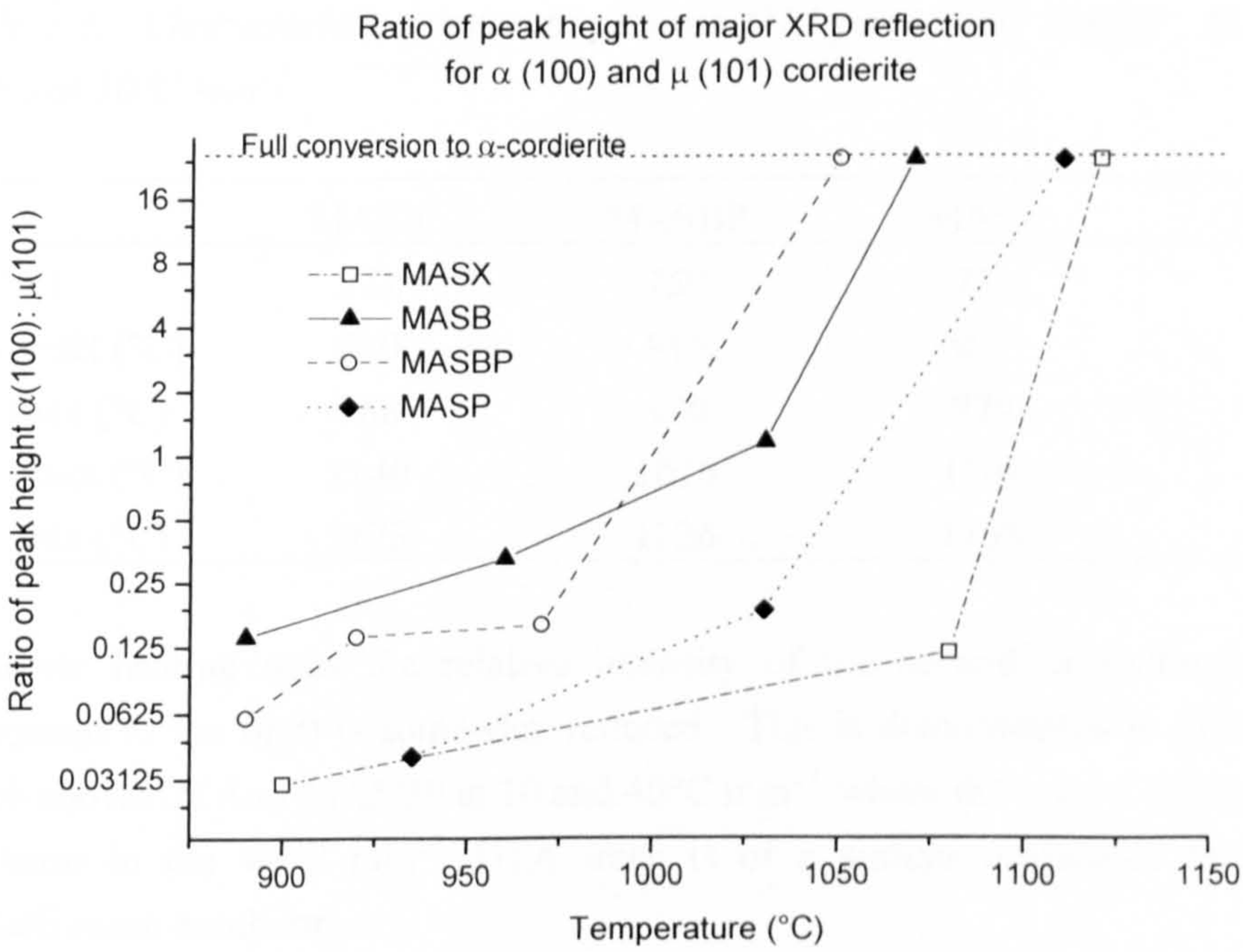

Figure 5.13: ratio of the peak height of the main XRD reflection for α (100) and μ -cordierite (101). The temperatures at which full conversion to α-cordierite occurs may be lower than those indicated.

In MASBP the pattern of μ-α phase development is very similar to that in MAS1, with full conversion to α-cordierite occurring by 1050°C. In contrast, in MASX, reduced α-cordierite formation is observed at lower temperatures, and even at 1080°C, the amount of α-cordierite formed is proportionately less than that in MASBP at 890°C.

The behaviour of MASB with respect to μ and α-cordierite formation is very similar to that in MASBP, with slightly higher levels of α-cordierite formation at low temperatures. The behaviour of MASP with respect to μ and α-cordierite formation, is similar to that in MASX, although formation of α-cordierite occurs at lower temperatures in MASP.

5.5.2 Effect of B_2O_3 and P_2O_5 - DTA results

DTA traces for MASX, MASBP, MASP and MASB at 10°C min^{-1} are shown in Figures 5.14-5.17. The onset of crystallisation, the peak crystallisation temperature, and Tg for these compositions are shown in Table 5.3.

Table 5.3: Characteristic temperatures from DTA for MASX, MASBP, MASP and MASB at 10°C min^{-1}

	MASX	MASBP	MASP	MASB
Tg (°C)	772	759	779	760
T1 - onset (°C)	890	916	927	880
T1 - max (°C)	968	976	979	960
T2 - onset (°C)	1140	1076	1107	1080
T2 - max (°C)	1173	1126	1155	1130

At lower heating rates the relative intensity of the second crystallisation peak (compared to the first) is somewhat reduced. This is demonstrated in Figure 5.15, which shows DTA of MASBP at 10 and 40°C min^{-1} where the second crystallisation exotherm in the 40°C min^{-1} DTA trace is of a similar magnitude to the first crystallisation exotherm.

The second peak sometimes displayed structure indicating that several processes may contribute to its formation. However, the dominant process is believed to be formation of α-cordierite directly from the glass.

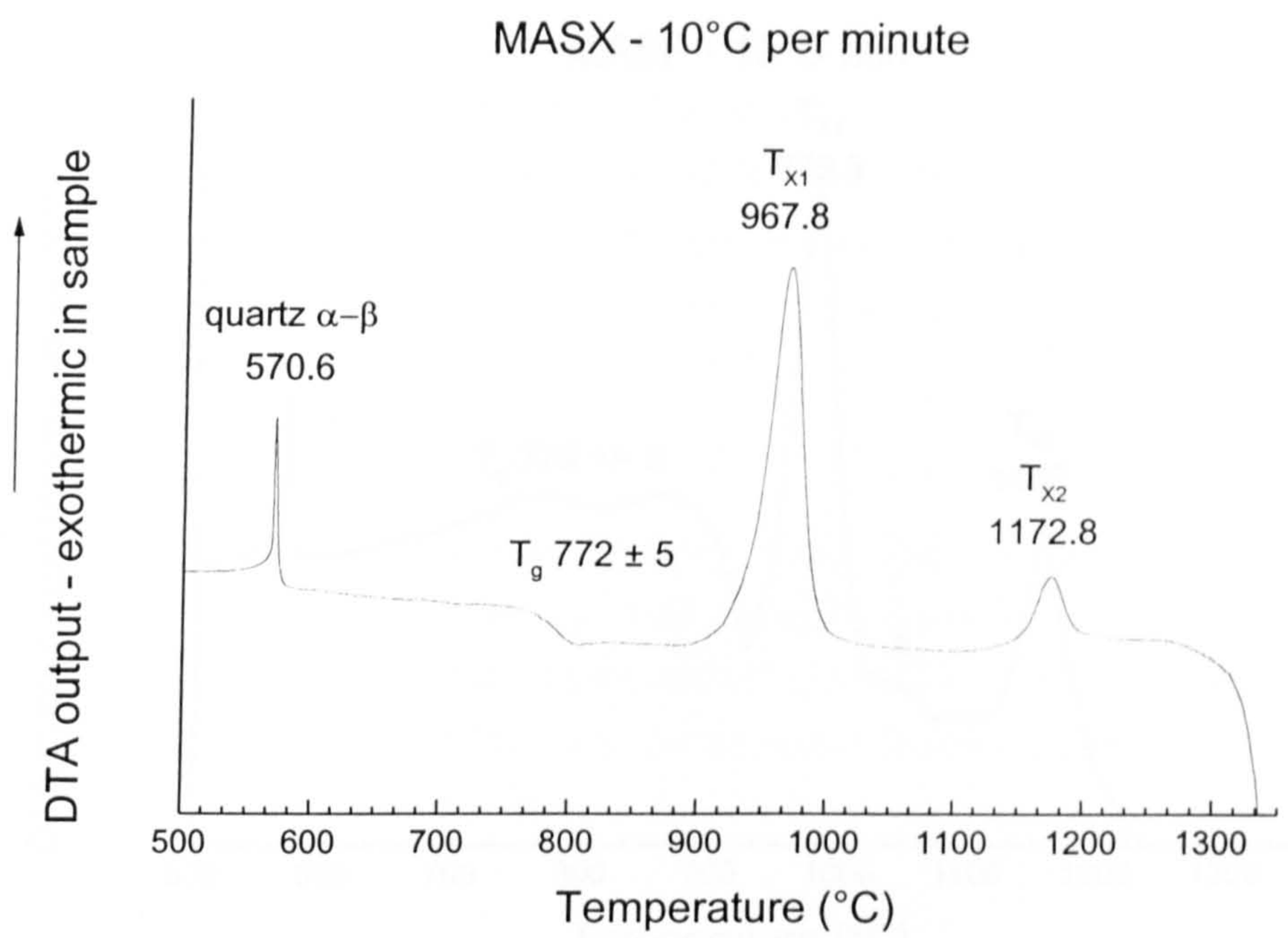

Figure 5.14: DTA trace for MASX at 10°C min^{-1}

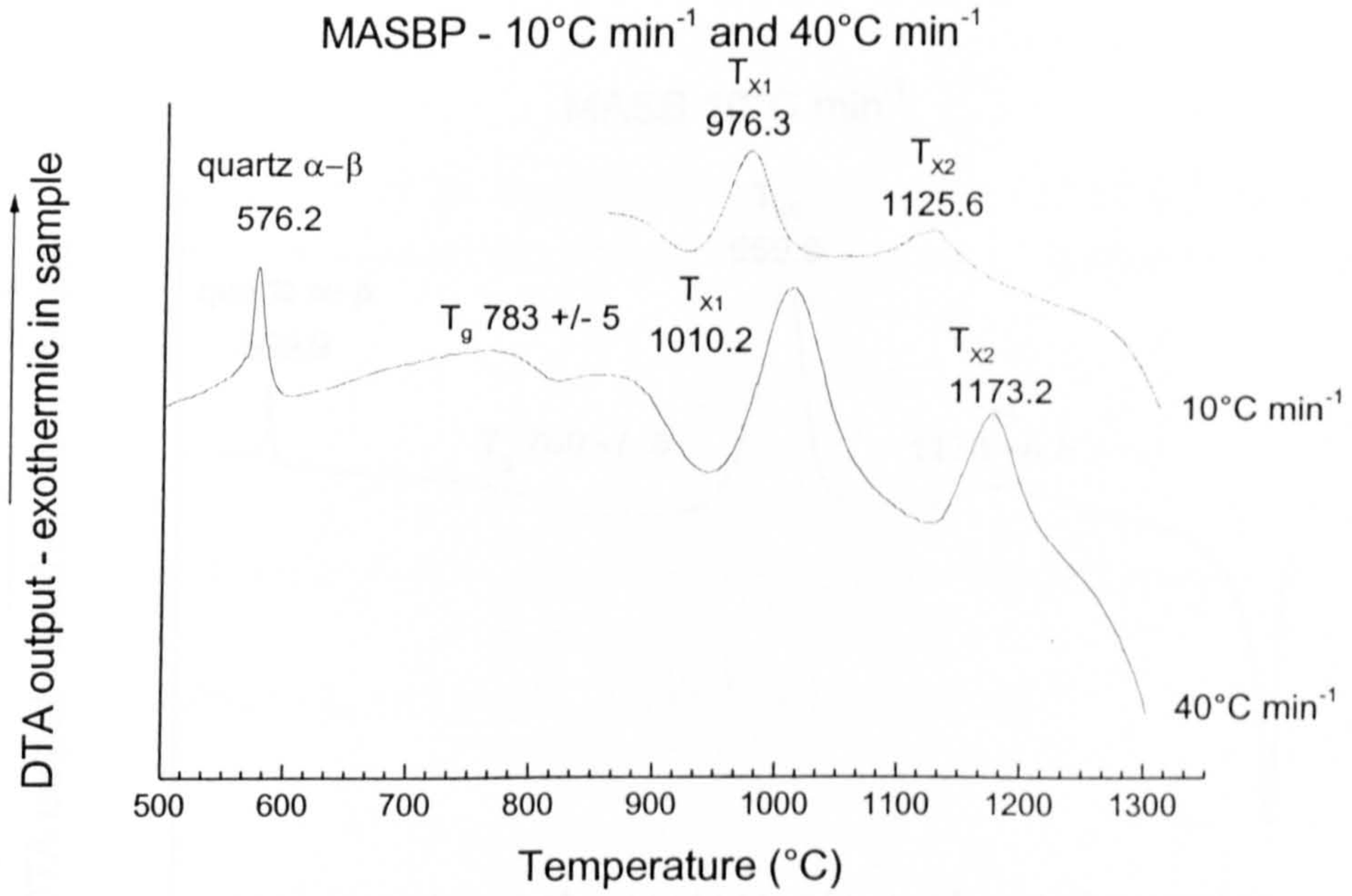

Figure 5.15: DTA trace for MASBP at 10 and 40°C min^{-1}

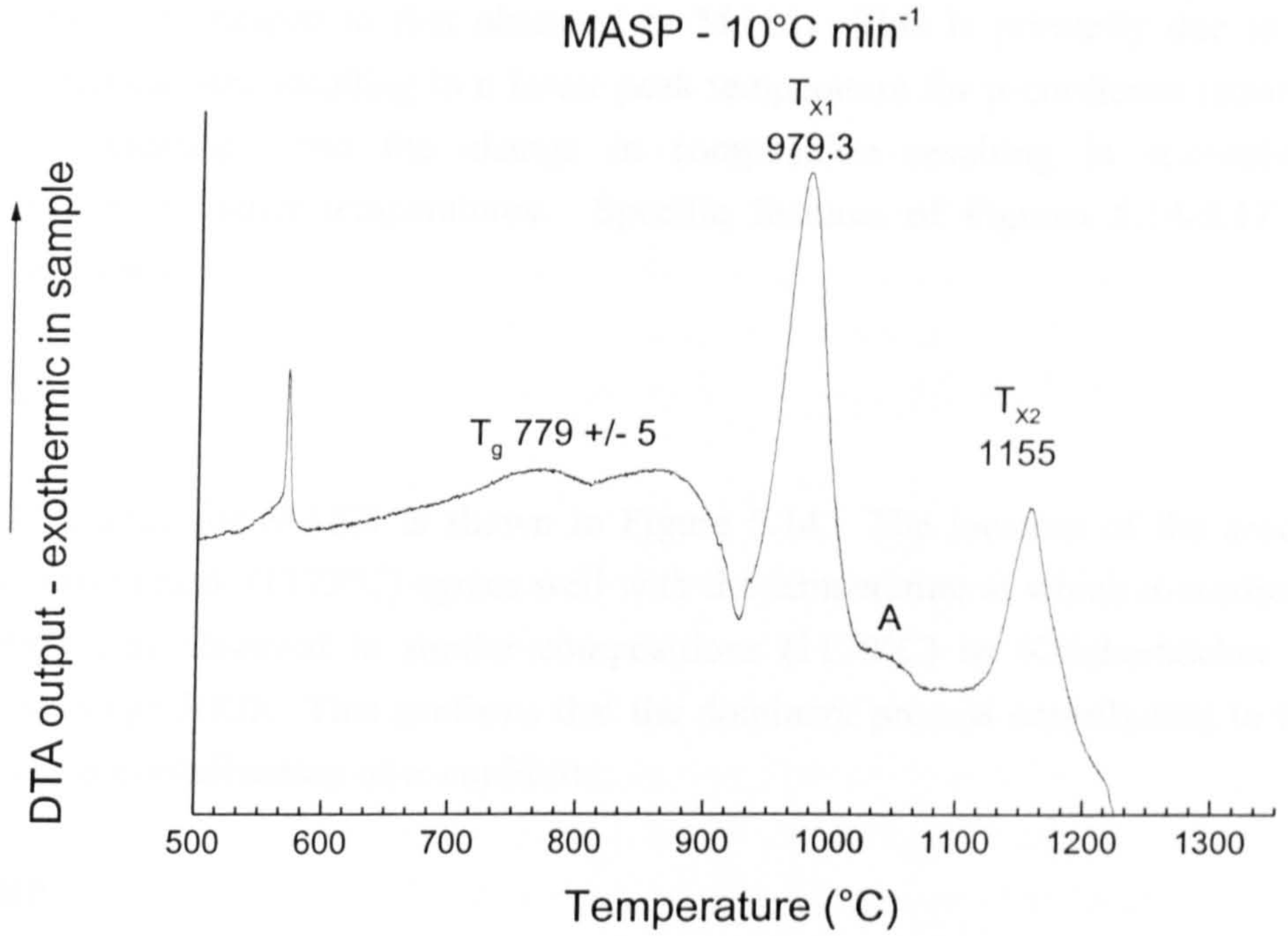

Figure 5.16: DTA trace for MASP at 10°C min^{-1}

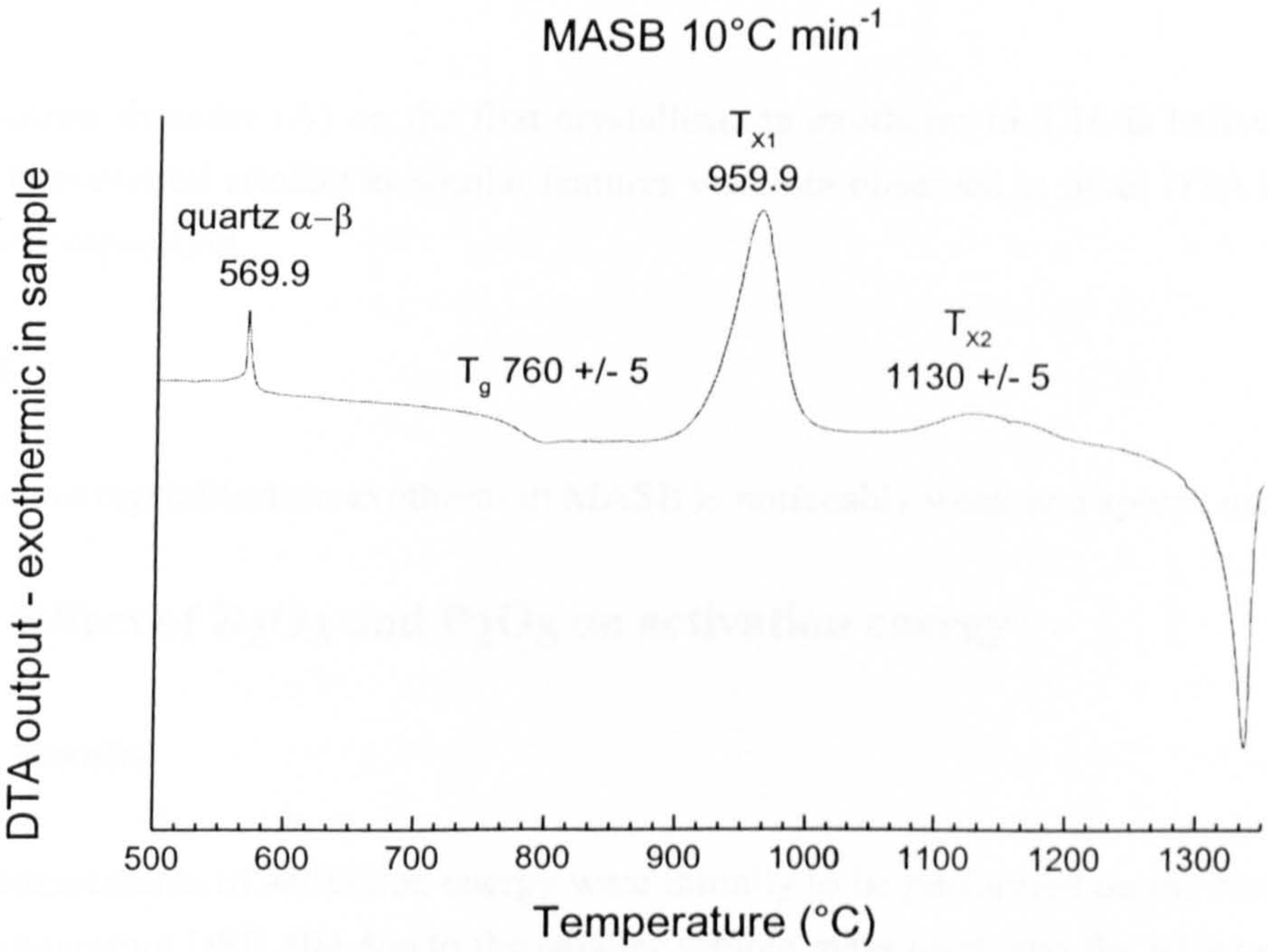

Figure 5.17: DTA trace for MASB at 10°C min^{-1}

The separation of the two crystallisation exotherms is much greater in these compositions compared to that observed in MAS1. This is primarily due to the smaller particle size resulting in a lower peak temperature for μ-cordierite (strongly surface nucleating), and the change in composition resulting in α-cordierite formation at a higher temperatures. Specific features of Figures 5.14-5.17 are discussed below.

MASX

The DTA trace for MASX is shown in Figure 5.14. The location of the second crystallisation peak (1173°C) agrees well with the temperature at which α-cordierite formation was observed in similar compositions (1170°C) by Knickerbocker [9] using hot-stage XRD. This confirms that the dominant process contributing to this exotherm is crystallisation of α-cordierite.

MASBP

As for MAS1, a minor feature (at~730°C) was sometimes observed in MASBP prior to the main Tg at 780°C. This is believed to be indicative of phase separation.

MASP

The trailing shoulder (A) on the first crystallisation exotherm in 5.16 is believed to be an instrumental artefact as similar features were not observed in other DTA traces for this composition.

MASB

The second crystallisation exotherm in MASB is noticeably weak and spread out.

5.6 Effect of B_2O_3 and P_2O_5 on activation energy

5.6.1 Results

The measurements of activation energy were initially to be performed on the Netzsch high temperature DSC 404 due to the smaller sample mass used, and the wider range of heating rates available. However, due to mechanical breakdown of the Netzsch, the work was completed using the Stanton Redcroft DTA 673-4.

The location of the quartz α-β reference transformation for the Netzsch DSC 404 samples agreed well with book values. However, the temperatures recorded by the Stanton Redcroft DTA 1500 were significantly different from reference values. As a result , the Stanton Redcroft DTA 1500 was calibrated as a function of heating rate using quartz and $SrCO_3$. The calibration of the quartz α-β peak maximum is shown in Figure 5.18. The observed variation of peak temperature with heating rate is assumed to be due to the combined effects of instrumental factors and the activation energy of quartz.

Due to the strongly exothermic nature of the crystallisation exotherms in MAS glass, crystallisation can result in significant heating of the sample and sample holder. This is illustrated in Figure 5.19 for MASB at 15°C min^{-1}. This effect results in uncertainty over the temperature and heating rate seen by the sample at the peak of the crystallisation exotherm, and is more pronounced at higher heating rates. In the current work, the effect on the uncertainty in the heating rate has been estimated (based on deviations in the actual heating rate) on a sliding scale from ± 6% at 40°C min^{-1} to ± 1% at 2°C min^{-1}. No attempt has been made to estimate the error on the peak temperature (T_p) due to this effect. However, it may lead to a slight reduction in the apparent activation energy as the exotherms corresponding to high heating rates are recorded at artificially low temperatures.

For all activation energy calculations the assumption has been made that crystallisation occurs predominantly from the surface, from a fixed number of nucleation sites, and in Equations 4.2 to 4.4, m = n =1. This assumption is justified for the first crystallisation exotherm corresponding to μ-cordierite (which is strongly surface nucleating) but may be less appropriate for the second exotherm corresponding to the formation of α-cordierite.

The apparent activation energies are calculated for the first crystallisation exotherm using the modified Kissinger, Ozawa and Marseglia method, and for the second crystallisation exotherm using the Kissinger method only. In both cases, although a composite event is occurring, the dominant processes are the crystallisation of μ and α-cordierite from the glass.

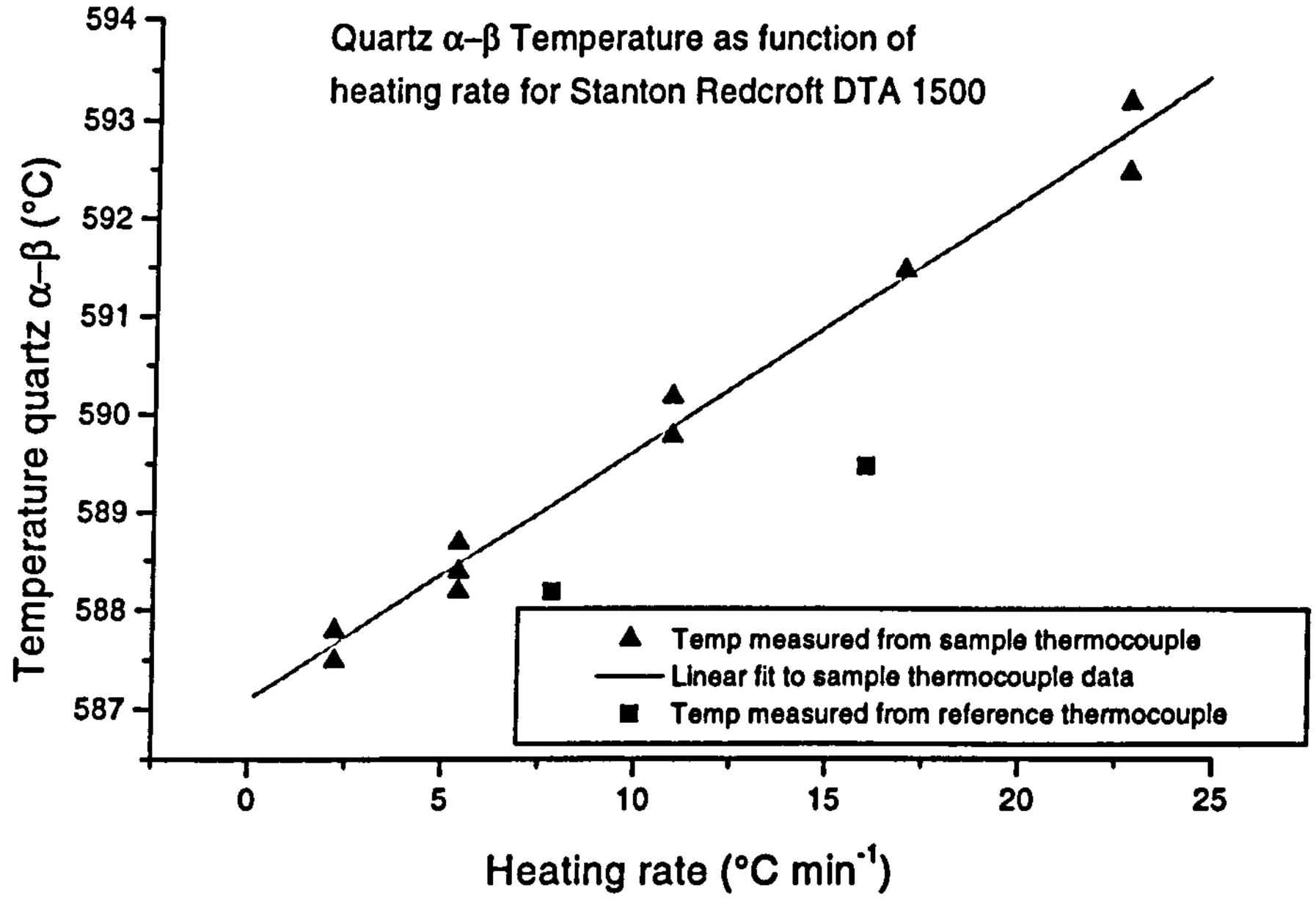

Figure 5.18: Calibration of the Stanton Redcroft DTA 1500 as a function of heating rate using the quartz α-β peak maximum.

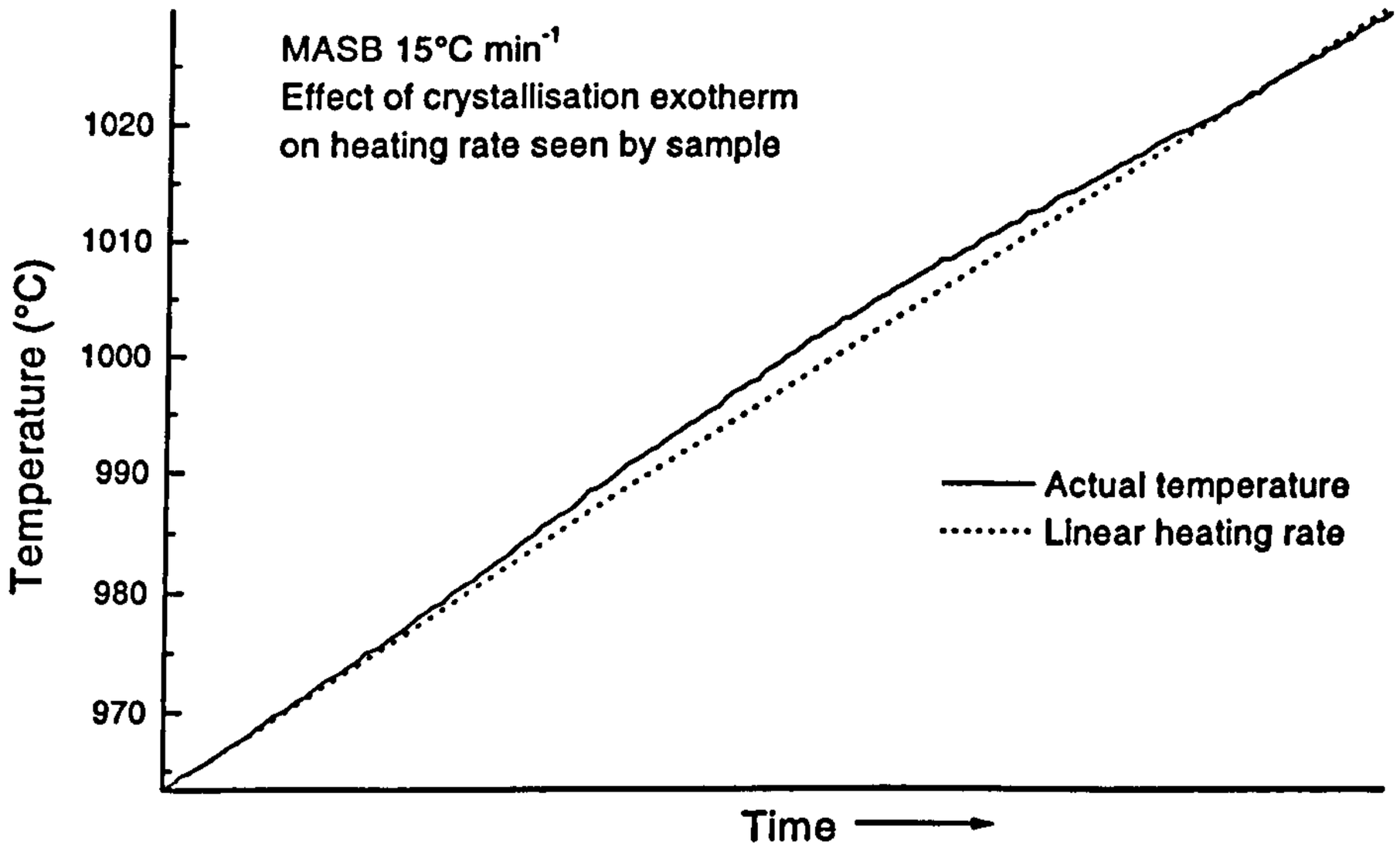

Figure 5.19: Effect of crystallisation exotherm on heating rate seen by the sample (MASB - 10°C min^{-1}).

The peak crystallisation temperatures are reported in Table 5.4 and the resulting activation energies in Table 5.5. The data is presented graphically in Figures 5.20 to 5.27, where the errors displayed for the peak temperature (T_p) are ± 1°C and ± 2°C for the first and second crystallisation exotherms respectively. The errors quoted in the activation energies are those calculated from the linear fit to the data.

Table 5.4: Recorded peak crystallisation temperatures as a function of heating rate for MASX, MASBP, MASP and MASB.

Composition	Heating rate	DTA used	X1 (°C)	X2 (°C)
MASX	2	N	929.3	-
	4.9	N	945.6	1162.2
	9.8	N	967.8	1172.8
	19.5	N	985.6	1187.7
	39.9	N	1011.4	1199.8
MASBP	2.1	ST/R	938.5	1060.1
	5.4	ST/R	958.2	1103.4
	10.7	ST/R	976.3	1125.5
	40.0	ST/R	1010.2	1173.2
MASP	5.3	ST/R	959.2	1138.8
	7.7	ST/R	970.0	1148.9
	10.7	ST/R	979.3	1155.3
	15.7	ST/R	987.7	1161.2
	22.4	ST/R	1001.1	1176.6
MASB	2.1	ST/R	926.7	1080.4
	5.4	ST/R	950.4	1106.6
	9.84	N	959.9	1130 ± 5
	16.1	ST/R	983.9	1141.6
	22.4	ST/R	993.4	1150.1

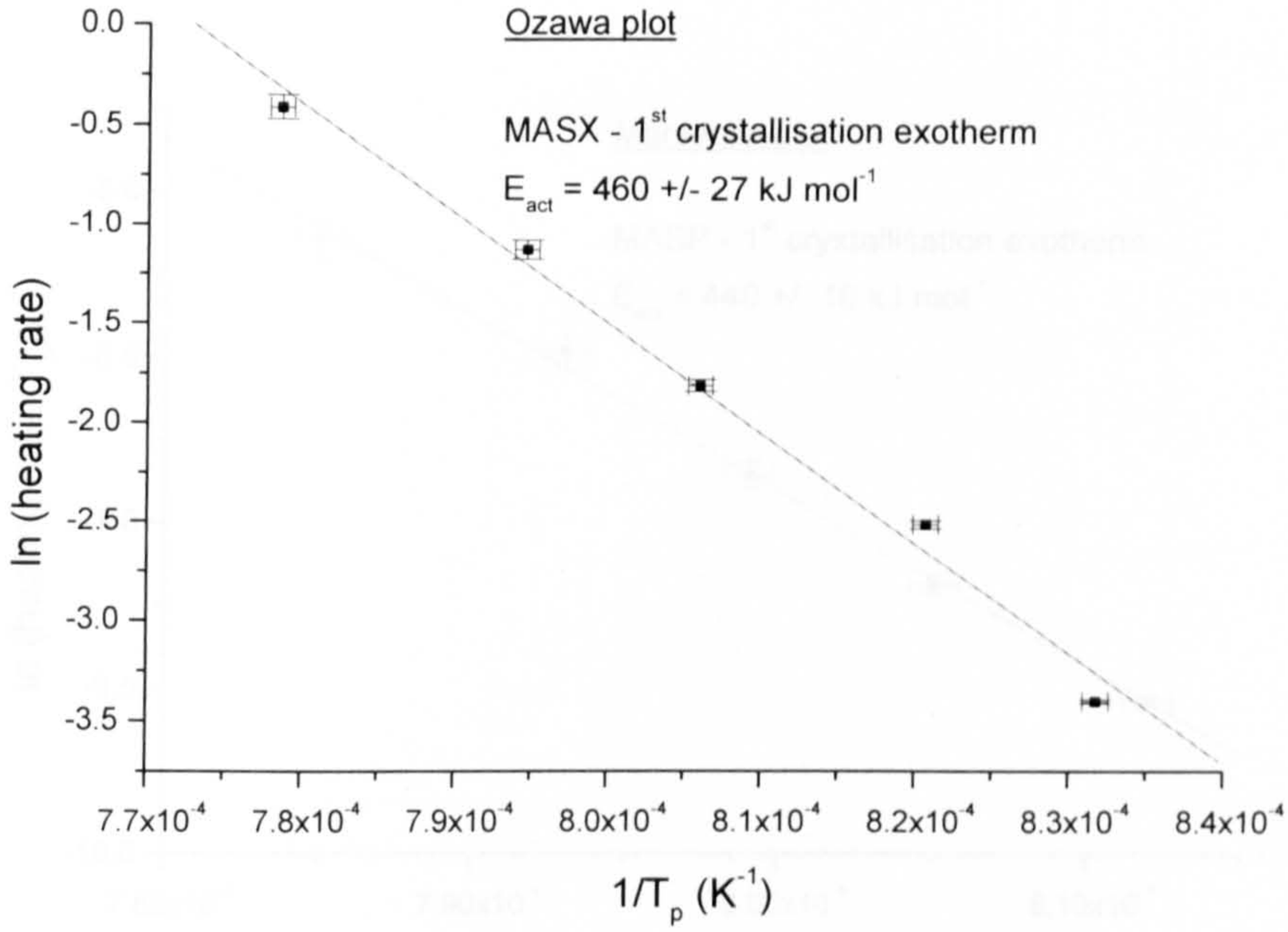

Figure 5.20: Ozawa plot for MASX - 1st crystallisation exotherm.

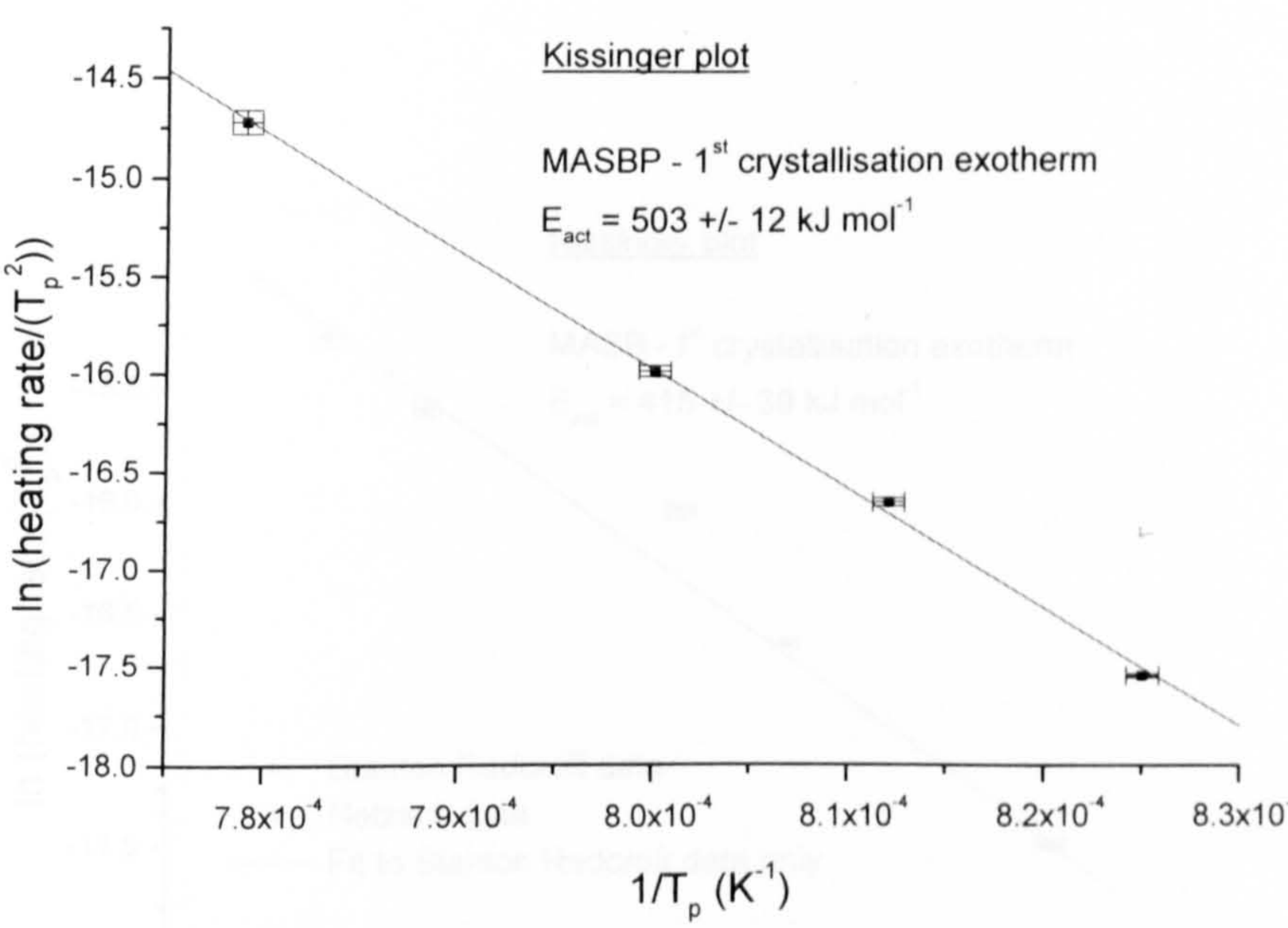

Figure 5.21: Kissinger plot for MASBP - 1st crystallisation exotherm.

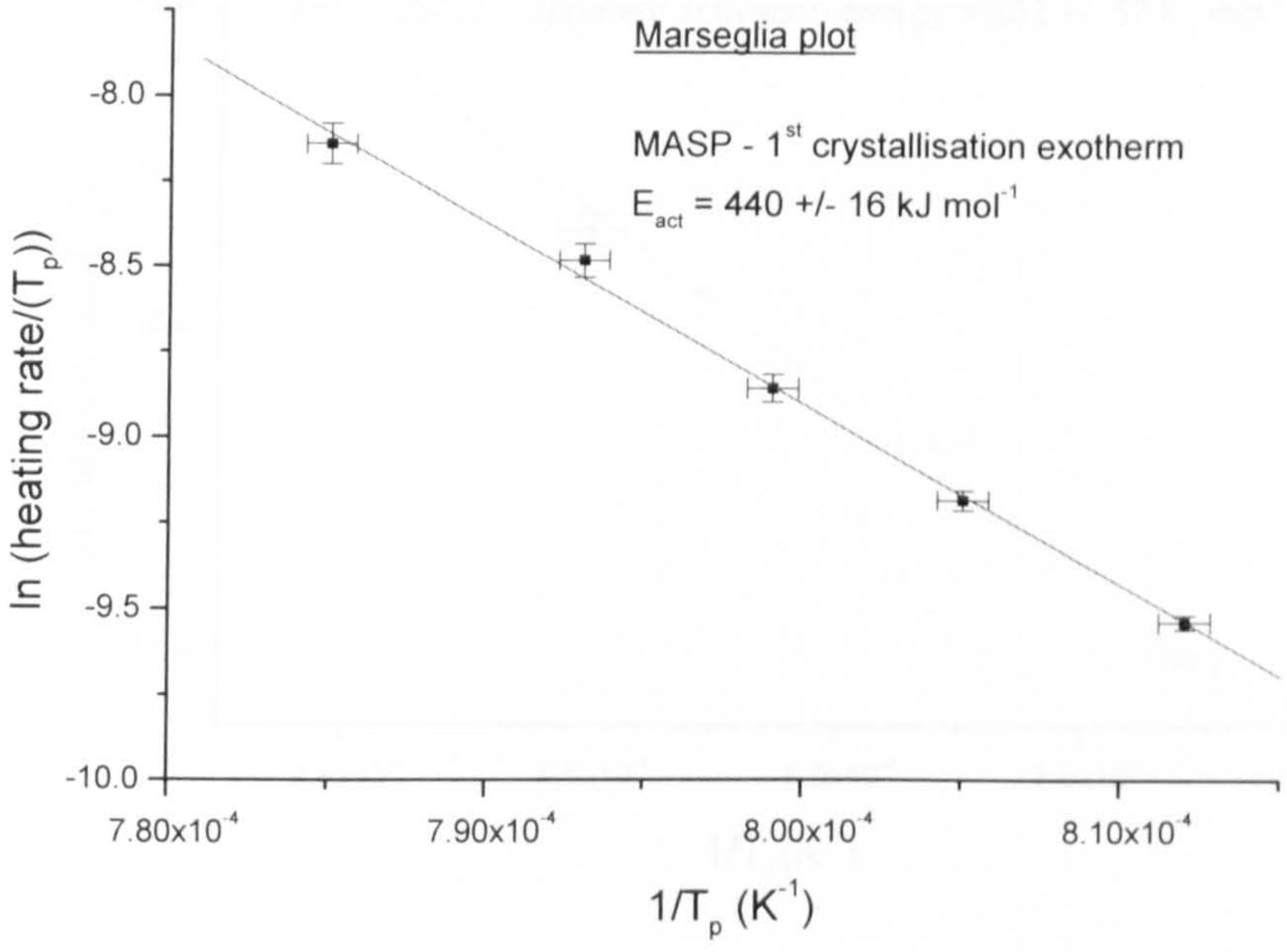

Figure 5.22: Marseglia plot for MASP - 1st crystallisation exotherm.

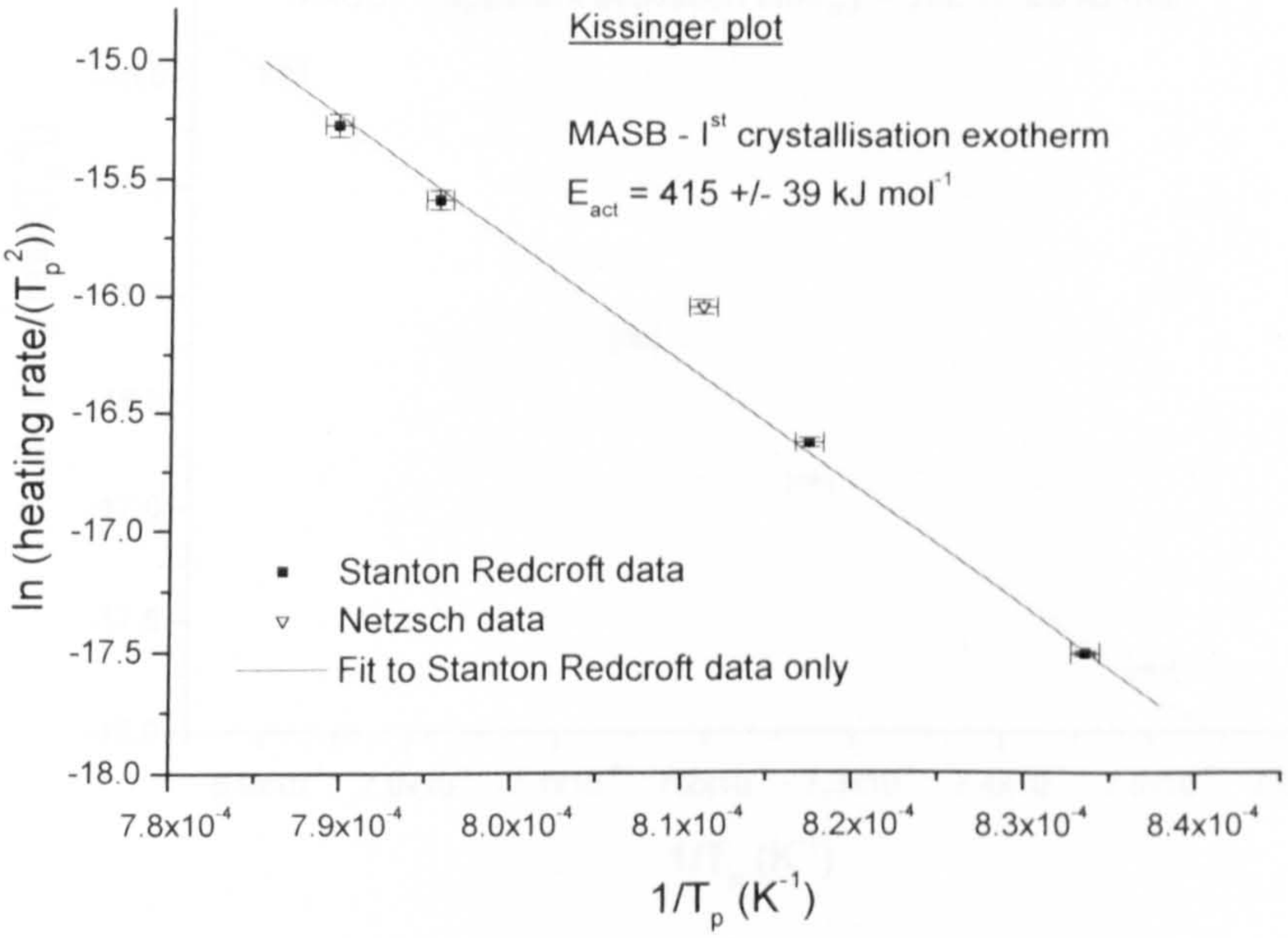

Figure 5.23: Kissinger plot for MASB - 1st crystallisation exotherm.

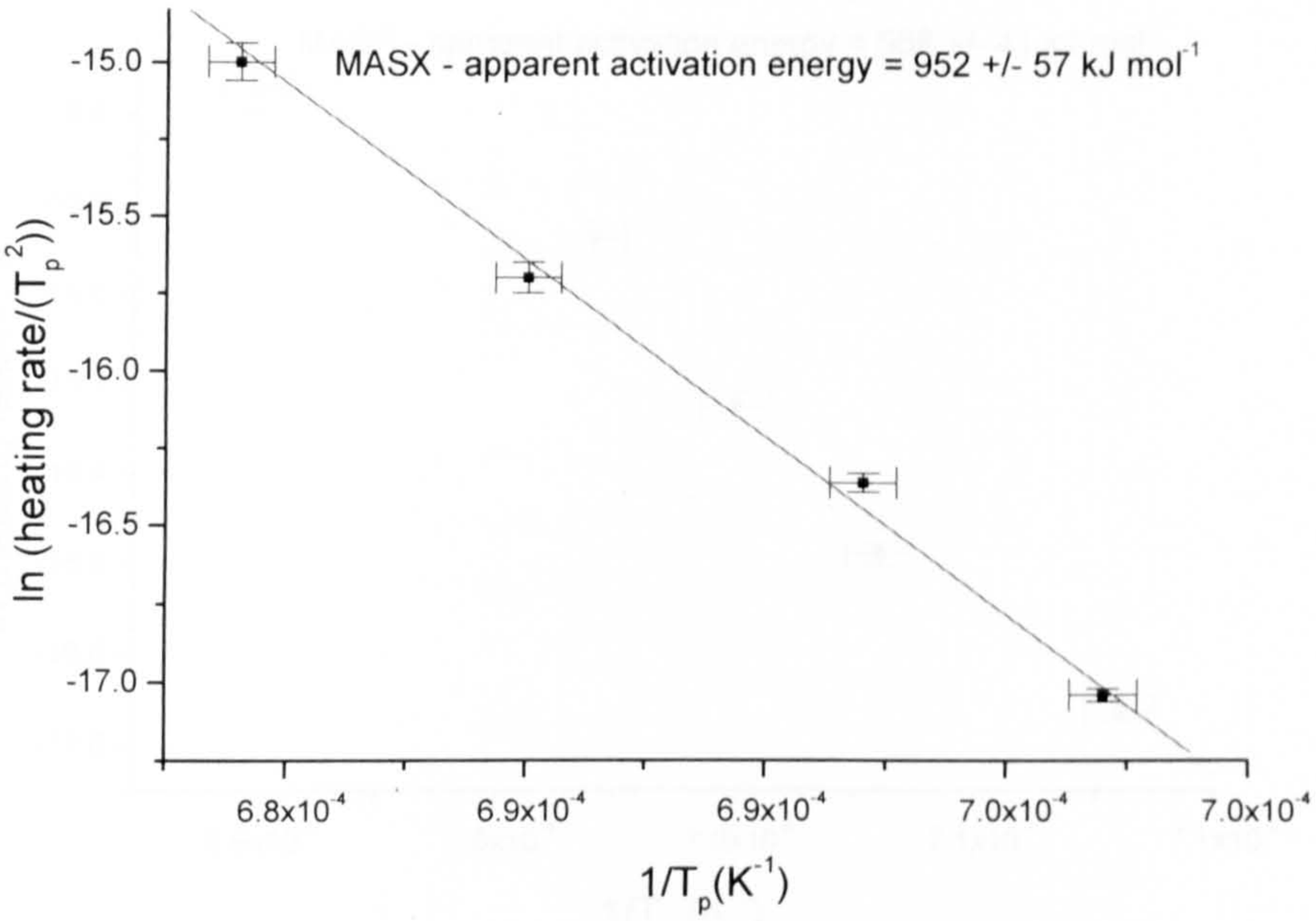

Figure 5.24: Kissinger plot for MASX - 2nd crystallisation exotherm.

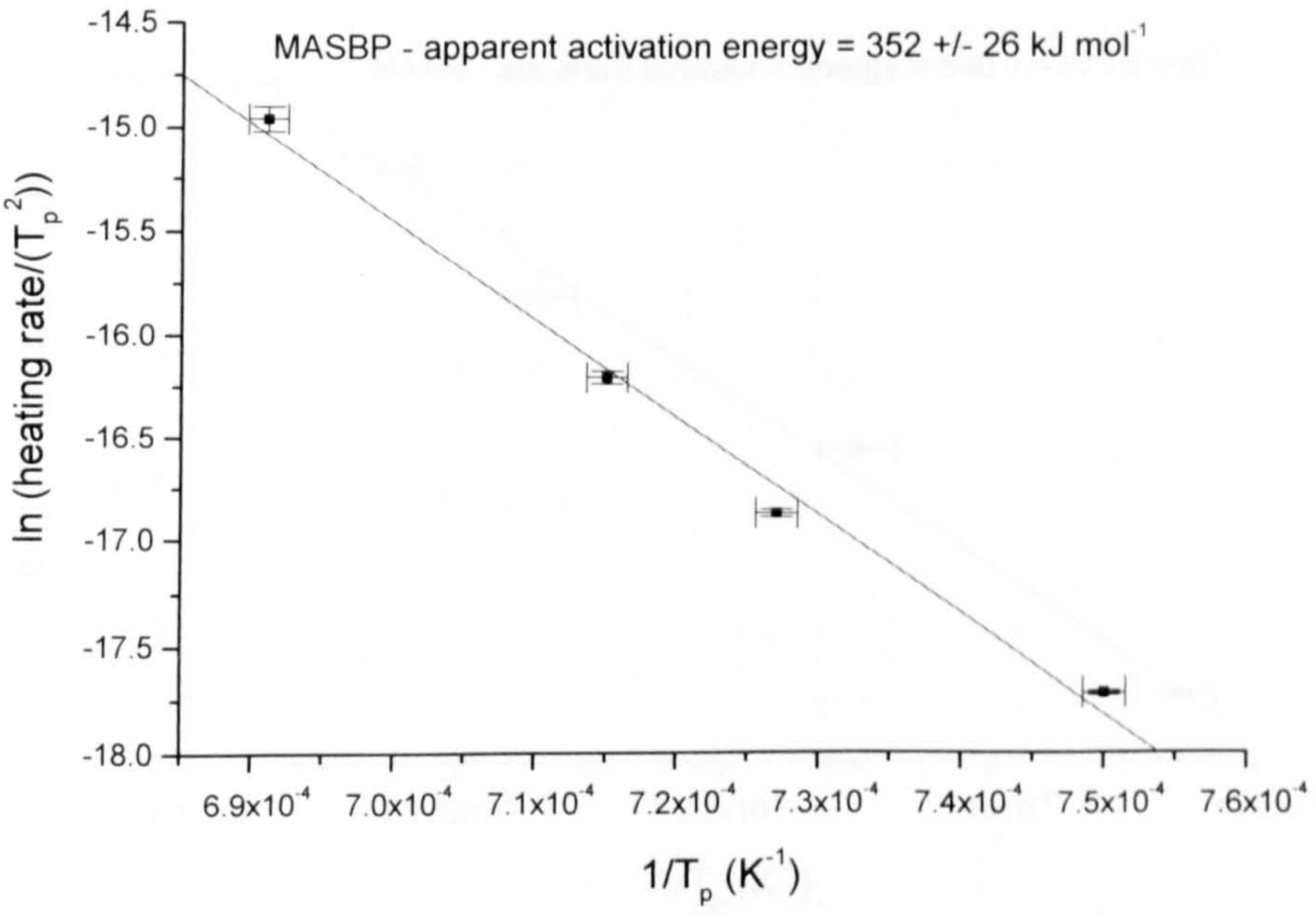

Figure 5.25: Kissinger plot for MASBP -2nd crystallisation exotherm.

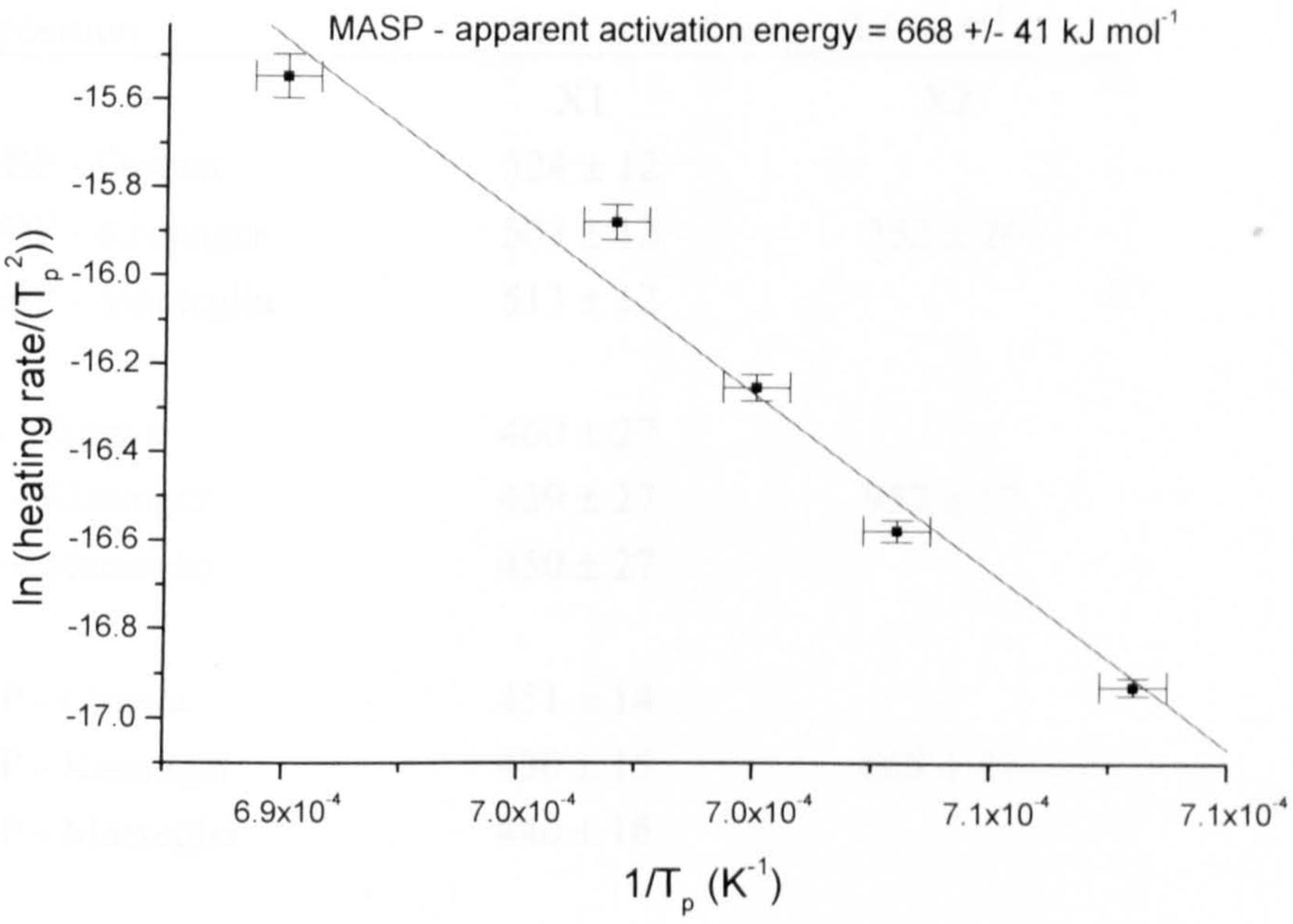

Figure 5.26: Kissinger plot for MASP - 2nd crystallisation exotherm.

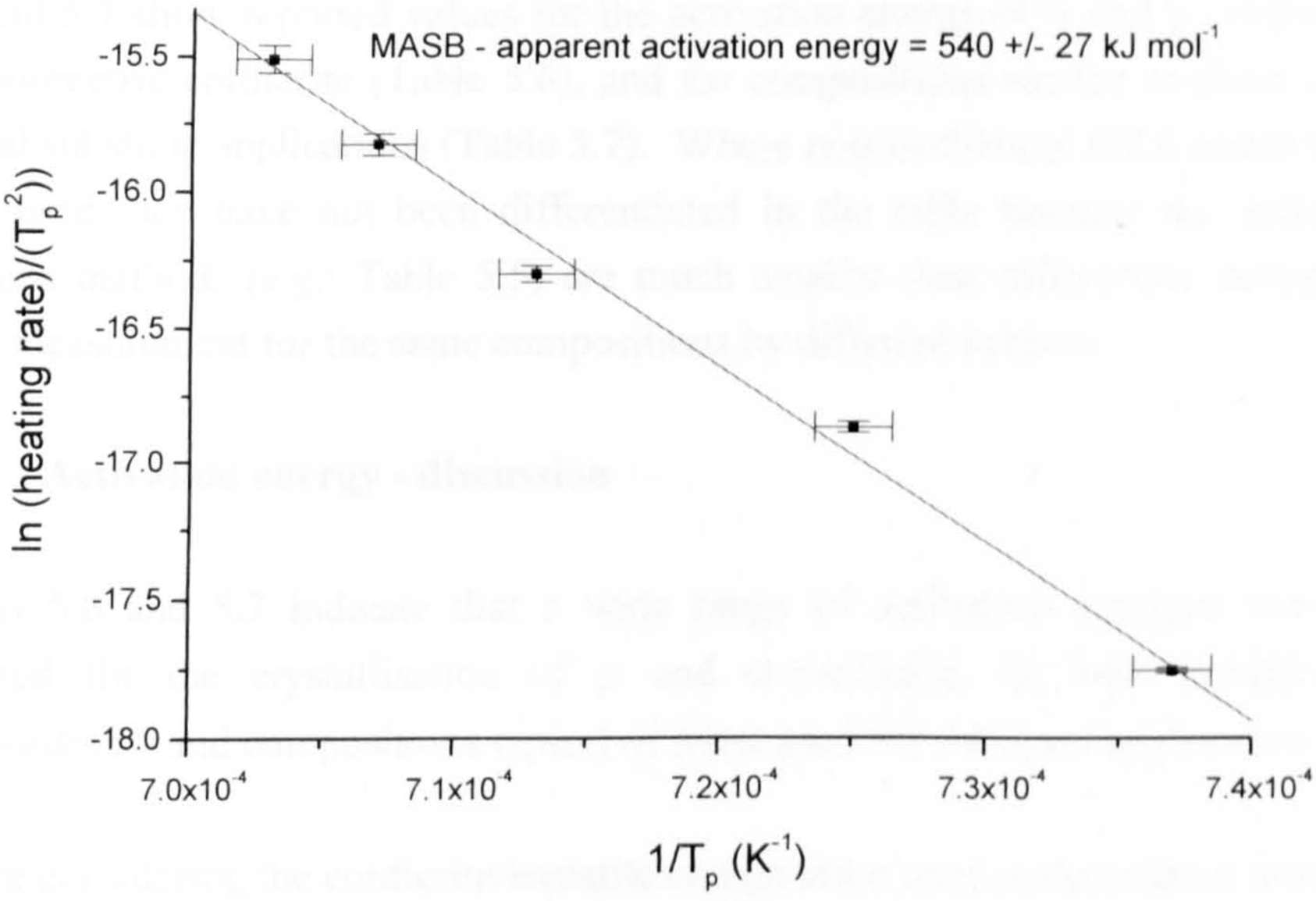

Figure 5.27: Kissinger plot for MASB - 2nd crystallisation exotherm.

Table 5.5: Calculated activation energies.

Composition	Activation Energy (kJ mol^{-1})	
	X1	X2
MASBP - Ozawa	524 ± 12	
MASBP - Kissinger	503 ± 12	352 ± 26
MASBP - Marseglia	513 ± 12	
MAS - Ozawa	460 ± 27	
MAS - Kissinger	439 ± 27	952 ± 57
MAS - Marseglia	450 ± 27	
MASP - Ozawa	451 ± 14	
MASP - Kissinger	430 ± 15	668 ± 41
MASP - Marseglia	440 ± 16	
MASB - Ozawa	436 ± 39	
MASB - Kissinger	415 ± 39	540 ± 27
MASB - Marseglia	429 ± 39	

In order to put the results from the calculation of activation energy in context, Table 5.6 and 5.7 show reported values for the activation energy of α and μ cordierite, in stoichiometric cordierite (Table 5.6), and for compositions similar to those used in typical substrate applications (Table 5.7). Where non-isothermal DTA methods have been used they have not been differentiated in the table because the differences between methods (e.g.: Table 5.5) are much smaller than differences between the same measurement for the same compositions by different authors

5.6.2 Activation energy - discussion

Tables 5.6 and 5.7 indicate that a wide range of activation energies have been reported for the crystallisation of μ and α-cordierite, in both stoichiometric compositions, and compositions typical of those used for substrate applications.

Before considering the cordierite/enstatite composition used in the current work, it is worthwhile to discuss stoichiometric cordierite as this is not complicated by variations from stoichiometry or formation of other phases, such as enstatite or forsterite.

Table 5.6: Reported values for the activation energy of stoichiometric cordierite

Composition	Method	Eα	Eμ	$E_{viscous}$	Particle size (μm)	Ref
Stoichiometric	Isothermal - crystal growth		628	1004		Yuritsin [10]
""	Isothermal - crystal growth		460	780		DiazMora [11]
""	Non-isothermal DTA	399-426	532-574	766		Donald [12]
""	Isothermal		532-577			""
""	Isothermal	477				Amista [13]
""	Non-isothermal DTA	565	356			""
""	Isothermal - crystal growth		415			Muller [14]
""	Non-isothermal DTA	901.2	364		< 125	Goller [15]
""	""	708.3	294.5		125-355	""
""	""	343.5	252.0		355-710	""
""	Isothermal XRD		422.8		<125	""
""	""		275.4		125-355	""
""	Non-isothermal DTA	863-872	303-323 *1			Sung [16]
""	Isothermal - XRD		348			Aleeksenko [17]
""	Isothermal XRD - after preliminary heat treatment at 800°C		280			""

*1 Not reported by Sung, calculated from his Figure

Table 5.7: Reported values for the activation energy of crystallisation in non-stoichiometric compositions.

Composition	Method	Eα	Eμ	$E_{viscous}$	Particle size (μm)	Ref
Stoichiometric + 2 wt% B_2O_3 and 2 wt % P_2O_5	Non-isothermal DTA	304-316				Sung [16]
Stoichiometric + 2 wt% B_2O_3, 2 wt % P_2O_5 and 2 wt % TiO_2	Non-isothermal DTA	313-338				""
Stoichiometric + 3 wt% P_2O_5 and 5 wt% Y_2O_3 stabilied ZrO_2	Isothermal - growth rate	410				Sue [18]
Cordierite/enstatite + 2 wt% P_2O_5 and 1 wt% B_2O_3	Non-isothermal DTA	430 ± 15				Bridge [1]
Cordierite/enstatite + 1.7 wt% P_2O_5 and 1% B_2O_3 + other minor additives	Non-isothermal DTA	272		585	<150	Watanabe 1985 [19]
""	Isothermal - fraction crystallised	301.9			<150	Watanabe 1994 [20]
""	Non-isothermal DTA	303.5			<150	""
Cordierite/enstatite + 4.5 wt% P_2O_5	Isothermal - growth rate		469			Rudolph [21]
""	Non-isothermal DTA peak max	300				""
""	Non-isothermal DTA peak onset		470-500			""

a) Stoichiometric compositions - discussion of literature values (Table 5.6)

For stoichiometric cordierite, a wide range of values have been reported for the activation energies of both α and μ-cordierite. If the spread in values is not due to the measurement technique or its application, this would suggest that the activation energy is highly sensitive, either to small changes in composition away from the stoichiometric, or to the nature of the particle surfaces. Other possible reasons for the scatter in measured values are discussed below.

The possibility of the activation energy being effected by particle size and thermal history is considered in the literature, with inconsistent results. Donald [1] found that the activation energies of μ and α-cordierite were insensitive to the initial glass particle size. In contrast, Goller [15] reported that the measured activation energy was strongly particle size dependent. Aleeksenko [17] reported that preliminary heat treatment of stoichiometric cordierite glass around T_g (800°C) lowers the activation energy for the formation of μ-cordierite by ≈ 20 %, from 350 ± 20 to 280 ± 20 kJ mol^{-1}, and attributed this reduction to a structural relaxation as a result of the heat treatment. However, Donald [12] found no shift in the peak crystallisation temperature for preliminary heat treatments below 860°C, and demonstrated that the shift in peak crystallisation temperature for preliminary heat treatments above 860°C was due to partial crystallisation.

As demonstrated in Figure 5.19, the heat output by the sample as a result of crystallisation may lead to the temperature and heating rate seen by the sample being significantly different from that recorded. For cordierite, the magnitude of the enthalpy of crystallisation measured by Donald [12] (361.5 ± 7 J g^{-1}), compared to the specific heat capacity of cordierite at 1000°C (1.25 J g^{-1} $°C^{-1}$ [22]), suggests that considerable local heating may occur. The enthalpy of crystallisation reported by Donald [12] agrees well with the molar heat of fusion of high-cordierite measured by Watanabe of 386 J g^{-1} (226 kJ mol^{-1}) [19]. For DTA, the local heating effect of the crystallisation exotherm may be particularly significant where large samples or fast heating rates are employed. This effect may be partly responsible for the wide range of activation energies reported. This effect could be minimised by dilution of the sample although this might be at the expense of resolution of minor features.

Problems due to the composite nature of the crystallisation peaks are unlikely to arise for stoichiometric cordierite unless extremely fine glass-powder is employed.

Donald [12], for isothermal crystallisation studies from 904 to 954°C (where crystallisation of μ-cordierite would be expected to dominate) showed close agreement with measured values for the activation energy of μ-cordierite using non-isothermal methods.

b) Non-stoichiometric compositions - discussion of literature values

The differences between the DTA trace of a typical cordierite/enstatite composition, and a stoichoimetric composition are discussed by Knickerbocker. The DTA trace they report for a cordierite/enstatite composition has a single peak with a leading, lower temperature shoulder. This would be consistent with the leading shoulder being crystallisation of μ-cordierite directly from the glass with the main peak being due to the crystallisation of α-cordierite directly from the glass. Knickerbocker reports, based on hot stage XRD, that full conversion to α-cordierite in a composition with no B_2O_3 and P_2O_5 occurs at temperatures in excess of 1170°C. They suggest that, in the absence of B_2O_3 and P_2O_5, the off-stoichiometry of the glass is better accommodated by the quartz structure which therefore becomes stabilised. However, if the second peak is due to formation of α-cordierite directly from the glass, this indicates that B_2O_3 and P_2O_5 may also stabilise the glass with respect to the formation of α-cordierite.

For the non-stoichiometric compositions, the scatter in the range of values reported for the activation energy is much lower. It is possible that sensitivity to small changes of composition, or surface condition is much reduced away from the stoichiometric composition.

However, due to the reduced separation between the two crystallisation exotherms, and the formation of enstatite, the possibility of obtaining a composite activation energy is increased. Rudolph [21] demonstrated that the activation energy for μ-cordierite calculated using the peak onset agrees well with isothermal experiments, whereas the figure obtained using the peak maximum is dominated by the crystallisation of α-cordierite.

Sung shows that the combined effect of the addition of 2 wt % B_2O_3 and 2 wt % P_2O_5 to stoichiometric cordierite is to reduce the activation energy from 863-872 kJ mol^{-1} to 304-316 kJ mol^{-1}.

c) Discussion of activation energy results

The fine particle size used in this work (~3 μm) reduces the temperature at which the μ-cordierite crystallisation exotherm occurs. As a result, the two cordierite crystallisation exotherms were well separated and separate measurement of the peak maxima were possible. The use of peak onset would not be appropriate with this particle size, as this event competes with an endotherm due to sintering which could give misleading results.

Despite the discrepancies in the values of activation energies reported in the literature, the differences in activation energies measured for the different compositions in the current work (Table 5.5) are believed to be significant.

The measured activation energy for the first crystallisation exotherm corresponds to the combined crystallisation of μ-cordierite and enstatite from the glass. It is not clear to what extent the crystallisation of enstatite contributes to the exotherm but the crystallisation of μ-cordierite is believed to dominate

The measured activation energies for μ-cordierite, for compositions MASX, MASB and MASP did not differ significantly and were in the range 415-460 kJ mol^{-1}. However the combined presence of B_2O_3 and P_2O_5 appears to raise the activation energy for μ-cordierite formation to 503-524 kJ mol^{-1}. The effect of this is to retard the crystallisation of μ-cordierite to a higher temperature and thus aid sintering.

The second, higher temperature, crystallisation exotherm is dominated by α-cordierite formation directly from the glass. However, some features were observed indicating the composite nature of this peak and it is possible that proto-enstatite formation, the exsolution of Al from the enstatite phase, and Al-Si ordering within the cordierite phase may contribute.

The apparent activation energy for this peak (corresponding to the formation of α-cordierite directly from the glass) when no additives are present was 952 ± 57 kJ mol^{-1}. This was substantially reduced by the presence of B_2O_3 (540 ± 27 kJ mol-1) and P_2O_5 (668 ± 41 kJ mol^{-1}) with the effect of B_2O_3 being more significant. The combined effect of the presence of B_2O_3 and P_2O_5 is greater still, with the activation energy reduced to 352 ± 26 kJ mol^{-1}. This figure, for the activation energy for α-cordierite formation in a typical substrate composition, shows reasonable agreement with the figures reported for similar compositions (Table 5.7).

The combined effect of B_2O_3 and P_2O_5 on the activation energy for the formation of α-cordierite shows excellent agreement with the results of Sung [16], for their combined effect in a stoichiometric composition (Table 5.8).

Table 5.8: A comparison of the effect of B_2O_3 and P_2O_5 on the activation energy for the formation of α-cordierite in stoichiometric and cordierite/enstatite compositions.

	Cordierite/enstatite	Stoichiometric [16]
MAS only	952 ± 57	863-872
with B_2O_3 and P_2O_5	352 ± 26	304-316

Glendenning and Lee [23] examined in detail the microstructural development of a stoichiometric cordierite with and without B_2O_3 and P_2O_5 and found that their combined role was to suppress the formation of μ-cordierite, to extend the gap between Tg and the onset of crystallisation, and to promote the direct crystallisation of α-cordierite. Similar effects have been observed in cordierite/enstatite compositions by both Knickerbocker [5] and Bridge [1]. The similar effect in both stoichiometric and typical substrate compositions suggests that the roles of B_2O_3 and P_2O_5 are similar in both compositions.

5.7 Graded glass-ceramic joints

Moxey [2] created co-fired glass-ceramic layered structures using mixtures of MAS1 and MAS2 as end members, and mixtures of the two compositions as interlayers. Layered structures with up to five layers were produced by co-sintering at 950°C and showed perfect interfacial contact. The TCE (50-850°C) of the two end members were 7.1 MK^{-1} (MAS1 - μ-cordierite, enstatite with some α-cordierite) and 2.1 MK^{-1} (MAS2 - α-cordierite with some enstatite). Where a significant TCE mismatch existed between layers, fracture of the layered structure was revealed by sectioning. An example of cracking in a three layer structure is shown in Figure 5.28. The result of the tensile stresses in the high thermal expansion layer is particularly dramatic. The TCE of the 50:50 MAS1:MAS2 interlayer was 3.6 MK^{-1}, lower than that suggested by the rule of mixtures. Moxey [2] suggests that the α-cordierite formed in MAS2 may have seeded its earlier formation in MAS1, resulting in the lower TCE.

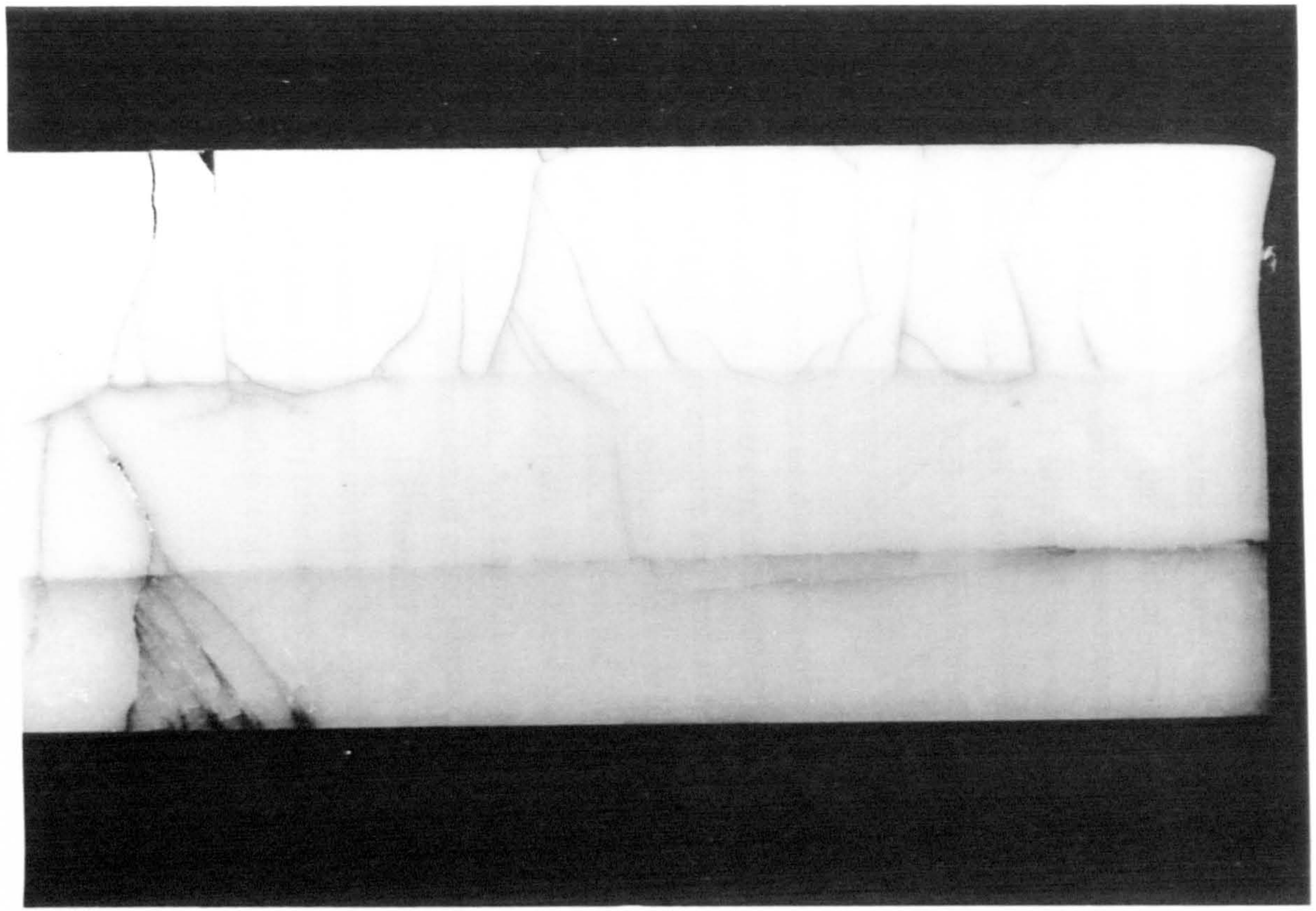

Figure 5.28: Cracking due to TCE mismatch in a three layer glass-ceramic structure. The TCE of the three layers are from the top, 7.1, 3.6 and 2.1 MK^{-1}.

From the pattern of cracking in a 5 layer joint, Moxey [2] recommended restricting the TCE mismatch between layers to 0.5 MK^{-1}. This is a more conservative estimate than the 0.8 MK^{-1} recommended by Budd [24]. However, as demonstrated in Section 3.3.5 the allowable TCE mismatch is strongly dependent on joint geometry.

Hillman [3] attempted to measure the residual stress in similar graded joints using the variation of crack length due to Vickers indentations. The TCE mismatch between MAS2 and MAS3 was designed to give a suitable mismatch for the residual joining stress to be insufficient to cause cracking, but sufficient to give a suitable distribution in crack sizes to enable the residual stress to be measured (using the method of Newman [25]). A preliminary measurement of the indentation fracture toughness (K_{IC}) of MAS1 of 1.2 MPa $m^{1/2}$ was used to estimate the fracture toughness of MAS2 and MAS3. All values for fracture toughness were obtained from measuring cracking due to Vickers indentations using the method of Anstis [26].

A 950°C/1 hour heat treatment was used and both compositions (MAS2 and MAS3) showed total conversion from μ to α-cordierite with small quantities of enstatite and forsterite present. Slightly more enstatite and forsterite were present in MAS3. The thermal expansion of the two compositions used were 2.9 and 2.2 MK^{-1} resulting in a forecast residual stress at the interface between the two compositions of ~ 30 MPa. However, the fracture toughness of both MAS2 and MAS3 (2.1 and 2.2 MPa $m^{1/2}$) was much higher than that planned. As a result, the crack extension due to residual stress was reduced. The measurements of crack length either side of the interface are shown in Figure 5.29. The general pattern of stress at the interface shows good agreement with the pattern of stress observed by photoelastic methods through the midpoint of a similar glass joint [27] (also shown in Figure 5.29). However, due to the extensive scatter in the indentation length, no attempt was made to calculate the residual stress.

(a)

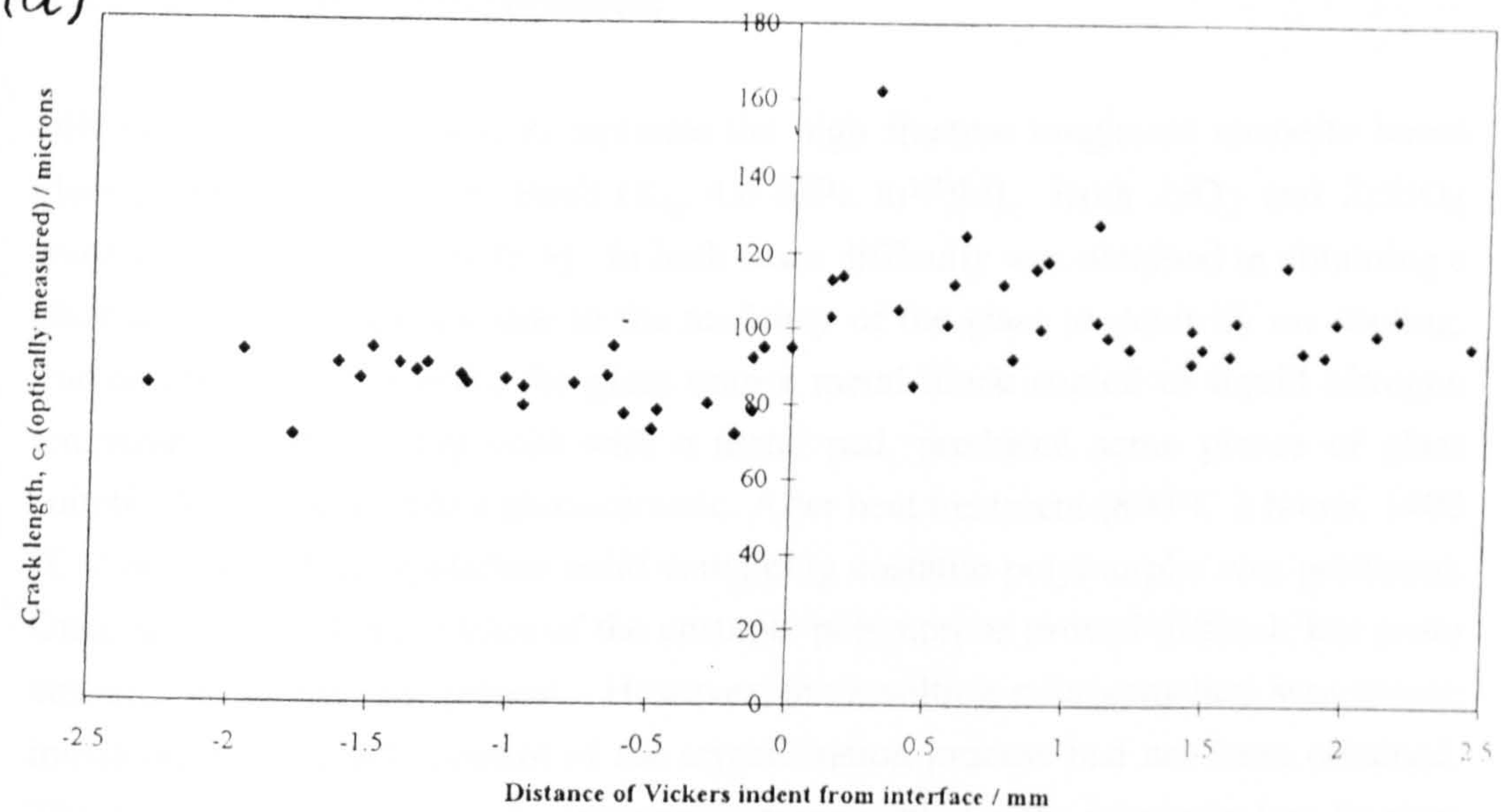

(b)

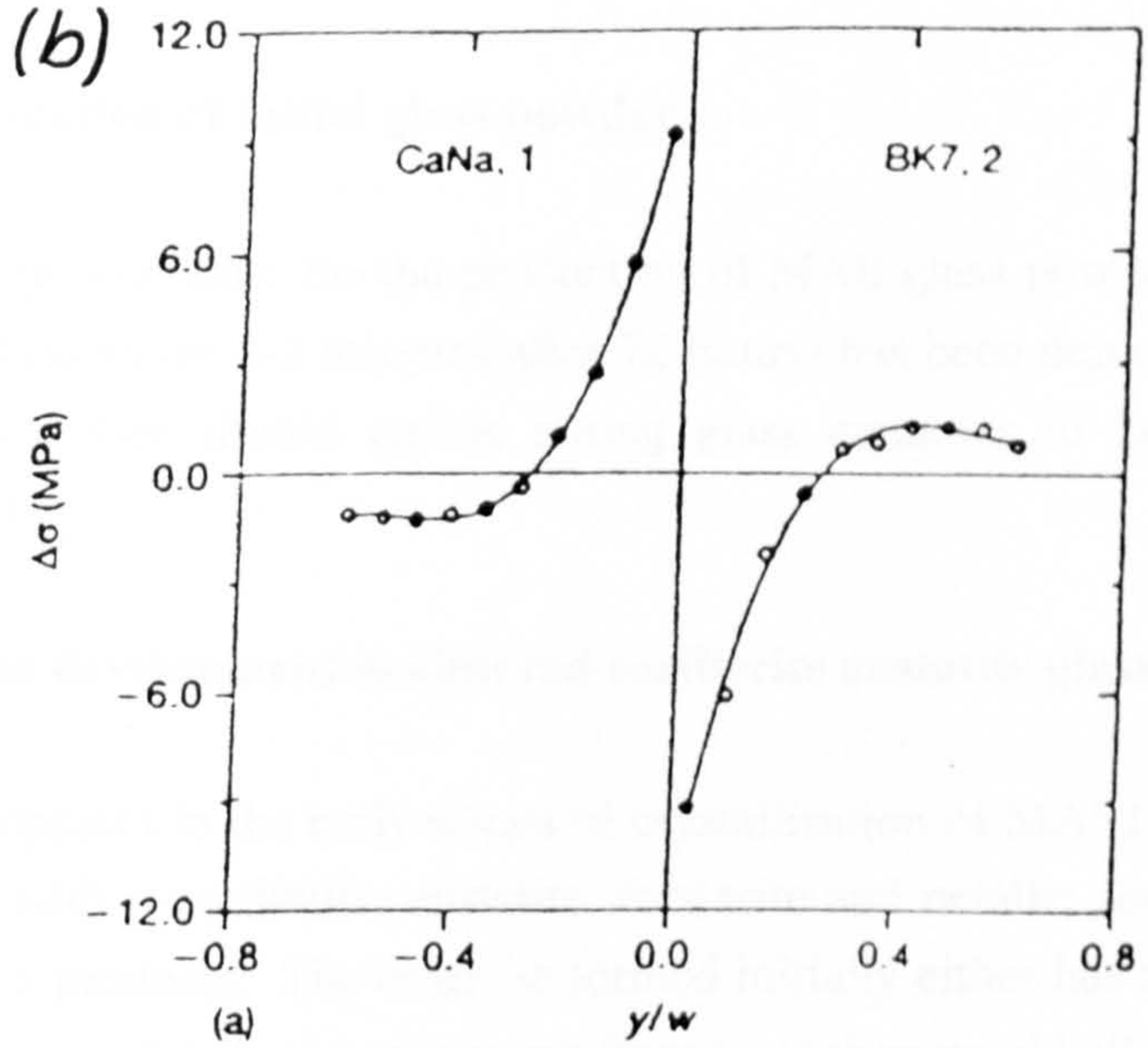

Figure 5.29: (a) Variation in the crack length of Vickers indendations either side of the interface between two MAS glass-ceramics with TCE 2.2 and 2.9 MK^{-1} [3]. (b) For comparison the pattern of stress observed by photoelastic methods through the midpoint of a similar glass joint is also shown [27].

5.8 Enstatite glass-ceramics

Hillman [3] also attempted to replicate the high fracture toughness enstatite based glass-ceramics reported by Beall (K_{IC} 4.6 MPa $m^{1/2}$)[4]. Both ZrO_2 and $ZrSiO_4$ were used as the source of ZrO_2. In both cases difficulty was obtained in obtaining a glass at room temperature due to the tendency of the glass to devitrify on cooling. Forced cooling, by pouring the glass onto a metal block cooled to liquid nitrogen temperature and pressing cold with a metal pad, produced some pieces of glass suitable for conversion to a glass-ceramic. After heat treatment (800°C 2 hours, 1400 °C 2 hours) a white crystalline solid containing enstatite polymorphs was produced. Once again, the identification of the enstatite polymorphs proved difficult but proto enstatite was definitely present. However, the resulting microstructure was coarse indicating that suitable control of the crystallisation process had not been obtained. The coarse microstructure was presumably responsible for the relatively low fracture toughness measurement (1.4 MPa $m^{1/2}$). Hillman [3] was not able to replicate the high fracture toughness materials reported by Beall [4]

5.9 Conclusions

5.9.1 Production of initial glass powder

A ball-milling procedure for the production of MAS glass powder ~ 3-4 microns in size after 48 hours (or 2-3 microns after 72 hours) has been demonstrated. This fine initial particle size should enable strong glass ceramics to be formed at lower temperatures.

5.9.2 Phase development in sintered cordierite enstatite glass-ceramics

Phase development in the early stages of crystallisation of MAS1 has been shown to be complex with μ-cordierite, enstatite, forsterite and petalite forming as the initial crystallisation products. The enstatite formed initially either has high levels of Al^{3+} substitution, or is distributed on a much finer scale than would allow the composition to be resolved using EDX.

On further heat treatment α-cordierite forms, either directly from the glass or via transformation from the μ-phase. The apparent level of Al^{3+} substitution within the enstatite phase (using EDX) is reduced at higher temperatures indicating either exsolution of Al^{3+} or coarsening of the microstructure. At temperatures above 1100

°C the formation of proto-enstatite is observed, the level of which increases at higher temperatures.

5.9.3 Effect of B_2O_3 and P_2O_5 on phase development

The effects of B_2O_3 and P_2O_5 in a cordierite/enstatite glass-ceramic have been demonstrated using XRD, SEM, and measurements of the apparent activation energy of crystallisation using non-isothermal DTA-based methods.

The crystallisation of μ-cordierite is strongly suppressed in compositions containing both B_2O_3 and P_2O_5 (MASBP) compared to compositions where no additives are present (MASX). Compositions with the addition of either P_2O_5 (MASP), or B_2O_3 (MASB) show intermediate behaviour with respect to μ and α-cordierite formation, with MASB being close in behaviour to MASBP, and MASP closely resembling MASX. Although the contribution of B_2O_3 appears to be more significant than that of P_2O_5 the effect is greater when both B_2O_3 and P_2O_5 are present. Two crystallisation exotherms are observed is these compositions corresponding to the crystallisation of μ and α-cordierite directly from the glass. The measured activation energies for the crystallisation of μ-cordierite, for compositions MASX, MASB and MASP did not differ significantly and were in the range 415-460 kJ mol^{-1}. When both B_2O_3 and P_2O_5 were present this was increased to 503-524 kJ mol^{-1}. The effect of this is to retard the crystallisation of μ-cordierite to a higher temperature, resulting in improved sintering behaviour.

The measured activation energy for α-cordierite formation when no additives were present (MASX) was 952 ± 57 kJ mol^{-1}. This was substantially reduced by the presence of B_2O_3 (540 ± 27 kJ mol-1) and P_2O_5 (668 ± 41 kJ mol^{-1}) with the effect of B_2O_3 being more significant. Once again the greatest effect was seen when both B_2O_3 and P_2O_5 were present, when the activation energy was reduced to 352 ± 26 kJ mol^{-1}. The reduction in activation energy for α-cordierite formation, when both B_2O_3 and P_2O_5 are present shows excellent agreement with the results of Sung [16], for their combined effect in a stoichiometric composition.

Based on XRD and DTA results, and activation energy measurements, the primary role of B_2O_3 is to promote early α-cordierite formation. B_2O_3 has also been shown to play the same role in sol-gel derived cordierites, where Okuyama [28] has demonstrated that doping concentrations above 1.5 mol % promote the direct

formation of α-cordierite from the amorphous state. The effect of B_2O_3 may be related to the structural role that it occupies in either the glass or the crystalline form.

P_2O_5 also affects the crystallisation behaviour, although to a lesser extent than B_2O_3. In contrast to B_2O_3, P_2O_5 reduces the viscosity in these compositions [29], which may partially account for the effect of P_2O_5. The fine-scale glass-in-glass phase separation observed by other authors [1][30] for compositions containing P_2O_5 may also be significant. In the current work this was manifest as a double Tg during some DTA runs.

It is possible that the greater combined effect of B_2O_3 and P_2O_5 observed previously [1][5][23] and in the current work, is due to the sum of their separate effect when both are present. However it is also possible that the structural role of B_2O_3 and/or P_2O_5 is modified when both are present.

In order to fully understand the microstructural development in these compositions the effect of the heat evolved as a result of crystallisation may need further consideration.

5.9.4 Graded glass-ceramic joints

MAS glass-ceramic layered structures with thermal expansions from 2.1 to 7.1 MK^{-1} have been produced. However, the resulting cracking due to residual joining stress has graphically illustrated the restrictions of this approach, and supports the conclusions of Chapter 3 on graded joints

The production of a crack-free glass-ceramic joint with graded TCE to bridge a TCE mismatch is possible. However, the geometrical restrictions severely limit the applications of such a joint. For suitable applications, using the MAS/MS system a graded joint from 2 MK^{-1} up to 12.8 MK^{-1} (enstatite based [31]) should be possible.

5.9.5 Enstatite glass-ceramics

An attempt to replicate the high fracture toughness enstatite based glass-ceramics reported by Beall [4] was not successful.

References for Chapter 5

[1] Bridge D.R., Aspects of electronic device packaging, Ph.D. Thesis, University of Warwick, 1986.

[2] Moxey T., Final year project report, University of Warwick, 1995.

[3] Hillman D., Final year project report, University of Warwick, 1996.

[4] Beall G.H., J. Non-Cryst. Solids 129 (1991) 163-173.

[5] Knickerbocker S.H., Kumar A.H.and Wynn Heron L., Am. Ceram. Soc Bull., 72 [1] 91-95 (1993).

[6] Logan E.A. and Holland D., Alvey 050 report (1989).

[7] Günter C., Ph. D. Thesis, University of Darmstadt, (1992).

[8] Lee W.E. and Heuer A.H., J. Am. Ceram. Soc., 70 [5] 349-60 (1987).

[9] Knickerbocker S.H., Kumar A.H. and Herron L.W., Am. Cer. Soc. Bull. 72 [1] 90-95 (1993).

[10] Yuritsin N.S., Fokin V.M., Kalinina and Filipovich V.N., Bol. Soc. Esp. Ceram. Vid. 31-C (1992) 5 pp 21-26.

[11] Diaz Mora N., Ziemath E.C. and Zanotto E.D, Bol. Soc. Esp. Ceram. Vid. 31-C (1992) 5 pp 117-118.

[12] Donald I., J. Mat. Sci. 30 (1995) 904-15.

[13] Amista P., Cesari M., Montenero A., Gnappi G. and Lan L., J. Non-Cryst. Solids 192 &193 (1995) 529-533.

[14] Muller R., Reinsch S. and Pannhorst W., Glasstech. Ber. Glass Sci. Tech. 69[1] 12-20 (1996).

[15] Goller M. and Pye L.D., Glasstech. Ber. Glass Sci. Technol. 68 C1 (1995) 169-174.

[16] Sung Y-M., J. Mater. Sci. 31 (1996) 5421-5427.

[17] Alekseenko V.I., Volkova G.K., Konstantinova T.E. and Popova I.B., Phys. Stat. Sol. (a) 144, (1994) 271.

[18] Sue Y-J., Chen S-Y., Lu H-Y. and Shen P., J. Mater. Sci. 26 (1991) 1699-1704.

[19] Watanabe K., Giess E.A. and Shafer M.W., J. Mater. Sci. 20 (1985) 508-515.

[20] Watanabe K. and Giess E.A., J. Non-Cryst. Solids 169 (1994) 306-310.

[21] Rudolph T., Pannhorst W. and Petzow G., J. Non-Cryst. Solids 155 (1993) 273-281.

[22] Morrell R., Handbook of properties of technical and engineering ceramics. Part 1: an introduction for the engineer and the designer, National Physical Laboratory, H.M.S.O., London, 1985.

[23] Glendenning M.D. and Lee W.E., J. Am. Ceram. Soc., 79 [3] (1996) pp705-713.

[24] Budd M., pp 187-189. Joining Ceramics, Glass and Metal 1997, DVS-Berichte.

[25] Newman J.C. and Raju I.S., Eng. Fract. Mech. 15 (1981) 185.

[26] Anstis G.R., J.Am. Ceram. Soc. 64 (1981) 533.

[27] Drier G., Elssner G. and Schmauder S., J. Mat. Sci. 29 (1994).

[28] Okuyama M., Fukui T. and Sakurai C., J. Mater. Sci. 28 (1993) 4465-4470.

[29] Giess E.A. and Knickerbocker S.H., J. Mater. Sci. Letts., 4 (1985) 835-837.

[30] Rudolph T., Szabo D.V., Pannhorst W., Weisskopf K.L. and Petzow G., Glasstech. Ber. 64 [8] (1991) pp 218-224.

[31] Sutherland S., and Holland D., Glass Ceramic Coatings for the Protection of High Temperature Titanium Alloys, 1991.

Chapter 6: Joining Silicon Nitride to Silicon Nitride

6.1 Properties of Tenmat Nitrasil S - sintered silicon nitride

The sintered silicon nitride used in this project was Nitrasil S, produced by Tenmat Ltd, which is densified by the addition of Y_2O_3 and Al_2O_3. A typical microstructure and XRD trace are shown in Figures 6.1 and 6.2. The microstructure consists of elongated β-Si_3N_4 grains up to ≈ 8 μm long and an intergranular YSiAlON residual glass. Roughly spherical intermetallic impurities approximately 5 μms across are also present throughout the material. These were identified by EDX as chromium silicides with traces of iron also present. The properties reported by the manufacturer for this material are summarised in Table 6.1.

Table 6.1: Properties reported by manufacturer for Tenmat - Nitrasil S [1]

Density	3.25 g cm^{-3}
Flexural strength (3-pt bend) - at 20°C	650 MPa
- at 1000°C	450 MPa
Fracture toughness (K_{IC}) at 20 °C	8 MPa $m^{1/2}$
Maximum use temperature - long term	1150°C
- short term	1400°C
TCE (20-800°C)	3 MK^{-1}

For joining applications, the TCE is of particular importance and, using the Netzsch dilatometer this was confirmed to be 3.0 ± 0.1 MK^{-1} (50-800°C). The contraction on cooling from the Tg of any residual glass present in the glass-ceramic is particularly critical. Although the composition (and thus Tg) of the residual glass may be significantly different from that of the "parent" MAS glass-ceramic, the Tg of the parent MAS glass (750-800°C (e.g.: Table 5.3)) may still be used as an initial estimate of the Tg of the residual glass present in the glass-ceramic after crystallisation. Figure 6.3 shows the contraction on cooling from 800°C for the silicon nitride together with that of the two glass ceramic compositions (MAS1 and MAS2) used in the joining experiments. The figures for both glass-ceramic compositions are after an 1100°C heat treatment. This demonstrates that the TCE of MAS2 (a cordierite glass-ceramic) is well matched to the silicon nitride. The TCE of MAS1 (a cordierite/enstatite glass-ceramic) is 5.7 MK^{-1} (50-800°C).

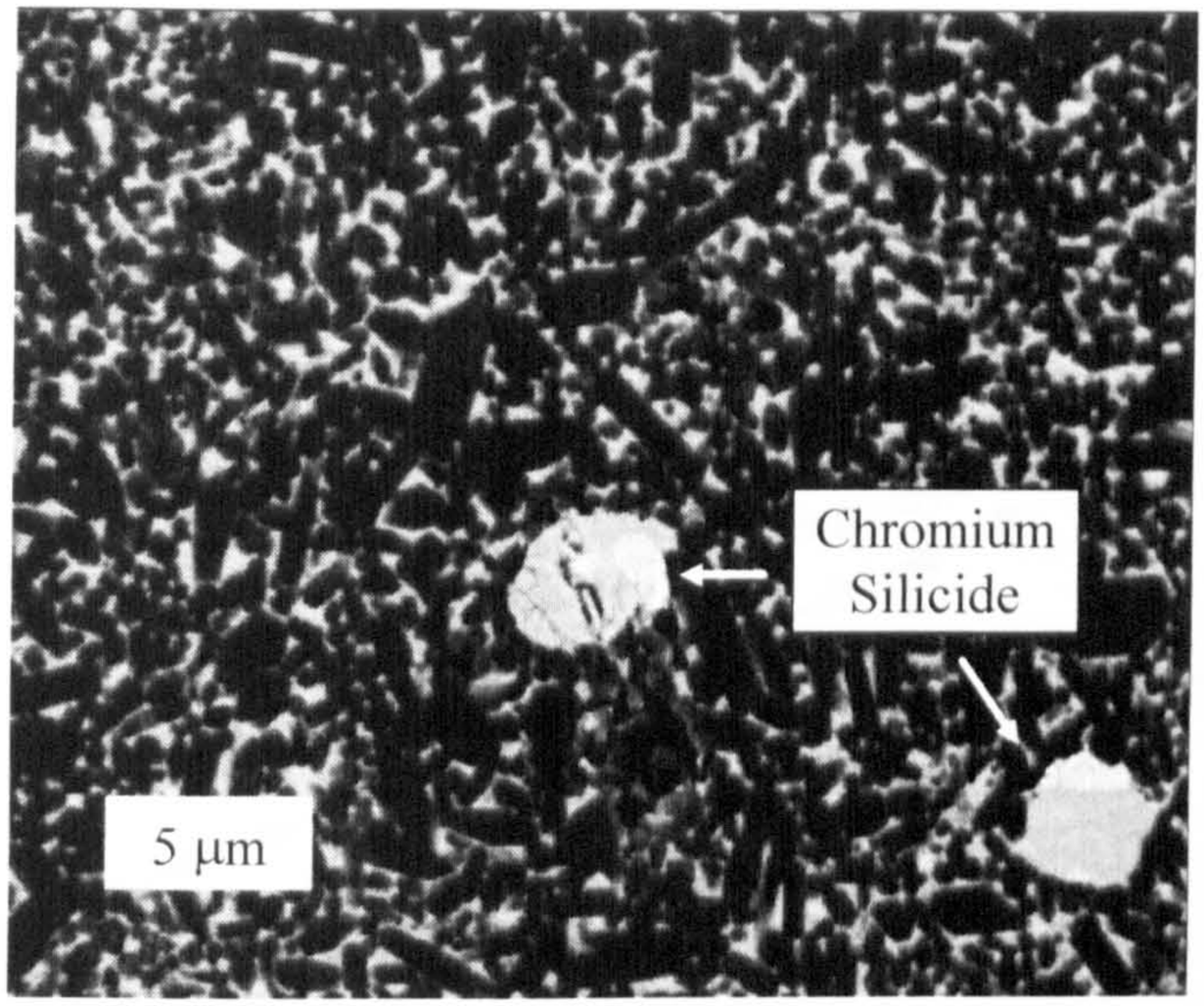

Fig 6.1: Back-scattered electron micrograph of Nitrasil S, showing a representative microstructure. This illustrates the typical size and distribution of: β-Si3N4 grains, YSiAlON residual glassy phase, chromium silicide impurities, and residual porosity

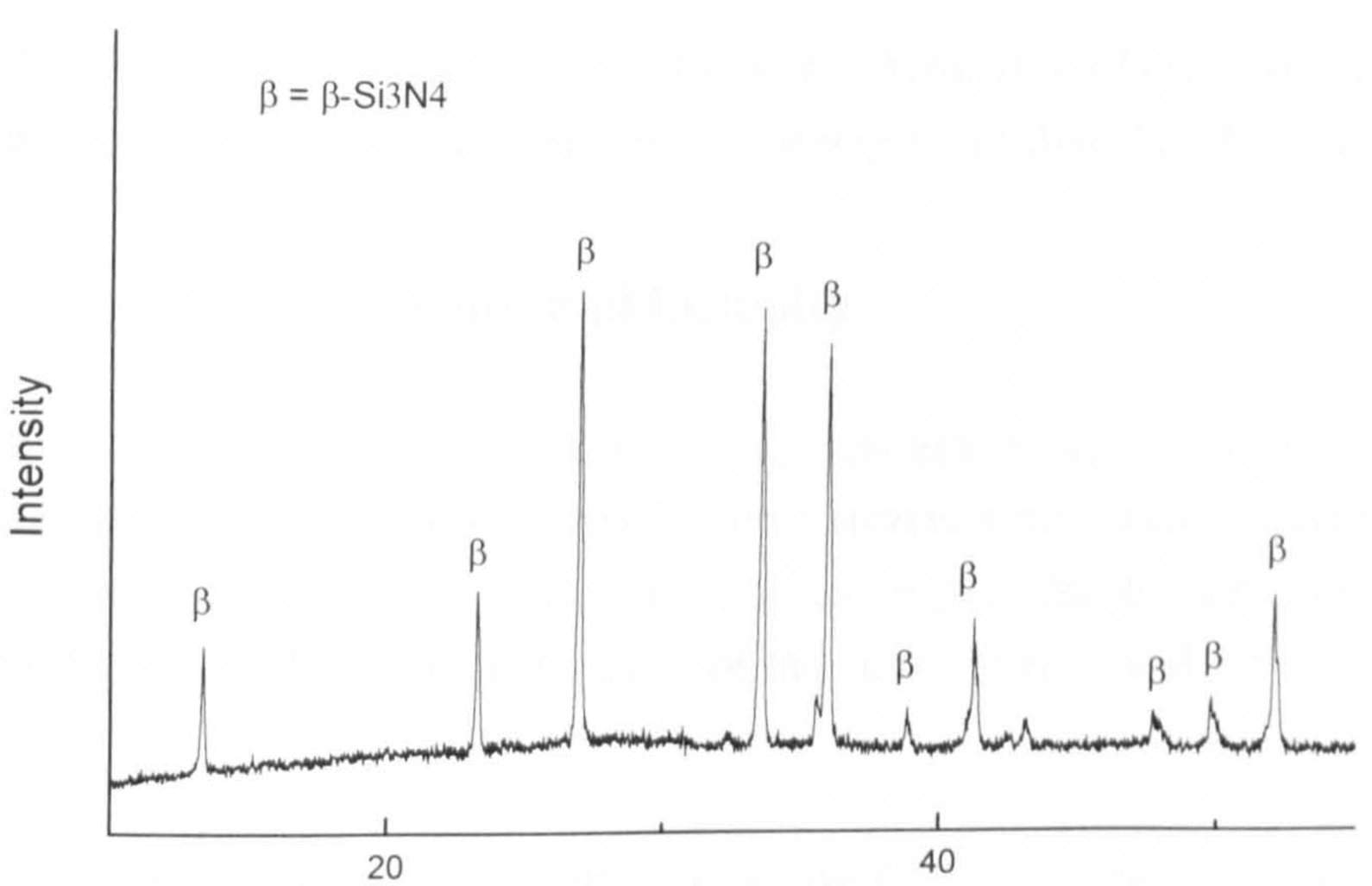

Fig 6.2: Example XRD trace of Tenmat - Nitrasil S (silicon nitride) showing β-Si_3N_4.

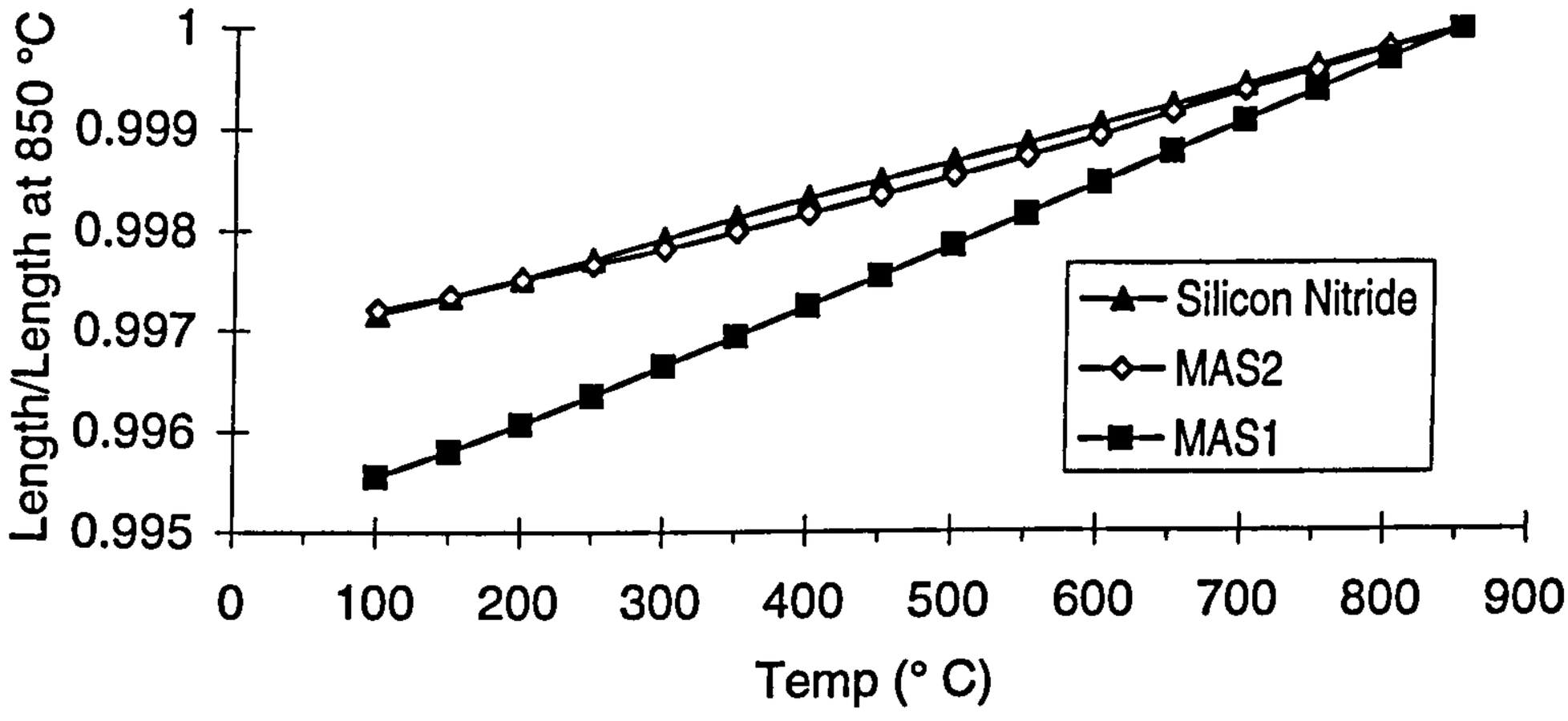

Fig 6.3: Contraction on cooling from 800°C for Nitrasil S silicon nitride, and the two glass-ceramics compositions used in the joining trials, MAS1 and MAS2.

6.2 Goal of joining/joining philosophy

The goal of this part of the work was to use a glass-ceramic interlayer to join silicon nitride to itself. The continuity in the electronic structure across the interface that is required for the formation of a strong bond is to be provided by the compatibility between the oxynitride intergranular glass of the silicon nitride and the oxide glass-ceramic.

A glass-ceramic joint may be particularly attractive for high temperature applications in order to take advantage of the exceptional thermomechanical properties of glass-ceramics. Although, as discussed in section 3.5.3, some joining solutions effective for use at high temperature already exist (eg: [2][3][4][5]), these require joining to occur at high temperatures (1450-1650°C). A glass-ceramic joint should enable a refractory joint to be produced at relatively low temperatures, and give improved mechanical and high temperature properties compared to a glass joint.

interlayer. In order to ensure that consistent sample microstructures, free from unwanted defects, could be obtained for mechanical testing, sectioned and polished microstructures of preliminary joining runs were examined using optical, and scanning electron microscopy.

The majority of the joining trials were performed in the three furnaces described in Section 4.3 and the results of this work are summarised below. Some additional trials were performed in air with no applied load. However, the use of temperatures of up to 1200°C did not result in either wetting or bonding, and no successful joints were produced.

6.3 TWI brazing furnace - initial joining trials

6.3.1 TWI brazing furnace - introduction

Joining trials were performed using the TWI brazing furnace at recorded temperatures from 950-1250°C, in a vacuum of ~ 0.1 Pa. Typically a load of 0.55 MPa was applied at room temperature which was increased to 1.1 MPa at the joining temperature. The glass was applied in the form of a loose powder.

There was some lack of consistency between results from this furnace, and comparison with other work suggests that temperatures recorded by the thermocouple may have been up to 50-100°C different to those seen by the sample. This conclusion is based on both the microstructure of the MAS, and the extent of the interaction at the interface between the glass-ceramic and the silicon nitride. Typical results from this furnace are presented below.

6.3.2 TWI brazing furnace - results

For samples joined at temperatures up to and including 1075°C, no reaction at the interface between the silicon nitride and the glass-ceramic, or diffusion of species across the interface, could be detected using SEM or EDX.

Figure 6.4: Silicon nitride/glass-ceramic/silicon nitride joint with TCE mismatch cracks perpendicular to the join due to higher TCE interlayer (MAS1, 1075°C, 45 minutes, 1.1 MPa).

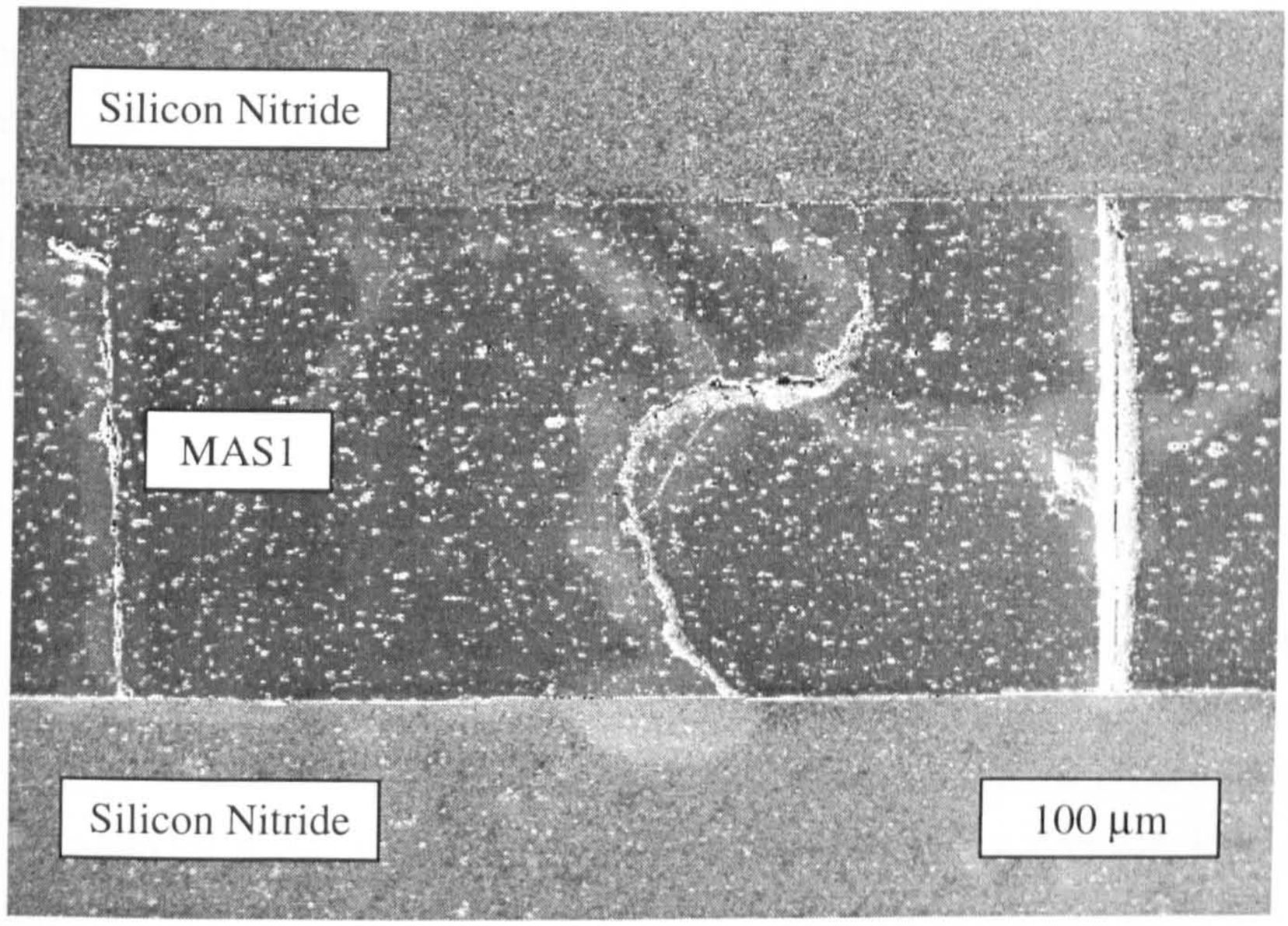

Figure 6.5: Silicon nitride/glass-ceramic/silicon nitride joint free from TCE mismatch cracks due to matched TCE glass-ceramic interlayer (MAS2, 1000°C, 45 minutes, 1.1 MPa).

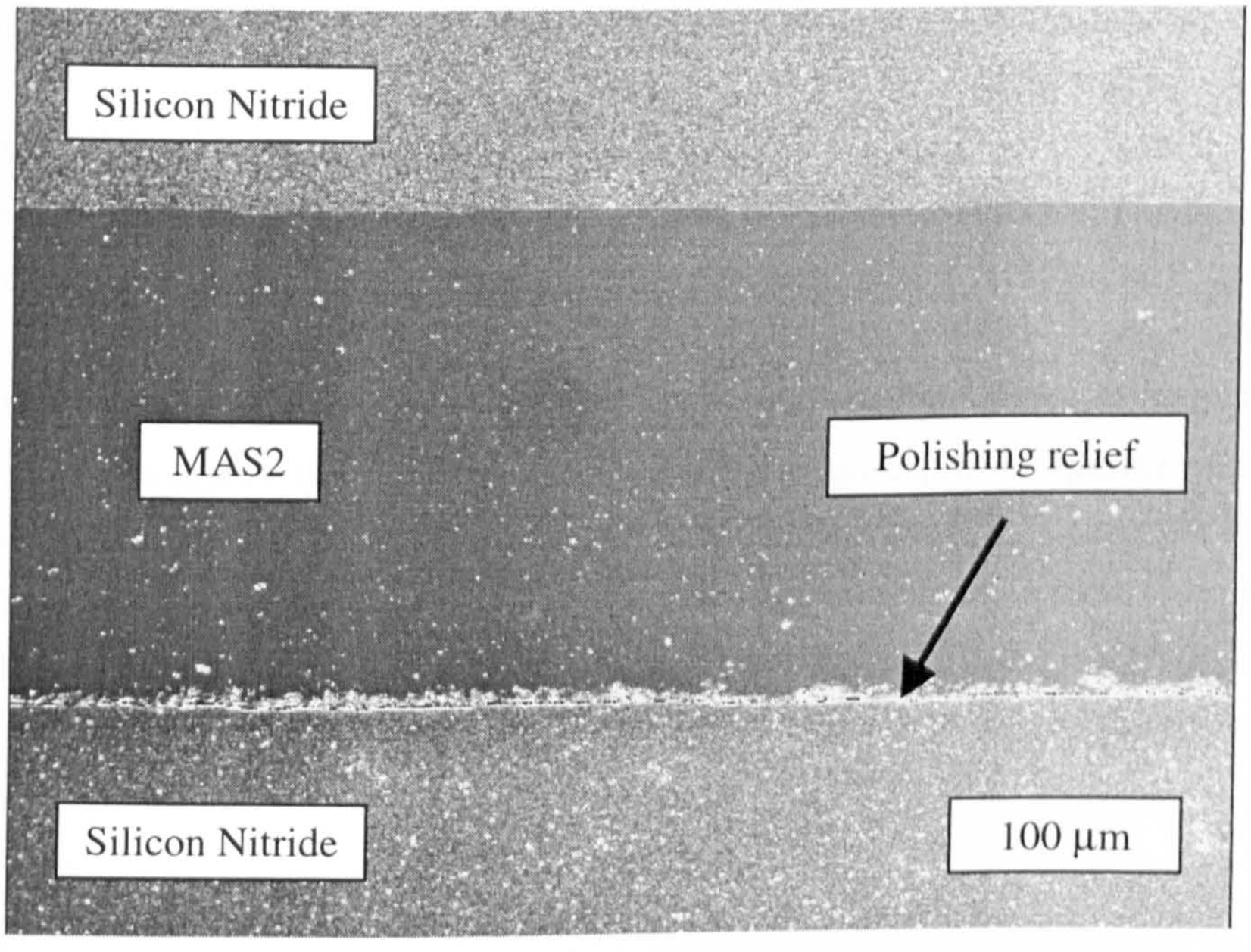

Figure 6.4 illustrates a typical joint using MAS1 (TCE 5.7 ± 0.1 MK^{-1} (50-800°C)) as the interlayer. The joining conditions were 1075°C for 45 minutes with an applied load of 1.1 MPa. The higher TCE interlayer has resulted in TCE mismatch cracking perpendicular to the join. The presence of TCE cracks in the glass-ceramic, rather than failure at the interface, implies that the bond between the silicon nitride and the glass-ceramic is roughly as strong as the bonding strength within the glass-ceramic. This suggests that joints with good strengths should be possible. The level of distributed porosity is typical for this glass-ceramic composition.

Figure 6.5 illustrates the microstructure of a joint using glass-ceramic MAS2 (TCE 2.7±0.1 MK^{-1} (50-800°C)). This is closely TCE matched to the silicon nitride. The joining conditions were 1000°C for 45 minutes with an applied load of 1.1 MPa. The joint is free from TCE mismatch cracks, displays excellent interfacial contact and there is no evidence of a reaction occurring at the interface between the silicon nitride and the glass ceramic. The glass-ceramic displays a very low level of residual porosity.

The average particle size of MAS 2 glass powder is ~ 2μm, rather than the ~ 8μm average particle size for MAS1. This reduction in particle size is partly responsible for the reduced amount and size of porosity within the glass-ceramic. The smaller particle size would also be expected to result in a stronger glass-ceramic [6].

Figure 6.6 shows a sample with a final joining temperature of 1100°C (MAS1, 45 minutes, 1.1 MPa applied load). An extensive reaction/diffusion has occurred at the interface between the glass-ceramic and the silicon nitride. There is a band a few microns wide in the silicon nitride next to the interface which appears to be depleted of the residual glass phase. EDX reveals that yttrium is absent from this region. There is a higher level of porosity within the glass-ceramic together with increased porosity at the interface. In comparison with other work (for example Figure 6.17) the extent of the interfacial reaction would suggest that the temperature seen by the sample was in excess of 1200°C. This is confirmed by the microstructure of the glass-ceramic which is similar to that for a pellet of a glass-ceramic of identical composition heat treated for 45 minutes at 1199°C (Figure 5.9).

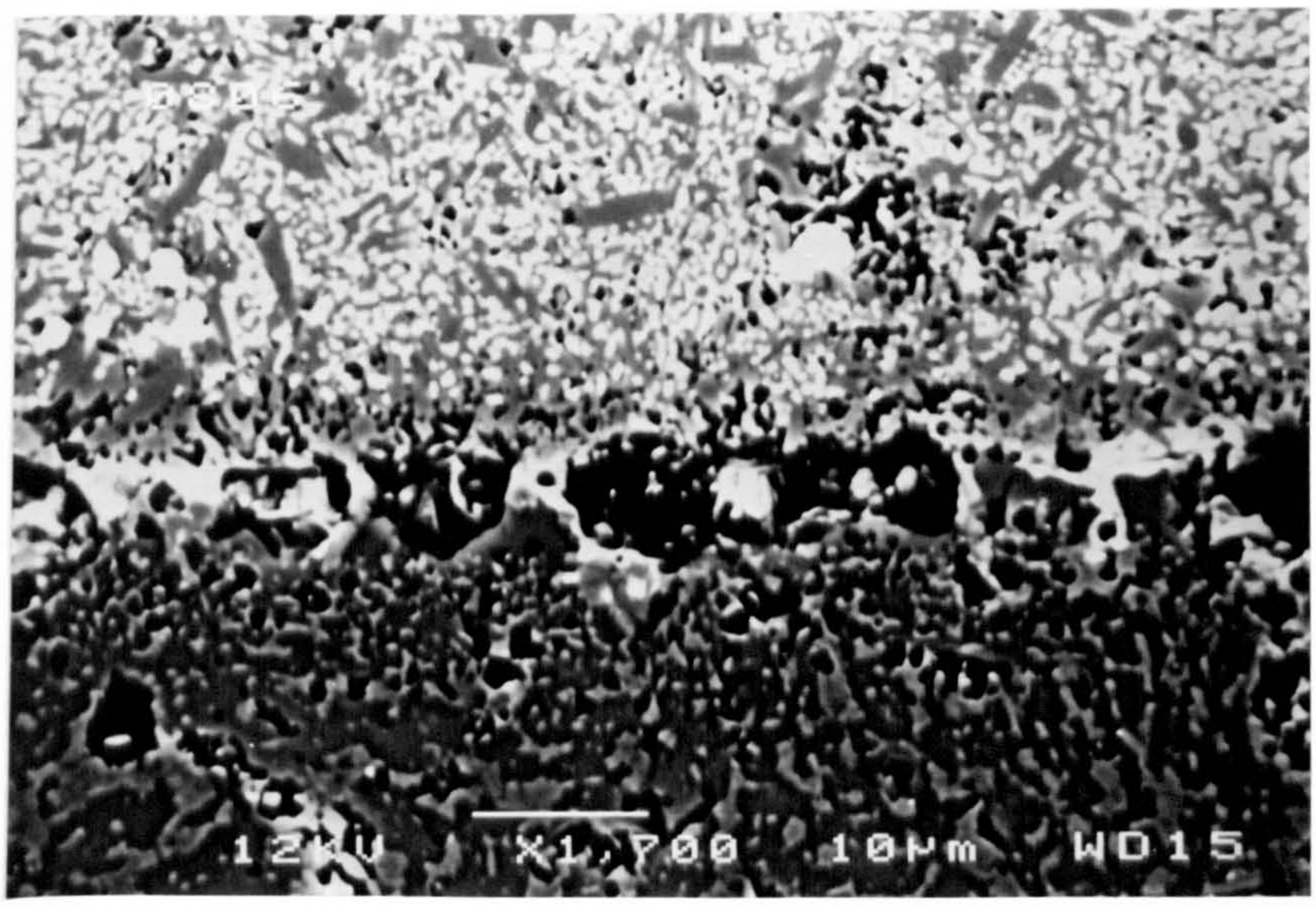

Figure 6.6: Interfacial microstructure between MAS1 and silicon nitride. Joining conditions – 1100°C for 45 minutes with 1.1 MPa applied load

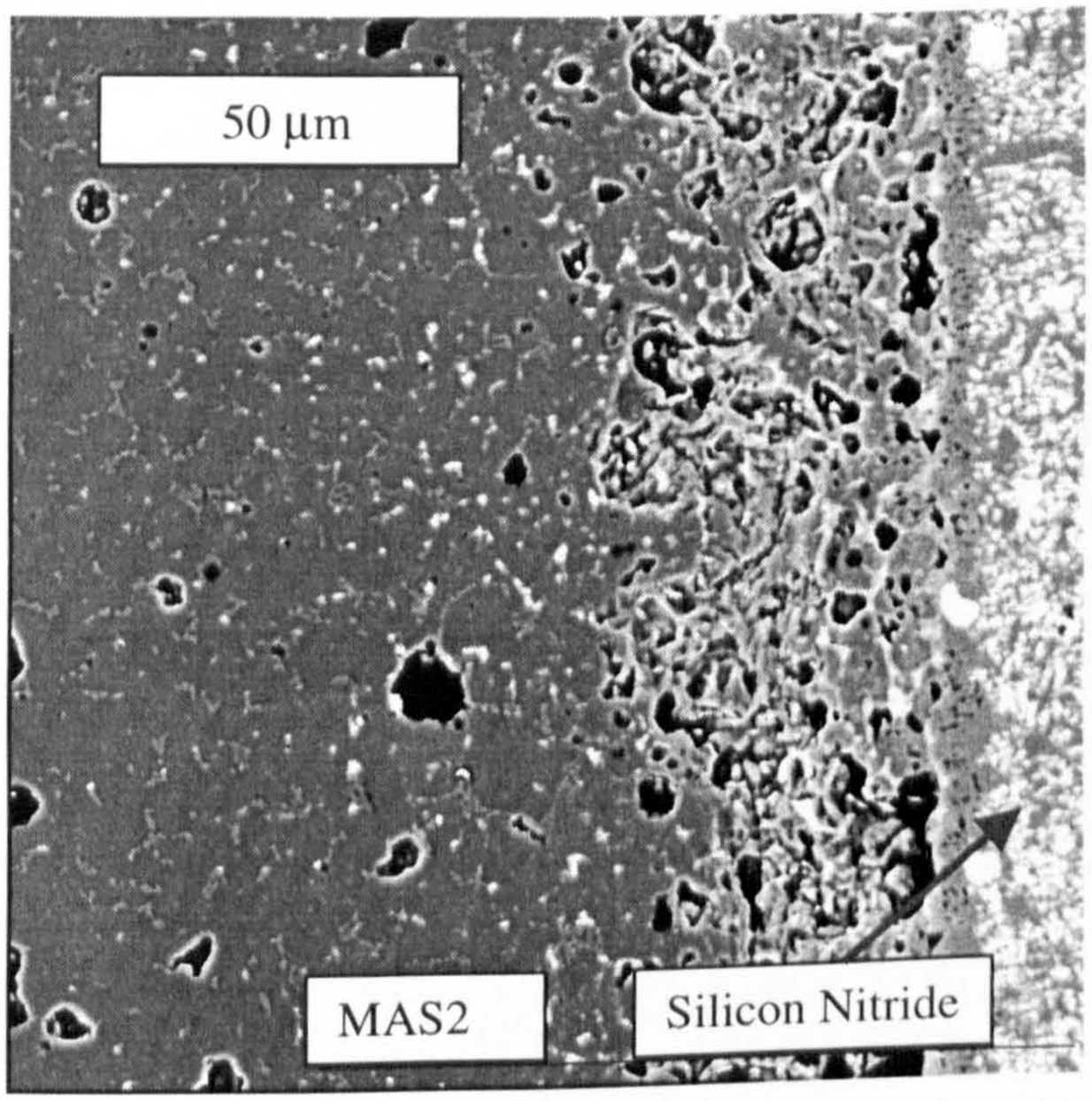

Figure 6.7: Interfacial microstructure between MAS2 and silicon nitride. Joining conditions – 1200°C for 45 minutes with 1.1 MPa applied load.

Figure 6.7 shows the extent of the interfacial reaction between MAS2 and silicon nitride for a joining temperature of 1200°C (45 minutes, applied load 1.1 MPa). The pattern of a 'glass free' reaction zone in the silicon nitride, increased porosity in the glass-ceramic together with further increased porosity at the interface is repeated. This indicates that the interfacial chemistry is very similar for MAS1 and MAS2. An MAS2 sample joined at 1250°C showed extensive porosity both at the interface and throughout the glass-ceramic.

Some results from this furnace using a lower joining temperature are also of interest. They further demonstrate the problems encountered with reproducibility of temperature and also illustrate the complexity of crystallisation in the MAS system.

For example, Figure 6.8 is of a joint produced using an MAS1 interlayer, a recorded joining temperature of 950°C for 30 minutes, and an applied load of 0.55 MPa. A primarily glass interlayer is observed with small isolated crystals, which appear to represent the early stages of crystallisation, occurring at isolated sites located at the former particle surfaces. Figure 6.8 is very similar to the initial stages of crystallisation reported by Bridge [7] for a glass ceramic with similar composition at a temperature of 875°. In comparison to the microstructure reported by Bridge, Figure 6.8 appears to be at a slightly earlier stage in the crystallisation process, and a lower density of nucleation sites appear to be present. This would seem to indicate that the sample has not seen a temperature as high as 950°C. Additional evidence that the temperature seen by the sample is less than 950°C can be obtained by comparing Figure 6.8 to Figure 5.6 (and corresponding XRD trace 5.4) for a pellet of a glass-ceramic of identical composition heat treated for 45 minutes at 945°C, which shows crystallisation having reached a comparatively advanced stage.

Further work involving the use of the brazing furnace was not performed due to the difficulties encountered in obtaining reproducible results. This is believed to be primarily due to the uncertainty over the temperature seen by the sample, although inadequate control of heating and cooling rate may also have contributed. The high heating and cooling rates also mean that damage to the joint due to dynamic thermal shock can not be ruled out. However, work from this furnace did indicate that promising interfacial microstructures could be obtained using an MAS glass-ceramic interlayer to join silicon nitride to itself.

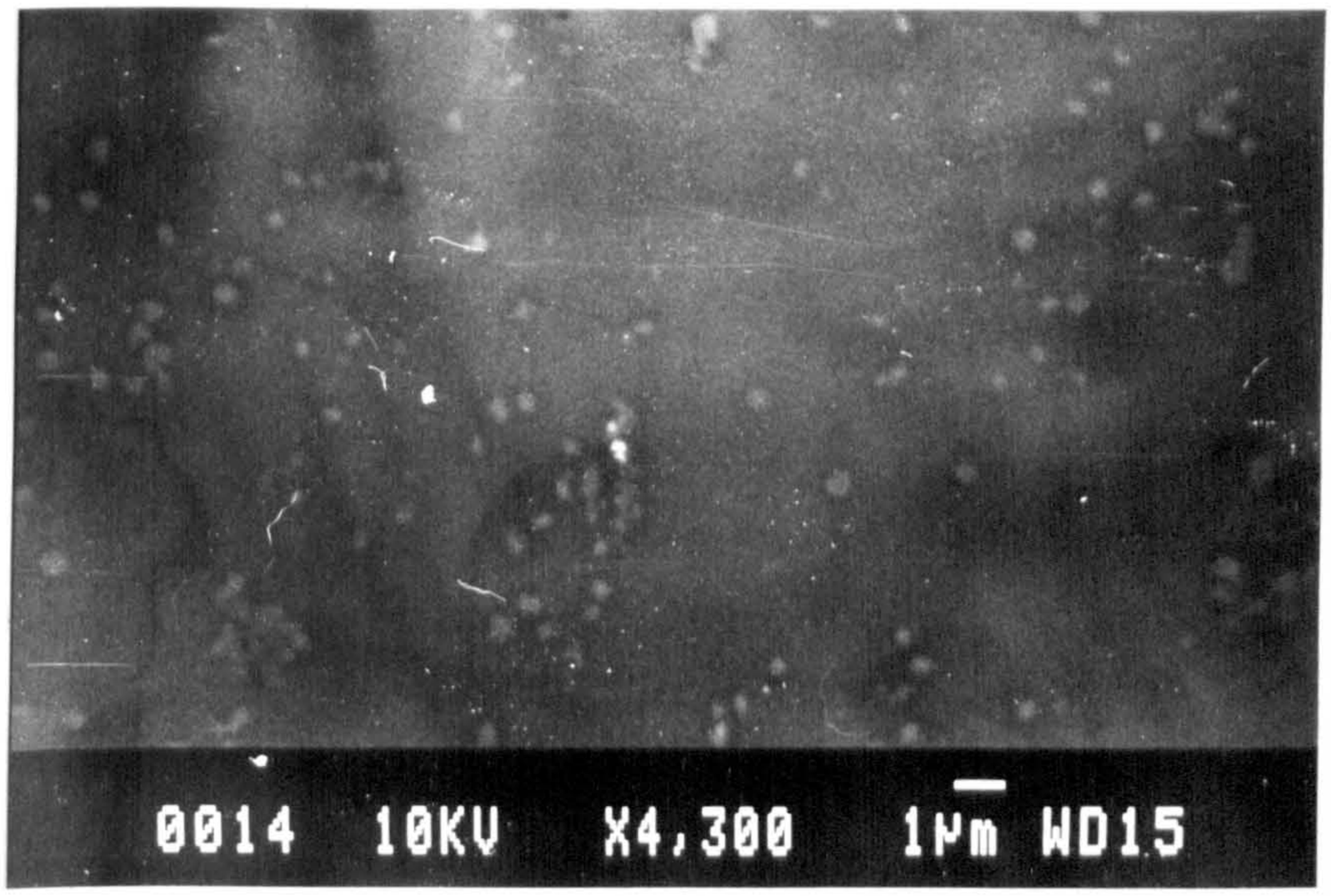

Figure 6.8: Glass interlayer showing the early stages of crystallisation occurring at isolated sites located at the former particle surfaces. Joining conditions - 950°C for 30 minutes with 0.55 MPa applied load.

6.4 Sintering furnace

6.4.1 Sintering furnace - introduction

A high temperature approach to joining using the sintering furnace was motivated by the work of Mecartney [5] (discussed in Section 3.5.3.b) who joined silicon nitride to itself in a nitrogen atmosphere at temperatures from 1550-1650°C with no applied load, using an MAS glass that had its composition matched to the intergranular phase in the silicon nitride. As discussed in Section 3.3.8, strong joints (maximum strength 460 MPa [8]) were obtained.

A tape cast glass-ceramic (MAS1 - with higher TCE than the silicon nitride) was used in this work. A two stage joining heat treatment was used, consisting of an initial degassing hold (typically at 850°C) followed by a joining hold in N_2. The range of joining temperatures investigated was from 1200-1650°C. The heating rates employed were ~ 20°C per minute up to the degassing temp, followed by ~ 15 °C per minute up to the joining temperature. The temperature chosen for the degassing hold (850°C) is above the glass transition temperature of MAS1 but does not result in a

pellet of the glass-ceramic sintering or crystallising. It was not possible to apply a load during the joining hold using this furnace.

6.4.2 Sintering furnace - results

Figure 6.9 shows the centre of a joint joined at 1650°C in N_2. Displacement of the top piece of silicon nitride resulted in a very thin layer of glass between the two pieces of ceramic to be joined. After bonding the join line appears to be "dry" with no glass present and the porous layer at the joint appears to consist of individual β-Si_3N_4 and chromium silicide grains bound together by little, if any, glassy phase. It appears that some form of solution reprecipitation reaction has occurred resulting in β-Si_3N_4 grains having grown across the joint. Magnesium was not present in the original silicon nitride but EDX of the glassy phase in the silicon nitride near to the join indicated that magnesium was present. The magnesium concentration was fairly constant out to ~ 300 μm from the joint, and was still detectable at a significantly reduced concentration ~ 600 μm from the joint. This indicates that some of the glass interlayer has been taken into the residual glass phase within the silicon nitride. Whilst this does not represent a glass-ceramic joint it may be a promising method of bonding silicon nitride to itself for some high temperature applications. Although the addition of Mg to the residual glass phase in the silicon nitride would compromise the high temperature properties of this material, the joint may possess improved high temperature properties. For, example Rouxel et al [9] reported that the exudation of the residual glass in sintered silicon nitride resulted in the creep resistance being improved by a factor of three.

A similar microstructure to Figure 6.9 was reported by Johnson [8] for joining silicon nitride with a thin layer of MAS glass. In this instance, Si_2N_2O grew across the joint rather than Si_3N_4, and the porosity in the joint resulted in a weak joint.

Where a thicker interlayer of glass had been present, there was still some glass left in the joint and a similar microstructure was observed to that reported by Mecartney et al [5]. This was also observed with samples joined at temperatures down to 1350°C. For example, Figure 6.10 shows the microstructure of a sample joined at 1350°C in N_2. Dissolution of the silicon nitride has resulted in silicon nitride crystals interlocking with the glassy bond line which is cracked due to TCE mismatch. The small bright particles in the glass close to the interface are chromium phosphide particles caused by the chromium silicide impurities within the silicon nitride reacting with the nucleating agent in the glass ceramic.

However, some problems were encountered due to uncontrolled crystallisation in the glass interlayer. For example, Figure 6.11 shows one edge of a joint produced at 1450°C, where crystallisation has resulted in a coarse microstructure and cracking of the joint. This occurred in the thinnest region of the joint and it is possible that dissolution of the silicon nitride resulted in saturation of the MAS glass and that crystals have precipitated either at the joining temperature or on cooling.

Figure 6.12 shows the microstructure of a joint produced at 1250°C in nitrogen. At this joining temperature porosity was widespread throughout the MAS.

It is not clear whether this was due to the glass not having sintered well (perhaps due to premature crystallisation) or due to the microstructure having been disrupted by the evolution of gaseous species arising from a reaction between the glass-ceramic and the silicon nitride. The contact between the Si_3N_4 and the MAS was in general poor. However, where contact occurs the MAS has a fine crystalline microstructure and chemical bonding across the interface is by a continuous glassy region that is intergrown with crystalline phases from the MAS and the silicon nitride. Chromium rich particles in the MAS indicate that some dissolution of the silicon nitride has occurred, and there is a band approximately 30 μm thick in the silicon nitride where the YSiAlON glass has been replaced by MgYSiAlON glass with an abrupt change in Y concentration.

If an interfacial microstructure of this nature can be achieved over the entire length of the joint then this may represent a promising joint microstructure if the porosity can also be eliminated from the interlayer. This may be possible by the use of a small applied pressure, or a sintering hold prior to the final bonding hold.

A reduction in the joining temperature to 1200°C resulted in the glass-ceramic neither wetting nor bonding to the silicon nitride.

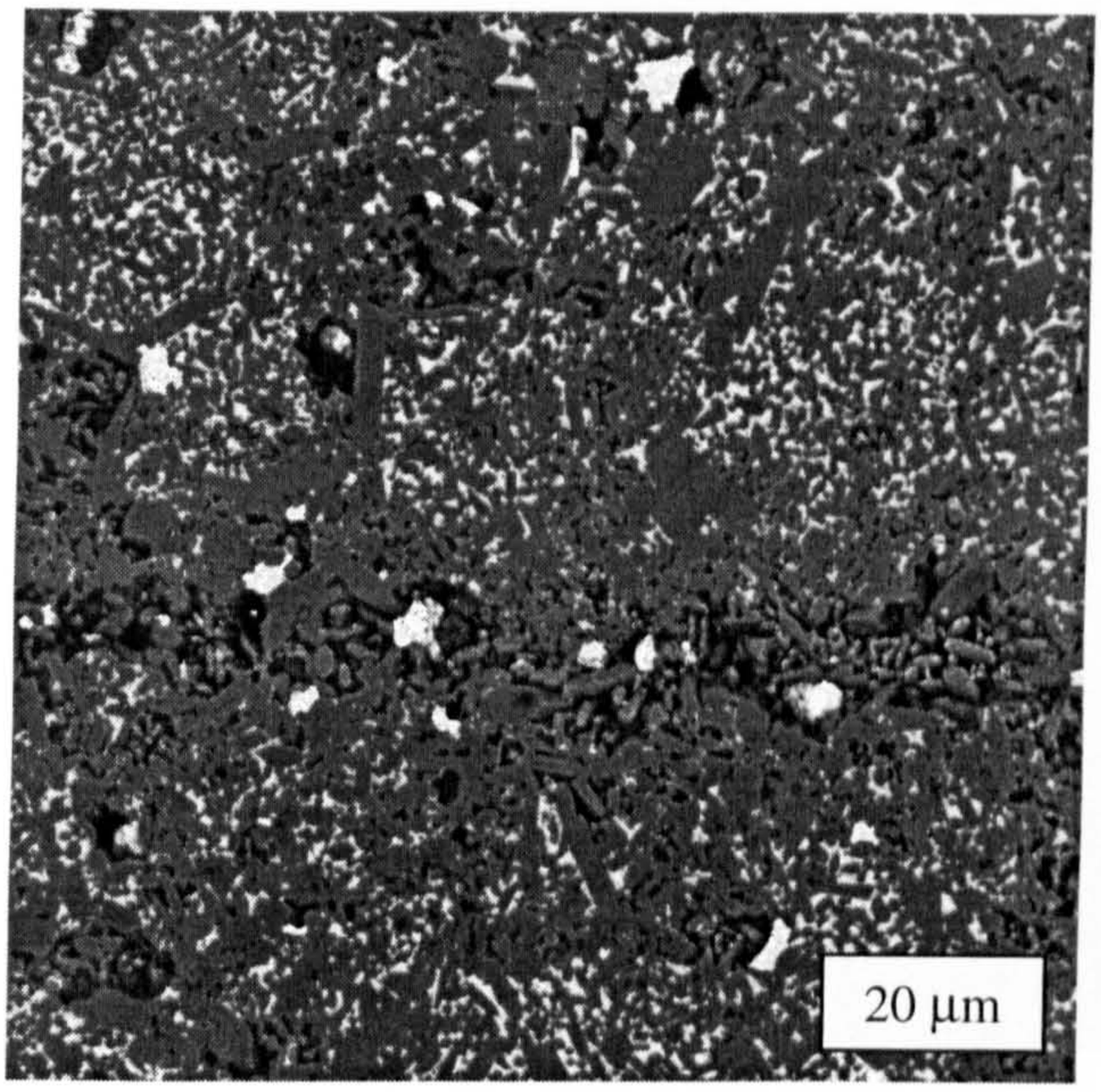

Figure 6.9: Centre of silicon nitride/MAS1/silicon nitride joint joined at 1650°C in a N_2 atmosphere.

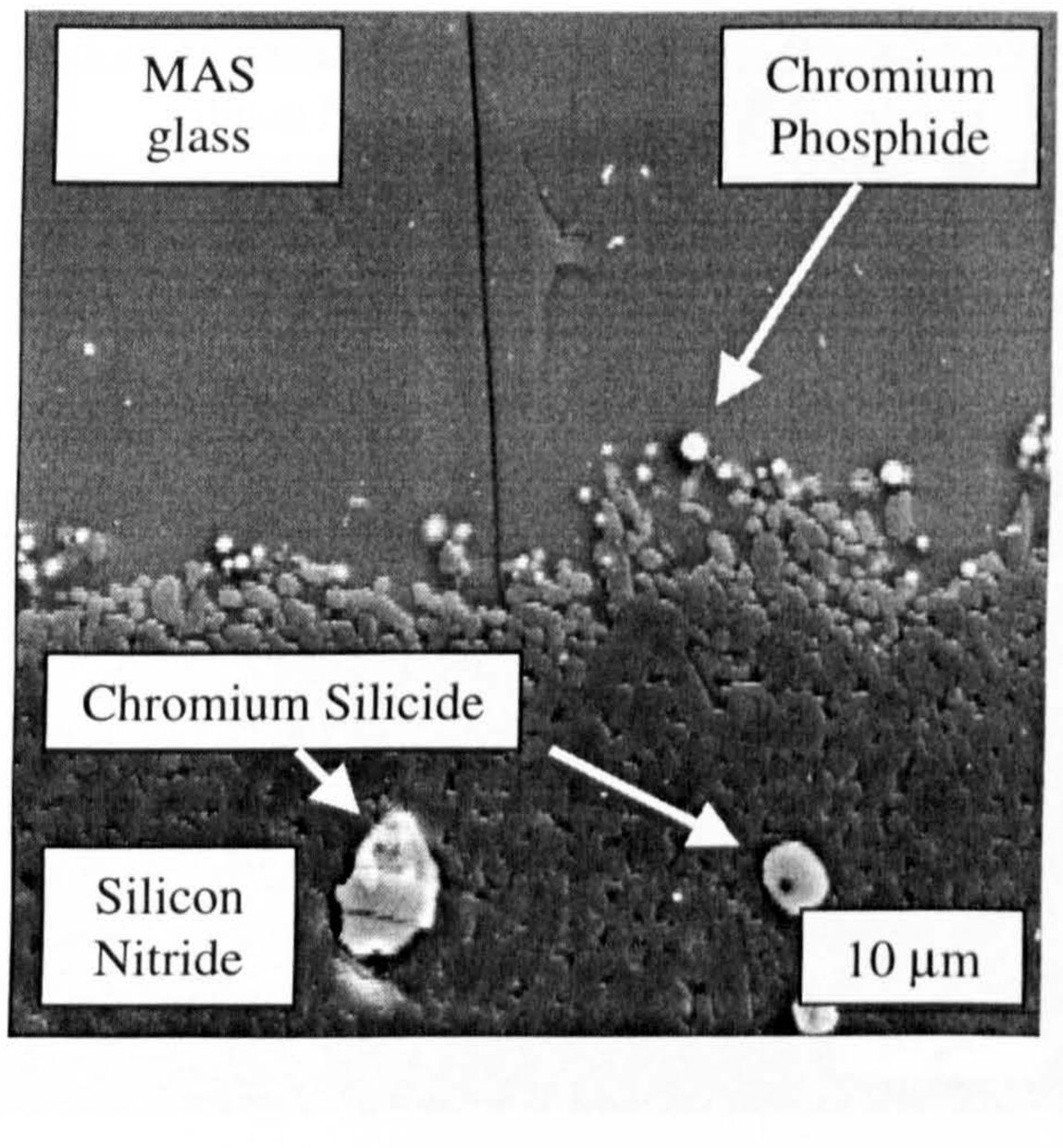

Figure 6.10: Silicon nitride/MAS1/silicon nitride joint produced at 1350°C in N_2. This illustrates silicon nitride crystals interlocking with the glassy bond line, cracking due to TCE mismatch, chromium phosphide particles caused by the chromium silicide impurities in the silicon nitride reacting with the P_2O_5 in the glass-ceramic.

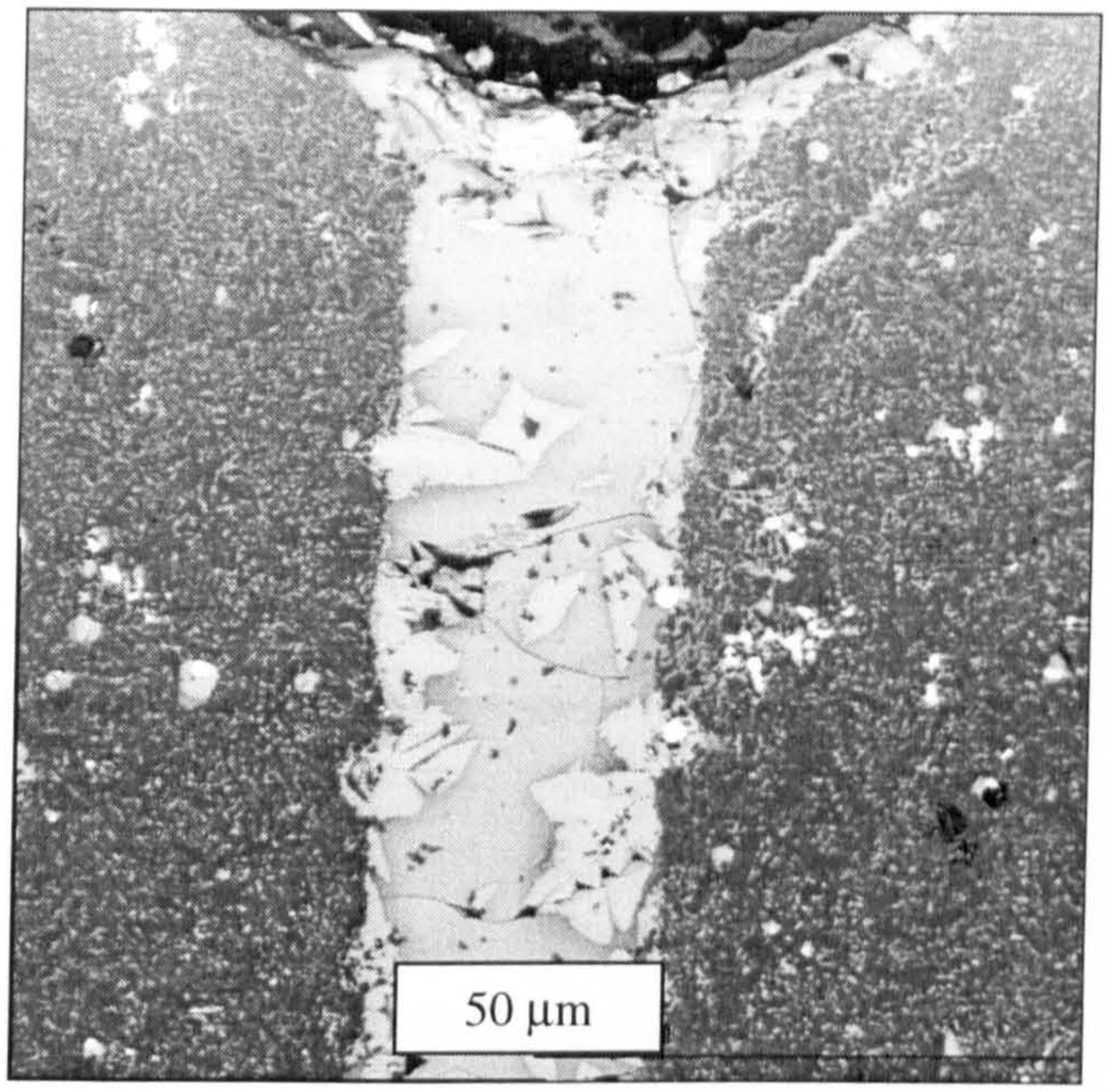

Figure 6.11: Silicon nitride/MAS1/silicon nitride joint produced at 1450°C in N_2 illustrating uncontrolled crystallisation of the glass interlayer.

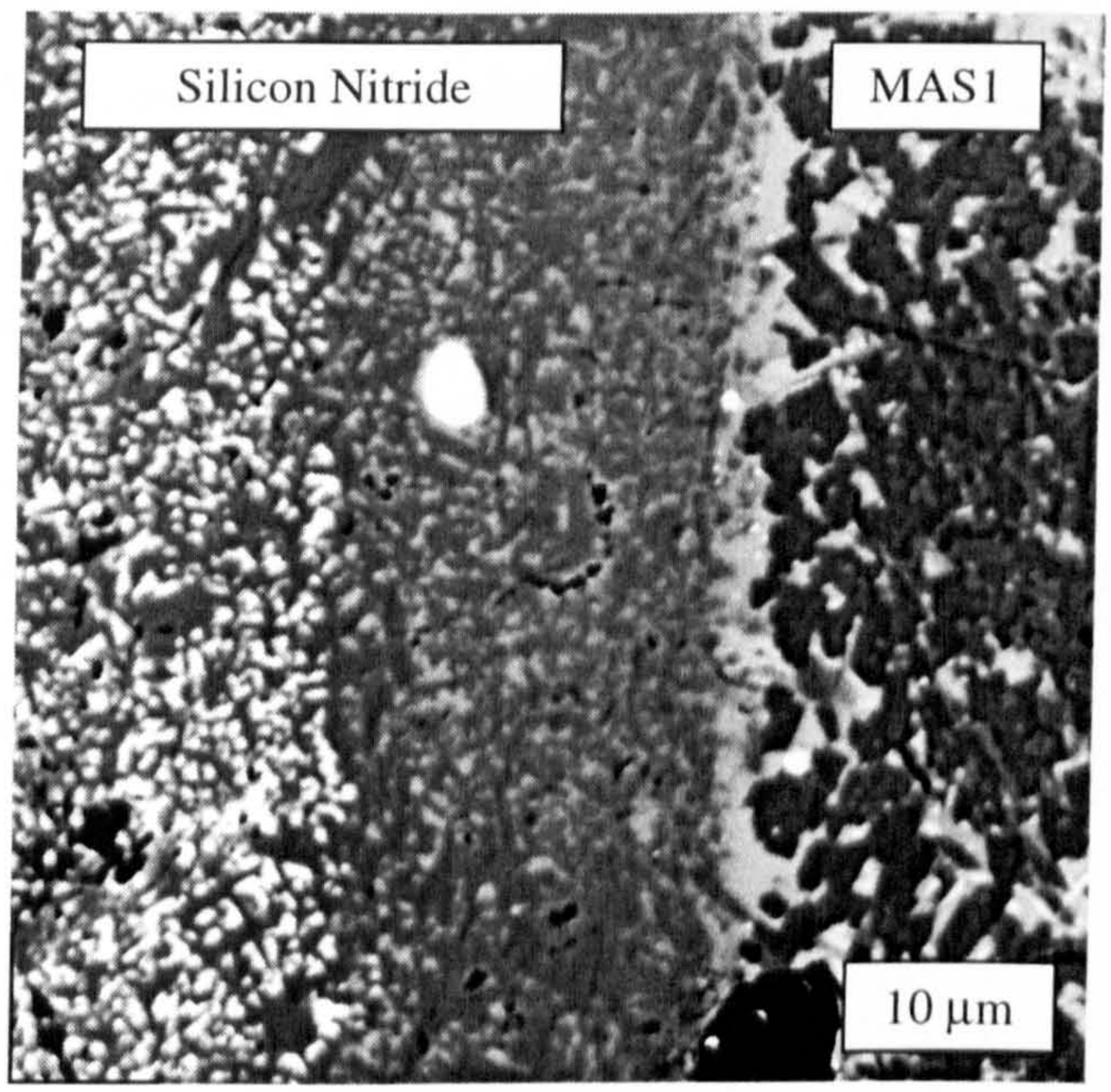

Figure 6.12: Silicon nitride/MAS1 interface (45 minutes, 1250°C, N_2 atmosphere).

6.4.3 Sintering furnace - results from MAS layer on top of sample

Because no load was applied to samples in this furnace it was possible to gain additional information on the wetting and crystallisation behaviour by putting an additional layer of tape cast glass on the top of the silicon nitride.

For example XRD of the MAS1 on the top of the sample corresponding to Figure 6.12 revealed α-cordierite (indialite), proto-enstatite and no other crystalline phases.

Figure 6.13 illustrates classic sessile drop wetting behaviour (viewed from above) for MAS1 glass on top of silicon nitride. This was for the sample subjected to 1450°C for 45 minutes in N_2. This demonstrates that wetting occurs readily, and that the glass cracks on cooling due to TCE mismatch. Similar behaviour was observed for the sample joined at 1350°C for 45 minutes in N_2.

Figures 6.14 and 6.15 show dendritic crystallisation occurring on the surface of MAS1 glass (1350°C, 5 minutes, N_2 atmosphere). Crystallisation appears to have been nucleated from impurities on the surface of the glass. A sample subjected to 1300°C for 45 minutes in N_2 resulted in the widespread crystallisation of large acicular crystals, as illustrated in Figure 6.16. The nature of crystallisation in Figure 6.16 agrees with that found by Watanabe et al [10] for an MAS glass-ceramic with similar composition, where for undercoolings of 70 to 7°C (corresponding to 1300 to 1363°C) crystallisation occurs in a layer growth regime, where "high cordierite crystals develop with an hexagonal prismatic form bound by well developed faces together with long prismatic crystals of proto-enstatite". The disparity between this description of crystal growth and that observed in Figures 6.14 and 6.15 probably indicates that the dendritic features developed on cooling.

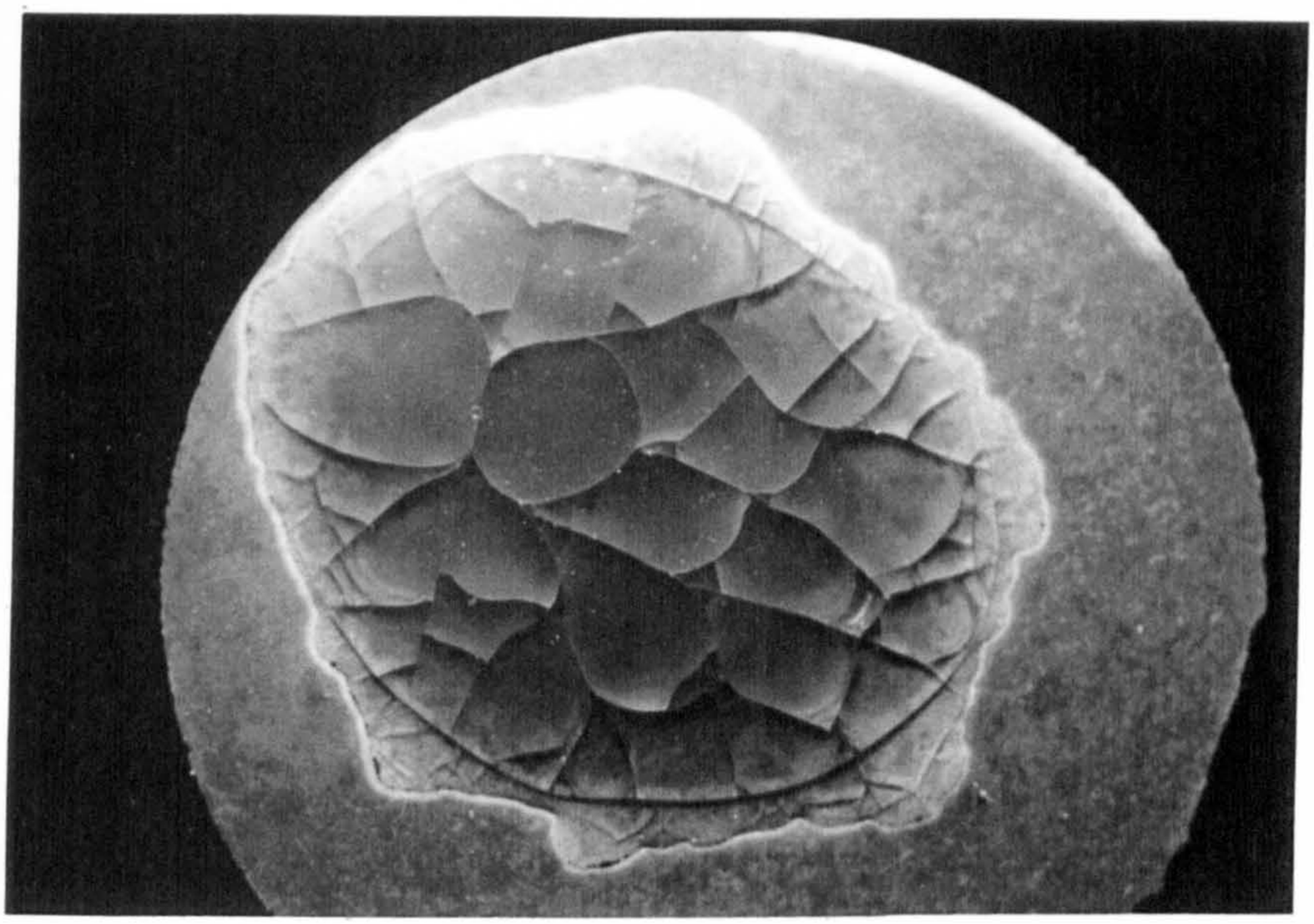

Figure 6.13: Sessile drop of MAS1 glass on top of silicon nitride viewed from above (1450°C 45 minutes N_2 atmosphere). This demonstrates that wetting occurs readily, and cracking arises due to TCE mismatch.

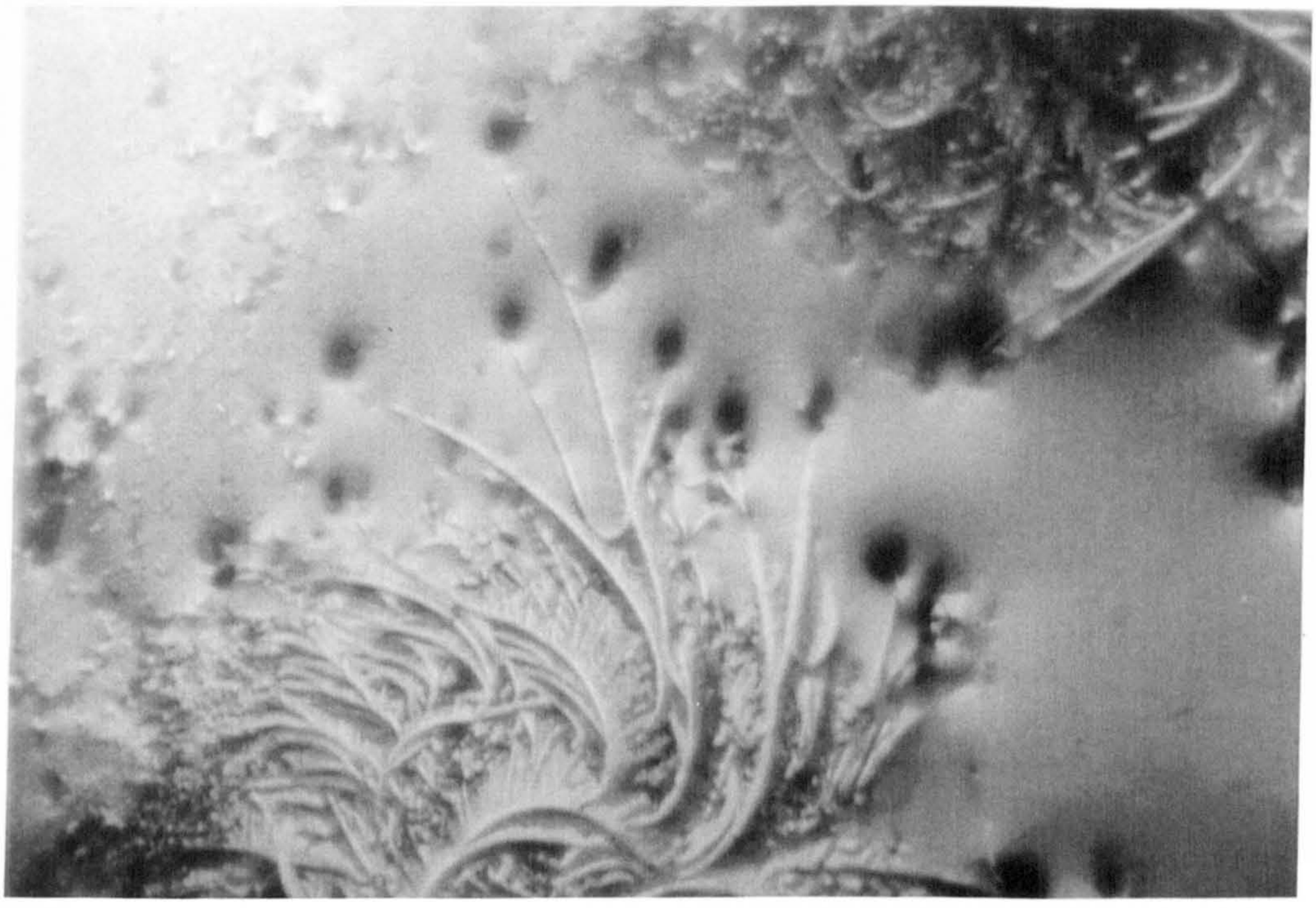

Figure 6.14: MAS1 on silicon nitride - dendritic crystallisation (1350°C, 45 minutes, N_2 atmosphere).

Figure 6.15: MAS1 on silicon nitride - close up of dendritic crystallisation (1350°C, 45 minutes, N_2 atmosphere). ~ 10 μm

Figure 6.16: MAS1 on silicon nitride - large acicular crystals (1300°C, 45 minutes, N_2). ~ 30 μm

6.4.4 Sintering furnace - discussion

The "dry joint" microstructure illustrated by Figure 6.9 has not been developed further, although it is possible that for some applications the production of a similar joint would result in excellent creep behaviour for high temperature applications.

The glass joints with microstructures typified by Figure 6.10 have also not been pursued further because similar glass joints have already been successfully reported in the literature [8]. In addition, solutions involving joining at similar temperatures (but with a small applied load) result in mechanical properties superior to those that could be obtained using a glass interlayer [3].

The instability of glasses towards crystallisation and the resulting loss of microstructural control illustrates one of the problems of using glasses for high temperature applications. Although the initial composition may be a stable glass, compositional change due to selective volatility, diffusion or dissolution of neighbouring materials, may make the glass less stable towards devitrification. This is particularly a problem for a thin glass interlayer where dissolution and diffusion cause more significant compositional changes and a high surface area is provided for surface nucleation. The increased thermal stability of a glass-ceramic compared to a glass interlayer is a significant advantage for high temperature applications.

The formation of a satisfactory glass-ceramic interlayer and the use of temperatures lower than 1250°C requires an applied load.

6.5 Vertical alumina tube furnace

6.5.1 Vertical alumina tube furnace - experimental approach

Due to problems previously encountered with lack of reproducibility and the importance of obtaining consistent sample microstructures prior to mechanical testing, experimental effort was focused on developing a robust experimental procedure. The inherent complexity of a multi-stage joining operation lead to the consideration of designed experiments based on fractional factorial methods to address the problem of reproducibility.

In the current work, a standard experiment (L8) based on the Taguchi method was used to optimise the joining parameters prior to the production of samples for

mechanical testing. The principle difference between the Taguchi method and other fractional factorial designs is that, rather than attempting to determine and control the sources of variation, the focus of the Taguchi method is to make the process or product insensitive to the sources of variation. The advantage of using the Taguchi method is that many of the benefits of a partial factorial method can be realised using a standard array and the resulting analysis is relatively straightforward. As for other fractional factorial methods, multiple responses can be measured in a single experiment.

The Design and Analysis of Experiments by Sir R.A.Fischer [11] is recommended as a good introduction to designed experimentation. A particularly clear guide to the use of Taguchi methods is given by Phadke [12], and a critical discussion of the Taguchi method is given by Montgomery [13].

Due to lack of space and the flaws in the implementation of the L8 Taguchi experiment performed in the current work, the full results are not reported here. However, the result from the Taguchi experiment together with modifications to the furnace detailed in Section 4.3.4 and an increase in the applied load to 2.5 MPa, allowed consistent results with reproducible microstructures to be obtained.

The following joining cycle was settled on, as a result of the Taguchi experiment. After an initial slow heating rate at 5°C min^{-1} to a 45 minute degassing hold in a recorded vacuum of ~ 0.1 Pa at 650°C (which is below the glass transition temperature for the interlayer), the joining furnace was flushed with nitrogen and backfilled to maintain a slight overpressure of nitrogen. This was followed by a faster ramp at 13°C min^{-1} to the joining temperature which was held for 45 minutes. The furnace was then cooled at 5°C min^{-1}. A uniaxial joining pressure of 2.5 MPa was maintained throughout the run.

A 15 mm diameter cylindrical butt joint geometry was chosen. With mechanical testing in mind the initial glass powder was applied in the form of a cast tape, this enabled consistent and even thickness of the interlayer to be achieved. The resulting glass ceramic has a similar TCE mismatch with the silicon nitride as that reported by Johnson [8] who reported excellent joint strengths using a glass interlayer. The pressure of 2.5 MPa was chosen to be slightly higher than that reported by Walls and Ueki [2] (2 MPa) to allow for some of the applied load to be taken up by the sliding end seal arrangement.

6.5.2 Vertical alumina tube furnace - results

Joining at temperatures above ~1200°C resulted in increased porosity in the glass-ceramic interlayer, with a further increase in porosity concentrated close to the interface between the silicon nitride and the glass-ceramic. The yttrium aluminosilicate grain boundary glass in the silicon nitride adjacent to the interlayer also migrates to the interlayer. An example joint microstructure for a joining temperature of 1230°C is shown in Figure 6.17. Temperatures significantly below 1200°C enabled joints free from this problem to be produced, an example joint microstructure is shown in Figure 6.18. Excellent interfacial contact is displayed and the joint is free from gross defects other than TCE mismatch cracking when a glass-ceramic of mismatched TCE is used.

6.6 Interfacial chemistry

The reactions and development of porosity occurring at the interface between the glass-ceramic and the silicon nitride can be explained using Equation 6.1 which was suggested by Brittain [14] to occur when silicon nitride was glazed with an MAS glass, or for commercial MgO densified silicon nitride. This was supported by measurements of Mg and SiO vapour pressure over samples, using Knudsen mass spectroscopy.

$$Si_3N_4(s) + 3\,MgO(s) = 3SiO(g) + 3\,Mg(g) + 2N_2(g) \qquad (6.1)$$

Using thermodynamics it is possible to estimate the equilibrium partial pressure of Mg due to the above equation. The following calculation represents a reworking of a method from Kubaschewski and Alcock [15] for the free evaporation of an oxide ceramic in a vacuum.

Using JANAF table E, the standard Gibbs free energy as a function of temperature (ΔG_T^0) can be estimated for Equation 6.1. The Gibbs free energy of the MgO environment in the glass is assumed to be similar to that in crystalline MgO. ΔG_T^0 is related to the equilibrium constant K, the absolute temperature T and the gas constant R by Equation 6.2.

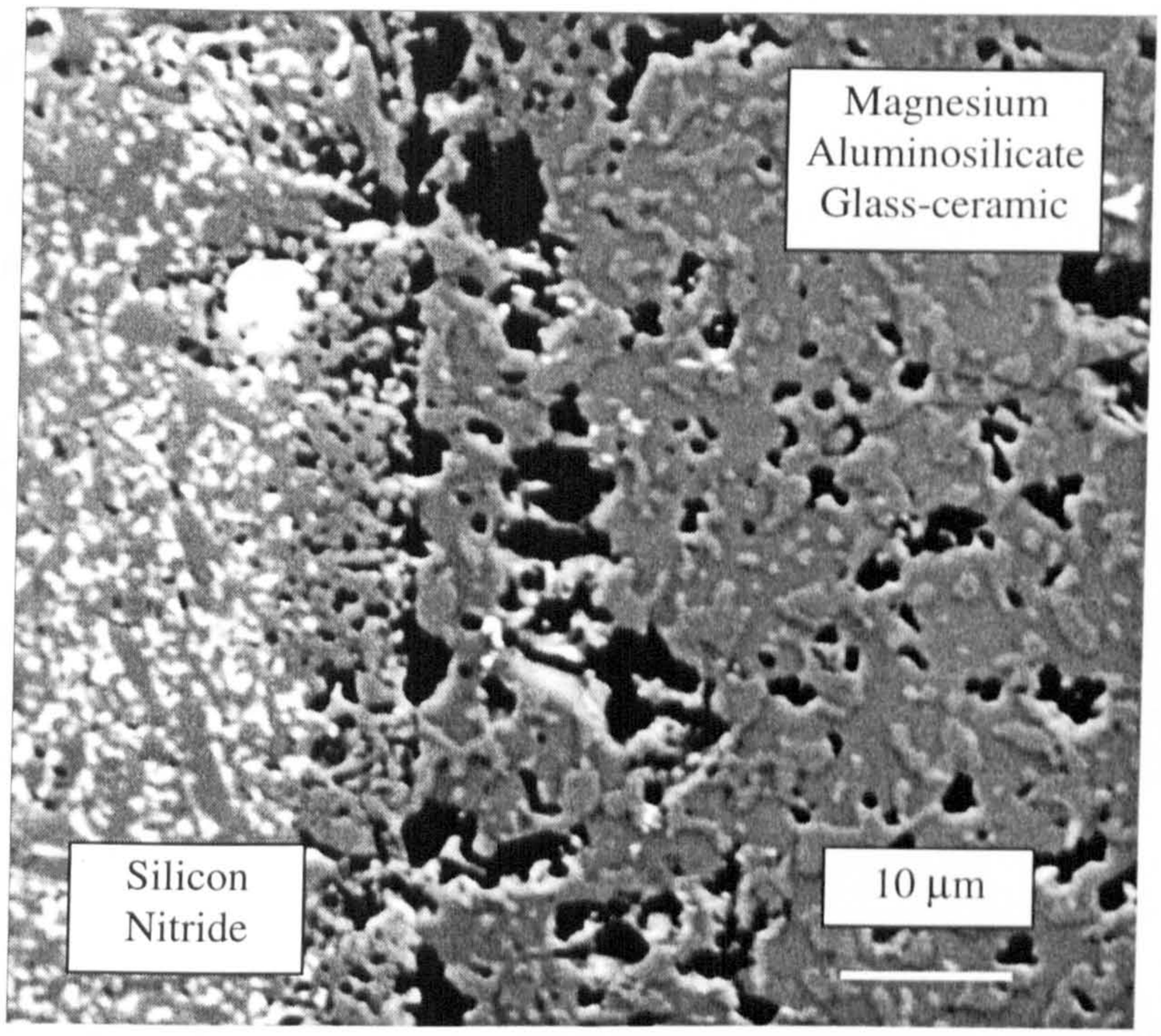

Figure 6.17: Joint microstructure for a joining temperature of 1230°C (N_2 atmosphere, 2.5 MPa applied load).

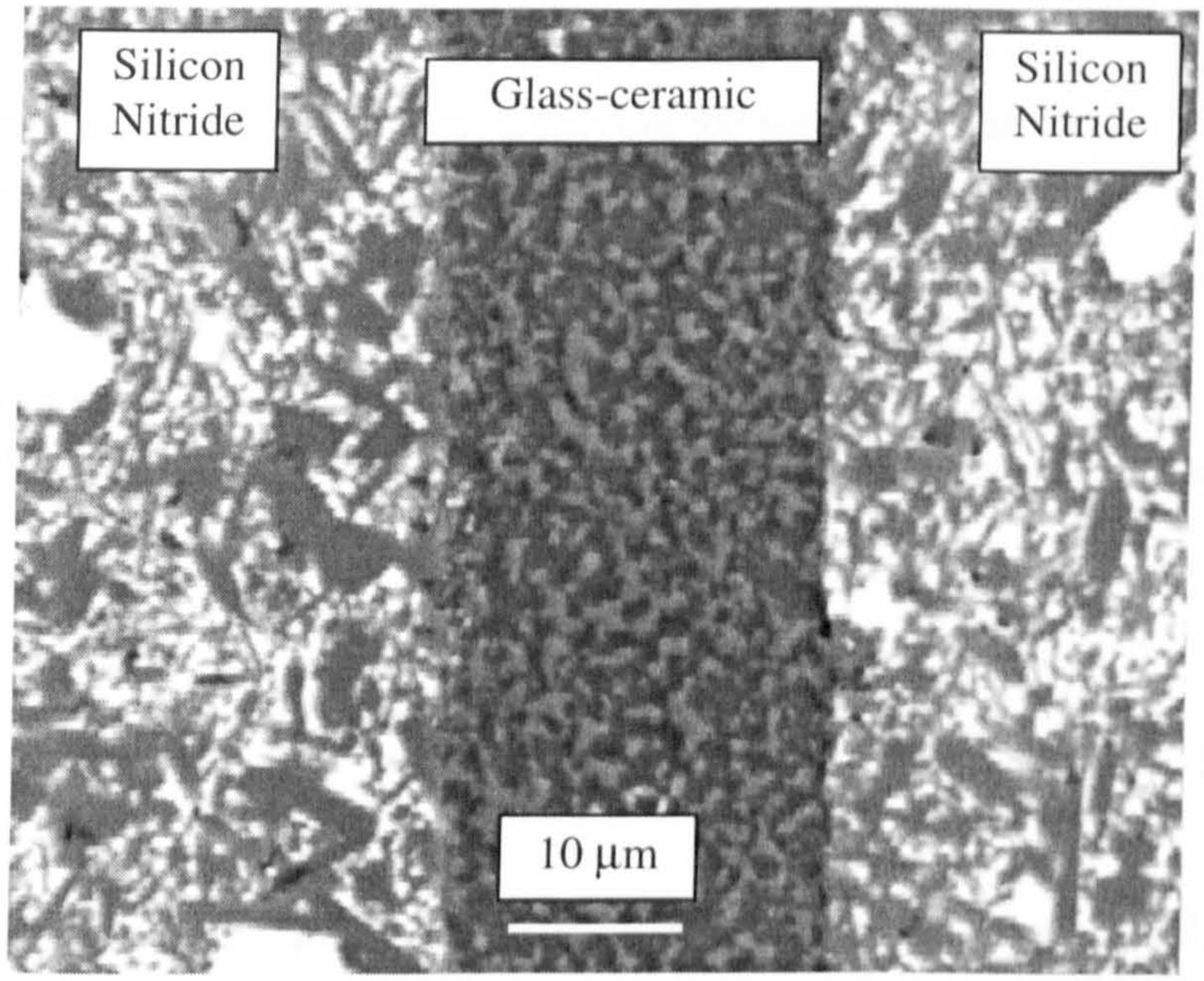

Figure 6.18: Joint microstructure for a joining temperature of 1150°C (N_2 atmosphere, 2.5 MPa applied load).

$$\Delta G_T^0 = -RT \ln K \tag{6.2}$$

The equilibrium constant K is given by Equation 6.3, where p and a represent the equilibrium partial pressures and activities.

$$K = \frac{(pSiO)^3 (pMg)^3 (pN_2)^2}{(aSi_3N_4)(aMgO)^3} \tag{6.3}$$

Equation 6.1 also determines the relative rates at which Mg atoms and SiO and N_2 molecules leave the surface. For example, the relationship between Mg atoms and N_2 molecules is given by Equation 6.4, and that between Mg atoms and SiO molecules by Equation 6.5.

$$\frac{n_{Mg}}{n_{N_2}} = \frac{m_{Mg}}{M_{Mg}} \frac{M_{N_2}}{m_{N_2}} = \frac{3}{2} \tag{6.4}$$

$$\frac{n_{Mg}}{n_{SiO}} = \frac{m_{Mg}}{M_{Mg}} \frac{M_{SiO}}{m_{SiO}} = 1 \tag{6.5}$$

n = the number of atoms/molecules leaving the surface in unit time
M = the atomic/molecular weight
m = the mass leaving the surface in unit time

The weight of each constituent leaving unit area in unit time is given by Knudsen's equation. This is shown for Mg in Equation 6.6. Similar equations exist for SiO and N_2.

$$m_{Mg} = 44.4 p_{Mg} \sqrt{\frac{M_{Mg}}{T}} \tag{6.6}$$

By suitable substitution and rearrangement the partial pressure of Mg can be expressed in the form of Equation 6.7.

$$p_{Mg} = [[\exp(\frac{\Delta G_T^0}{RT})] \frac{9}{4} \frac{(M_{Mg})^{5/2}}{(M_{N_2})(M_{SiO})^{3/2}} (a_{MgO})^3 (a_{Si_3N_4})]^{1/8} \tag{6.7}$$

If an estimate is made for aSi_3N_4 and $aMgO$, this enables the partial pressure of Mg to be estimated as a function of temperature. Figure 6.19 shows the calculated partial pressure assuming that aSi_3N_4 and $aMgO$ are both equal to 1, and assuming that aSi_3N_4 is equal to 1 and that $aMgO$ is equal to 0.05. The two values chosen for $aMgO$ (which is unknown) were selected to illustrate the sensitivy of the calculation to $aMgO$. It can be seen that there is some sensitivity to the estimated activity. If the calculated partial pressure of Mg is compared to the estimated atmospheric pressure in the furnace (assumed to be ~ 1 Pa - allowing the pressure seen by the sample to be an order of magnitude higher than that recorded at the head of the diffusion pump) then the partial pressure is predicted to become significant at temperatures around 1100°C.

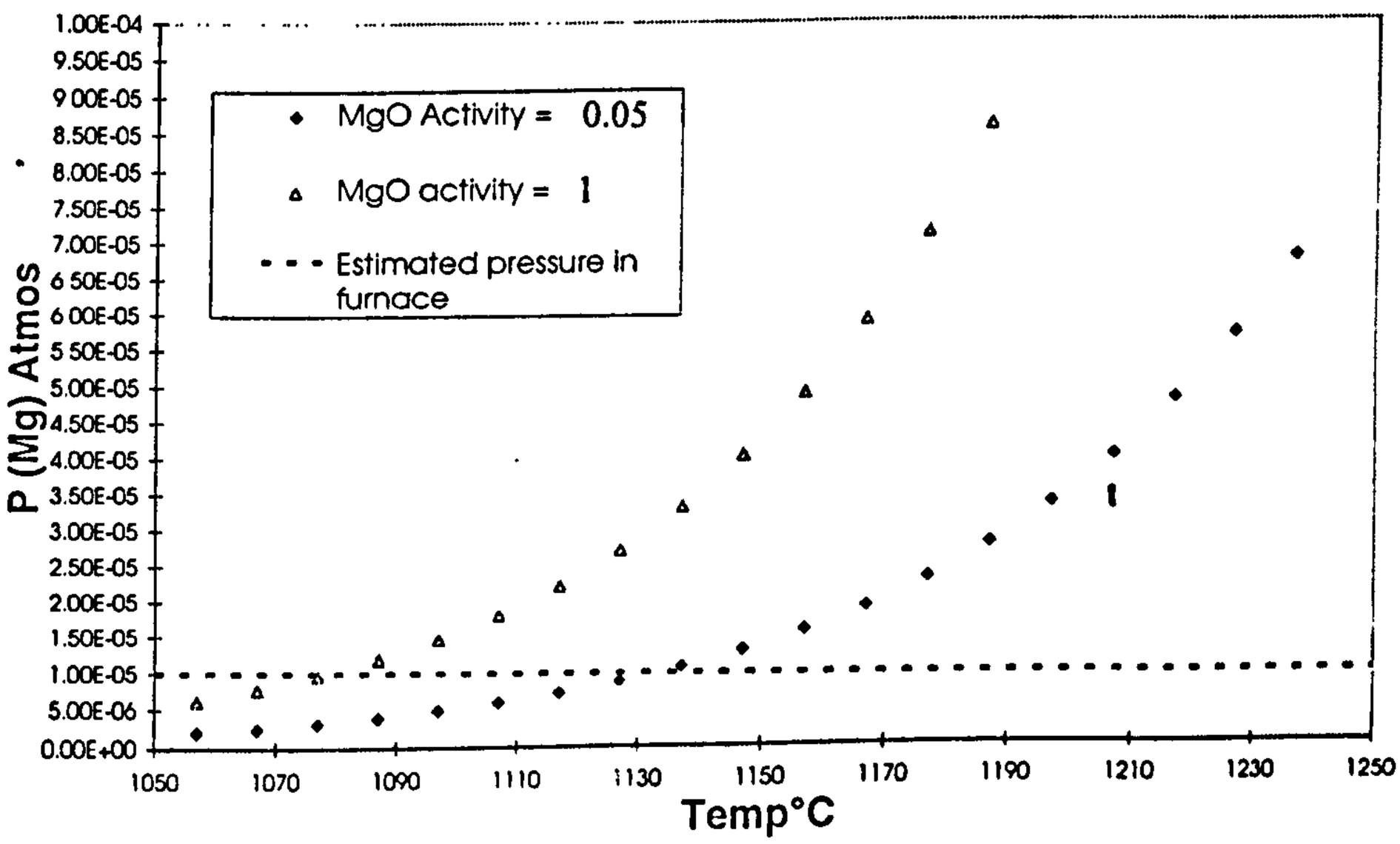

Figure 6.19: Partial pressure of Mg due to Equation 6.1 as a function of T.

This calculation must be viewed as a guide to the nature of what is occurring and the 'critical temperature' as an estimate, as there are many assumptions that will affect the calculation (eg: the assumption that the Gibbs free energy of the MgO environment in the glass similar to that in crystalline MgO, the estimates for aSi_3N_4 and $aMgO$, and the pressure seen by the sample). In addition the possible effects of Y, N, P and B have not been considered.

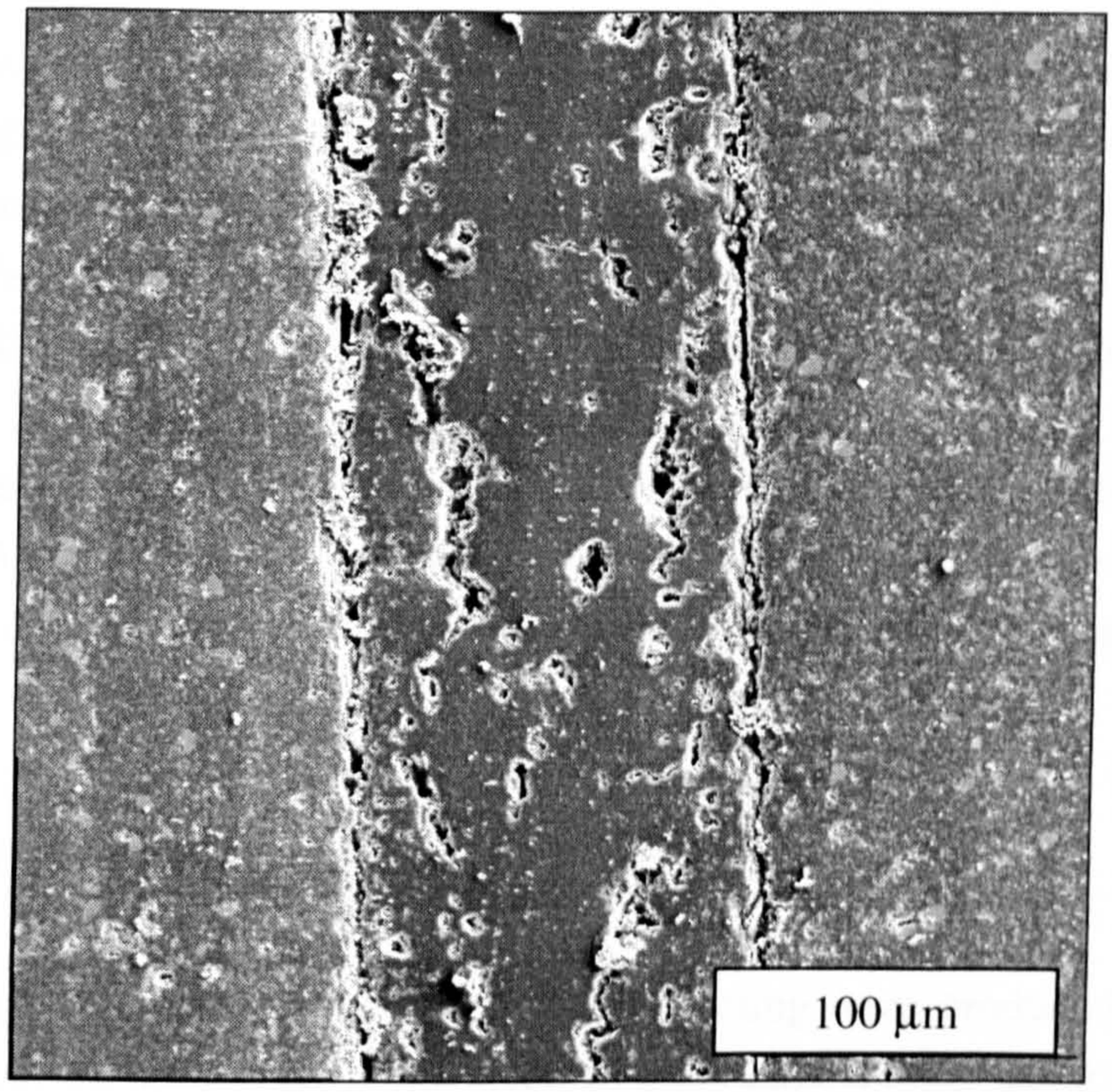

Figure 6.21: Joint microstructure for a joining temperature of 1198°C (Vacuum ~ 1 Pa, 2.5 MPa applied load.

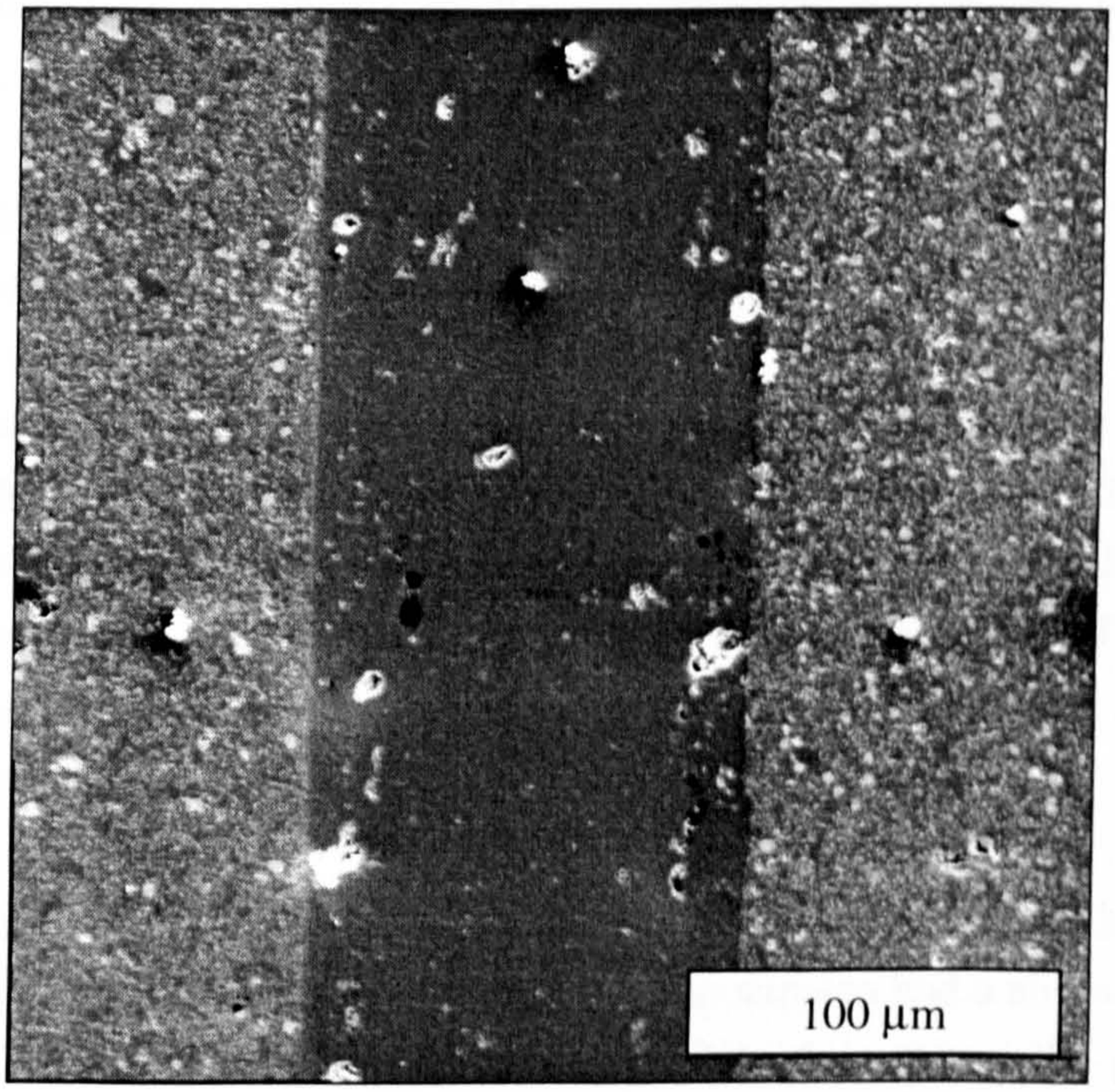

Figure 6.22: Joint microstructure for a joining temperature of 1190°C (N_2 atmosphere, 2.5 MPa applied load).

Nevertheless, the results of the calculation agree fairly well with experimental findings, although the critical temperature appears to be nearer 1200°C. Figure 6.20 shows a sample joined in a vacuum at 1198°C, a significant level of porosity is observed both in the MAS and concentrated at the interface between the silicon nitride and the glass-ceramic. Figure 6.21 shows a sample joined in N_2 at 1190°C, only a low level of residual porosity is observed in the glass-ceramic with no porosity generated at the interface. As expected the effect of a N_2 atmosphere is to suppress Equation 6.1 to higher temperatures. The porous interfacial microstructure typified by Figure 6.20 was not encountered in a N_2 atmosphere at temperatures of below 1230°C.

Mechanical testing

All joining runs for samples for 4-pt flexure testing were produced in the alumina tube furnace, using an MAS1 interlayer, in a N_2 atmosphere, using the joining heat treatment derived from the Taguchi experiment and final joining temperatures of 1167, 1100 and 1050°C. The observed MAS and interfacial microstructures were consistent with those seen both in Section 5.4, and the development work earlier in this chapter, with the interlayer cracked perpendicular to the join due to TCE mismatch.

Mechanical testing was also performed on silicon nitride, both in the as-received condition and after an 1167°C joining heat treatment.

The mechanical testing was performed on three separate occasions at TWI who are an ISO 9000 accredited test centre. As discussed in Section 4.4.2 the testing was performed in accordance with Japanese standard JIS R 1601 with the exception that for the first two batches of testing, the samples were not bevelled. The samples were polished on the tensile and two adjacent faces. The order of testing and the numbers of samples tested are given in Table 6.2 below.

The standard JIS R 1601 specifies a sample cross-section of 4 mm by 3 mm. Often, as a result of sample preparation, the finished specimens had a slightly smaller cross-section. Due to the low Weibull modulus of the joints (and the glass-ceramic) a reduction in the size can have a significant effect on the strength. Results are reported both as-tested and as-'corrected' to the standard sample size using the Weibull size-strength relationship (Equation 4.10). For joints, the Weibull modulus has been estimated using the Weibull modulus of J1100 (m = 6, ignoring the first six

samples where testing problems were encountered). For silicon nitride an estimate of the Weibull modulus of 20 was used. If this correction is not applied, the strength variation which is a function of the joining heat treatment is confused with the variation due to the volume under test.

Table 6.2: Chronological order of mechanical testing

Testing Order	Sample description	Number of tests	Reference*
I	Joint 1167	6	J1167
I	Joint 1100	15	J1100
II	Silicon nitride as received	14	SN
II	Silicon nitride after 1167°C joining heat treatment	14	SN1167
III	As received silicon nitride (with bevel)	6	SNB
III	Joint 1100 (with bevel)	5	J1100B
III	Joint 1050 (with bevel)	11	J1050B

* SN = silicon nitride, J = joint, B = bevelled and '1100' = final joining temperature.

A correction of this nature is particularly important when performing significance testing between populations. In the current work significance testing has been performed using Student's t test, as a function of the number of degrees of freedom (n), as adjusted for small sample sizes using Bessel's correction [16].

6.7 Testing of joints

For the silicon nitride/MAS1/silicon nitride joints significant sample losses were encountered during specimen preparation. The number of joints to survive was as follows: J1100 (15/16), J1167 (6/16), J1100B (5/12) and J1050B (11/12). The high failure rate is believed to be due to the low strength and fracture toughness of the interlayer material in comparison with the silicon nitride. A crack initiated in the silicon nitride encounters much less resistance to crack propagation in the glass-ceramic interlayer.

Figure 6.22 shows the strength of J1167 and J1100 samples in the order tested. There appears to be a clear division in strength between the first six, and the last nine J1100 samples, illustrating either a problem due to specimen preparation or testing.

Figure 6.22: Specimen strength of J1167 and J1100 in testing order.

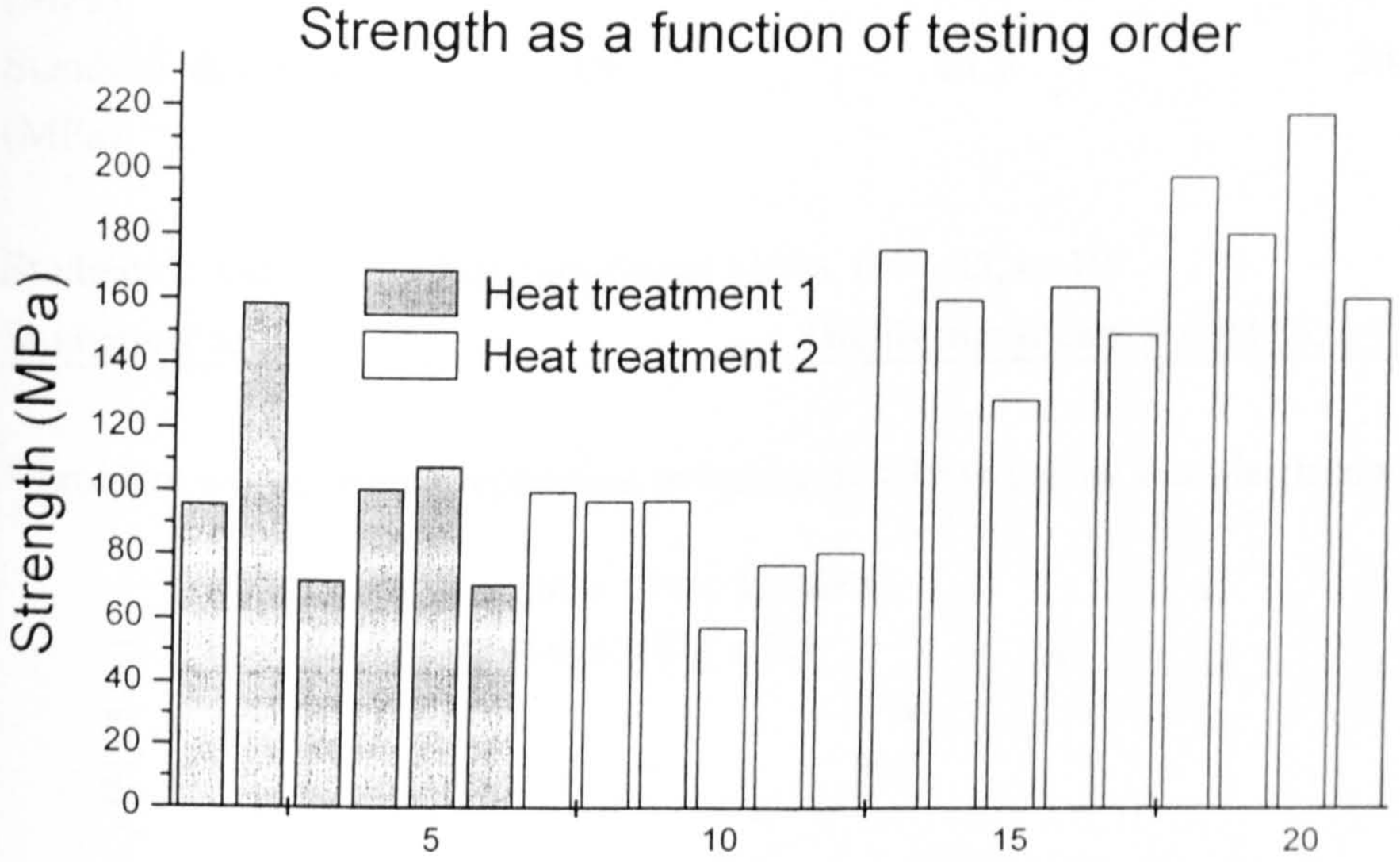

Table 6.3 gives the as-measured strengths and Table 6.4 the strengths as adjusted for sample volume, illustrating that there is less than a 1 in 2000 chance that all J1100 samples represent the same population. A Weibull plot of the strengths of the last nine J1100 samples tested is shown in figure 6.23. This gives a Weibull modulus of 6.2 ± 2.1.

Table 6.3: As-measured sample strengths for J1167 and J1100.

	J1167*	J1100*	J1100
Number of samples	6	6	9
Mean strength (MPa)	101	85	171
Standard deviation (MPa)	32	17	27

Table 6.4: Student's t test illustrating preparation or testing bias (all strengths as adjusted for sample volume).

	1st six samples J1167*	2nd six samples J1100*	Last 9 samples J1100
No. of samples	6	6	9
Mean strength (MPa)	94.2	78.5	159.8
Standard deviation (MPa)	29.9	14.9	24.2
Students 't' test	Not significant >10%, t = 1.05, n=10		
Students 't' test		Highly significant > 0.05 %, t = 6.8, n =13	

* problem with sample preparation or testing resulting in low sample strengths.

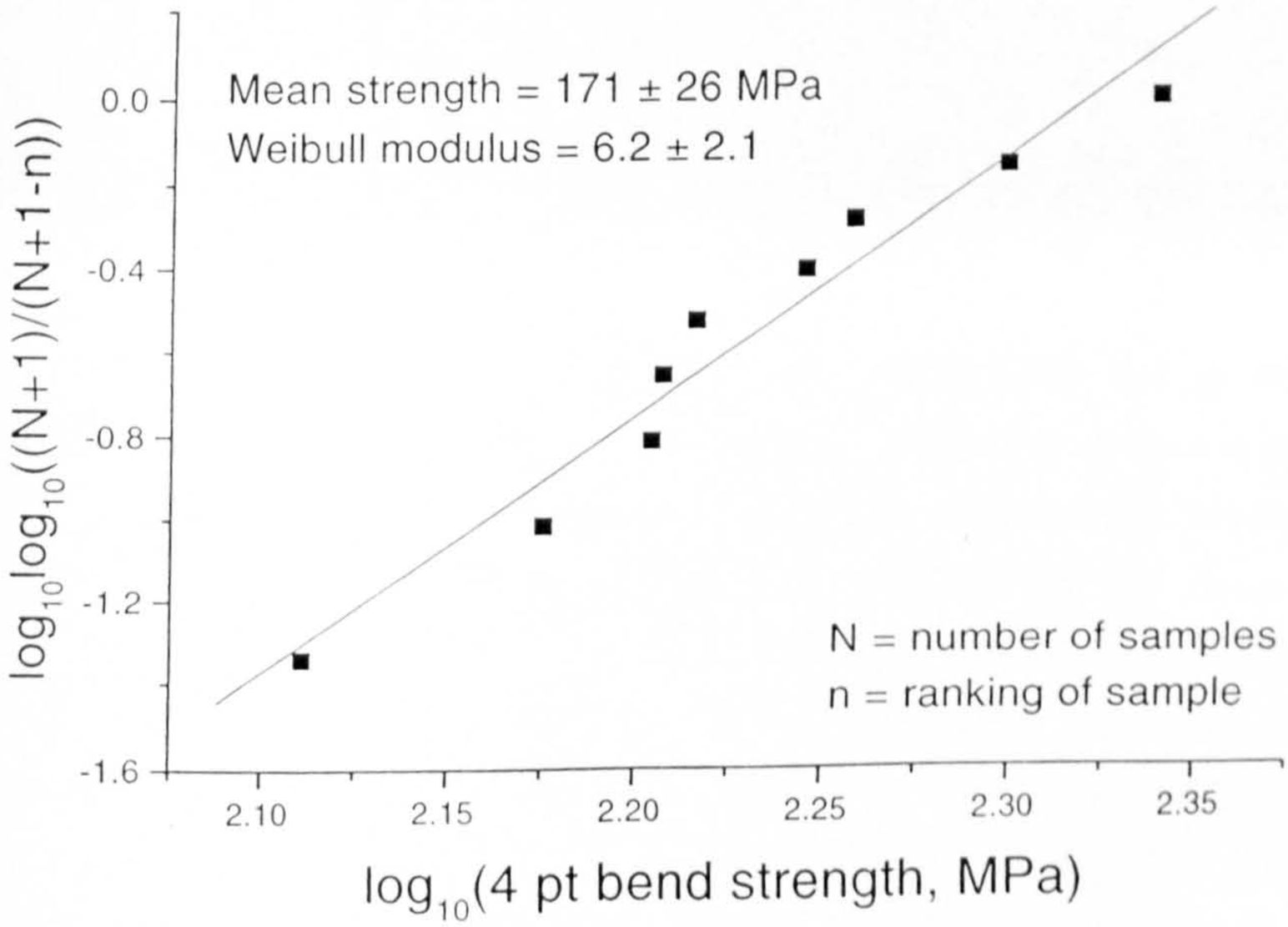

Figure 6.23 Weibull plot for J1100 (before adjustment for sample volume)

The problems due to sample preparation or testing may also have obscured the significance of the two heat treatments, as the difference in strengths between J1167* and J1100* is not significant. However, the behaviour during cutting of the J1167* samples was significantly different (with many samples suffering badly from cutting damage) and the number of joints surviving through to testing was low. Figure 6.24 shows an extreme example of cutting damage, in this case the joint survived but was obviously not suitable for mechanical testing.

Figure 6.24: Example of severe cutting damage to J1167 sample. 1 mm

Fractographic analysis of these samples was problematic and it was not always possible to identify the failure site conclusively. The most common apparent site of failure was from within the silicon nitride close to the tensile corners. This was assumed to be related to cutting damage in the silicon nitride. Two examples are shown in Figures 6.25 and 6.26. Figure 6.26 closely resembles an example of cutting damage given by Quinn and Morrell [17]. Paradoxically this result suggests that a sample failing at 161.2 MPa is failing from within the strong silicon nitride rather than from within the much weaker glass-ceramic interlayer. For this to occur the silicon nitride must be significantly damaged, or an unfavourable stress distribution must exist in the silicon nitride close to the MAS interlayer, either as a result of joining, or arising during mechanical testing.

Unfortunately, on this occasion the order of testing was not randomised or systematically ordered prior to mechanical testing. The order of mechanical testing was identical to the order in which the test specimens was prepared. As a result, it is not possible to determine whether the significant difference between the first 12 and last nine samples tested is due to specimen preparation or testing.

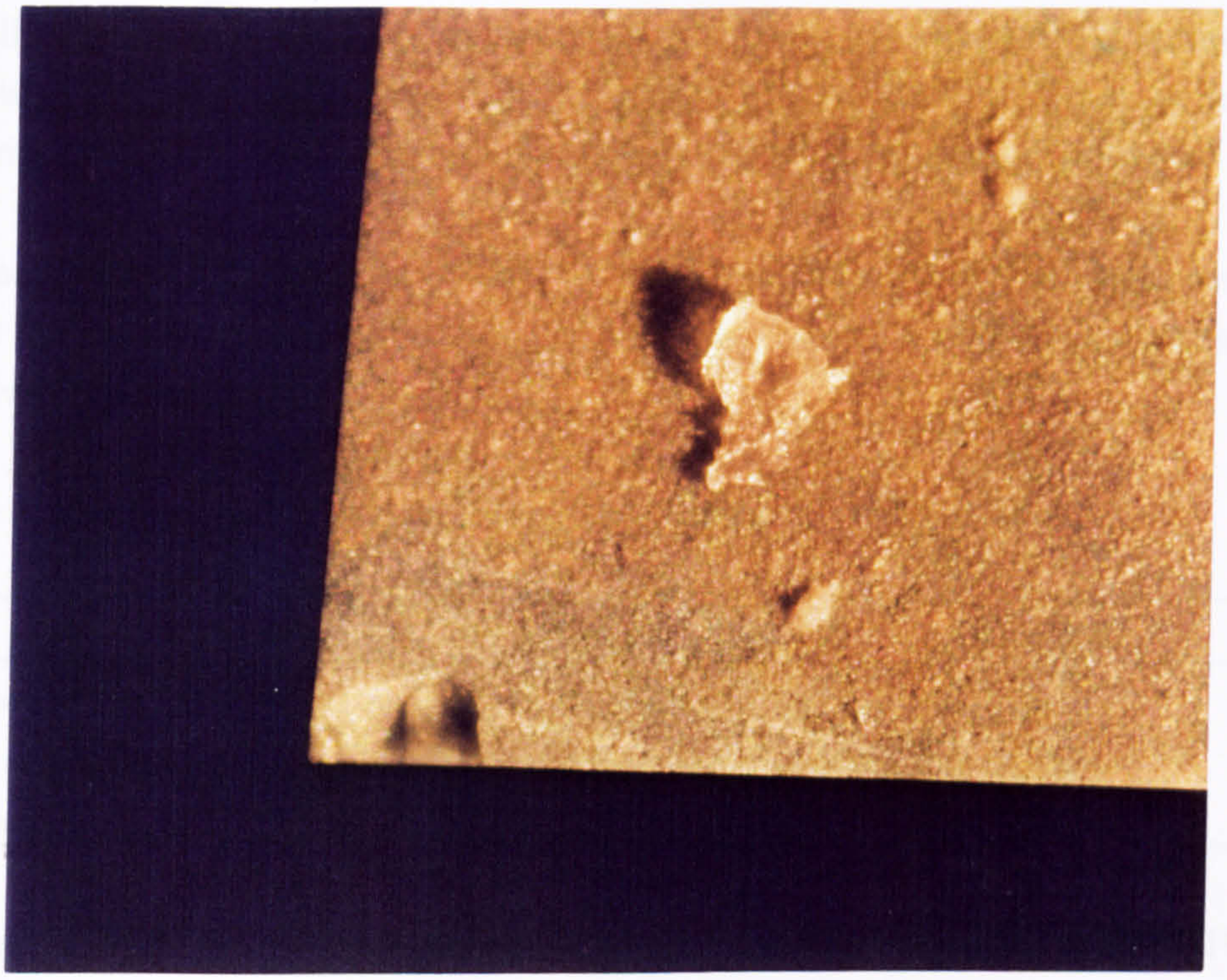

Figure 6.26: Optical micrograph of failure initiating within silicon nitride, from J1167. This sample failed at 96.1 MPa.

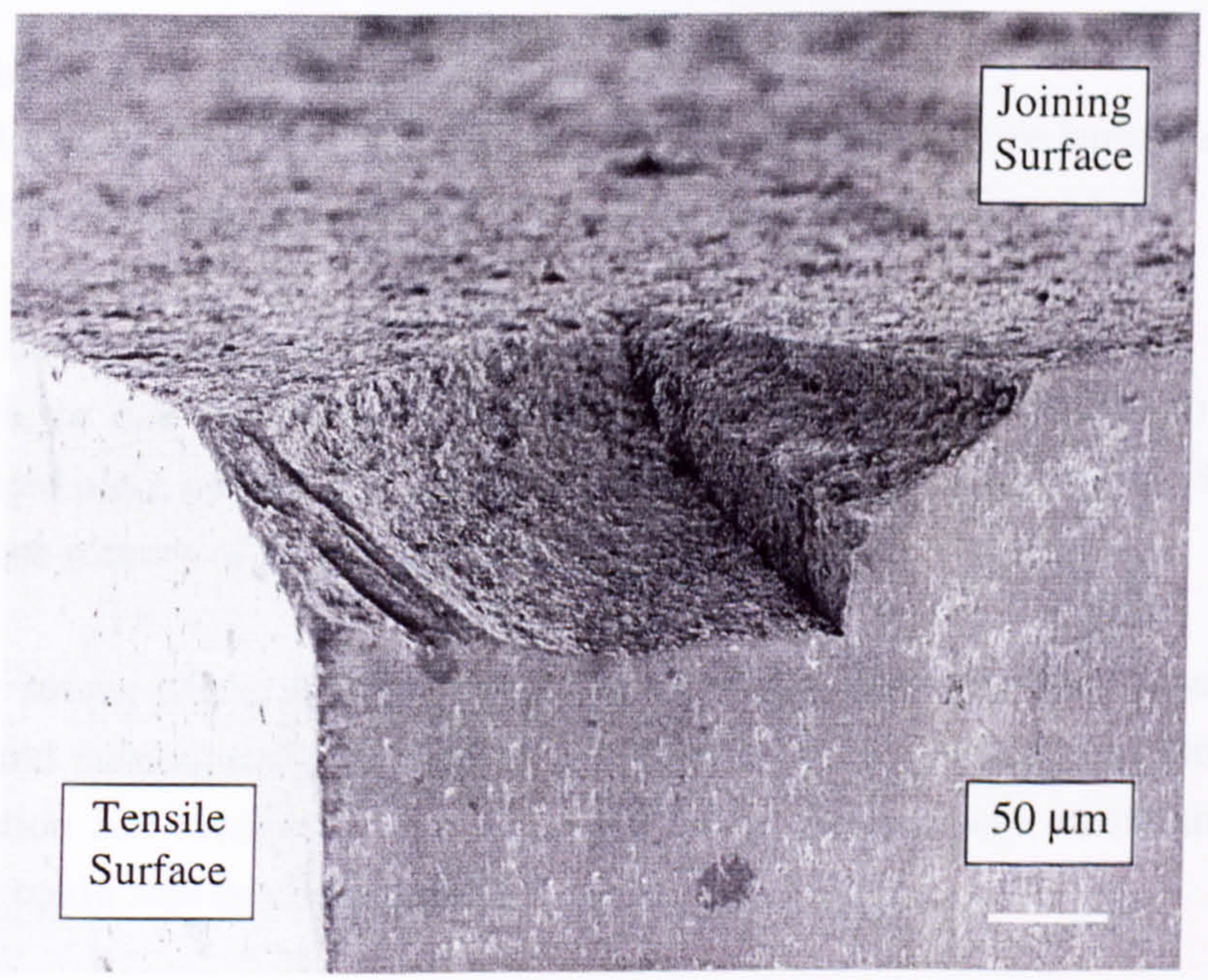

Figure 6.27 Electron micrograph of failure initiating within silicon nitride from J1100. This sample failed at 161.2 MPa.

For all subsequent sets of mechanical testing (II and III), randomisation or systematic ordering was employed at every stage in the sample preparation and testing to enable systematic bias, as a result of specimen preparation or testing, to be identified.

For joint samples J1100B and J1050B there was no evidence of systematic bias in either the mechanical testing or the sample preparation. The as-measured strengths are given in Table 6.5.

Table 6.5: As measured strengths for sample J1100B and J1050B.

	J1100B	J1050B
Number of samples	5	11
Mean strength	85.8	108.3
Standard deviation (MPa)	35.6	21.6

In contrast with the joint specimens that were not bevelled (J1167 and J1100), fractography of J1100B and J1050B revealed no failures from defects in the silicon nitride. It proved difficult to identify fracture sites conclusively. However, all four samples that failed at strengths of less than 90 MPa exhibited defects at or near the tensile surface which were in each case considered to be the likely failure site. The defects considered to have caused failure were:

- brass inclusions - on two occasions
- an inclusion containing Ba and S (Figure 6.27 - presumed to be barium sulphate)
- a macroscopic pore ~ 60 μms across in the glass-ceramic (Figure 6.28)

The brass contamination may have arisen due to sieving the glass powder through a brass sieve, or due to cutting the MAS tape with a brass cork cutter to obtain a suitable sized piece of tape-cast glass powder for the joining experiments. With care, both of these sources of contamination could be eliminated.

The likely source of the $BaSO_4$ contamination is less obvious, but as the MAS is prepared and subsequently handled in an open lab it is possible that some cross-contamination has occurred. In a more controlled environment, contamination of this nature could also be eliminated.

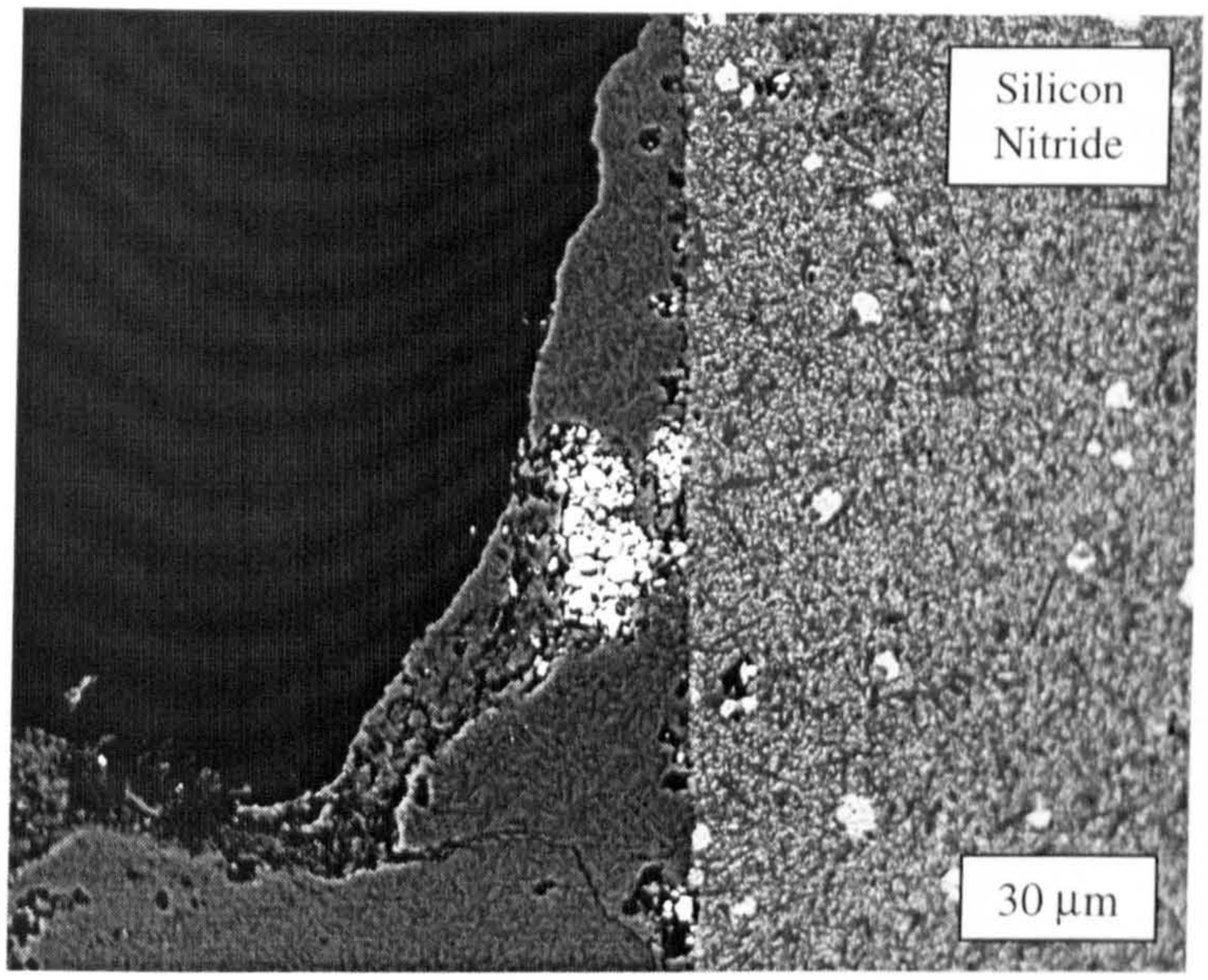

Figure 6.27: $BaSO_4$ inclusion in MAS1 glass ceramic on tensile surface.

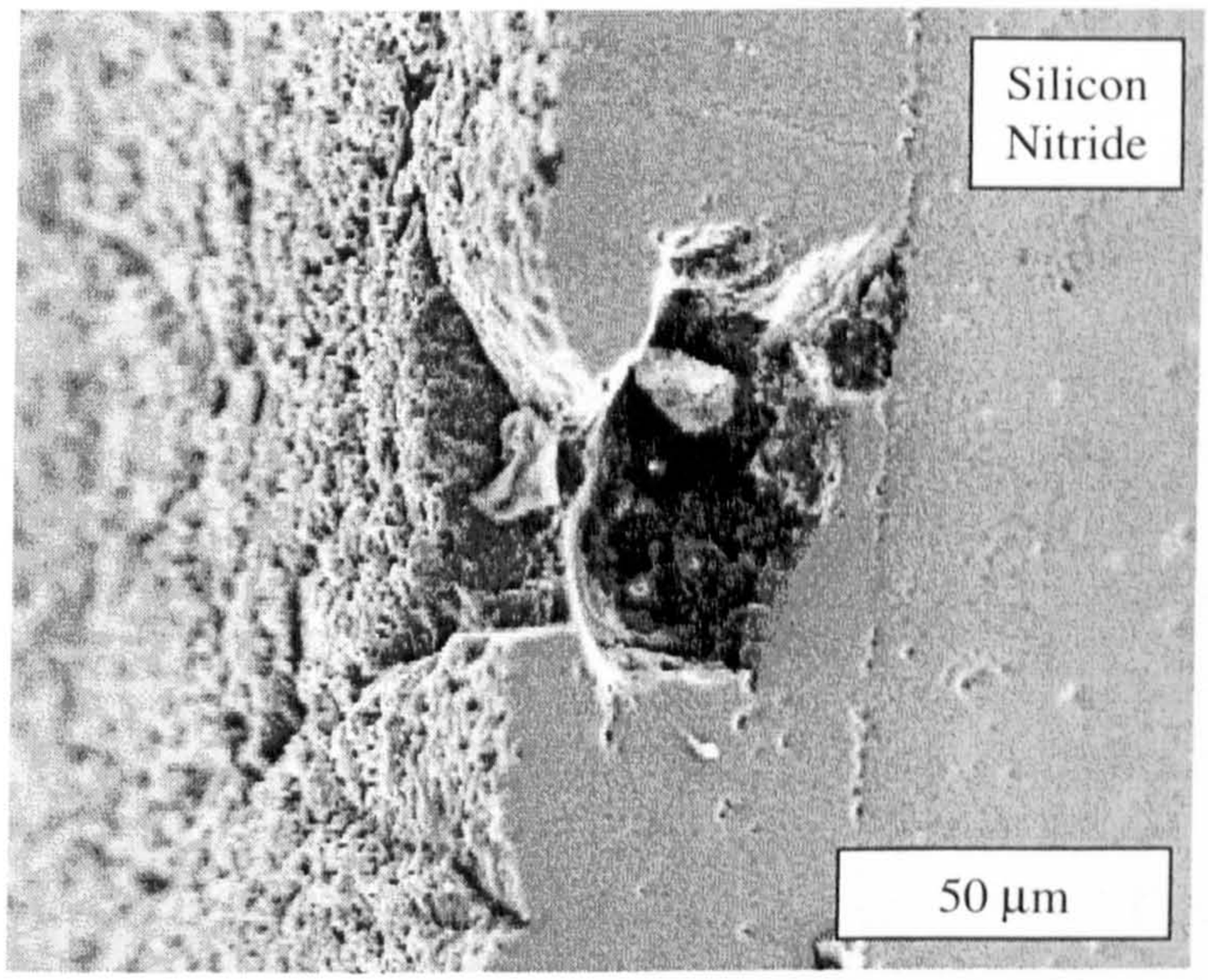

Figure 6.28: Pore in MAS1 glass-ceramic on tensile surface.

Although one sample appeared to fail from a pore 60 μm across, large pores were nearly eliminated in the final joints. In the development work, a strong correlation was found between the presence of such pores and a fast initial heating rate up to the degassing hold. Macroscopic pores are thought to arise mostly from organic burnout problems, although they may also be due to pinholes in poor quality tape. In either event, macroscopic pores of this nature could be virtually eliminated.

Table 6.6 shows the strengths of the two batches of samples J1050 and J1100B. The four failures due to gross macroscopic defects have been removed from the populations, and the joint strength is corrected to the standard sample size. For these samples the volume adjustment was very small as they were very close to the dimensions required by the standard.

Table 6.6: Strengths of sample batches J1050 and J1100B without failures due to gross macroscopic defects and with the joint strength corrected to the standard sample size.

	J1050B	J1100B
Number of samples	9	3
Mean 4pt bend strength	117	110
Standard deviation	12	14
Weibull Modulus	9 ± 3	-
Student's t test	Not significant > 10%, t = 0.73, n = 10	

The three J1100B samples should be identical to the nine J1100 samples reported earlier except for the presence of the bevel. Even though the size of the sample is small, it is possible to compare the results to determine whether the difference is statistically significant, this is shown to be the case in Table 6.7. This does not take into account the lower strength of the bevelled specimens due to reduced moment of inertia which is reported to result in a 4% error [17]. Even if this is taken into account, the mean strength of the J1100B specimens is still only 72% of that of the J1100 specimens. This is despite the fact that (by comparison with J1167 and J1100) the bevel has removed many of the sites from which failure would have occurred in its absence. The possible reasons for this reduction in strength will be discussed in Section 6.9.

Table 6.7: Strength of joints joined at 1100°C with and without bevel.

	J1100	J1100B
Number of samples	9	3
Mean 4pt bend strength	159.8	110.0
Standard deviation	24.2	14.1
Weibull Modulus	6 ± 2	9 ± 3
Student's t test	Significant < 1%, t = 3.08, n = 10	

6.8 Silicon nitride mechanical testing

6.8.1 Silicon nitride mechanical testing - introduction

Mechanical testing was performed on the silicon nitride both in the as received condition and after an 1167°C joining heat treatment. The objectives were to assess the strength of the silicon nitride and, by comparison with the figure reported by the manufacturer, to gain some indication of the adequacy of our specimen preparation and testing procedures. The flexure strength reported by the manufacturer was 650 MPa using 3-pt bend testing, the specimen size is not disclosed.

Some as received silicon nitride was bevelled prior to testing to allow the effect of the bevel to be evaluated. The silicon nitride samples for bevelling (SNB) were randomly selected from the as received group to ensure that they arose from the same sample population as the previous group (SN). Any significant difference between the two populations can then only be due to either the strength measurement or the bevel.

The 1167°C heat treatment was also tested as this had resulted in a considerable change in the cutting behaviour of silicon nitride joints (Figure 6.24). It is important to determine if any proposed joining operation significantly effects the mechanical properties of the silicon nitride.

All samples were cut from cylindrical specimens, and surface grinding and polishing were performed at the same time, with the samples ordered so that sample preparation bias was eliminated as far as possible.

In contrast to the joints, fractography of the monolithic silicon nitride specimens proved much more straightforward and it was normally possible to identify clearly the probable fracture sites using optical microscopy.

6.8.2 Silicon nitride mechanical testing - results

The measured strengths, in 4-pt bend testing, of the as received material (SN) and the heat treated material (SN1167) are shown in the form of a Weibull plot on Figure 6.29.

Figure 6.29: Weibull plot of silicon nitride strength

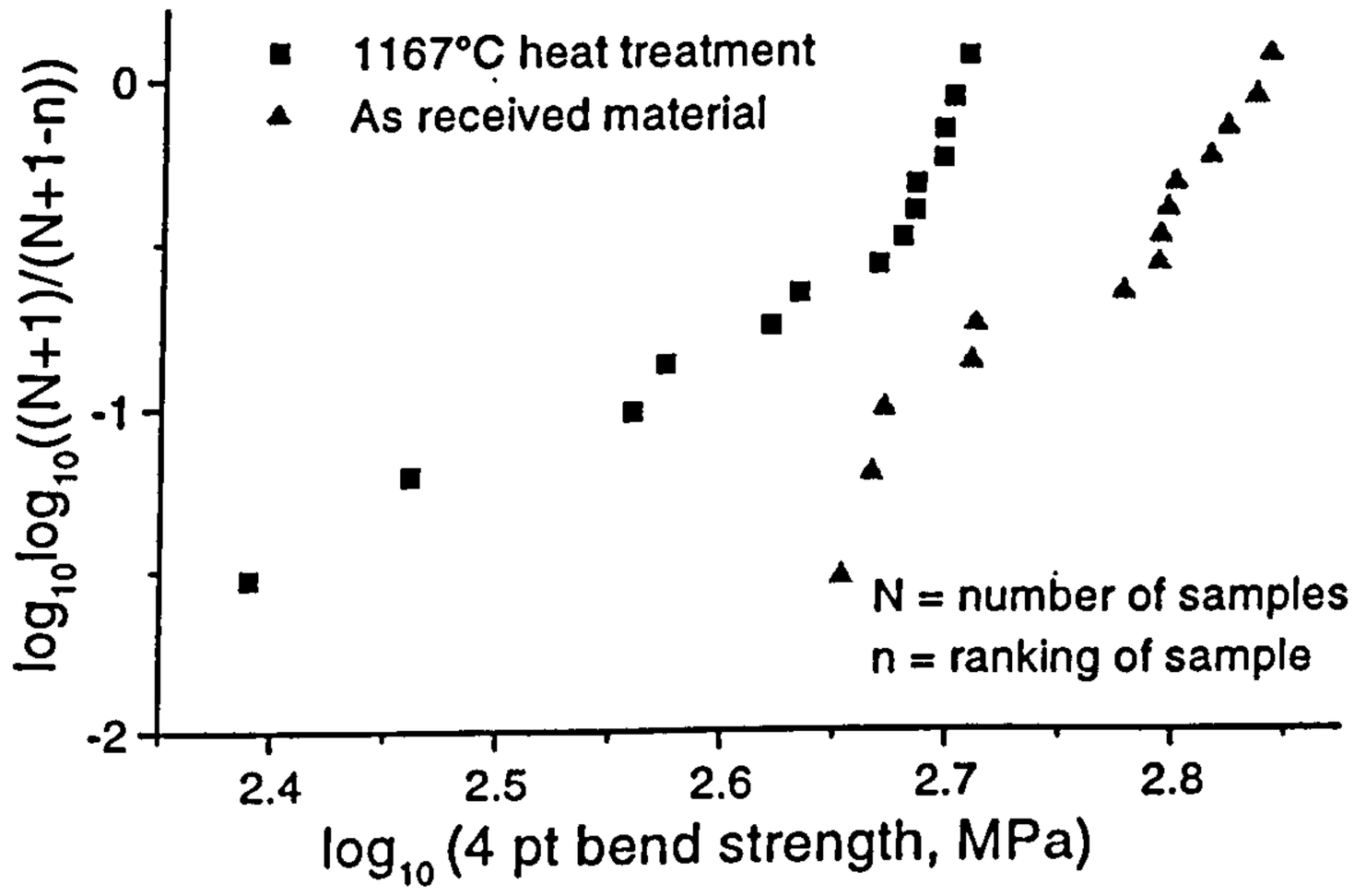

Both samples show a bimodal distribution which can be split into the high strength failures due to the material itself and low strength failures which are assumed to be due to problems encountered in the specimen preparation. If these results are taken as a whole this gives a mean measured strength for as-received material of 584 ± 85 MPa and a Weibull modulus, m, of 6.7 ± 1.8, and for the samples subjected to a 1167 °C joining heat treatment a mean strength of 430 ± 83 MPa with a Weibull modulus , m, of 4.4 ± 1.2.

A more realistic guide to the intrinsic strength and Weibull modulus of the silicon nitride can be obtained if the points due to specimen preparation problems are disregarded. This results in, for the as-received material, a mean strength of 641 ± 32 MPa, m = 19 ± 6, and for the 1166°C heat treatment a mean strength of 488 ± 15 MPa, m = 32 ± 11. If the results are adjusted to account for the sample volume effect, assuming a Weibull modulus of 20 this results in, for the as-received material, a mean strength of 627 ± 31 MPa, m = 19 ± 6, and for the 1166°C heat treatment a

mean strength of 477 ± 22 MPa, m = 28 ± 10. Table 6.8 demonstrates that the effect of the heat treatment on the sample strength is highly significant.

Table 6.8: Significance test of SN and SN1167.

	SN	SN1167
Number of samples	9	8
Mean 4pt bend strength	627	477
Standard deviation	34	16
Weibull Modulus	19 ± 6	28 ± 10
Student's t test	Highly significant < 0.05%, t = 11.67, n = 15	

In this instance the possibility that the difference is due to sample preparation or testing can be eliminated, as both were ordered to eliminate possible bias. The only difference between the samples is the heat treatment.

X-ray diffraction of the silicon nitride after the 1167°C joining heat treatment indicated that crystallisation of the intergranular glass had occurred with some cristobalite having formed. Another unidentified phase (presumed to be an yttrium silicate) had also crystallised from the intergranular glass. Material subjected to an 1100°C heat treatment showed traces of crystallisation of the intergranular glass but to a much lesser extent than the 1167°C heat treatment. The crystallisation of cristobalite in the intergranular glass may be particularly significant as the cristobalite phase change on cooling is accompanied by a 3.7 % volume change which may result in the generation of significant stress and weakening of the material. The fracture toughness of silicon nitride is strongly affected by the TCE relationship between the silicon nitride and the matrix phase [18] and any crystallisation will obviously effect this.

6.8.3 As received silicon nitride - bevelled samples

The strength of the bevelled, as-received silicon nitride was 498 ± 23 MPa (488 ± 22 MPa as adjusted for sample volume). This is compared to the as-received silicon nitride without bevel as adjusted for sample volume in Table 6.9 and in the form of a Weibull plot in Figure 6.30. The difference in strength is shown to be highly significant. Table 6.9 does not take into account the reduction in strength of the bevelled specimens due to their reduced moment of inertia. When this is accounted

for the strength of the bevelled specimens (SNB) is ~ 81 % of the strength of the non-bevelled specimens (SN).

Figure 6.30: Weibull plot of as received silicon nitride both with (SB) and without bevel (S).

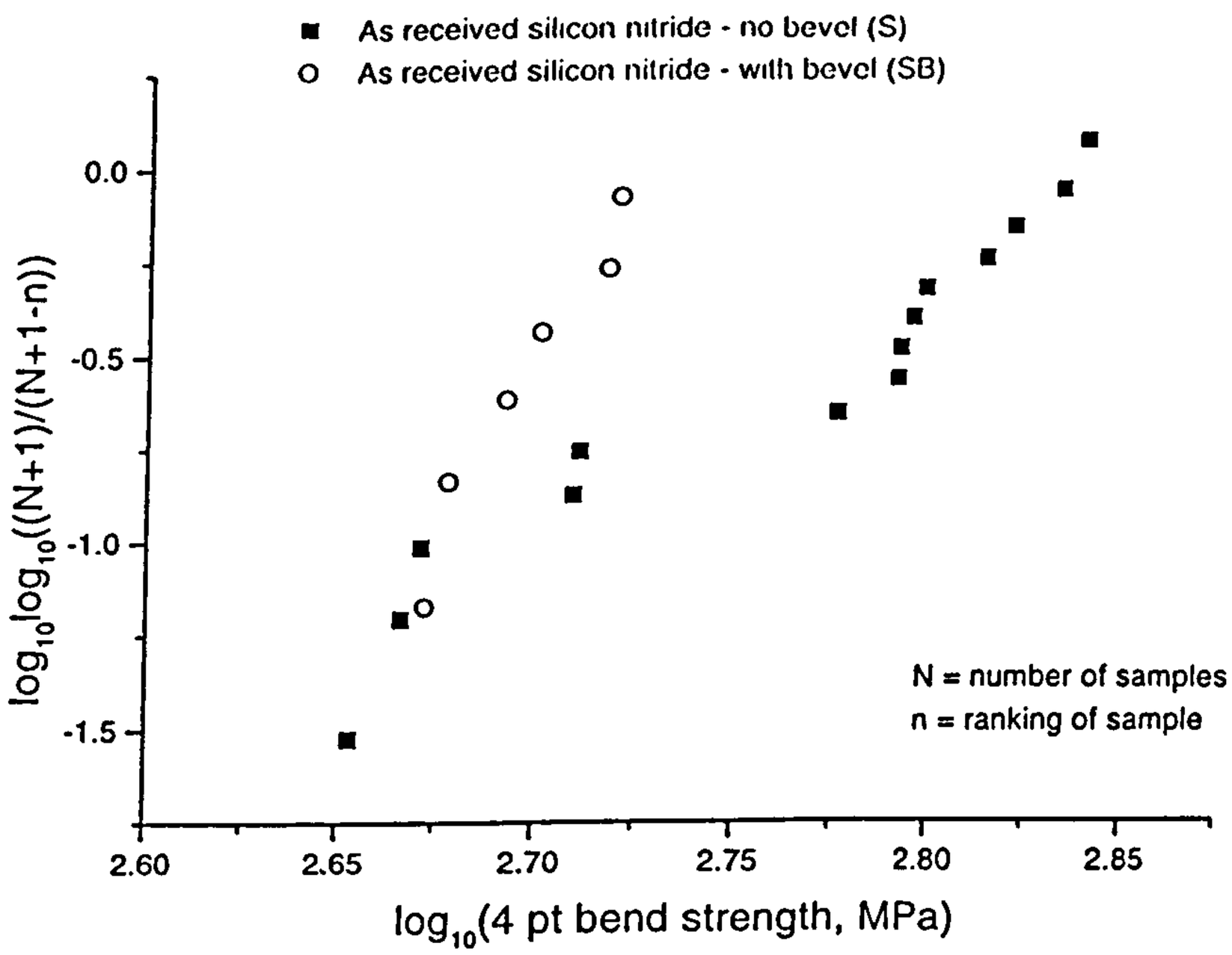

Table 6.9: Significance test of SN and SNB

	SN	SNB
Number of samples	9	6
Mean 4pt bend strength	627	488
Standard deviation	31	22
Weibull Modulus	19 ± 6	18 ± 7
Student's t test	Highly significant < 0.05%, t = 8.85, n = 13	

The possibility that bevelling induces defects which limit strength can be discounted. Firstly, it is very unlikely that if this occurred the consistency of the strength distribution would be as it is, and secondly, fractography of all six SNB samples revealed that failure occurred from at, or near, the tensile edge away from the corners and that no samples failed near the bevel. A typical failure site is shown in Figure 6.31. The other possible causes of the strength reduction in the bevelled samples are discussed in conjunction with the similar reduction in strength seen in the bevelled joints in Section 6.9.

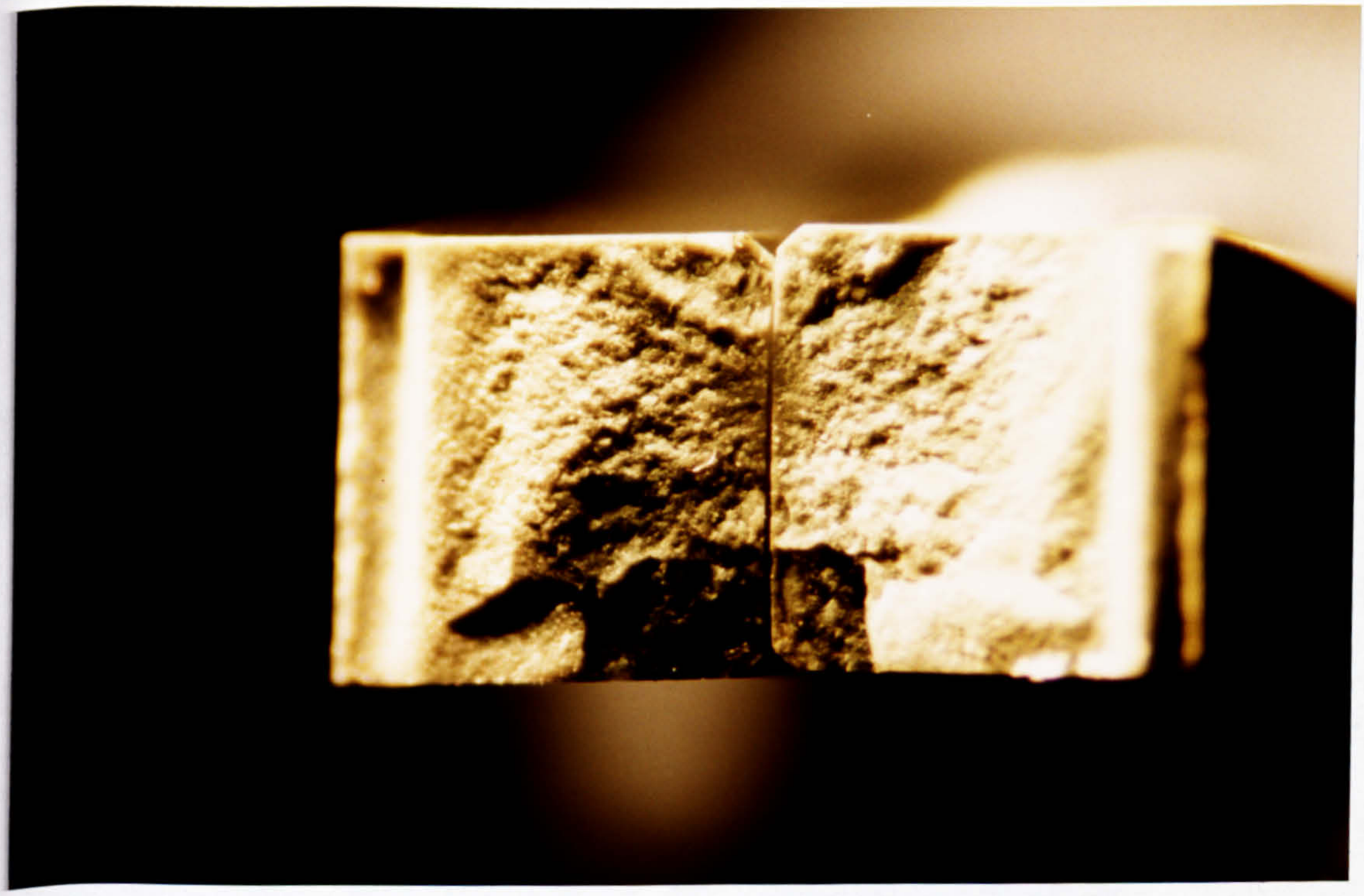

Figure 6.31: Failure of SNB sample from at, or near, tensile surface. 1 mm

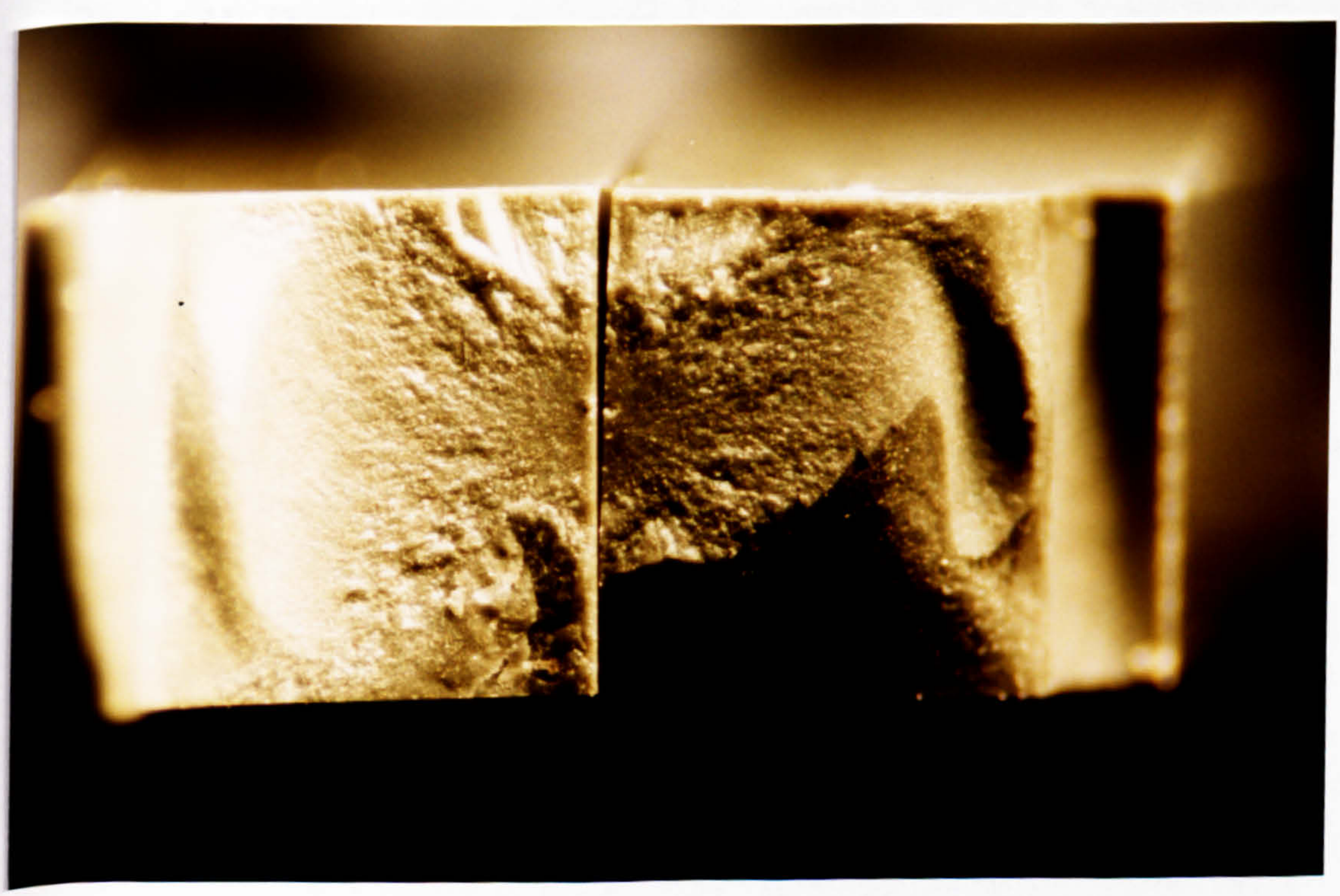

Figure 6.32: Example of failure from (or near) the tensile edge (SN1167). 1 mm

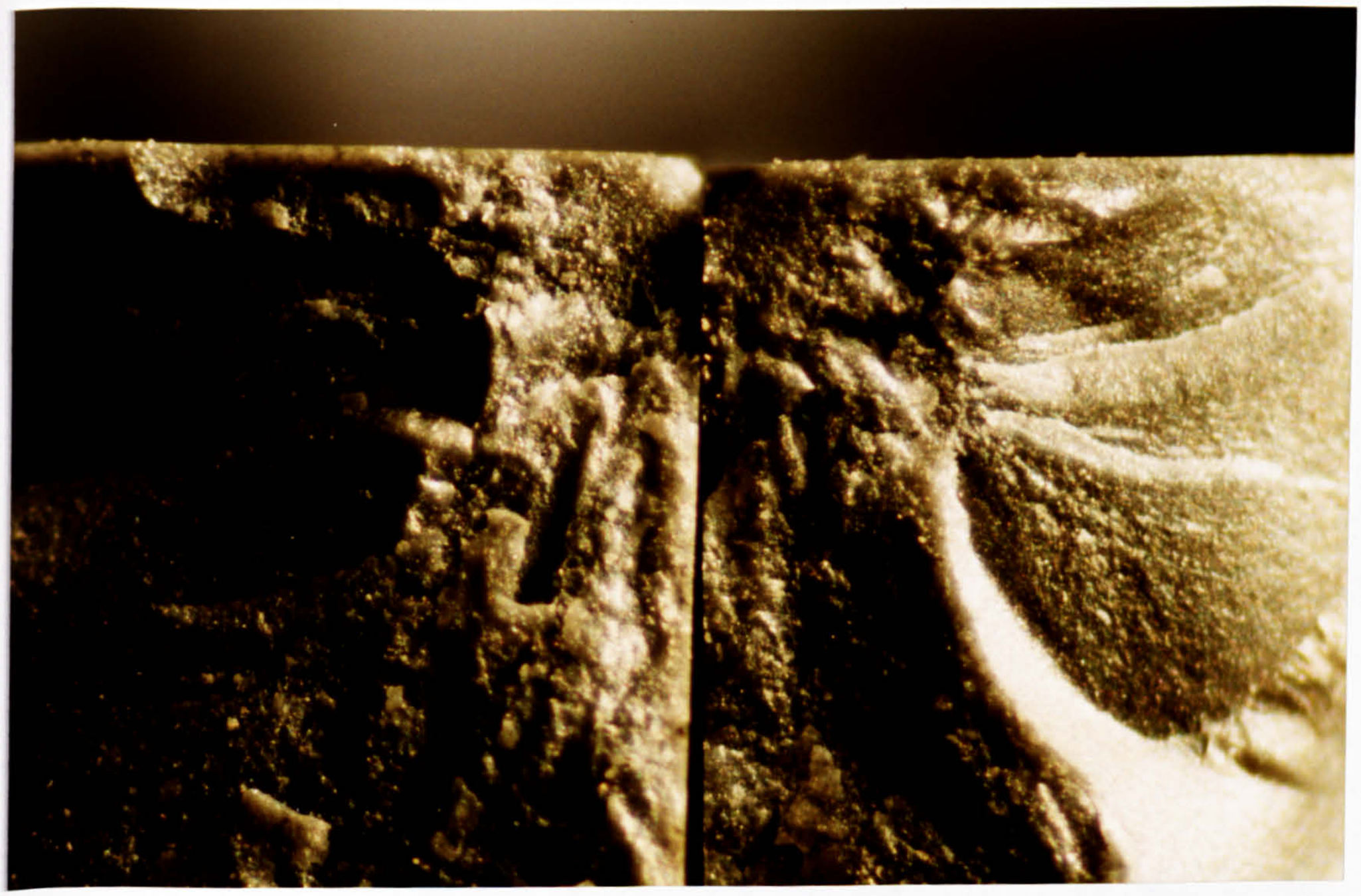

Figure 6.33: Example of failure from (or near) the corner (SN1167). *0.5 mm*

Although the sample size of SNB is small (6 specimens), the lack of any comparatively low strength failures, and the fact that all failure sites were identified as being away from the corners, would seem to indicate that the bevel is effective in removing the cutting damage from the corners of the samples.

A detailed fractographic examination of SN and SN1167 reveals that the origin of fracture for the low strength, or 'sample preparation' failures, is mixed. For the six low strength SN1167 specimens, four failure sites were identified on the tensile face, with one unidentified failure site and only one corner related failure. In this case it appears that the increased susceptibly to cutting damage as a result of the heat treatment has lead to the polishing procedure not removing all damage from the tensile surfaces. For the five low strength SN specimens one failed from (or near) the tensile edge and four failed from the corner, or from (or near) the tensile edge close to the corner.

An example of failure from (or near) the tensile edge is shown in Figure 6.32, and an example of corner failure is shown in Figure 6.33.

The low strength failures are therefore not all removed by bevelling. There appears to be some remaining cutting damage on the tensile faces (to which the SN1167 is more susceptible) that is not adequately removed by sample polishing. The low strength failures in the as-received (non heat treated) silicon nitride which were not (0/6), or would not have been (1/14), removed by bevelling amount to one failure from twenty specimens. This isolated failure may arise from cutting damage during the preparation of four point bend specimens which was not removed by the polishing procedure or from the initial cutting of the silicon nitride prior to the joining process, as joining was performed with as-cut rather than polished surfaces.

The failure sites of both sets of strong samples are similarly mixed between corner and tensile edge failures.

6.9 Discussion of mechanical testing results

6.9.1 General comments

Due to the problems touched on in Section 4.4.2, the standard used for mechanical testing (JIS R 1601) although 'simple to use' and 'less stringent in some technical details' is unsuitable for accurate strength measurements. The most severe problems occur due to the fixed load points and the lack of articulation in the fixture.

The fixed load points exert a frictional restraint on the bending of the specimen and lead to higher apparent strengths than if the loading point is free to rotate as the specimen bends. The friction errors can be up to 15% [19].

The lack of articulation in the fixture means that any misalignment of the test head or lack of parallelism in the specimen leads to twisting forces in the specimen. This will normally result in lower measured strengths. Mis-alignment of the fixture is considered to be the most likely cause of the low strengths measured in the later testing work in this project.

The small radius of curvature of the loading edges may also have resulted in problems due to the generation of high contact stresses.

For future work, testing in accordance with a standard requiring an articulated fixture such as United States MIL-STD 1942 (1983) is recommended. The details for the construction of a suitable fixture are given by Quinn [19].

To put the variation in measured strengths (of nominally identical specimens) encountered in the current work in context, it is worthwhile to compare the results of a round robin on the flexural strength of advanced structural ceramics reported by Quinn [19]. Part of this round robin involved six labs testing bars of alumina (which was chosen for its uniform microstructure and consistent properties and centrally prepared to eliminate bias due to specimen preparation) in accordance with United States MIL-STD 1942 (1983), which is considered to be in line with current best practice. Although four labs produced consistent results (with a characteristic strength of 379 MPa), two labs produced results which would have occurred "much less than 1% of the time" (395 MPa) and "well beyond the 99th percentile" (345 MPa). Even with best practice using identical samples and identical test fixtures two labs reported results which differed by 13-14%. The largest departure from the 'correct value' represents a 9 % error, indicating that strength measurements should be possible using this standard with a confidence of 10 %.

In the first set of mechanical testing in this work, problems were encountered due to inconsistency in either the sample preparation or the testing procedure. If the order of each step in the preparation process had been randomised or systematically ordered this would have enabled the cause of the inconsistency to be identified. For the preparation and testing of the other mechanical test samples a suitable randomising or systematic ordering of samples was employed at each stage in the testing process. The adoption of this practice is strongly recommended if information is not to be lost unnecessarily.

Another factor to be considered when embarking on a programme of mechanical testing is that allowance must be made for loss of samples during the preparation process.

6.9.2 Silicon nitride

The measured strength of the as-received silicon nitride was:

- without bevel - 641 ± 32 MPa (volume corrected 627 ± 31 MPa)
- with bevel - 498 ± 23 MPa (volume corrected 488 ± 22 MPa)

The strength reported by the manufacturer is 650 MPa measured using 3-pt testing. The dimensions of the test bar are not given. The strength measured in 4-pt bending

is likely to be at least 10-15 % lower. (Data reported by Quinn and Morrell [17] suggests that the strength of small 3-pt specimens is nearly 15% higher than that of small 4-pt specimens.) Therefore the equivalent 4-pt bend test strength is approximately 550-585 MPa.

If the manufacturers data is reliable, this suggests that the strength of the non-bevelled samples is overstated whereas that of the bevelled samples is understated. As friction error can result in strength being overstated by up to 15 % this represents the probable explanation for the high measured strength of the samples without the bevel. The most likely explanation for the low strength of the bevelled specimens is problems due to fixture alignment, resulting in low measured strengths. Friction errors and problems due to alignment of the fixture and specimens are the biggest experimental weaknesses of JIS R 1601.

The strength of the heat treated silicon nitride (SN1167) was 488 ± 14 MPa (volume adjusted 477 ± 16 MPa). Although the absolute value of the measured strength is open to doubt due to the errors mentioned, the significance in the reduction in strength compared to SN holds because the experiment was conducted so that any sample preparation or testing bias was common to both sets of samples.

The reduction in strength of the silicon nitride subjected to the 1167°C joining heat treatments indicates the need to be aware of the effect of the joining heat treatment on the sample, particularly where there is an intergranular glass phase, the crystallisation of which may compromise the properties of the material. This effect was particularly significant in the current work due to the formation of cristobalite and the disruptive effect of the ~ 3.7 % [20] volume change accompanying the phase change on cooling.

The non-bevelled sample displayed a bi-modal distribution which was not evident when the small sample of bevelled specimens was tested. The bevel appears to have been effective in removing cutting damage from the corners. However, fractography revealed that some low strength specimens (1/14 for SN, 0/6 for SNB, 4/14 for SN1167) failed away from the corners. The high occurrence of this in SN1167 specimens is due to the crystallisation of the intergranular glass increasing the susceptibility of the silicon nitride to cutting damage. The single occurrence in the as-received silicon nitride may indicate that there is still some residual damage after the polishing procedure or may be due to joining as-cut rather than polished silicon nitride.

6.9.3 Silicon nitride joints

The mean measured strength of silicon nitride joints ranges from 110-170 MPa, or from 110 to 160 MPa as corrected to the standard sample volume. The highest recorded joint strength was 219 MPa.

All mechanical testing was performed on joints with a glass ceramic interlayer with a higher TCE than the silicon nitride resulting in TCE mismatch cracks perpendicular to the join. These do not appear to compromise the strength of the joints which compare well with typical reported strengths for similar glass-ceramics. For example, [21] gives typical reported strengths for MAS glass-ceramics from 110-170 MPa, and Knickerbocker et al [6] report a strength of 120 MPa for a glass-ceramic with similar composition and initial glass particle size.

A low level of porosity, both within the glass ceramic and at the interface between the glass-ceramic and the silicon nitride, does not appear to compromise the joint strength significantly.

Macroscopic defects do significantly compromise the strength of the glass-ceramic and the resulting joints. However, defects which resulted in joint strengths below 90 MPa, such as inclusions (brass, barium sulphate) and macroscopic pores could be eliminated with improved preparation procedures.

The bevelled joints were significantly different from the non-bevelled joints in two respects:

1. The strength of bevelled joints was lower.
2. For many non-bevelled joints failure was initiated from within the silicon nitride

Even when the reduced moment of inertia due to the bevel is allowed for, the strength of the bevelled joints (J1100B) is only 72 % of that of the non-bevelled joints subjected to the same joining heat treatment. Although the sample size of J1100B is small, the difference in strength is still highly significant. If the mean strength of bevelled joints prepared at 1050°C (J1050B) is similarly compared (from the microstructure similar strengths to J1100B would be anticipated), the mean strength corresponds to 76% of that of the non-bevelled joints. Both sets of bevelled joints were tested on the same occasion. Bevelled silicon nitride (also tested on this

occasion) was also 81% weaker than previous strengths obtained on non-bevelled specimens, and on this occasion the possibility of a reduction in strength due to flaws induced by the bevelling procedure could be eliminated. The consistent reduction in strength for samples tested on the same occasion suggests a common cause. The most likely explanation is a problem with the alignment of the test head. An additional contribution may have been due to inconsistent friction errors on the separate occasions when testing was performed.

For the silicon nitride joints, the sample preparation and testing problems have obscured the significance of the differences in joint strengths due to differing heat treatments. However, joining at 1050-1100°C is preferred over 1167°C due to the detrimental effect of the high temperature heat treatment on the mechanical properties of the silicon nitride.

The failure of non-bevelled joints from within the silicon nitride (at the corners of the specimens close to the interface), at much lower strengths than monolithic silicon nitride, indicates that the silicon nitride joints suffered from severe cutting damage. The joints may be more susceptible to cutting damage than monolithic silicon nitride. It is possible that, as the cut traverses the interlayer, from the high elastic modulus silicon nitride into the lower elastic modulus glass-ceramic, the corners of the sample are particularly prone to chipping or cracking damage. This effect may be exacerbated by stress concentrations due to residual thermal stress or loading in the presence of an elastic modulus mismatch. The damage would appear to be highly localised and easily removed by bevelling.

A further contribution to the low measured stress at failure for samples failing from within the silicon nitride (compared to monolithic silicon nitride) is that, as discussed in Section 3.3.8, the higher TCE interlayer may strengthen the interlayer at the surface, at the expense of weakening the silicon nitride either side. This effect may be exacerbated by sub-critical crack growth in the silicon nitride.

It is also possible that the bevel may affect the distribution of stress, either arising from joining or during mechanical testing.

Joining silicon nitride to itself using an MAS glass-ceramic interlayer has enabled joints with strengths comparable to the intrinsic strength of the glass ceramic to be produced, this should offer sufficient strength for practical applications. Compared to other solutions for joining silicon nitride (Table 3.2) this offers a refractory joint

of reasonable strength which does not involve the use of unduly high temperatures in its production.

It is possible that the strength of the joints could be significantly improved by the use of a thinner glass ceramic interlayer, or by improving the mechanical properties of the interlayer by either using a finer initial glass particle size or using a glass-ceramic with intrinsically higher strength and fracture toughness (eg: an enstatite based glass-ceramic [22]).

Johnson [8] found that the thickness of a glass interlayer had a significant effect on joint strength (Figure 6.34). If a similar relationship between interlayer thickness and joint strength holds for a glass-ceramic interlayer then the use of a thinner interlayer should result in a significant increase in joint strength, as long as this is not at the expense of incomplete coverage of the joint area.

The effect of the particle size on the strength of a glass-ceramic with similar composition is shown in Figure 6.35 [6].

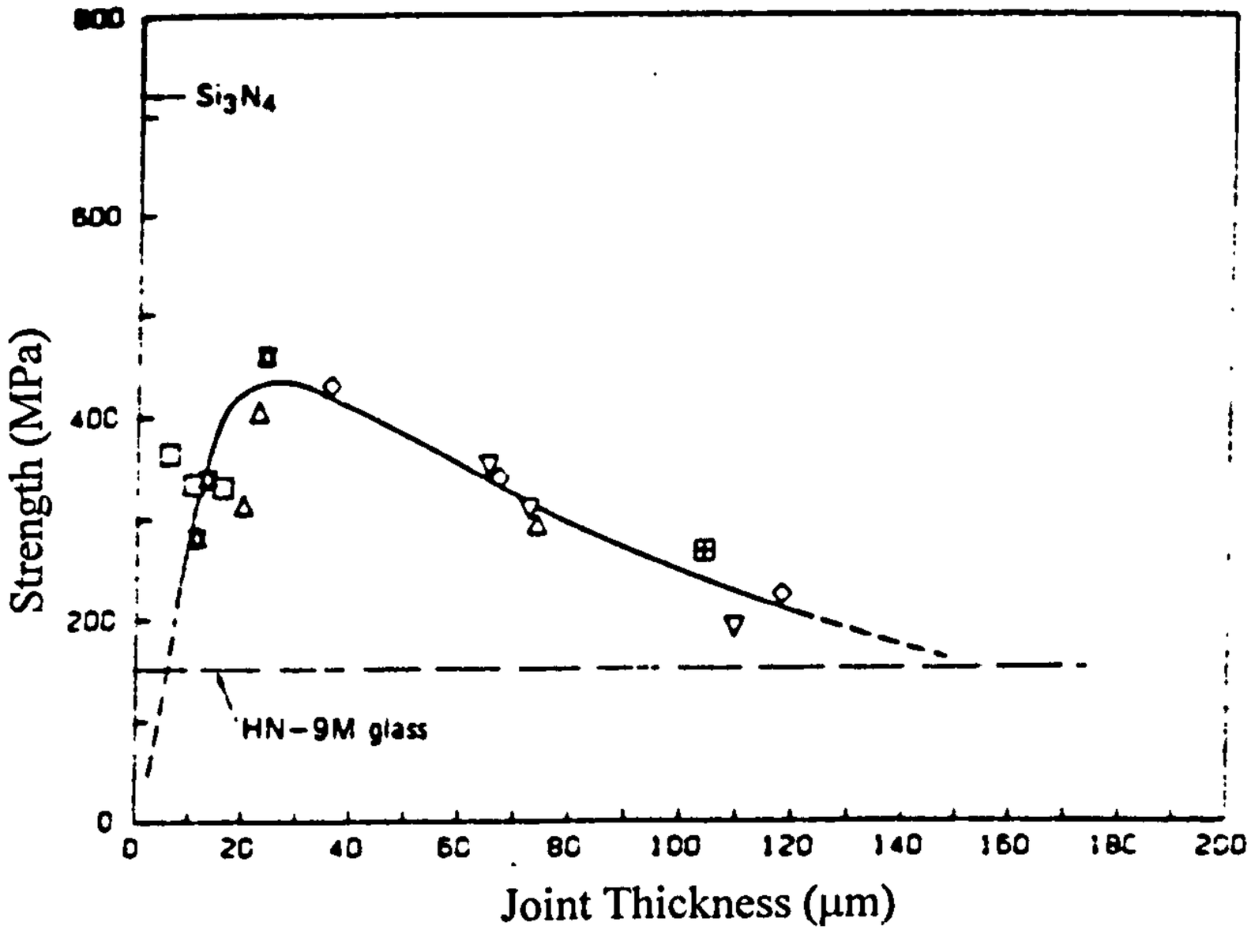

Figure 6.34: Strength of silicon nitride/MAS glass/silicon nitride joint for bars joined at 1580°C for 45 minutes under 0.2 MPa of N_2, like symbols indicate test bars cut from single joined specimens [8].

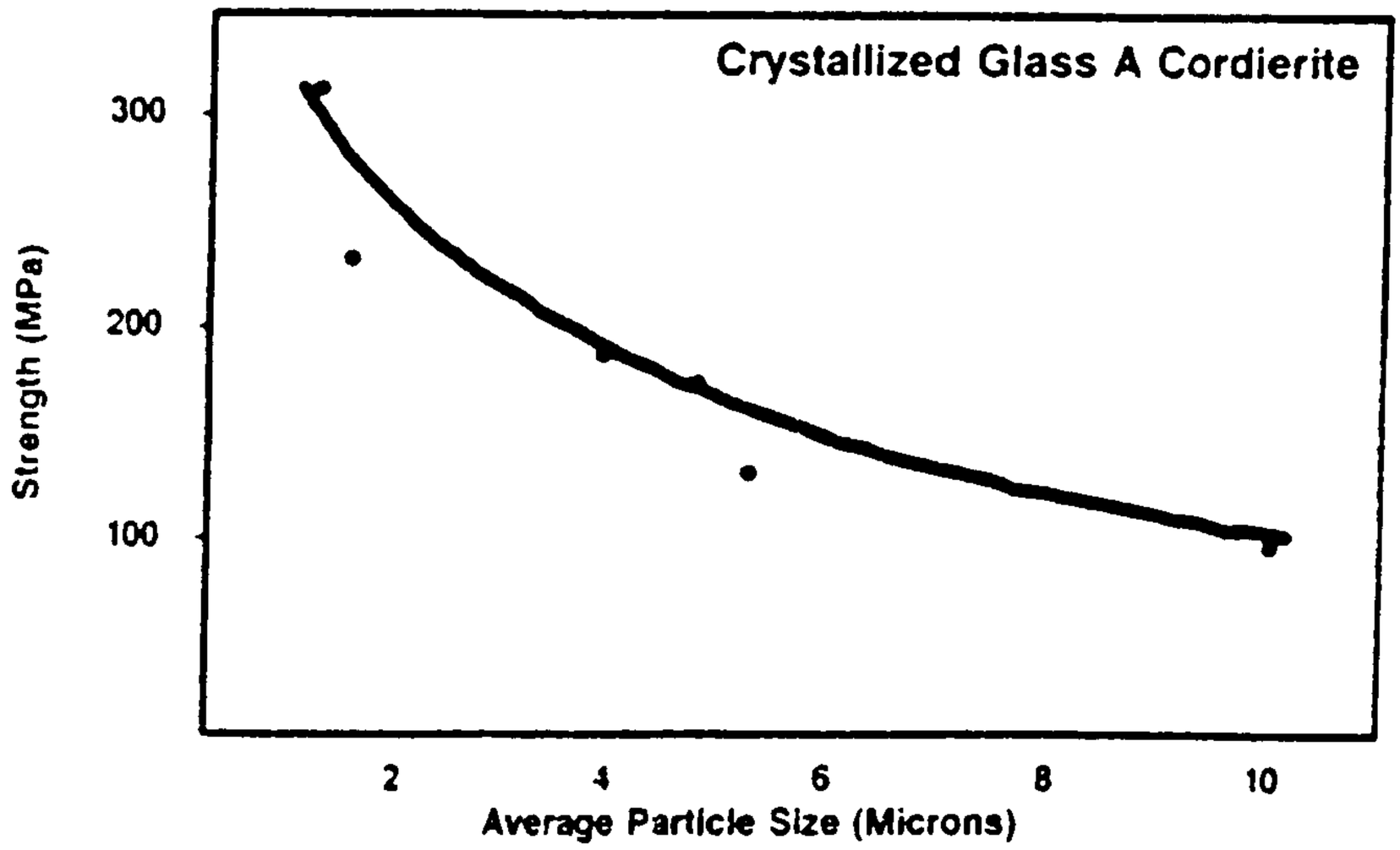

Figure 6.35: Strength versus powder particle size for a cordierite/enstatite glass-ceramic containing B_2O_3 and P_2O_5 [6].

The issue of the optimum TCE for the interlayer is still not resolved and is likely to be a function of joint geometry. It is however possible that a carefully chosen TCE mismatch can result in a strengthening of a relatively weak interlayer at the expense of weakening the silicon nitride either side.

It has been possible to confirm that high strength joints are possible using an interlayer with higher TCE. It would be worthwhile to investigate systematically the effect of TCE mismatch on joint strength. However, this requires comparable joint microstructures and consistent defect populations which were not achieved by Zdaniewski [23], which must raise some doubt over his conclusion, that the measured strength and fracture toughness of ceramic adhesive joints decreases with increasing TCE mismatch both positive and negative. The optimum interlayer TCE is also likely to be a function of joint geometry and interlayer thickness.

To assess the potential long term performance of glass-ceramic joints, further mechanical testing is required. This would include testing of the fracture toughness of the joint, the thermal cycling, fatigue and creep behaviour.

6.10 Joining silicon nitride to silicon nitride using a glass-ceramic interlayer - conclusions

Silicon nitride may be joined to itself using a magnesium aluminosilicate glass interlayer with no applied load at temperatures in excess of 1300°C. Similar joints have been previously reported in the literature [5] and have displayed excellent mechanical strength [8]. However the high temperature performance of a glass joint would be limited and problems due to uncontrolled crystallisation may be encountered.

For joining silicon nitride to itself using a cordierite-enstatite glass-ceramic interlayer, temperatures of < 1250°C are required, and a small uniaxial load is required to ensure even spreading and wetting. At temperatures in excess of 1200°C in a vacuum, the MgO is reduced by the silicon nitride resulting in the evolution of gaseous N_2, SiO and Mg [14]. This results in considerable disruption to the microstructure of the interface and the glass-ceramic. Joining at below 1200°C in a nitrogen atmosphere enables this problem to be avoided.

The use of a glass ceramic interlayer with the TCE matched to that of the silicon nitride enabled a virtually defect free joint to be produced. Joining using an interlayer with a TCE higher than that of the silicon nitride resulted in TCE mismatch cracks perpendicular to the interlayer. The use of a cast tape was found to be an excellent way of applying a controlled thickness of glass powder. Mechanical (4-pt bend) testing of joints using magnesium aluminosilicate glass-ceramic with a higher TCE (5.7 MK^{-1}) than the silicon nitride (3.0 MK^{-1}) enabled joints with strengths (110-170 MPa) comparable to the intrinsic strength of the glass ceramic to be produced, which is considered sufficient for practical applications. Further improvements to the joint strength may be obtained by:

- The use of a thinner interlayer, although it is essential that this is not at the expense of incomplete coverage of the joint area.
- A finer initial glass powder.
- The use of an intrinsically stronger, higher fracture toughness glass-ceramic interlayer.
- Optimising the TCE mismatch (if any) of the interlayer as a function of interlayer thickness and joint geometry.

The maximum strength obtained of 219 MPa (for a glass-ceramic interlayer ~ 90 μm thick) compares to the maximum joint strength reported by Johnson of 460 MPa which was for an interlayer 30 μm thick. If a similar relationship between interlayer thickness and joint strength to that observed by Johnson [8] (Figure 6.34) holds for a glass-ceramic interlayer, then a substantial improvement in joint strength should result from the use of a thinner glass-ceramic interlayer.

Due to problems encountered in mechanical testing it was not possible to differentiate between the strengths of joints produced from 1050, 1100 and 1167°C. Joining at 1050-1100°C is preferred due to the detrimental effect of the 1167°C heat treatment on the microstructure of the silicon nitride.

The results of this work indicate that diffusion across the interface on a scale that can be measured using EDX is not necessary for the formation of a strong joint. The issue of the optimum TCE for the interlayer is still not resolved although it is possible that a carefully chosen TCE mismatch can result in a strengthening of the relatively weak interlayer at the expense of the silicon nitride either side.

The following recommendations are made as a result of the problems encountered during mechanical testing:

- Every stage in the sample preparation should be reordered/randomised so that any systematic bias arising as a result of specimen preparation or testing can be pinned down.
- For 4-pt mechanical testing a standard requiring an articulated fixture such as United States MIL-STD 1942 (1983) is recommended. The details for the construction of a suitable fixture are given by Quinn [19].

References for Chapter 6

[1] Tenmat Ltd - manufacturers data sheet for Nitrasil S.

[2] Walls P.A. and Ueki M.., J. Am. Ceram. Soc., 75(9) 2491-97 (1992).

[3] Walls P.A. and Ueki M., J. Am. Ceram. Soc., 78(4) 999-1005 (1995).

[4] Becher P.F. and Halen S.A., Am. Ceram. Soc. Bull., 58(6) 582-586 (1979).

[5] Mecartney M.L., Sinclair R. and Loehman R.E., J. Am. Ceram. Soc., 68(9) 472-478 (1985).

[6] Knickerbocker S.H., Kumar A.H. and Wynn Heron L., Am. Ceram. Soc Bull., 72 [1] 91-95 (1993).

[7] Bridge D.R., Aspects of electronic device packaging, Ph.D. Thesis, University of Warwick, 1986.

[8] Johnson S.M. and Rowcliffe D.J., J. Am. Ceram. Soc., 68(9) 468-472 (1985).

[9] Rouxel T., Besson J.L. and Goursat P., J. Am. Ceram. Soc., 76 [11] 2790-2794 (1993).

[10] Watanabe K., Giess E.A. and Shafer M.W., J. Mater. Sci. 20 (1985) 508-515.

[11] Fischer R.A., The design of experiments, 8th edition, Hafner Publishing, 1966.

[12] Phadke, Quality engineering using robust design, Prentice Hall, 1989.

[13] Montgomery D.C., Design and Analysis of Experiments, Wiley, 1991.

[14] Brittain R.D., Johnson S.M., Lamoreaux R.H. and Rowcliffe D.J., J. Am. Ceram. Soc., 67(8) 522-526 (1984).

[15] Kubaschewski O. and Alcock C.B., Metallurgical Thermochemistry - 5th Edition, Pergamon, 1979.

[16] M.J.Moroney, Facts from Figures, Pelican books, 1958.

[17] Quinn G.D. and Morrell R., J. Am. Ceram. Soc., 74 [9] 2037-66 (1991).

[18] Peterson I.M., Tien T.Y.: J. Am. Ceram. Soc., 78(9) 2345-2352 (1995).

[19] Quinn G.D., J. Am. Ceram. Soc., 73 [8] 2374-2384 (1990).

[20] McColm, Ceramic Science, p38, Blackie and Son Ltd, 1983.

[21] ASM Engineered Materials handbook, Vol. 4 - Ceramics and Glasses, p859 (1991).

[22] Beall G.H., J. Non-Cryst. Solids 129 (1991) 163-173.

[23] Zdaniewski W. A., Conway C. J. Jnr., Kirchner H.P.: J. Am. Ceram. Soc., 70(2) 110-118 (1987).

Chapter 7: Joining Si_3N_4 to metals using a glass-ceramic interlayer

7.1 Joining silicon nitride to Nimonic 80A

One of the initial goals of this project was to investigate the possibility of producing a glass-ceramic joint with a graded thermal expansion to bridge the thermal expansion mismatch between Nimonic 80A (TCE ~ 16) and silicon nitride (TCE ~ 3). However, as demonstrated in Chapters 3 and 5, although this remains a possibility, the geometrical constraints would severely limit the practical applications of such a joint.

Instead, in order to utilise the high compressive strength of ceramics an attempt has been made to use a compressive geometry to minimise the tensile stresses in the ceramic. The geometry of the compression joints is described in section 4.3.6. Initial investigations to determine suitable joining parameters and interfacial chemistry were performed using a simple butt joint geometry.

7.1.1 Introduction - Nimonic 80A properties and uses

Nimonic 80A is a wrought, age-hardenable nickel-chromium alloy, strengthened by additions of titanium, aluminium and carbon, developed for service at temperatures of up to 815°C. Current applications include gas turbine components (blades, rings and discs), bolts, nuclear boiler tube supports, die casting inserts and cores, and automobile exhaust valves [1].

The limiting chemical composition is given in Table 7.1, and some of the more relevant physical properties are given in Table 7.2. The properties show some dependence on the heat treatment. The standard heat treatment for extruded bar consists of solution annealing for 8 hours at 1080°C/air cool, followed by precipitation hardening for 16 hours at 700°C/air cool. More information on properties and recommended heat treatments can be found in the manufacturers' literature [1].

Table 7.1: Limiting chemical composition, % by weight [1].

Chromium	18.0-21.0
Titanium	1.8-2.7
Cobalt	2.0 max
Aluminium	1.0-1.8
Silicon	1.0 max
Manganese	1.0 max
Iron	0.3 max
Copper	0.2 max
Zirconium	0.15 max
Carbon	0.10 max
Sulphur	0.015 max
Boron	0.008 max
Lead	0.0025 max
Nickel	Balance

Table 7.2: Properties of Nimonic alloy 80A [1].

Density	8.19 g cm^{-3}
Melting point	1320-1365°C
TCE (20-800°C)	16.2 MK^{-1}
Young's modulus at 20°C	183 GPa
Young's modulus at 800°C	123 GPa
Tensile strength	802 MPa

It is important that the required alloy microstructure is either preserved by any proposed joining heat treatment or can be restored with a subsequent heat treatment. One possible solution to this problem is to combine the joining heat treatment with the alloy heat treatment. Fortunately, the initial high temperature heat treatment (1080°C) coincides with temperatures suitable for creating a strong bond with the silicon nitride (1050-1100°C Chapter 5). As a result, although it is recommended that machining should be carried out on the fully heat treated alloy, machining was performed prior to the heat treatment to enable the joining heat treatment to be combined with the alloy heat treatment.

7.1.2 Nimonic 80A - oxidation behaviour

The oxidation behaviour of Nimonic alloy 80A must be seen in the context of the oxidation behaviour of a basic 80:20 Ni:Cr alloy. Initially both NiO and Cr_2O_3 are formed, the faster growth rate of NiO resulting in the growth of an overlayer of NiO. However, once a complete layer of Cr_2O_3 is formed, further NiO formation is prevented as the partial pressure of oxygen at the alloy-scale interface falls below the dissociation pressure of NiO. The oxidation rate is then controlled by the diffusion of chromium ions through the Ni doped Cr_2O_3 layer. A layer of $NiCr_2O_4$ spinel may form at the interface between the NiO and Cr_2O_3 and this may become the rate determining layer.

Alloys that form protective Cr_2O_3 scales suffer from accelerated degradation at high temperature due to the following reaction:

$$Cr_2O_3(s) + \tfrac{3}{2}O_2(g) \rightarrow 2CrO_3(g)$$

In high $p(O_2)$ this may become significant at temperatures above 1000°C and represents one of the major limitations for the high temperature use of Cr_2O_3 forming alloys and coatings [2].

In Nimonic 80A, the surface scale of Cr_2O_3 is formed as before, but the presence of additional reactive elements results in subsurface oxidation, and particles of aluminium and titanium oxides form beneath the surface. The rate of subsurface oxidation diminishes once a fully protective Cr_2O_3 scale is established [3].

In common with other commercial superalloys, the oxidation behaviour and oxide scale adhesion are subtly dependent on, and significantly improved by, the other minor additives present. "The precise compositional effects on the oxidation mechanisms of complex superalloys involve multi-element interactions that are beyond present day understanding" [2]. Smialek and Meier [2], and Betteridge and Heslop [3] give further information on the oxidation behaviour of Nimonic 80A and other nickel based superalloys.

Hong [4] working on coating Nimonic alloy 263 with lithium silicate glass-ceramics showed that pre-oxidation creates an adherent Cr_2O_3 layer which is stable in contact with the glass due to its low diffusivity. Hong showed that a longer heat treatment at

a lower temperature results in a "well-formed" oxide layer, and found that a suitable heat treatment was 900°C for 4 hours.

7.1.3 Nimonic 80A oxidation trials

For preoxidation trials for Nimonic 80A, small discs were polished to a 1 μm diamond finish, degreased in acetone and used for oxidation trials with temperatures from 800-900°C and times from 1 to 16 hours.

7.1.4 Nimonic 80A oxidation trials - results

XRD of the oxide scale developed as a result of 16 hour heat treatment is shown in Figure 7.1. A Cr_2O_3 scale is seen to dominate with some TiO_2 also present. Preoxidation at 800°C for 16 hours produced an oxide scale approximately 0.25-0.5 μm thick and no visible formation of sub-surface oxides. The preoxidation heat treatment at 900°C for 16 hours produced an oxide scale a few μms thick and sub-surface oxides to a depth of slightly less than 10 μms, as shown in Figure 7.2. EDX confirms XRD evidence for the existence of Cr_2O_3 and TiO_2 oxide scale, but also reveals subsurface titanium and aluminium oxides, and a thin layer of Al_2O_3 under the surface oxide scale.

Interestingly, back-scattered micrographs with high levels of contrast (Figure 7.3), allowed the grain boundaries to be revealed due to channelling contrast from grains within the Nimonic 80A with differing crystallographic orientations to the incident beam. This illustrates that etching is not always necessary in order to reveal grain boundaries.

The 900°C/16 hour pre-oxidation heat treatment was chosen for the joining trials. Although oxidation to this extent may be neither necessary nor beneficial, it does ensure that the oxide scale and the resulting interaction zone with the glass-ceramic are of a suitable size for investigation using EDX and SEM. A lower temperature/shorter time preoxidation may well be sufficient and would be less disruptive to the alloy microstructure.

7.1.5 Joining trials

Butt joint trials were used initially to evaluate the interaction between the glass-ceramic and the pre-oxidised (900°C/16 hours) Nimonic alloy 80A. The joining heat

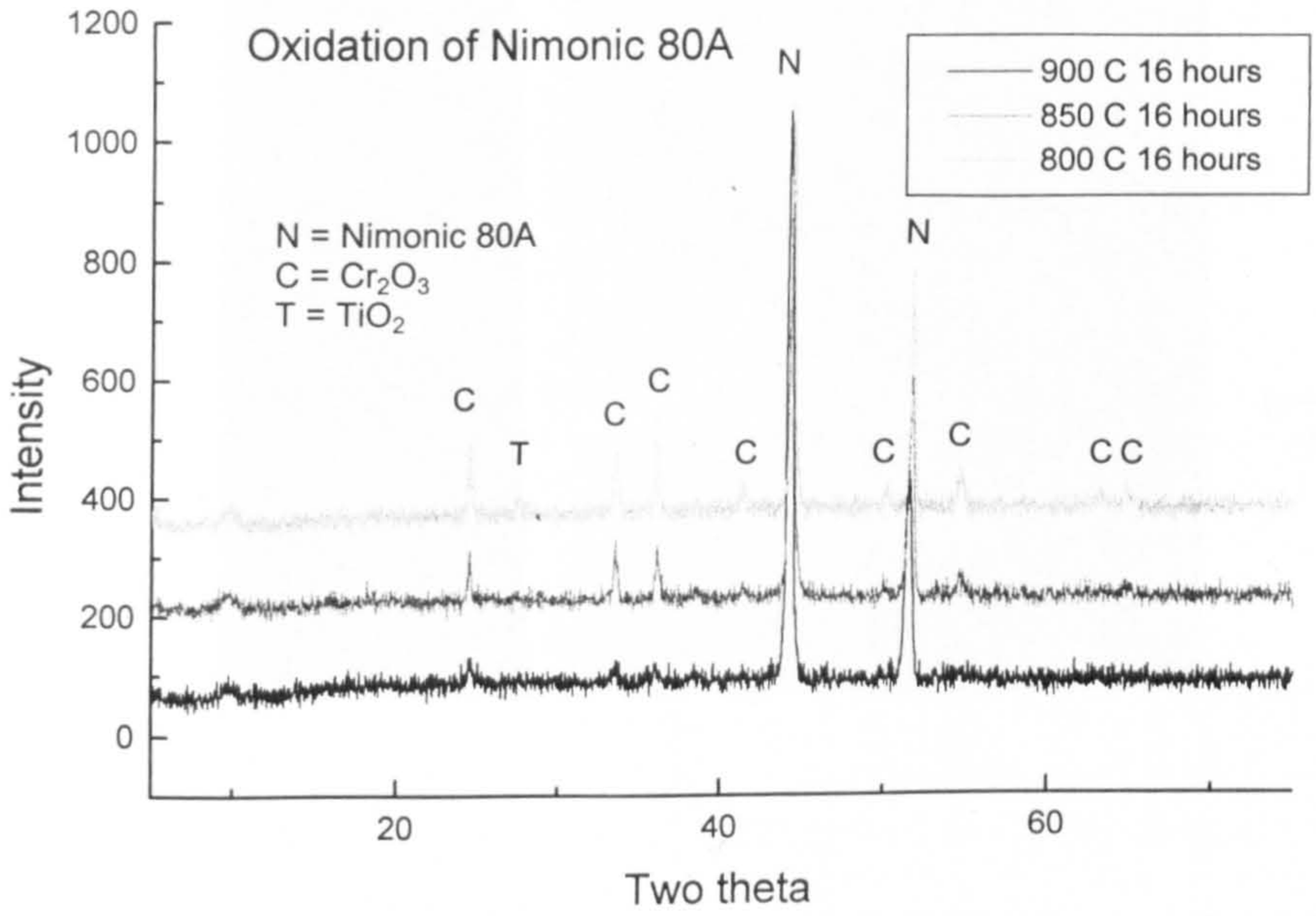

Figure 7.1: X-ray diffraction pattern of oxidised Nimonic 80A.

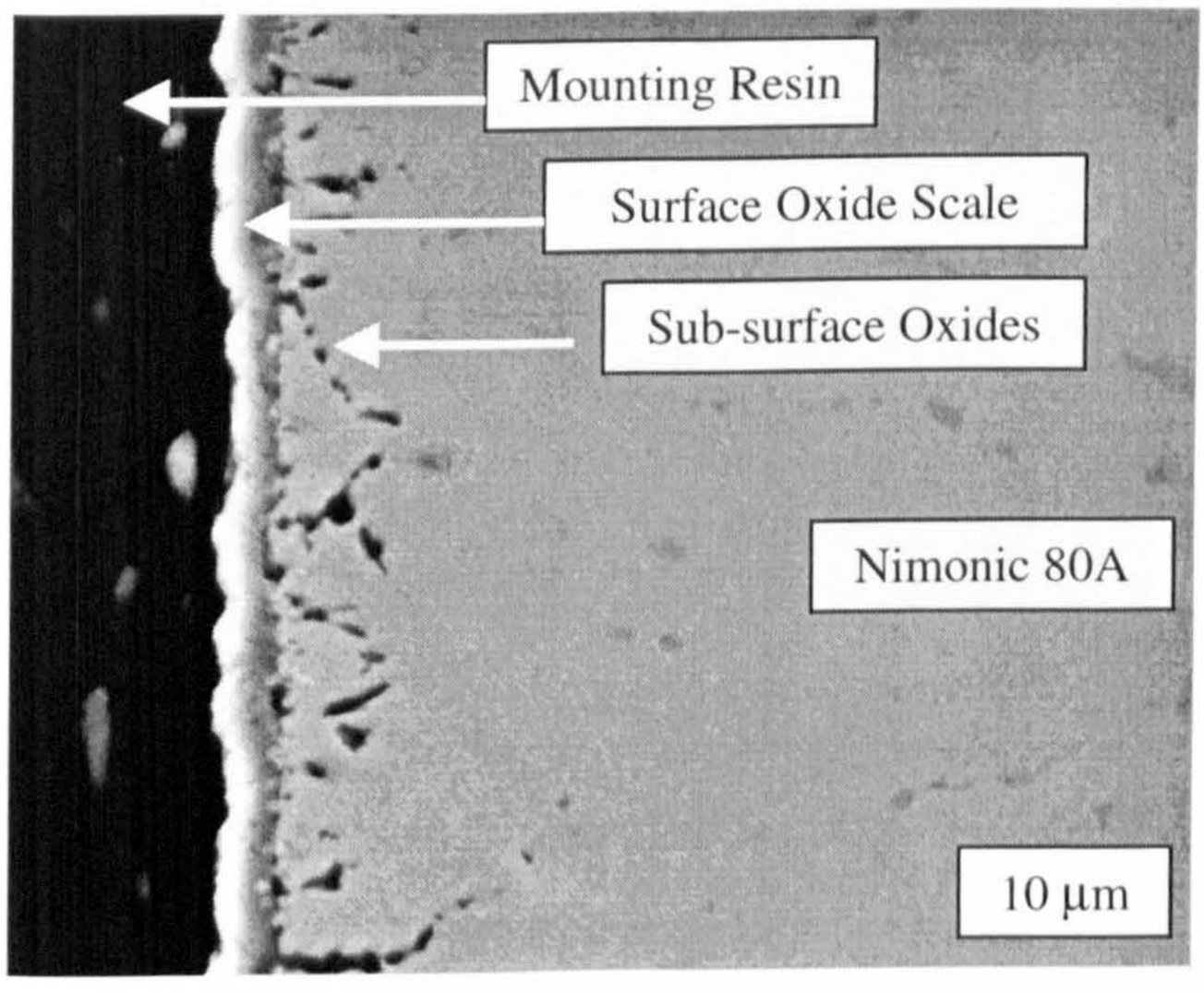

Figure 7.2: Oxide scale on Nimonic 80A after 900°C/16 hour heat treatment.

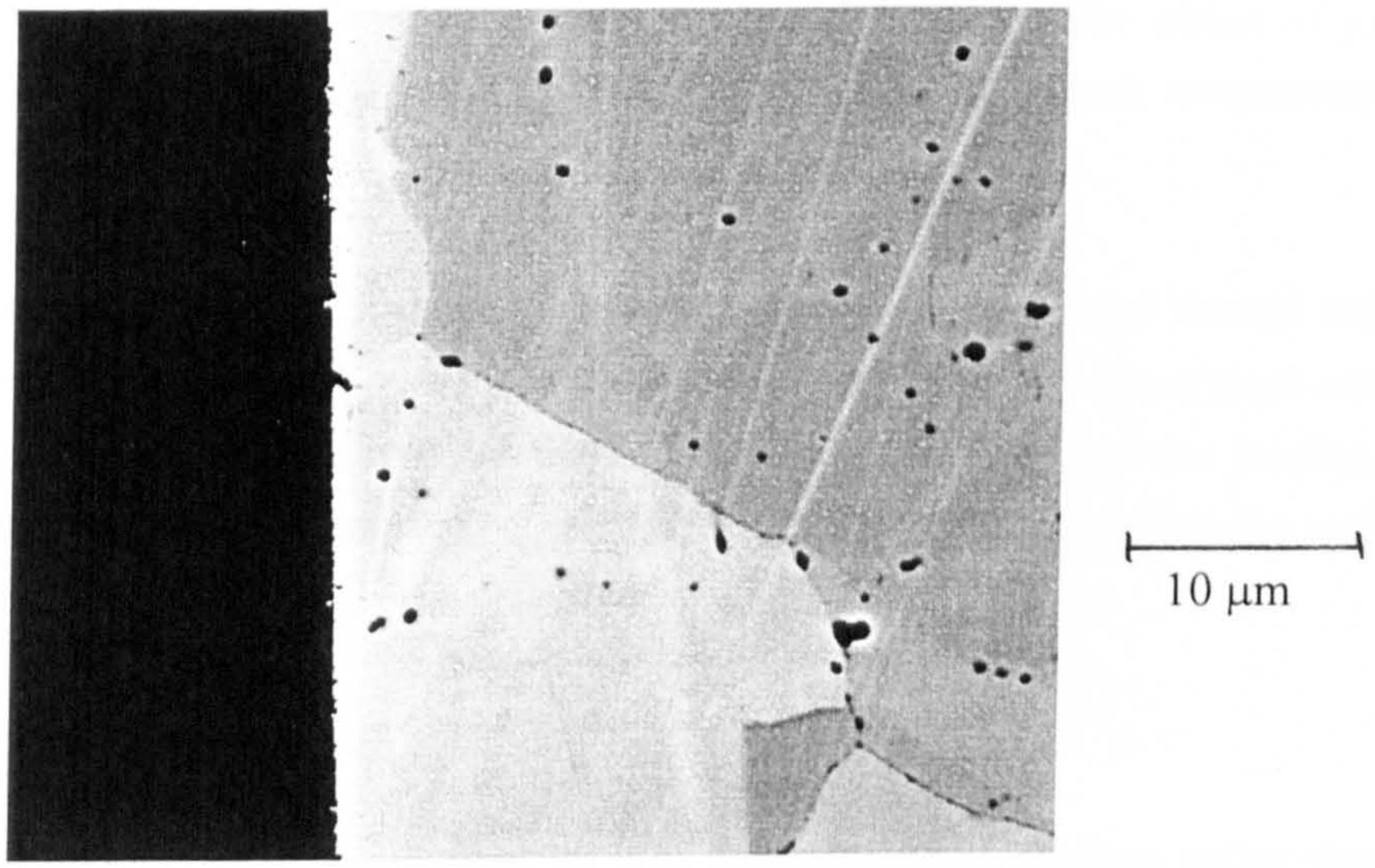

Figure 7.3: High contrast back-scattered electron micrograph of Nimonic 80A (oxidised at 800°C for 16 hours) showing grain boundaries.

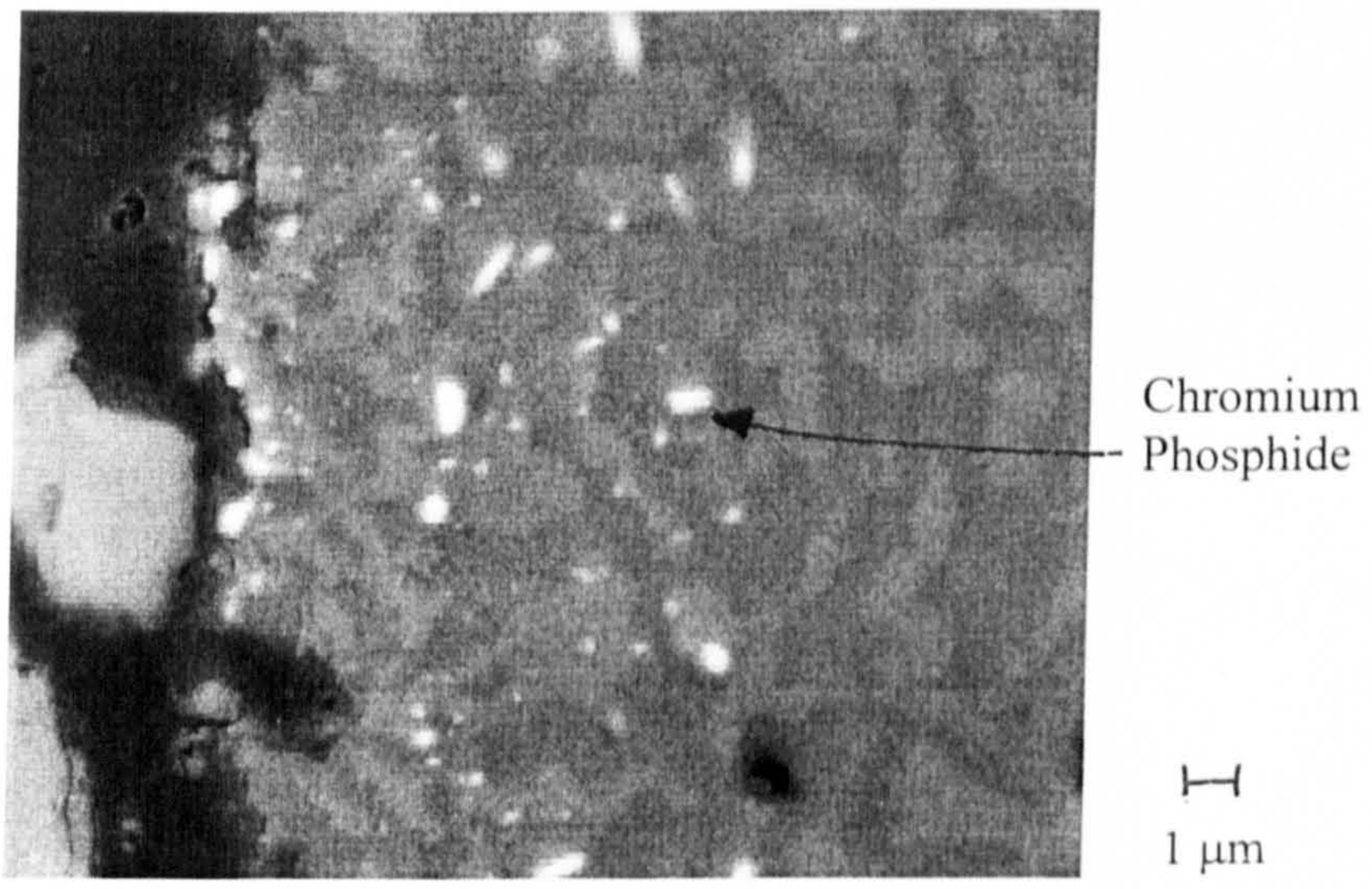

Figure 7.4: Magnesium aluminosilicate glass-ceramic detached from preoxidised Nimonic 80A alloy.

treatment was the same as that for joining silicon nitride to itself with a final 45 minute joining hold in N_2 and an applied load of 2.5 MPa. The effect of joining temperatures of 1200°C and 1080°C (the solution heat treatment temperature for Nimonic 80A) were investigated.

For the compression joints, the same joining conditions were used except that the joining pressure was increased to ~ 6 MPa to ensure that the glass/glass-ceramic filled the gap between the silicon nitride and the Nimonic 80A, and the joining hold was increased to two hours at 1080°C, so that it more closely resembled the required solution heat treatment of the Nimonic 80A.

7.1.6 Joining trials - results

Due to the high level of residual stress all butt joints failed on cooling, either through the MAS, through the oxide scale, or at the glass-ceramic/scale or scale/metal interface. However, sufficient MAS adhered to enable the interfacial reactions and microstructure to be investigated.

Joining at 1080°C, corresponding to the solution heat treatment temperature for the Nimonic alloy 80A, resulted in partial dissolution of the chromium oxide scale and the formation of $MgTi_2O_5$-Al_2TiO_5 solid solution at the interface. The chromium reacted with the phosphorus present in the glass-ceramic to form chromium phosphides (Figure 7.4) although no notable coarsening of the glass-ceramic microstructure has occurred.

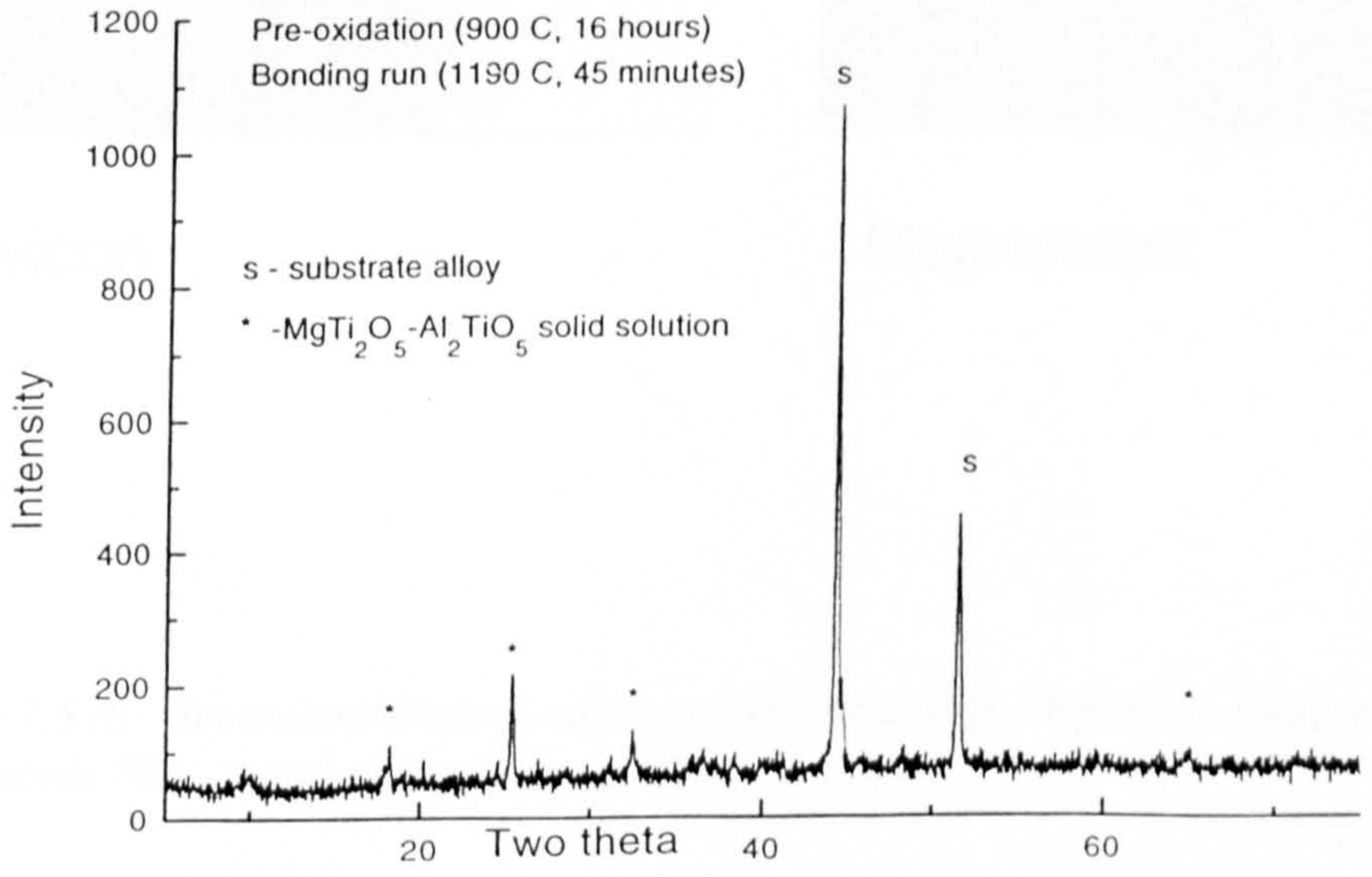

Fig 7.5: X-ray diffraction pattern of Nimonic 80A alloy detached from MAS glass ceramic.

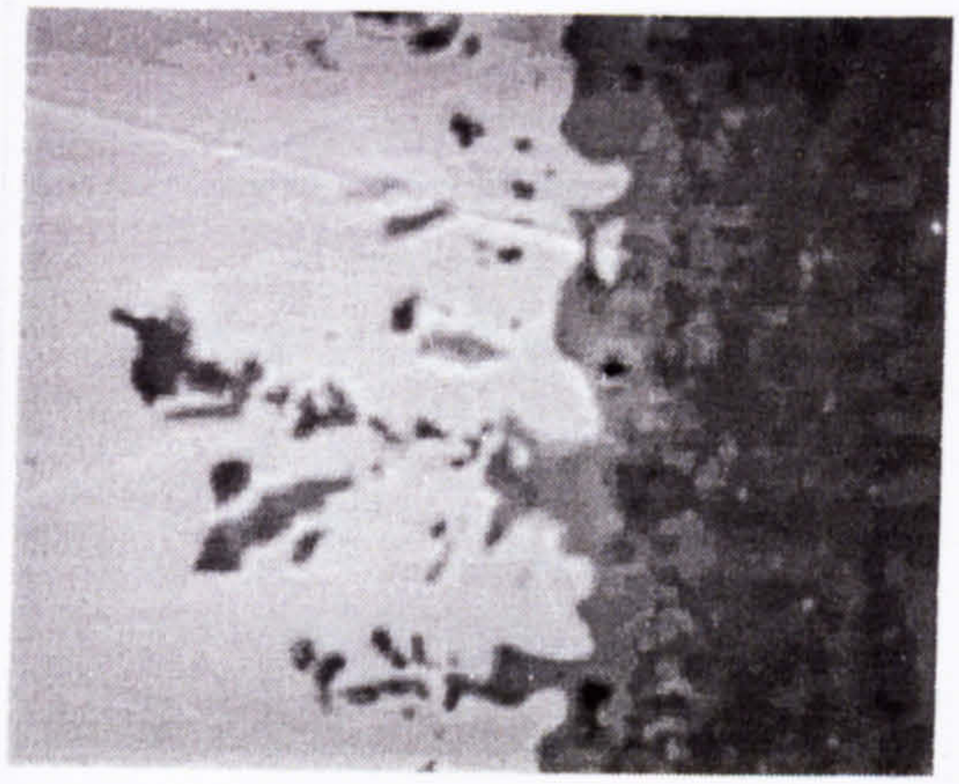

Secondary Electron Image

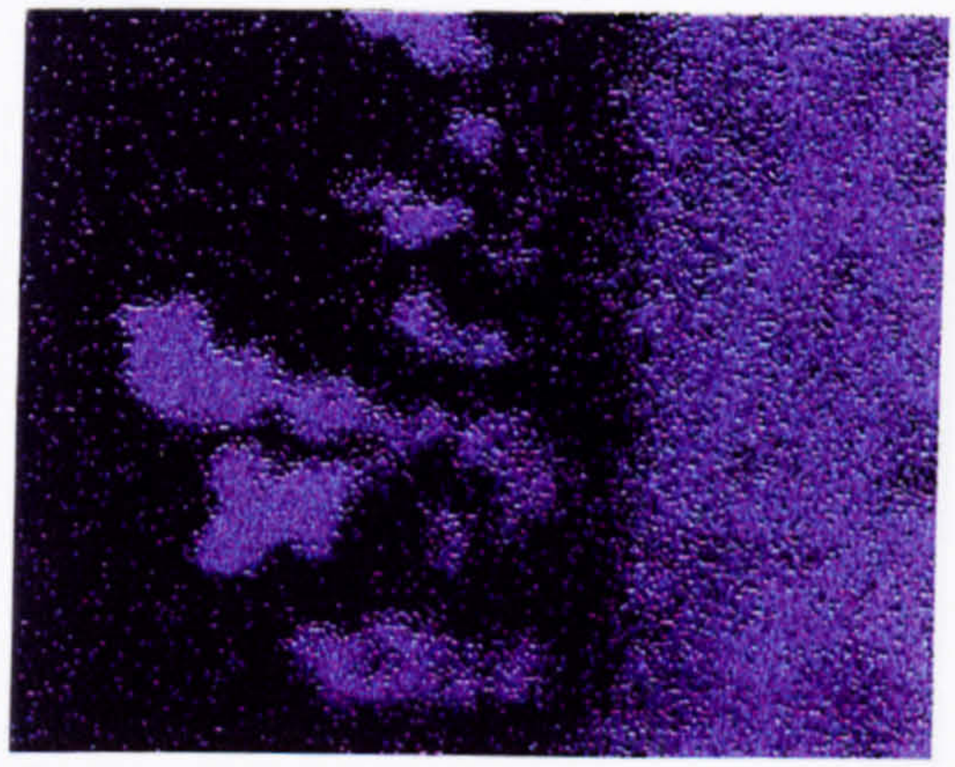

Aluminium

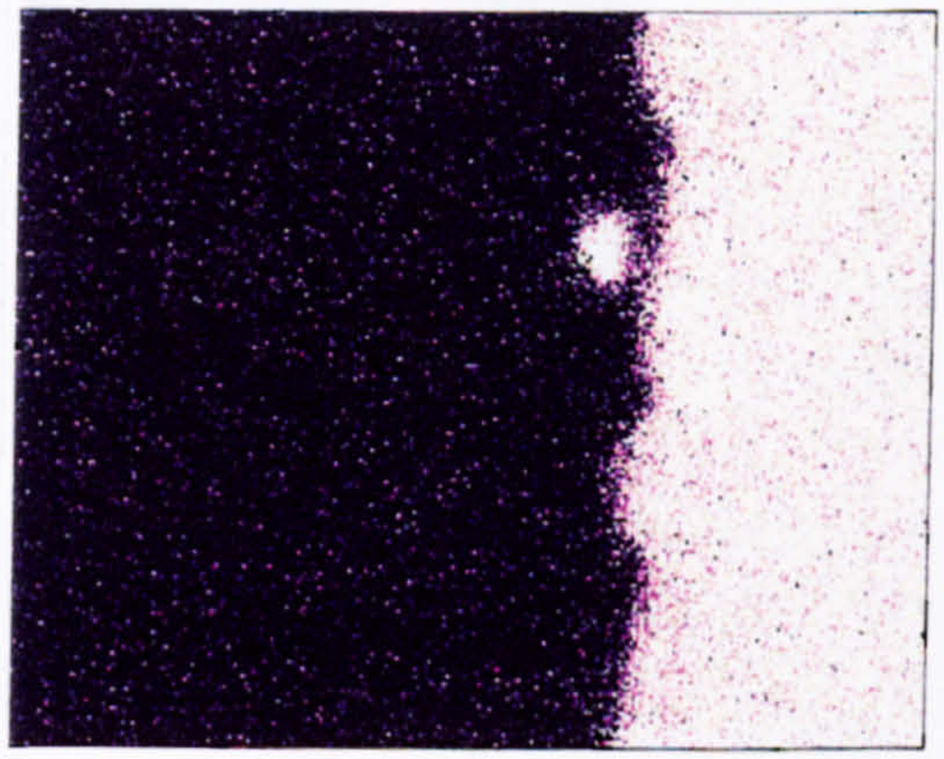

Silicon

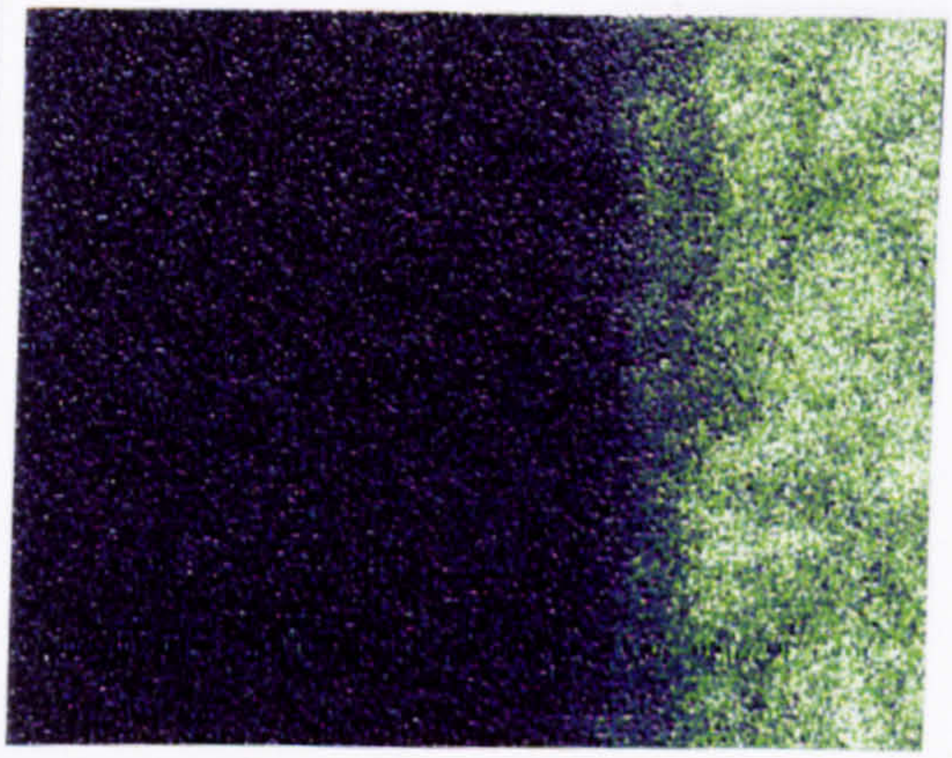

Magnesium

1 μm

Fig 7.6 (i): Secondary electron micrograph and energy dispersive x-ray maps of Nimonic 80A - metal oxide - glass-ceramic interface.

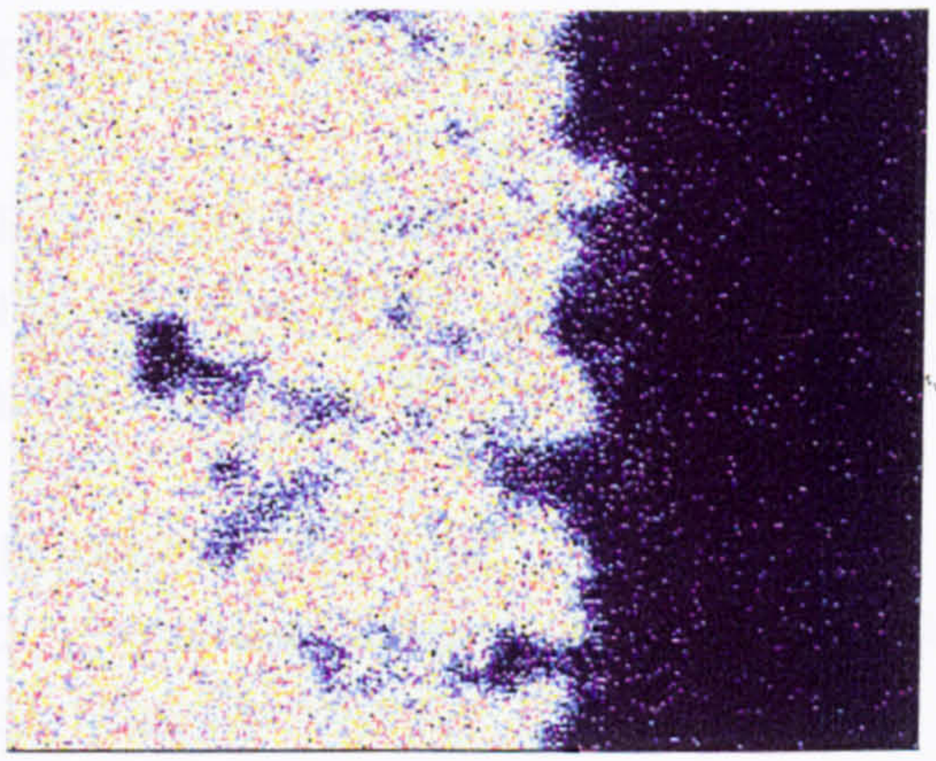

Nickel

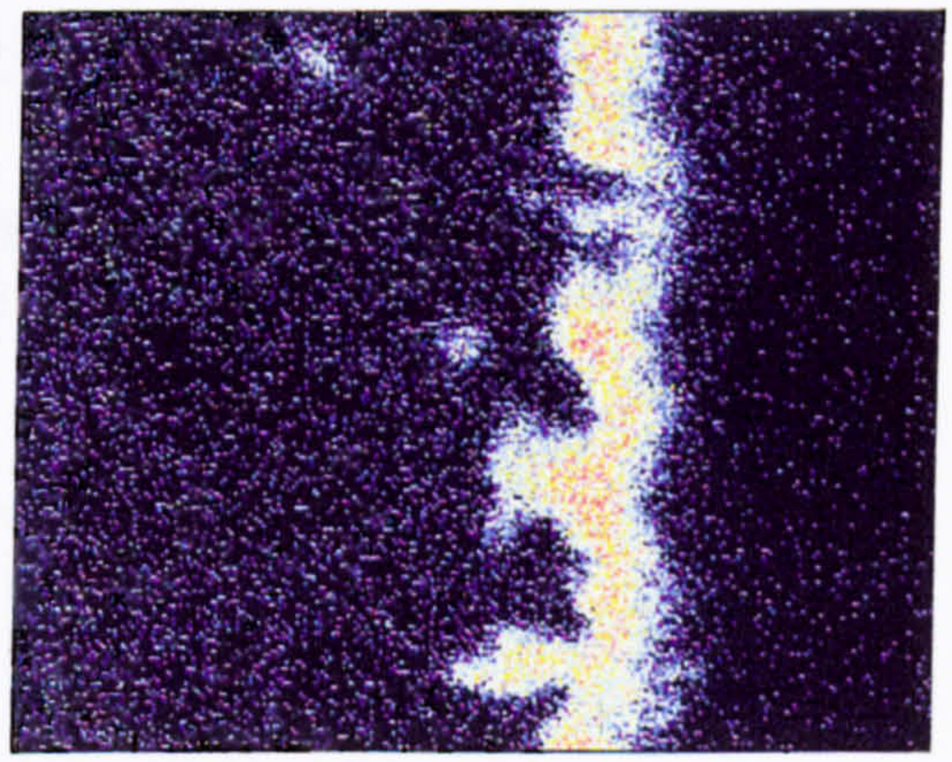

Titanium

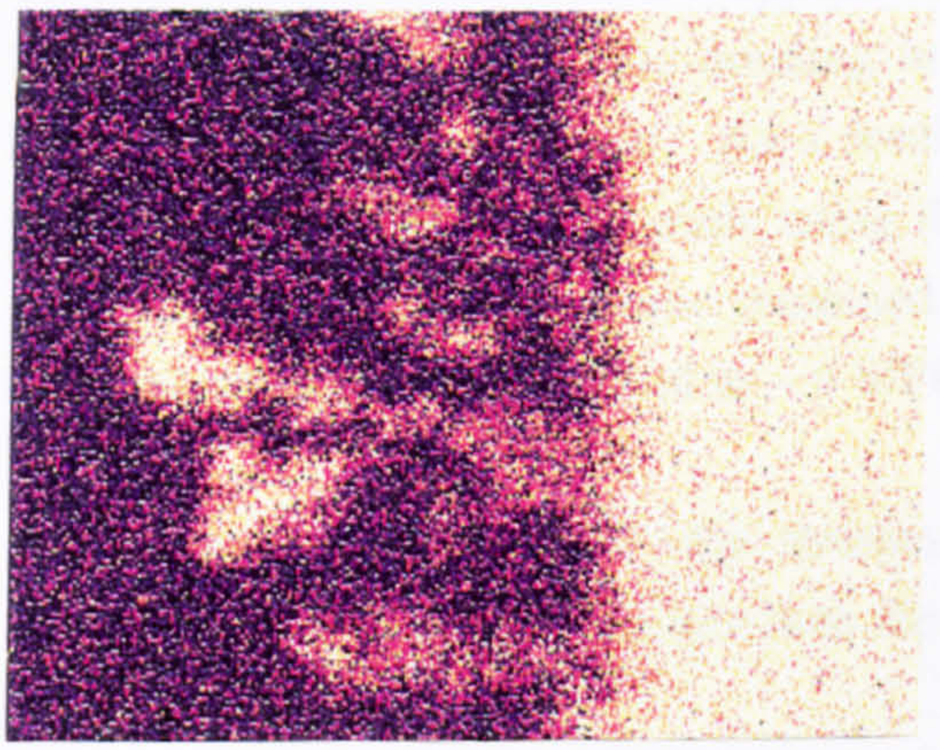

Oxygen

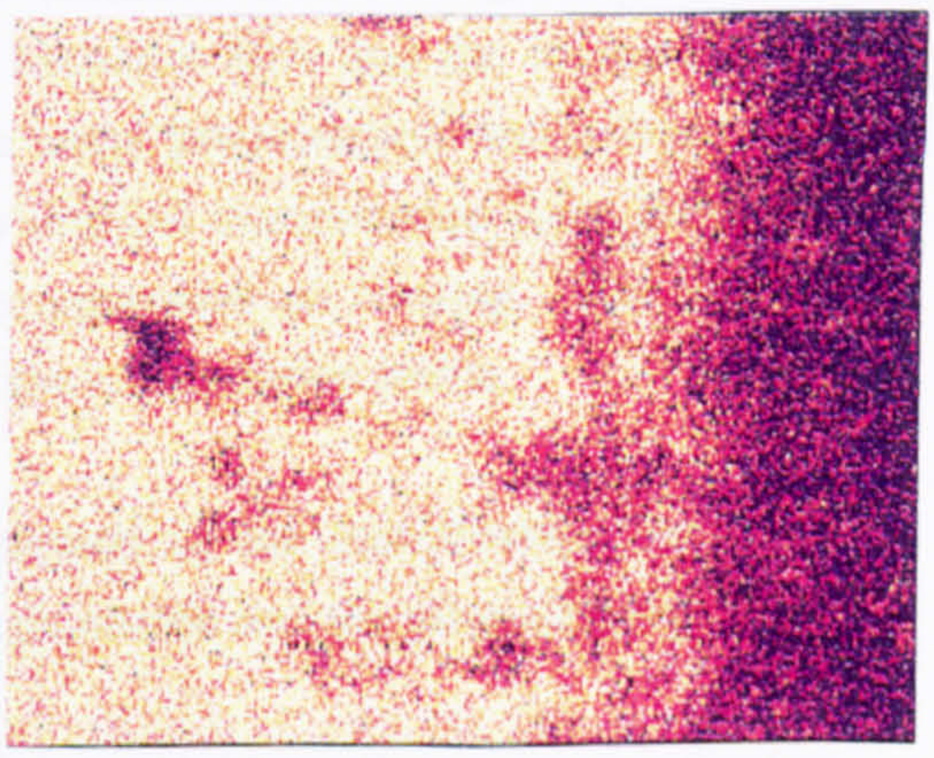

Chromium

1 μm

Fig 7.6 (ii): Energy dispersive x-ray maps of Nimonic 80A - metal oxide - glass-ceramic interface.

Joining at a slightly higher temperature (1200°C) resulted in further dissolution of the chromium oxide and increased formation of $MgTi_2O_5$-Al_2TiO_5 solid solution. An XRD of Nimonic alloy 80A detached from MAS glass-ceramic is shown in Figure 7.5 demonstrating presence of the $MgTi_2O_5$-Al_2TiO_5 solid solution phase.

EDX maps of the Nimonic 80A-metal oxide-glass-ceramic interface are shown in Fig 7.6 (i) to 7.6 (ii). In crossing the interface from the Nimonic 80A to the oxide glass-ceramic the following layers are seen:

1. Nimonic 80A alloy
2. Nimonic 80A alloy with subsurface oxides
3. Titanium oxides
4. $MgTi_2O_5$-Al_2TiO_5 solid solution with titanium and chromium oxides
5. Magnesium aluminosilicate glass-ceramic with chromium phosphide precipitates
6. Magnesium aluminosilicate glass-ceramic

This interfacial microstructure appears to be effective at ensuring continuity of bonding between the metallic bonding in the Nimonic 80A and the ionic/covalent bonding in the glass-ceramic. As a result the same preoxidation and joining heat treatments were used in the trials using the cylindrical compression joint geometry which ensured that the ceramic remained in compression on cooling. The applied uniaxial pressure was increased to ~ 6 MPa for the compression joints.

As illustrated in Figure 7.7, the stresses generated in the compression joints on cooling were sufficient to fracture both the silicon nitride and the glass-ceramic.

Where the MAS remained adhered to the Nimonic 80A after cross sectioning (perpendicular to the diameter) and polishing, the interfacial microstructure was similar to that obtained in the butt joint trials. An example interfacial microstructure between the Nimonic 80A and the MAS1 glass-ceramic (for a compression joint) is shown in Figure 7.8.

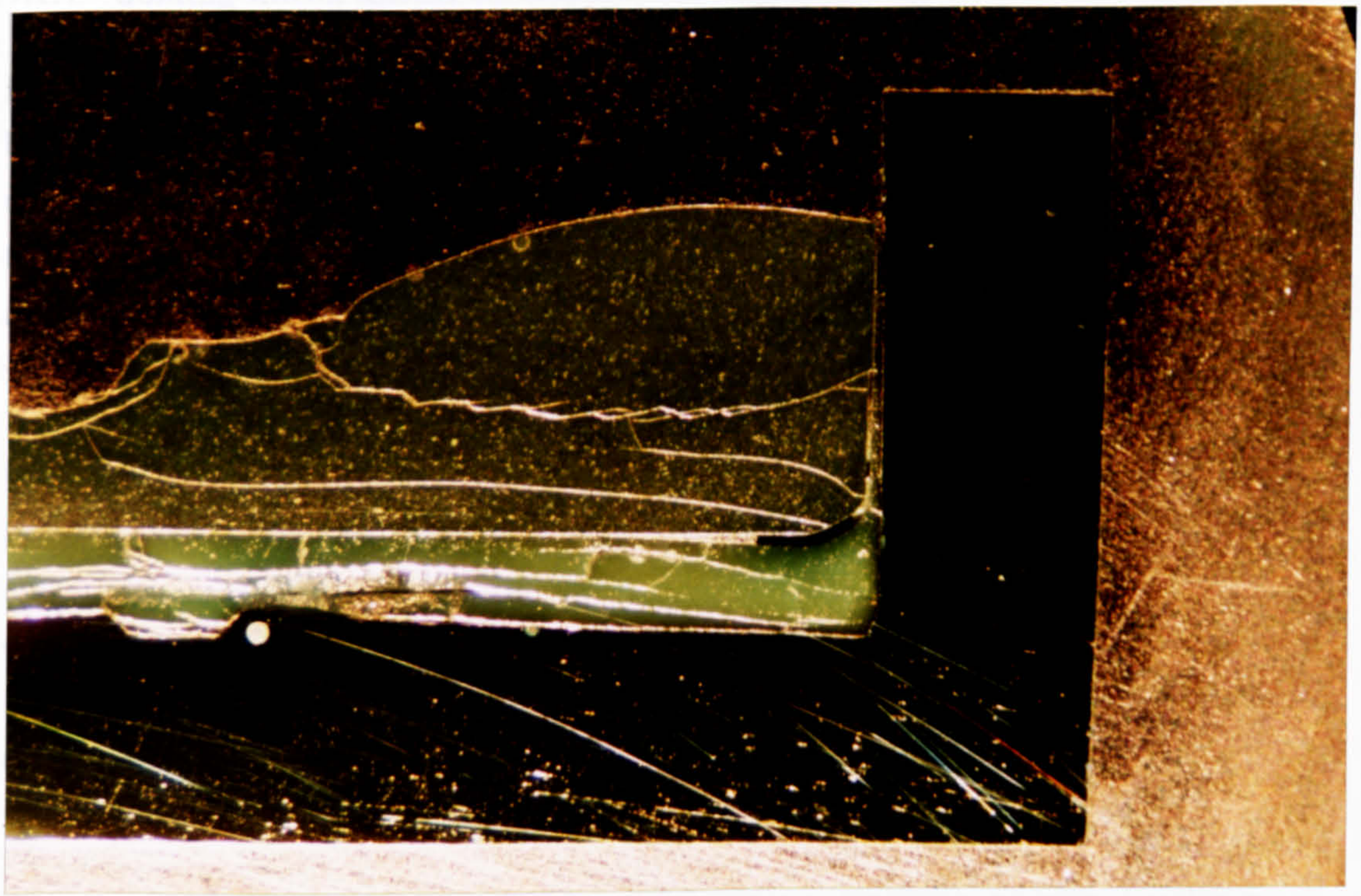

Figure 7.7: Cross section of Nimonic 80A - MAS interlayer - silicon nitride compression joint showing extent of the fracture in the silicon nitride and the glass-ceramic. 1 mm

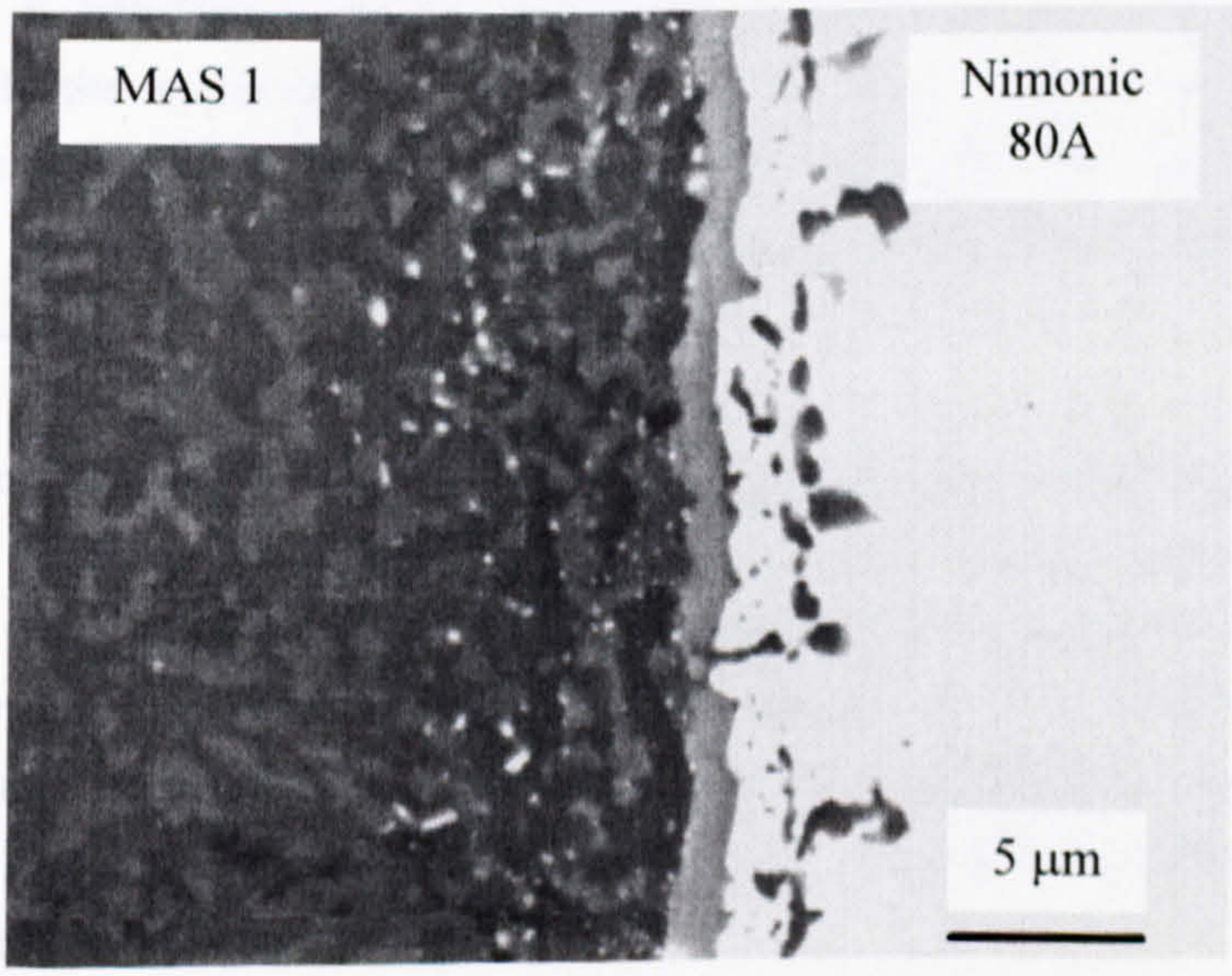

Figure 7.8: Microstructure of Nimonic 80A - MAS1 interface in silicon nitride - MAS1 - Nimonic 80A compression joint

7.1.7 Joining silicon nitride to Nimonic 80A - discussion

Pre-oxidation at 900°C for 16 hours has been shown to result in a suitable interlayer between the Nimonic 80A and the MAS glass-ceramic. However, in contrast to LS on Nimonic 263 [4] this does not rely on the stability of the Cr_2O_3 in contact with the glass/glass-ceramic but is due to the reaction between the pre-oxidised surface and the glass/glass ceramic producing a stable interlayer of $MgTi_2O_5$-Al_2TiO_5 solid solution.

For the temperature and glass-ceramic composition used in this work, the Cr_2O_3 interlayer appears to dissolve readily in the glass. Both the glass-ceramic composition and the higher temperatures involved for MAS compared to LS may contribute to the reduced stability of the Cr_2O_3 scale. It is possible that a shorter, or lower temperature, pre-oxidation heat treatment would be sufficient and less damaging to the alloy microstrucure.

The Cr reacts with the P_2O_5 present in the glass-ceramic resulting in the formation of chromium phosphide precipitates. In contrast to where this has been reported in LS [5] glass-ceramics, this did not result in a coarsening of the glass-ceramic microstructure at the interface . This illustrates that, in contrast to LS and LZS glass-ceramics, the role of P_2O_5 in MAS glass-ceramics is not that of a conventional nucleating agent and particle surface nucleation is dominant

In this work it has been possible to develop a joining heat treatment to satisfy simultaneously the requirements for the formation of a strong bond between the glass-ceramic and both the silicon nitride and the Nimonic 80A, and combine this joining heat treatment with the recommended solution heat treatment for the Nimonic 80A alloy.

However, for the compression geometry chosen, the residual stress generated on cooling was sufficient to fracture the silicon nitride. If the compression joint demonstrated here is to be developed further, then either the joint must be designed with a lower level of residual stress, or the degree of TCE mismatch must be reduced. It may be possible to successfully join Nimonic 80A to a ceramic with a significantly higher TCE than silicon nitride (eg: zirconia or alumina) using a similar compression joint geometry.

7.2 Joining silicon nitride to titanium

As demonstrated in Section 7.1, the excessive TCE mismatch between Nimonic 80A and silicon nitride resulted in fracture of the silicon nitride when a compressive joining geometry was used. Due to the lower TCE mismatch between Ti and silicon nitride, Ti was selected to demonstrate a 'proof of concept' for a compression joint using a glass-ceramic interlayer. The work has concentrated on the possibility of simultaneously obtaining a satisfactory chemical bond to the glass-ceramic for both the Ti and the silicon nitride. The following issues, which would need detailed consideration if such a joint were to be considered for practical applications, have not been considered:

- The effect of the heat treatment on the Ti microstructure, or the possibility of restoring the microstructure with a subsequent post joining heat treatment.
- The potential mechanical performance of the joint.
- The optimum joint geometry and dimensions.
- The optimum TCE for the glass-ceramic interlayer.

Although joining trials have been performed with Ti metal, some of the conclusions should be transferable with caution to Ti alloys. The geometry of the compression joints used was the same as those used for Nimonic 80A (detailed in Chapter 4).

7.2.1 Introduction - titanium: properties and uses

Titanium is widely used in aerospace and other commercial and military applications due to its high specific strength, excellent corrosion resistance (due to the formation of a stable oxide layer), and other attractive physical properties (see Table 1.1). In particular it is used for highly loaded aerospace components, where moderately high temperatures are encountered (normally less than 600°C). Production of titanium and titanium alloys in The United States peaked at 25 million kg per year in 1990, and the estimated USSR capacity at the height of the cold war was 90 million kg per year [6].

Titanium exists in two crystallographic forms: the hexagonal closepacked α-phase which transforms to a body centred cubic β-phase via a reversible phase transformation at 883°C. The α and β forms have different properties and with choice of doping and heat treatment, it is possible to control the extent of the α-β

transformation and tailor the properties of the alloy for specific applications. The use and properties of titanium and titanium alloys are discussed in [7] and [6].

Table 7.1: Properties of Titanium

Density	4.507 g cm^{-3}
Young's Modulus	102.7 GPa
Poisson's ratio	0.41
Melting point	1668°C
Tensile strength	620 MPa
TCE (25-1000°C)	10.6 MK^{-1}

There is much interest in joining titanium to ceramics and coating titanium with a ceramic layer in order to improve both the high temperature and corrosion properties. One possible benefit of a ceramic layer or coating is to act as a diffusion barrier to prevent runaway oxidation of the titanium at high temperature. Previous work at Warwick has looked at the use of both LS [4] and MAS/MS [8] glass-ceramics as possible protective coatings. MAS/MS glass-ceramics, based on enstatite or forsterite, enable the TCE and elastic modulus to be closely matched with that of Ti.

Pre-oxidation is often used when coating metals with an oxide glass or glass-ceramic. The possibility of pre-oxidation of titanium is therefore considered briefly.

7.2.2 Oxidation of Titanium

Oxidation of titanium is quite complicated due to the presence of several oxides of different formula, and the existence of non-stoichiometric phases sometimes varying widely from the stoichiometric compositions. According to Simons [9], at 610°C Ti burns with great brilliancy in oxygen producing TiO_2, and burns violently in nitrogen, ignition occurring at 800°C to form TiN. When heated in air a mixture of oxides and nitrides results. According to Evans [10] "The oxidation of titanium is largely a process of oxygen passing inwards through the film, probably by oxygen anions taking advantage of vacant anion sites in the lattice. On reaching the metal/oxide interface part of it enters into solid solution and part of it is used to form fresh oxide and thus increases the thickness of the film. The film is in a state of strain and when it reaches a certain thickness it breaks away and becomes non-protective".

The nature of oxidation of Ti is strongly temperature dependent. Oxidation at temperatures in excess of 700°C results in a succession of sublayers, the thickness depending on the temperature and the oxidation atmosphere. Ti is able to take oxygen into solid solution. Where this occurs above a certain level it results in the formation of α-case, which results in embrittlement of the Ti/Ti alloy. Any high temperature treatment heat treatment needs to be performed in an inert atmosphere if significant α-case formation is to be prevented. Under certain conditions, Ti is able to reduce its own oxides. The oxygen may be taken into solid solution, or result in increased formation of α-case.

Where preoxidation is used to create an interlayer for joining or coating applications, the strength of oxide adherence is critical, as this may be strength limiting. In addition, in order to remain protective the oxide scale must stay in contact with the Ti.

Coddet [11] studied the adherence of oxide films on a titanium substrate using a tensile pull test. He found that oxide films produced below 650°C have high adhesion strength. In general the adherence of the oxide films decreases with increasing film thickness although this is also a function of oxidation temperature. For films produced at 650°C the reduction in adhesive strength is only significant beyond a thickness of 5-7 μm. The maximum adhesion strength of nearly 70 MPa was for films grown for 100 hours in air at 650°C. The possibility of using this pre-oxidation treatment in the current work is considered below.

The adhesion strength of films grown above 700°C tended towards zero. This corresponded to a change to a layered oxide structure. This indicates that the breakaway of oxide scales is not solely related to oxide thickness. One possibility is that above a certain temperature the flux of oxygen arriving at the interface through the film is exceeded by that being taken into the titanium alloy, the dynamic equilibrium at the interface is not maintained and a weakly adherent scale results

Preoxidation of Titanium

Pre-oxidation for 100 hours at 650°C resulted in a dense green/grey TiO_2 layer 4 μ ms thick. EDX analysis revealed the existence of an oxygen gradient through the film with a lower oxygen concentration at the metal/oxide interface. However, heat treatment in air, nitrogen and argon at 1100°C (the sort of temperature required to

join the glass-ceramic to the silicon nitride), revealed that the oxide scale was not stable at higher temperatures.

For example, heat treatment of a pre-oxidised sample in air at 1100°C resulted in catastrophic oxidation and a thick scale of orange rutile. The colour of the scale indicates that TiN was also present. The thickness of the oxide scale was sufficient for residual thermal stress on cooling to distort the titanium. The resulting oxidised titanium was extremely weak and brittle.

Heat treatment of a pre-oxidised sample at 1100°C in an nitrogen atmosphere resulted in a thicker (4-12 μm), porous white/orange oxide scale. A layer of TiN was identified at the interface between the oxide scale and the Ti using EDX.

For the pre-oxidised sample heat treated at 1100°C in the furnace vacuum (~ 1 Pa) no adherent oxide scale was observed using SEM.

Although Coddet [11] has demonstrated that preoxidation of Ti can produce a strongly adherent scale, this is not stable when exposed to higher temperatures than those encountered in its growth. The use of preoxidation at lower temperature (for example 650°C) to provide a protective film at higher temperatures is limited. This is due partly to the non-protective nature of the oxide scale at high temperatures, but also due to the ability of titanium to take oxygen into solid solution and reduce its own oxides.

Using the MAS glass-ceramic in the current work, the temperatures required for joining are too high for preoxidation to provide a suitable interlayer. However, for less refractory glass-ceramic compositions the pre-oxidation heat treatment reported by Coddet [11] may be suitable.

7.2.3 Titanium-silicon nitride joining trials

Titanium-silicon nitride compression joints were produced using the same heat treatment as the silicon nitride-silicon nitride and silicon nitride-Nimonic 80A joints, except that argon was used in place of N_2.

The final joining hold was 1100°C for 45 minutes with an applied uniaxial load of ~ 6 MPa. All the titanium and silicon nitride used was joined in as-cut condition and thoroughly cleaned, and degreased in acetone prior to joining.

The TCE of the glass ceramic used (MAS1 which contains B_2O_3 and P_2O_5, TCE - 5.7 MK^{-1} (50-800°C) is intermediate between that of the silicon nitride (TCE - 3 MK^{-1} (50-800°C)) and the titanium (TCE - 10.6 MK^{-1} (25-1000°C).

7.2.4 Titanium-silicon nitride joining trials - results

Figure 7.9 shows a Ti/silicon nitride compression joint viewed from above. The MAS glass-ceramic has completely filled the gap between the Titanium and the silicon nitride and extruded over the top of the silicon nitride. Before sectioning, this appears to be a successful joint. The thin white scale (which was only loosely attached to the titanium) indicates that some oxidation has occurred.

Figure 7.9: Silicon nitride/MAS1/titanium compression joint viewed from above.

Because of the considerable residual joining stress generated on cooling, the joint was sectioned to produce a circular cross-section, as shown in Figure 7.10. Cross-sectioning perpendicular to the diameter was not performed as the resulting relaxation of residual stress would have caused considerable damage to the MAS/silicon nitride and the MAS/Ti interfaces. Such damage was observed in the cross-sections of the Nimonic 80A/MAS/silicon nitride compression joints. Figure 7.10 illustrates the even distribution of the glass ceramic in the silicon nitride/MAS1/titanium compression joint. A small crack can be seen in the silicon

nitride, which is shown in more detail in Figure 7.11. This crack was not observed initially, and although it may have been missed in the original observation, it is believed to arise from sub-critical crack growth due to the high levels of residual joining stress present. Sectioning, or damage due to sectioning may also have contributed.

TCE mismatch cracks can be seen in the MAS interlayer, these are shown in more detail in Figure 7.12. Some of these cracks appear to run along the interface between the silicon nitride and the glass-ceramic However, close contact is maintained along most of the interface. The level of porosity in the glass-ceramic appears to be slightly higher than when (as in the silicon nitride butt joints in Chapter 6) the glass-ceramic is subjected to a small uniaxial pressure.

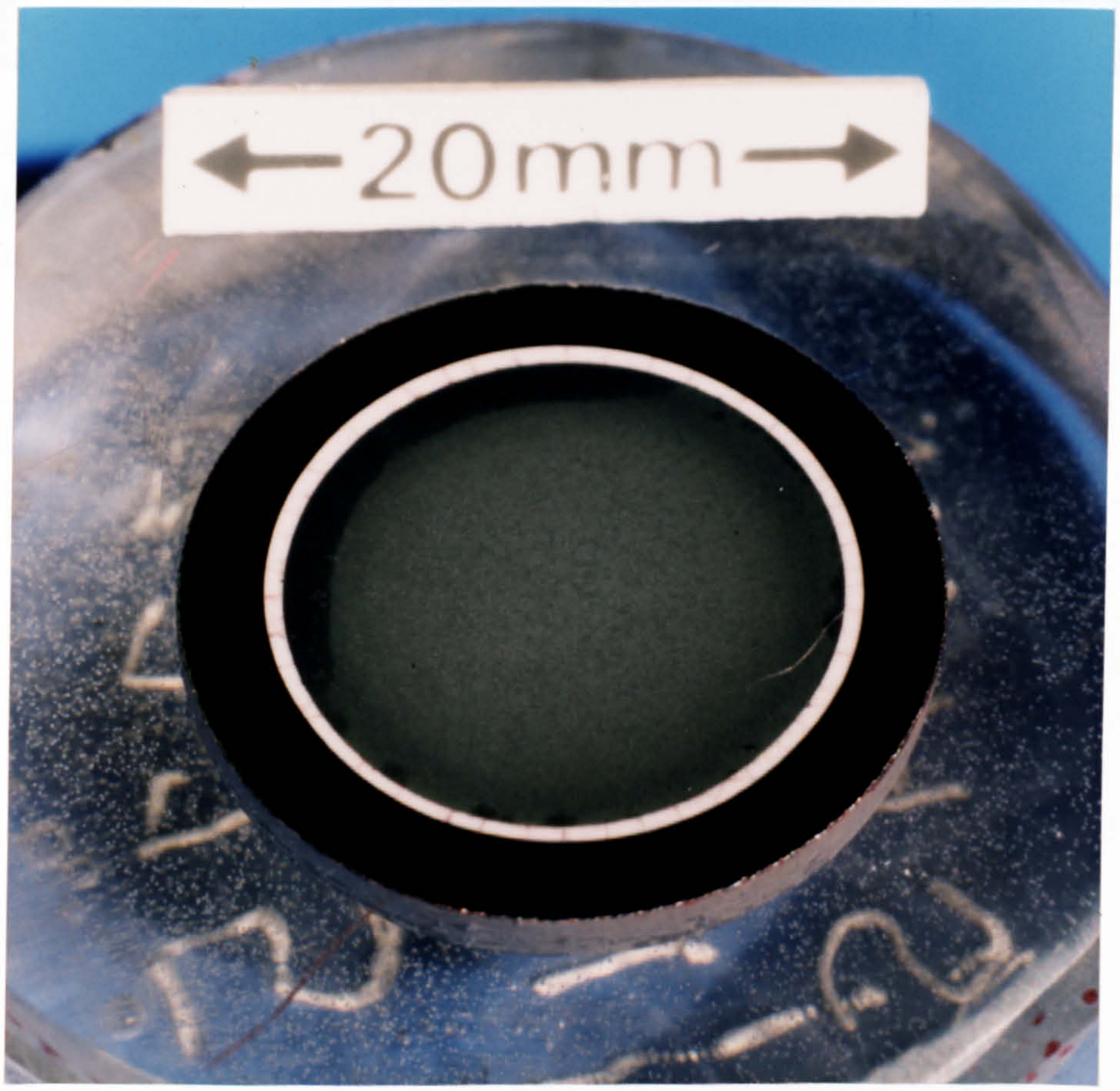

Figure 7.10: Polished cross-section of silicon nitride/MAS1/Ti compression joint indicating even distribution of glass-ceramic.

Figure 7.11: Optical micrograph of silicon nitride/MAS1/Ti compression joint. TCE mismatch cracks can be seen in the glass-ceramic interlayer. The crack in the silicon nitride may be due to either residual stress or cutting damage. *0.5 mm*

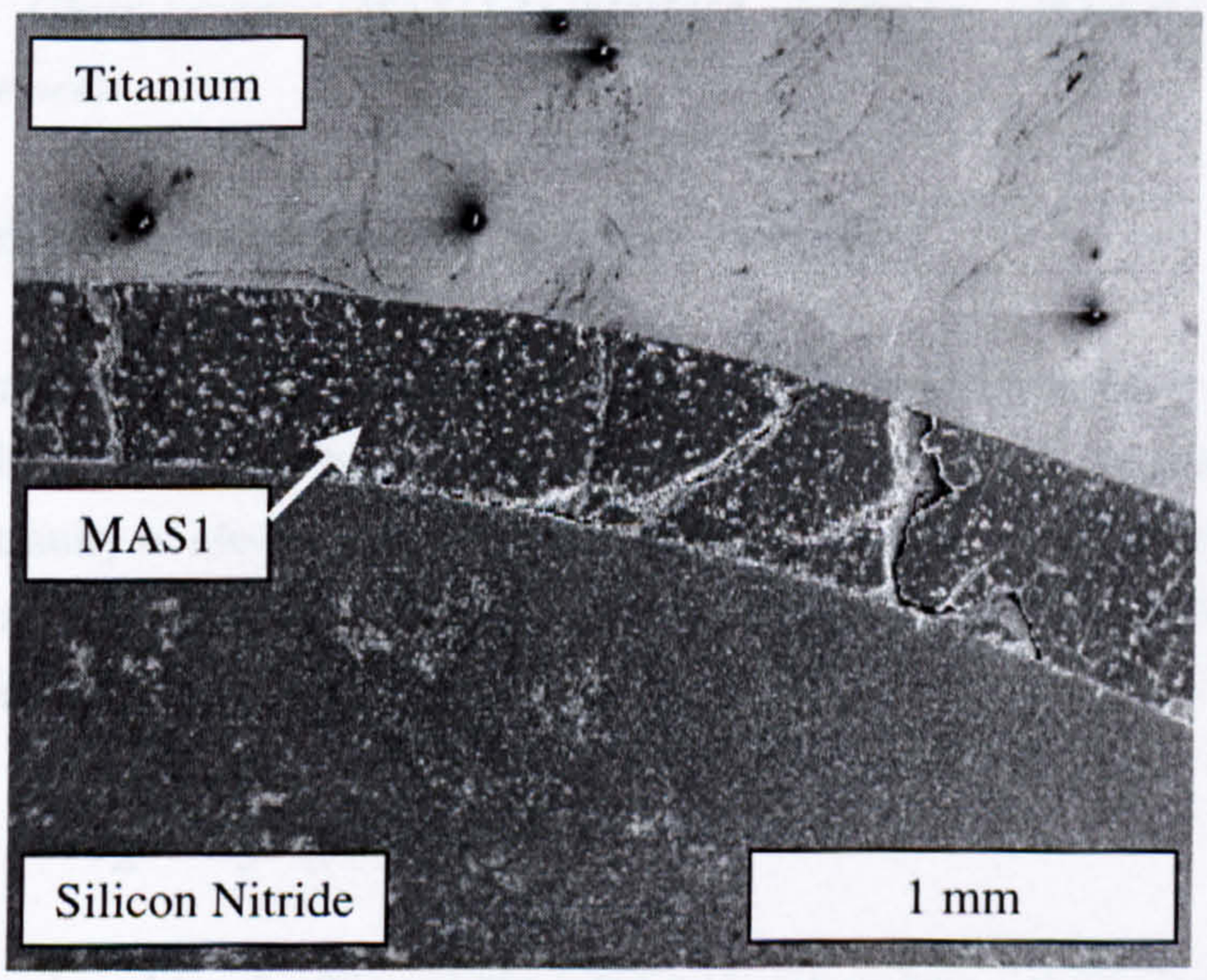

Figure 7.12: MAS interlayer showing TCE mismatch cracking and the level of porosity in the glass-ceramic.

A close up of the MAS1-Ti interface is shown in Figure 7.13, the thin interlayer was confirmed by EDX to be Ti_5Si_3.

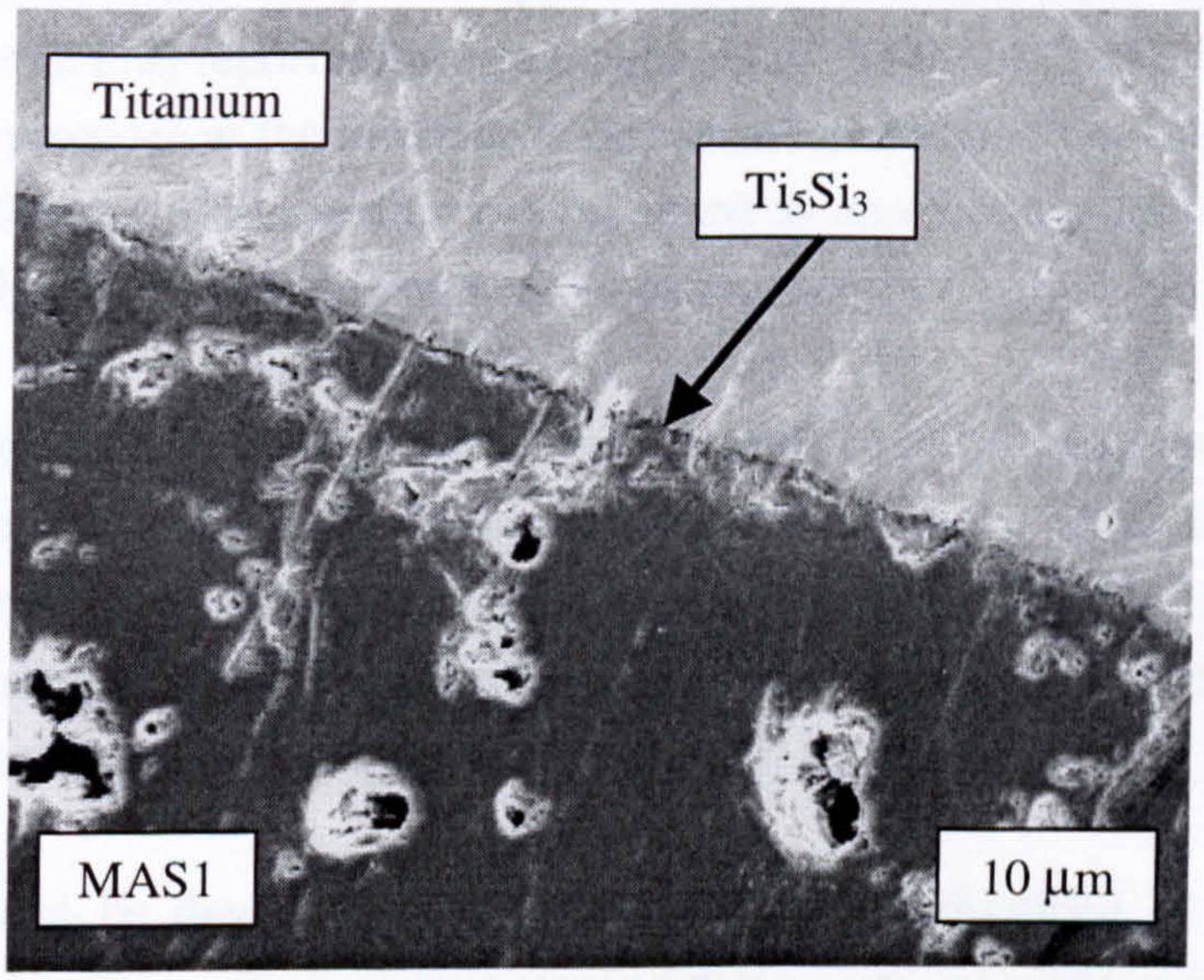

Figure 7.13: Glass-ceramic (MAS1)-Ti interface. A thin (~ 0.1 µm) interlayer of Ti_5Si_3 can be seen

7.2.5 Titanium glass-ceramic interactions - discussion

Pre-oxidation of the titanium was not necessary with this glass-ceramic composition (MAS1) as the Ti reacts to form a thin Ti_5Si_3 interlayer. This intermetallic phase provides continuity of electronic structure between the metallic bonding in the Ti and the ionic/covalent bonding in the glass-ceramic The Ti_5Si_3 is formed via Equation 3.1.2. (repeated below) with TiO_2 also formed.

$$8Ti + 5SiO_2 = Ti_5Si_3 + 3TiO_2 \qquad (3.1.2)$$

The TiO_2 is reduced by the Ti, and the oxygen is taken into solid solution Once a layer of Ti_5Si_3 is present, further direct reaction at the interface is prevented. Presumably, this is what occurred at the interface between the IMI 834 Ti alloy and a glass-ceramic with similar composition reported by Sutherland [8], where a thin unidentified interlayer was formed after 100 hours at 750°C. The thicker interlayer

formed at the higher joining temperature used in the current work (1100°C against 1000°C) enabled the interlayer to be identified. Conventional joining wisdom suggests that the presence of "brittle" intermetallics at the interface should be avoided. However, although they are brittle in comparison with metals, their fracture toughness compares favourably with typical values for oxide glass-ceramics. For example Min et al [12] report a fracture toughness of 2.69 ± 0.21 for a fine grained Ti_5Si_3 and its presence at the interface is not considered a problem. Sutherland [8] demonstrated that the glass-ceramic coating acted as an effective barrier to oxygen and extended the upper working temperature of the alloy.

The concept of a compression joint with a glass-ceramic interlayer has been successfully demonstrated using silicon nitride and titanium. With the geometry used in the current work the residual joining stress is still too high resulting in sub critical crack growth in the silicon nitride. This could be prevented by modifying the joining geometry and/or reducing the TCE mismatch.

If this joint is to be developed further the problems highlighted in Section 7.2 (mechanical properties, effect of heat treatment on joint microstructure, optimum joint geometry and TCE of glass-ceramic interlayer) would need to be addressed.

For Ti and Ti alloys a lower joining temperature would be particularly beneficial. The joining temperature could be reduced by at least 50°C with the current composition and further by slight compositional manipulation. However, for coating/joining to Ti or Ti alloys a less refractory glass-ceramic may be appropriate.

7.3 Joining silicon nitride to metals using a glass-ceramic interlayer - conclusions

An interlayer is required to provide continuity between the metallic bonding and the ionic-covalent bonding in the glass ceramic. The possibility of pre-oxidation to produce a strongly adherent oxide scale compatible with the oxide glass-ceramic has been investigated for both Nimonic 80A and titanium.

For Nimonic 80A, although the Cr_2O_3 based oxide layer produced by preoxidation does not directly provide the required continuity in the bonding between the Nimonic 80A and the glass-ceramic, this role is fulfilled by the $MgTi_2O_5$-Al_2TiO_5 solid solution phase formed by the reaction between the pre-oxidised surface and the glass/glass-ceramic. The Cr_2O_3 layer is not stable in contact with the glass and

reacts with the P_2O_5 present in the glass-ceramic to form chromium phosphide precipitates. This does not result in a coarse glass-ceramic (MAS) microstructure illustrating that the P_2O_5 does not fulfil the role of a conventional nucleating agent.

For Ti, although it is possible to preoxidise Ti to produce a strongly adherent oxide film this is not stable at the temperatures required for coating/joining with the glass-ceramic composition used in this work

However, pre-oxidation of the Ti was not required due to the formation of a Ti_5Si_3 interlayer by direct reaction between the glass/glass-ceramic and the titanium. This intermetallic phase provides the continuity of bonding required. TiO_2 is also produced as a result of the reaction, but it is reduced by Ti and the oxygen taken into solid solution. In comparison with Sutherland's work [8] the resulting Ti_5Si_3 interlayer and MAS glass-ceramic should be strongly adherent, act as an effective barrier to oxygen and extend the upper use temperature of the Ti.

Silicon nitride has been joined to both Nimonic alloy 80A and Titanium using a cylindrical compression joint geometry and a glass-ceramic interlayer.

For Nimonic alloy 80A a joining heat treatment was developed that resulted in the formation of a strong bond at both the glass-ceramic/silicon nitride and the glass-ceramic/Nimonic 80A interfaces. This joining heat treatment could have been combined with the solution precipitation heat treatment of the alloy. However, for the geometry chosen the residual joining stress generated on cooling was too great, resulting in failure of the silicon nitride. This indicated that either an altered geometry, or a reduced thermal expansion mismatch was required.

For the silicon nitride/titanium compression joint trials, the effect of the heat treatment on the microstructure was deliberately ignored. However, the concept of a compression joint with a glass-ceramic interlayer was successfully demonstrated. However sub-critical crack growth in the silicon nitride indicated that the level of stresses in the joint are marginal and need to be further reduced either by a slight alteration to the joint geometry and/or a smaller TCE mismatch.

References for Chapter 7

[1] Nimonic alloy 80A, Inco Alloys International Ltd, Publication Number IAI-5-1, 1991.

[2] Smialek J.L. and Meier G.H., Chapter 11 - High Temperature Oxidation, Superalloys II, 1987.

[3] Betteridge W. and Heslop J., The Nimonic Alloys 2nd Edition, Edward Arnold Publications Ltd.

[4] Hong F., Ph.D. Thesis, Interactions Between Glass-Ceramic Coatings and Metals, University of Warwick, 1991.

[5] Hong F. and Holland D., J. Non-Cryst. Solids 112 (1989) 357.

[6] Froes F.H., Yau T.L. and Wendinger H.G., Ti, Zr and Hf -Chapter 8 in Structure and Properties of Nonferrous Alloys, Volume Editor Matocha K.H., Volume 8 in Materials Science and Technology - A Comprehensive Treatment edited by Cahn R.W., Haasen P. and Kramer E.J., 1996.

[7] Destefani J.D., Introduction to Titanium and Titanium Alloys, ASM Metals Handbook, Volume 2, 10th edition 1990, Properties and Selection: Non-ferrous alloys and special purpose materials.

[8] Sutherland S., and Holland D., Glass Ceramic Coatings for the Protection of High Temperature Titanium Alloys, 1991.

[9] Simons E.N., Guide to Less Common Metals, Frederick Muller, 1967.

[10] Evans U.R., The Corrosion and Oxidation of Metals, Edward Arnold, 1960.

[11] Coddet C., Chaze A.M. and Beranger G., J. Mat. Sci. 22 2969-2974 (1987).

[12] Min K.S., Ardell A.J., Eck S.J. and Chen F.C., J. Mat. Sci., 30(21) 5479-5483 (1995).

Chapter 8: Conclusions and suggestions for further work

8.1 Sintered cordierite-enstatite glass-ceramics

The cordierite/enstatite glass-ceramics used in this project rely on the presence of B_2O_3 and P_2O_5 to control the dynamics of sintering and crystallisation. This work suggests that the primary role of B_2O_3 is to reduce the activation energy for the formation of α-cordierite directly from the glass, resulting in its increased formation at lower temperatures. The measured activation energy for α-cordierite formation when no additives were present (MASX) was 952 ± 57 kJ mol^{-1}, which was substantially reduced by the presence of B_2O_3 (540 ± 27 kJ mol-1) and P_2O_5 (668 ± 41 kJ mol^{-1}). The effect of B_2O_3 was of greater significance. The greatest effect was seen when both B_2O_3 and P_2O_5 were present, when the activation energy was reduced to 352 ± 26 kJ mol^{-1}. The reduction in activation energy for α-cordierite formation when both B_2O_3 and P_2O_5 are present shows excellent agreement with the results of Sung [1] , for their combined effect in a stoichiometric composition.

The reason for the effect of B_2O_3 on the crystallisation of α-cordierite is not clear, but is unlikely to be due to a viscosity effect. In contrast to P_2O_5, B_2O_3 increases the viscosity [2] in these glasses. The reduction in activation energy is likely to be related to the structural role that B_2O_3 plays, either in the glass or in the crystalline form. When both B_2O_3 and P_2O_5 are present, in addition to reducing the activation energy for α-cordierite formation, the crystallisation of μ-cordierite is suppressed, resulting in improved sintering behaviour. This is reflected in the measured activation energies for the crystallisation of μ-cordierite, which, for compositions MASX, MASB and MASP, did not differ significantly and were in the range 415-460 kJ mol^{-1}. When both B_2O_3 and P_2O_5 were present this was increased to 503-524 kJ mol^{-1}.

The effect of P_2O_5 may be related to the associated reduction in viscosity or may be due to small scale glass-in-glass phase separation. It is possible that the greater combined effect of B_2O_3 and P_2O_5, observed previously and in the current work, is due to some synergy in the sum of their separate effects. However, it is also possible that the presence of both species modifies the structural role of B_2O_3 and/or P_2O_5. To further determine the effect on nucleation and growth of B_2O_3 and P_2O_5, more information is needed on the structural role of B_2O_3 and P_2O_5 in the early stages of crystallisation. This would require the use of a technique which is sensitive to local order in the sample, e.g:, nuclear magnetic resonance spectroscopy.

For a full understanding of the phase development and sintering behaviour of these glass-ceramics, more consideration may have to be given to the heat evolved as a result of crystallisation.

8.2 Joining silicon nitride to silicon nitride

Cordierite/enstatite glass-ceramics have been successfully used to join silicon nitride to itself. Joining at 1050-1100°C in N_2 with an applied load of ~ 2.5 MPa resulted in joint strengths, measured in 4-pt bending, of 110-170 MPa. This is comparable to the intrinsic strength of the glass-ceramic and sufficient for practical applications. These strengths were obtained using an interlayer with a TCE (5.7 MK^{-1}) greater than that of the silicon nitride (3.0 MK^{-1}). The TCE mismatch resulted in cracking of the glass-ceramic interlayer perpendicular to the join.

The issue of the optimum TCE for the interlayer is still not resolved, although it is possible that a carefully chosen TCE mismatch can result in a strengthening of the relatively weak interlayer at the expense of weakening the much stronger silicon nitride either side. The optimum thermal expansion for the interlayer may be a function of interlayer thickness and joint geometry. Further work on the optimum TCE for an interlayer should result in improved joint strengths and an understanding of the mechanism resulting in high joint strengths.

The intrinsic strength and fracture toughness of glass-ceramics are still poor compared to many engineering ceramics. More work is required on the development of glass-ceramics with improved mechanical properties, incorporating microstructural toughening mechanisms. Given the exceptional mechanical properties reported for enstatite-based glass-ceramics [3], further work on similar compositions would be appropriate.

Joining at temperatures in excess of 1100°C resulted in crystallisation of the intergranular glass in the silicon nitride and compromised the mechanical properties. This illustrates the importance of considering the effect of the joining heat treatment on the materials being joined.

8.3 Joining silicon nitride to Nimonic 80A and Ti

The concept of a ceramic/metal compression joint with a glass-ceramic interlayer has been demonstrated for joining silicon nitride to both Nimonic alloy 80A and Ti.

The requirements for continuity of electronic structure are fulfilled: (1) at the Nimonic 80A/glass-ceramic interface by the $MgTi_2O_5$-Al_2TiO_5 solid solution phase formed by the reaction between the pre-oxidised surface of the alloy and the glass/glass-ceramic: and (2) at the Ti/glass-ceramic interfaces by the direct reaction between the glass/glass-ceramic and the Ti to form Ti_5Si_3. TiO_2 is also produced as a result of this reaction, but it is reduced by Ti and the oxygen taken into solid solution. In comparison with Sutherland's work [4] the resulting Ti_5Si_3 interlayer and MAS glass-ceramic should be strongly adherent, act as an effective barrier to oxygen, and extend the upper use temperature of the Ti.

The heat treatment for joining silicon nitride to Nimonic 80A using a glass-ceramic interlayer enabled strong bonds to be obtained at both the glass-ceramic/Nimonic 80A and glass-ceramic/silicon nitride interface, and could be combined with the solution precipitation heat treatment of the alloy. However, for the geometry chosen the residual joining stress generated on cooling was too great, resulting in failure of the silicon nitride. This indicated that either an altered geometry or a reduced thermal expansion mismatch was required.

For the Ti/silicon nitride compression joint, sub-critical crack growth in the silicon nitride indicated that the level of stresses in the joint are marginal and need to be further reduced, either by a slight alteration to the joint geometry and/or a smaller TCE mismatch.

8.4 Outlook for the use of glass-ceramics for ceramic-ceramic and ceramic-metal joining applications

Glass-ceramics present an attractive combination of properties for some joining applications. They offer many of the advantages of glass together with improved mechanical and high temperature properties, and greater flexibility and control of thermal expansion.

Joints with sufficient strength for practical applications have been demonstrated for joining like materials. The optimisation of the TCE of the interlayer as a function of joint geometry, and the effect of the resulting residual joining stresses have yet to be resolved.

More progress is still required in the development of solutions for joining ceramics to metals if the full benefits of ceramic materials are to be realised. This is

principally related to the fundamental thermomechanical problem of TCE mismatch. The production of practical joints for high temperature applications, especially where large joined areas are involved, remains problematic. The long term stability and thermal cycling behaviour of joints also needs further consideration.

For some applications, the use of a joint with graded composition (and TCE) may offer a satisfactory solution. The use of graded glass joints has been successful in joining glasses with mismatched TCE. A graded glass-ceramic joint is able to offer a more refractory solution than a graded glass joint, and can withstand a higher level of residual joining stress. A procedure for estimating the stress in the joint has been outlined. In order to bridge a significant TCE mismatch, the length of the graded joint must be significant compared to the diameter, and therefore to join silicon nitride to a nickel superalloy, a graded glass-ceramic joint several diameters in length would be required. This restriction may be eased by the development of higher fracture toughness glass-ceramics.

The use of ceramic interlayers with designed microstructures, which allow transformation related strain to accommodate TCE mismatch, may be an idea worth further investigation. The possible use of the martensitic phase transformation between enstatite polymorphs is particularly promising.

Further progress in ceramic metal joining technology is likely to arise from a methodical interdisciplinary approach.

References for Chapter 8

[1] Sung Y-M., J. Mater. Sci. 31 (1996) 5421-5427.

[2] Geiss E.A. and Knickerbocker S.J., J. Mater. Sci. Letts., 4 (1985) 835-837.

[3] Beall G.H., J. Non-Cryst. Solids 129 (1991) 163-173.

[4] Sutherland S., and Holland D., Glass Ceramic Coatings for the Protection of High Temperature Titanium Alloys, Unpublished work, (1991).

Appendix I: Composition and source of precursor materials

SiO_2 - Wacomcil Japan Quartz

Contaminant	p.p.m
Al_2O_3	281.7
Fe_2O_3	5.6
Na_2O	5.7
Cr	0.4
Co	0.2
Cu	0.2
Mn	0.2
Ni	0.2

Al_2O_3

BDH - GPR

Contaminant	Wt %
Water soluble matter	0.5
Sulphate (SO_4)	0.05
Fe	0.02

Loss on ignition - 1.0 %

MgO

BDH - GPR Magnesium Oxide (heavy)

Contaminant	Wt. %
Chloride (Cl)	0.05
Sulphate (SO_4)	1.0
Arsenic (As)	0.0004
Iron (Fe)	0.07
Lead (Pb)	0.002

Loss on ignition at 1000°C - 5.0 %

H_3BO_3

BDH Analar Orthoboric Acid - minimum assay 99.8 %

Contaminant	Wt. %
Non esterifiable impurities	0.05
Cl	0.0003
Phosphate	0.0005
Sulphate (SO_4)	0.0005
Arsenic	0.00005
Calcium	0.002
Copper	0.0002
Heavy metals (As, Pb)	0.0005
Iron	0.0001
Lead	0.0005
Magnesium	0.0005

P_2O_5

BDH GPR Aluminium orthophosphate

Contaminant	Wt. %
Chloride	0.005
Sulphate (SO_4)	0.05
Iron	0.01

Loss on ignition at 1000°C - 3 %

ZrO_2

BDH Chemicals Ltd, Poole - lab reagent.
- level of contamination not known.

$ZrSiO_4$

Zircon X10 - Super refractories Ltd., St. Marys, Winchcomb, Glos.
- level of contamination not known.

Appendix II: Composition and source of DTA standards

SiO_2

Wacomsil Japan Quartz - composition given in Appendix I.

$SrCO_3$

Fisons Scientific Equipment (99%)

Contaminant	Wt. %
Fe	< 0.002
Cl	< 0.005
SO_4	< 0.01